

**Exploring the therapeutic potential of the  
apelin receptor signalling axis, and  
angiotensin-converting enzyme 2 (ACE2)  
as the SARS-CoV-2 viral entry receptor, in  
the cardiovascular system**

By

Thomas Lloyd Williams

Pembroke College

Experimental Medicine and Immunotherapeutics

Research Supervisor

Professor Anthony P. Davenport

July 2022

This dissertation is submitted for the degree of

Doctor of Philosophy

## **Declaration**

This thesis is the result of my own work and includes nothing which is the outcome of work done in collaboration except as declared in the Preface and specified in the text.

It is not substantially the same as any work that has already been submitted before for any degree or other qualification except as declared in the Preface and specified in the text.

The length of this does thesis not exceed the prescribed word limit for the Clinical Medicine and Clinical Veterinary Medicine Degree Committee (60,000 words).

Thomas Williams

## Contents

Acknowledgements .....	9
Publications .....	11
Published abstracts .....	13
Presentations .....	14
Personal Training Record.....	16
Abstract .....	18
Abbreviations & Acronyms .....	19
Tables & Figures .....	24
Chapter 1. Thesis introduction .....	30
1.1. Background .....	30
1.2. Apelin receptor .....	32
1.2.1. G protein-coupled receptors.....	32
1.2.2. Apelin receptor overview .....	33
1.2.3. Apelin receptor expression.....	33
1.2.4. Apelin peptides .....	34
1.2.5. ELA peptides.....	35
1.2.6. Apelin receptor signalling .....	36
1.3. Apelin receptor in physiology .....	37
1.3.1 Apelin receptor in cardiovascular development .....	37
1.3.2. Apelin receptor in cardiovascular regulation .....	38
1.3.3. Apelin receptor in angiogenesis .....	42
1.3.4. Apelin receptor in haemostasis .....	42
1.3.5. Apelin receptor in fluid homeostasis .....	43
1.3.6. Apelin receptor in metabolism .....	44
1.4. Apelin receptor in pathophysiology .....	44
1.4.1. Apelin receptor in pulmonary arterial hypertension.....	45
1.4.2. Apelin receptor in heart failure.....	46
1.4.3. Apelin receptor in HIV .....	47
1.4.4. Apelin receptor in immune-mediated injury.....	48
1.4.5. Apelin receptor in diabetes.....	48
1.5. Apelin receptor as a therapeutic target .....	50
1.5.1. G protein bias.....	50
1.5.2. Peptide therapeutics .....	50
1.5.3. Small molecule therapeutics.....	53

1.6. Apelin receptor structure.....	55
1.7. Apelin receptor mutations .....	61
1.7.1. GPCR mutation.....	61
1.7.2. The NIHR BioResource Rare Diseases BRIDGE consortium sequencing project .....	62
1.8. Aims for the apelin receptor .....	63
1.9. ACE2.....	64
1.9.1. ACE2 overview .....	64
1.9.2. ACE2 expression .....	64
1.10. ACE2 in physiology.....	65
1.10.1. Renin angiotensin aldosterone system.....	65
1.10.2. ACE2 counter-regulates the renin angiotensin aldosterone system.....	66
1.10.3. ACE2 substrates outside the RAAS .....	66
1.10.4. ACE2 and the apelin signalling axis .....	66
1.10.5. ACE2 in the gastrointestinal tract .....	68
1.11. ACE2 in pathophysiology.....	68
1.11.1. ACE2 in cardiovascular disease.....	68
1.11.2. ACE2 in Hartnup disease .....	69
1.11.3 ACE2 as a viral entry receptor.....	69
1.12. ACE2 structure .....	72
1.13. Aims for ACE2.....	73
<b>Chapter 2. Materials &amp; Methods.....</b>	<b>74</b>
2.1. Overview .....	74
2.2. COVID-19 statement .....	74
2.3. Materials.....	74
2.4. Cell culture .....	75
2.4.1. General cell culture .....	75
2.4.2. Generation of apelin receptor plasmid DNA .....	75
2.4.3. Transfection of cells with apelin receptor DNA .....	76
2.4.4. hESC cell culture.....	76
2.4.5. hESC differentiation to cardiomyocytes.....	77
2.4.6. Generation of shRNA apelin receptor knockdown hESC-CMs.....	78
2.4.7. Generation of R168H variant apelin receptor cardiomyocytes.....	79
2.5. Cell infection with virus in SARS-CoV-2 studies.....	79
2.5.1. Pseudotyped virus production .....	79
2.5.2. Pseudotyped viral infection of hESC-CMs.....	80
2.5.3. SARS-CoV-2 viral infection of hESC-CMs.....	81

2.6. Protein preparation .....	81
2.6.1. Cell membrane preparation .....	81
2.6.2. Tissue homogenisation .....	82
2.6.3. Protein assay .....	82
2.7. Radioligand binding .....	83
2.7.1. Fixed concentration binding .....	83
2.7.2. Saturation binding .....	84
2.7.3. Competition binding .....	84
2.7.4. Radioligand binding data analysis .....	84
2.8. <i>In vitro</i> assays.....	86
2.8.1. Dynamic mass redistribution assay .....	86
2.8.2. cAMP accumulation assay .....	87
2.8.3. Internalisation assay .....	91
2.9. Imaging .....	93
2.9.1. Fluorescent markers .....	93
2.9.2. Opera Phenix High Content Screening System .....	94
2.9.3. Opera Phenix acquisition .....	94
2.9.4. Opera Phenix analysis .....	95
2.9.5. Zeiss Axio Scan Z1 slide scanner .....	96
2.9.6. Zeiss LSM 510 Meta Inverted Confocal Microscope.....	96
2.9.7. Multiphoton Microscope Leica TCS SP8 MP .....	97
2.9.8. Data analysis and statistics .....	97
Chapter 3. Design and characterisation of novel fluorescent peptide ligands at the apelin receptor .....	98
3.1. Introduction.....	98
3.2. Methods.....	100
3.2.1. Design of four novel fluorescent apelin receptor ligands.....	100
3.2.2. Radioligand binding assays.....	100
3.2.3. <i>In vitro</i> GPCR assays .....	101
3.2.4. Human tissue .....	101
3.2.5. Fluorescent ligand binding in human kidney tissue.....	102
3.2.6. Zeiss LSM 510 Meta Inverted Confocal Microscope.....	102
3.2.7. Fluorescent ligand binding in cells.....	102
3.2.8. Opera Phenix High Content Screening.....	103
3.2.9. Data analysis and statistics .....	103
3.3. Results .....	104
3.3.1. Design of the four novel fluorescent ligands .....	104

3.3.2. Validation of apelin receptor binding in CHO-APLNR .....	106
3.3.3. Validation of the four novel fluorescent ligands in competition binding .....	108
3.3.4. Validation of the four novel fluorescent peptides in in vitro GPCR assays .....	109
3.3.5. Apelin647 is a versatile tool for exploring apelin receptor pharmacology.....	113
3.3.6. Apelin647 allows for visualisation of apelin receptor internalisation.....	116
3.4. Discussion .....	118
3.4.1. Novel fluorescent ligands bind and activate the apelin receptor .....	118
3.4.2. Apelin488 and apelin647 bind to apelin receptor in the kidney .....	120
3.4.3. Apelin647 binds to apelin receptor in human embryonic stem cell-derived cardiomyocytes .....	120
3.4.4. Exploration of apelin receptor pharmacology using apelin647 .....	121
3.4.5. Observation of apelin receptor internalisation in near real-time .....	121
3.5. Conclusions.....	124
Chapter 4. Characterisation of apelin receptor variants identified in a patient cohort in the NIHR BRIDGE project .....	125
4.1. Introduction.....	125
4.2. Methods.....	130
4.2.1. Cell culture .....	130
4.2.2. Radioligand binding assays.....	130
4.2.3. Assessment of apelin receptor expression, membrane localisation, and fluorescent ligand binding .....	130
4.2.4. Opera Phenix High Content Screening.....	131
4.2.5. In vitro GPCR assay.....	131
4.2.6. Data analysis and statistics .....	132
4.3. Results .....	132
4.3.1. Several apelin receptor variants identified in the BRIDGE project show perturbed binding in a preliminary screen.....	132
4.3.2. Apelin receptor variants can impact receptor expression at the membrane .....	135
4.3.3. Fluorescent ligands identify further effects of apelin receptor variants on binding .....	137
4.3.4. Further binding studies confirm the impact of the T89M variant on binding of ELA ligands .....	140
4.3.5. Assessment of apelin receptor variants on GPCR function .....	142
4.3.6. R168H is unable to bind apelin647 in a clinically relevant cardiomyocyte model .....	145
4.4. Discussion .....	146
4.4.1. Apelin receptor variants identified in the BRIDGE project impact on ligand binding, receptor density, and receptor expression.....	146
4.4.2. Discrepancies in apelin and ELA binding at the T89M apelin receptor variant..	147

4.4.3. The R168H variant shows abolished function.....	149
4.4.4. The V38L variant shows good binding, but little internalisation, of apelin647....	149
4.4.5. The R168H variant does not bind apelin647 in cardiomyocytes .....	149
4.5. Interpretation of results .....	150
4.5.1. Summary of the V38L variant.....	150
4.5.2. Summary of the T89M variant .....	150
4.5.3. Summary of the R168H variant .....	151
Chapter 5. ACE2 as the SARS-CoV-2 entry receptor in cardiomyocytes.....	152
5.1. Introduction.....	152
5.2. Methods.....	156
5.2.1 Cell culture .....	156
5.2.2. Opera Phenix High Content Screening.....	156
5.2.3. Immunohistochemistry and slide scanner imaging .....	157
5.2.4. Pseudotyped virus production and infection of hESC-CMs.....	158
5.2.5. SARS-CoV-2 infection in hESC-CMs .....	159
5.2.6. Data analysis and statistics .....	159
5.3. Results .....	160
5.3.1 Human left ventricle and hESC-CMs express ACE2 and ancillary proteins utilised by SARS-CoV-2 to infect host cells .....	160
5.3.2. Infection of hESC-CMs with SARS-CoV-2 spike pseudotyped virus, and identification of novel inhibitors of infection .....	162
5.4. Discussion .....	167
5.4.1. Cardiomyocytes express ACE2 and the ancillary protein machinery necessary for SARS-CoV-2 infection.....	167
5.4.2. hESC-CMs provide a model for SARS-CoV-2 spike protein pseudotyped viral infection and screen for novel inhibitors .....	168
5.4.3. Drug treatments and pseudotyped virus were not toxic in cardiomyocytes .....	170
5.4.4. Cardiomyocytes are susceptible to SARS-CoV-2 virus.....	171
5.5. Conclusions.....	171
Chapter 6. Tissue distribution of ACE2 and a novel short ACE2 isoform – implications in COVID-19 .....	173
6.1. Introduction.....	173
6.2. Methods.....	178
6.2.1. Immunohistochemistry and slide scanner imaging .....	178
6.2.2. Immunocytochemistry – ACE2 antibody validation .....	179
6.2.3. H&E staining .....	180
6.2.4. Slide Scanner quantification.....	180
6.2.5. Opera Phenix High Content Screening.....	184

6.2.6. Multiphoton Microscope Leica TCS SP8 MP imaging.....	184
6.3. Results .....	184
6.3.1. Tissues and organs targeted by SARS-CoV-2 express ACE2 .....	184
6.3.2. The short dACE2 isoform localises to epithelial cells in lung and liver but is not enriched in the kidney or heart .....	187
6.3.3. Tissue structures that are enriched with dACE2 show low binding with a fluorescently tagged spike protein monomer .....	194
6.4. Discussion .....	196
6.4.1. ACE2 is present in organs infected and/or damaged by SARS-CoV-2 .....	196
6.4.2. Short dACE2 shows distinct localisation in epithelial cells in lung and liver .....	196
6.4.3. Implications of dACE2 in SARS-CoV-2 infection .....	198
6.5. Conclusions .....	199
7. Concluding remarks .....	201
7.1. Apelin receptor summary .....	201
7.2. Apelin receptor study results.....	203
7.3. ACE2 summary .....	206
7.4. ACE2 results .....	208
7.5. Final conclusions .....	211
Bibliography .....	212

## Acknowledgements

Many thanks to my supervisor, Professor Anthony Davenport for all of his guidance, encouragement, and support throughout my PhD. He has always found the time to discuss issues and ideas, no matter how big or small, and is always willing to share his own expertise and experience of scientific research, general knowledge, and college dinners. His guidance in the completion of this thesis itself is also much appreciated, as is his enthusiasm for publishing and presenting data at conferences to ensure that research is shared with anyone and everyone who wishes to access it.

Many thanks also to Dr Janet Maguire and Ms Rhoda Kuc, for their invaluable insight into laboratory technique, data analysis, scientific writing, and radioligand binding. They have both helped me become not only a better researcher, but a more well-rounded individual over the course of my PhD. Their kindness, friendliness, and provision of cake can also not go unacknowledged.

Thanks must be given to the other students in Professor Davenport's lab. I have seen Cai Read and Duuamene Nyimanu become Drs in my time here, and they were instrumental in my training in the laboratory, in academia, and in Cambridge itself. I am lucky to consider myself their friends. Dr Nicola Owen, Dr Petra Sulentic, and Dr George Abraham, who have worked in clinical roles in Professor Davenport's group, have provided a 'behind the curtain' look at the translation of scientific research to people and patients, which has been a privilege to observe and be a part of. Special thanks to my colleague and friend, Ms Robyn Macrae, whose own research has overlapped considerably with mine, meaning we spent considerable time helping each other in the lab and office, all while signing along to the radio. I am sure we will remain good friends for life.

I particularly thank the Wellcome Trust for funding this PhD project, and introducing me to the other students on this programme, Dr Filip Cvetko, Dr Joy Shih, and Dr Vicky AuYeung. I must also mention Dr Sam Galvin who joined us at the same time on the BBSRC programme, and with whom I lived, together with Filip, for two years. They will all be friends for life as well.

I must also thank collaborators of the work described in this thesis. Particular thanks go to Mr Gregory Strachan in the MRL Imaging Hub, and collaborators at Sosei Heptares (Mr Jason Brown, Dr Heather Currinn, and Dr Alastair Brown) who have been instrumental in allowing me to conduct research in an industrial setting through the ORBIT (Opportunities in Receptor Biology for Industrial Translation) collaboration.

Thank you to the Wellcome Trust for providing the funding and support needed to complete the work outlined in this thesis. Appreciation is also given to the British Pharmacological Society for the frequent opportunities to present work at national conferences, and for providing travel grants to make it to these events when we were able to.

Thank you to Pembroke College for hosting me as a graduate student in Cambridge over my PhD. It has been, and still is, a privilege to call this college my home. The graduate community at the college has been a great source of knowledge, inspiration, and friendship. Particular mention must go to Ms Helena Gellersen and Ms Anna Francis, fellow scientists at Pembroke – my experience of Cambridge was so much better for having become friends with them.

I would like to thank my family, my mother and father (Catherin and Phil Williams) and sister (Olivia Williams) for their love and support both in my PhD, and in all things outside of it, and for reminding me that this thesis wasn't going to write itself. I would not have made it here without them. Thanks to my best friend, Jack Thompson, for keeping me sane, and providing top tier entertainment whenever it was needed. Finally, I would like to thank Ms Aisha Sobey, my wonderful partner, who has been amazingly supportive, encouraging and just all around lovely... and who somehow put up with me during the writing of this thesis.

## Publications

**Williams, T.L.**, Strachan, G., Macrae, R.G.C., Kuc, R.E, Nyimanu, D., Paterson, A.L., Sinha, S., Maguire, J.J. & Davenport, A.P. Differential expression in humans of the viral entry receptor ACE2 compared with the short deltaACE2 isoform lacking SARS-CoV-2 binding sites. *Scientific Reports* (2021).

**Williams, T.L.**, Colzani, M.T., Macrae, R.G.C., Robinson, E.L., Bloor S., Greenwood E.J.D., Zhan, J. R., Strachan, G., Kuc, R.E., Nyimanu, D., Maguire, J.J., Lehner, P.J., Sinha, S. & Davenport, A.P. Human embryonic stem cell-derived cardiomyocytes express SARS-CoV-2 host entry proteins: screen to identify inhibitors of infection. *Communications Biology* **4**, 926 (2021).

Macrae, R.G.C., Colzani, M.T., **Williams, T.L.**, Bayraktar, S., Kuc, R.E., Bernard, W.G., Robinson, E.L., Maguire, J.J., Sinha, S. & Davenport, A.P. Knockdown of apelin receptor reduces cardiomyocyte differentiation efficiency and contractility of human embryonic stem cell-derived cardiomyocytes. *Cardiovascular Research* **00**, 1–12 (2022)

Brevini, T., Maes, M., Webb, G.J., W.T.H., Forrest, S., Mlcochova, P., Dillon, S., Varankar, S., Darvish-Damavandi, M., Mulcahy, V.L., Kuc, R.E., **Williams, T.L.** ... & Sampaziotis, F. FXR inhibition reduces ACE2 expression, SARS-CoV-2 infection and may improve COVID-19 outcome. *Nature* (2021). In review. Pre-print available on BioRxiv (<https://www.biorxiv.org/content/10.1101/2021.06.06.446781v1>).

Read, C., Nyimanu, D., Yang, P., Kuc, R.E., **Williams, T.L.**, Fitzpatrick, C.M., Foster, R., Glen, R.C., Maguire, J.J. & Davenport, A.P. The G Protein Biased Small Molecule Apelin Agonist CMF-019 is Disease Modifying in Endothelial Cell Apoptosis *In Vitro* and Induces Vasodilatation Without Desensitisation *In Vivo*. *Front Pharmacol.* **11**: 588669 (2021).

Read, C., Yang, P., Kuc, R.E., Nyimanu, D., **Williams, T.L.**, Glen, R.C., Holt, L.J., Arulanantham, H., Smart, A., Davenport, A.P. & Maguire, J.J. Apelin peptides linked to anti-serum albumin domain antibodies retain affinity in vitro and are efficacious receptor agonists *in vivo*. *Basic Clin Pharmacol Toxicol.* 6: 96-103 (2020).

Read, C., Nyimanu, D., **Williams, T.L.**, Huggins, D.J., Sulentic, P., Macrae, R.G.C., Yang, P., Glen, R.C., Maguire, J.J. & Davenport, A.P. International Union of Basic and Clinical Pharmacology. CVII. Structure and Pharmacology of the Apelin Receptor with a Recommendation that Elabela/Toddler Is a Second Endogenous Peptide Ligand. *Pharmacological Reviews* 71(4): 467-502 (2019).

Nyimanu, D., Kuc, R.E., **Williams, T.L.**, Bednarek, M., Ambery, P., Jermutus, L., Maguire, J.J. & Davenport, A.P. Apelin-36-[L28A] and Apelin-36-[L28C(30kDa-PEG)] peptides that improve diet induced obesity are G protein biased ligands at the apelin receptor. *Peptides.* 121: 170139 (2019).

Yang, P., Read, C., Kuc, R.E., Nyimanu, D., **Williams, T.L.**, Crosby, A., Buonincontri, G., Southwood, M., Sawiak, S.J., Glen, R.C., Morrell, N.W., Davenport, A.P. & Maguire, J.J. A novel cyclic biased agonist of the apelin receptor, MM07, is disease modifying in the rat monocrotaline model of pulmonary arterial hypertension. *Br J Pharmacol.* 176(9): 1206-1221 (2017).

## Published abstracts

Macrae, R.G.C., **Williams, T.L.**, Colzani, M.T., Bloor, S., Zhan, J.R., Nyimanu, D., Kuc, R.E., Maguire, J.J., Lehner, P.J., Sinha, S. & Davenport, A.P. Abstract 10463: Angiotensin-Converting Enzyme 2 (ACE2) is Rate-limiting for Severe Acute Respiratory Syndrome Coronavirus 2 (SARS-CoV-2) Viral Infection in Beating Stem Cell-Derived Cardiomyocytes. *Circulation*. 2021.

Davenport, A.P., Nyimanu, D., **Williams, T.L.**, Kuc, R.E., Foster, R., Glen, R.C. & Maguire, J.J. Abstract 18896: G Protein Biased Peptide Apelin Receptor Agonist Reverses Sugen/hypoxia-induced Pulmonary Hypertension as Effectively as the Endothelin Antagonist, Macitentan. *Circulation Research*. 2020.9

## **Presentations**

*'Mining the 100,000 Genome Bridge Project and validating new receptor targets in cardiovascular disease'*

Oral communication at BPS Pharmacology 2021 Apelin Symposium, online (Invited Speaker)

*'Human embryonic stem cell-derived cardiomyocytes express SARS-CoV-2 host entry proteins: a drug screen model that identifies two novel inhibitors of viral entry'*

Oral communication at BPS Pharmacology 2021, online

*'ACE2, the viral entry 'receptor' for SARS-CoV-2 in the human cardiovascular system'*

Oral communication at Cambridge Institute of Therapeutic Immunology & Infectious Disease (CITIID) COVID-19 Meeting 2021, online

*'High content high resolution confocal imaging to determine fluorescent ligand binding at apelin receptor variants identified in human patients with rare cardiovascular disease'*

Poster and Flash talk at BHF CRE Annual Research Symposium 2021, online; Poster at BPS Pharmacology 2020, online

*'Apelin receptor mutations identified in human patients with rare diseases impact receptor distribution, binding, and function'*

Oral communication at BPS Pharmacology 2019, Edinburgh (UK); Metabolic Research Laboratories (MRL) Student Symposium 2019, Cambridge (UK)

*'High content high resolution confocal imaging to characterise mutations in the apelin receptor identified in patients from the 13,000 Genomes Project'*

Poster at Milner Therapeutics Symposium 2019, Cambridge (UK)

*'Using High-Content Imaging to characterise apelin receptor mutations identified in patients with rare cardiovascular diseases'*

Poster at Physiological Society, Biochemical Society and British Pharmacological Society Life Sciences 2019: Post-Translational Modifications and Cell Signalling Meeting, Nottingham (UK)

*'HIGH CONTENT HIGH RESOLUTION CONFOCAL IMAGING TO CHARACTERISE MUTATIONS IN THE APELIN RECEPTOR IDENTIFIED IN PATIENTS FROM THE 100,000 GENOMES PROJECT'*

Poster at BSCR/BAS Joint Spring Meeting 2019, Manchester (UK); Department of Medicine Research Day 2019, Cambridge (UK)

*'Mining 13,000 genomes to characterise rare apelin receptor mutations in disease'*

Poster at BPS 7th Focused Meeting on Cell Signalling 2018, Nottingham (UK); BAS Annual Meeting 2018, Cambridge (UK); Department of Medicine Research Day 2018, Cambridge (UK)

*'Does apelin signalling act in a paracrine manner to influence glucose uptake in the gastro-intestinal tract?'*

Poster at BPS Pharmacology 2017, London (UK)

## **Personal Training Record**

### ***Laboratory equipment training***

March 2019	MRL Zeiss Axio Scan Z1 slide scanner training
Nov 2018	MRL Opera Phenix High Content Screening System training
Nov 2018	CRUK Image Analysis with Fiji
March 2018	MRL Multiphoton Microscope Leica TCS SP8 MP training
March 2018	BRC Phenotyping Hub BD FACS Cant II flow cytometry training
Feb 2018	ACCI Level 6 Cell Culture Induction training
Oct 2017	MRL Zeiss LSM 510 Meta Inverted Confocal Microscope training

### ***Safety courses***

2016-2021	EMIT Annual Health & Safety seminar
2016-2021	Fire Safety Training
2016-2021	Equality & Diversity Training
Sep 2017	Bribery Act Training
Sep 2017	Health & Safety Induction
Sep 2017	NHS Fire Safety Seminar
March 2017	IMS Safety Seminar
Jan 2017	Sharps Safety Seminar
Oct 2016	Radioactive Substances
Oct 2016	Chemical Safety Course
Oct 2016	Microbiological Safety Cabinets
Oct 2016	Health & Safety Induction
Oct 2016	Graduate Induction Seminars

***Graduate School of Life Sciences (GSLs) Core Skills and Training Programme (CSTP)***

April 2018	CSTP Time Management Package
Feb 2018	CSTP Writing an Academic Report Course
Dec 2016	CSTP Introduction to Scientific Writing Course
Oct 2016	CSTP Skills Analysis Survey
Oct 2016	CSTP Development Plan

***Other***

Jan 2018	Effective Researcher Training Day
March 2017	IMS volunteer at Cambridge Science Festival
Jan 2017	Rising Stars Public Engagement Course
Oct-Dec 2016	BBSRC DTP Statistics Course
Nov 2016	The "Big Four" Databases For Your Literature Search Course
Oct 2016	Research Integrity Course

## Abstract

The apelin receptor is a class A GPCR that binds two endogenous peptide ligands, apelin and elabela/Toddler (ELA), to induce positive cardiac inotropy and vasodilatation in the cardiovascular system. The apelin receptor provides a tractable therapeutic target for multiple cardiovascular diseases, such as pulmonary arterial hypertension, heart failure, and bleeding disorders, where the receptor also mediates antithrombotic responses.

Here, four novel fluorescent ligands, designed as functional analogues of endogenous apelin and ELA peptides, were validated and used as a versatile tool for the qualitative and quantitative determination of pharmacological parameters of the apelin receptor. The fluorescent ligands were also used, with other techniques, to study apelin receptor variants identified in the genomes of human patients with rare cardiovascular diseases recruited to the NIHR BRIDGE project. The V38L, T89M, and R168H variants showed distinct effects on apelin receptor pharmacology. V38L reduced receptor localisation at the membrane, but was able to bind fluorescent apelin and showed little internalisation. T89M, uniquely, was able to bind fluorescent apelin but not fluorescent ELA. R168H was unable to bind apelin receptor ligands, and was consequently inactive, pointing to loss of pharmacological function.

ACE2 is a zinc-metalloproteinase type 1 transmembrane protein that cleaves angiotensin peptides to counter-regulate the renin-angiotensin-aldosterone system in the cardiovascular system and mediate hypotensive responses. The protein also acts as the membrane receptor for human coronaviruses, including SARS-CoV-2, the cause of the COVID-19 pandemic.

Here, ACE2 was identified in human left ventricle tissue, and in a human embryonic stem cell-derived cardiomyocyte model that was used to screen for novel inhibitors of viral infection. Benztropine (an inhibitor targeting B<sup>0</sup>AT1 that complexes with ACE2) and DX600 (a peptide antagonist of ACE2), were shown to exhibit antiviral properties for the first time. Additionally, the tissue expression and distribution of a recently identified novel short ACE2 isoform that does not bind SARS-CoV-2, revealed enrichment of the short isoform in respiratory and bile duct epithelia.

The work in this thesis advancement our understanding of both the apelin receptor and ACE2 as regulators human cardiovascular health and disease.

## Abbreviations & Acronyms

ACE = angiotensin-converting enzyme

ACE2 = angiotensin-converting enzyme 2

ADAM17 = A disintegrin and metallo-protease 17

ADP = adenosine diphosphate

AGTRL1 = angiotensin like receptor 1, alias for apelin receptor

Akt = protein kinase B

AlbudAb = anti-serum albumin domain antibody

AMPK = 5' adenosine monophosphate-activated protein kinase

ANOVA = analysis of variance

*APELA* = human ELA gene, apelin receptor early endogenous ligand

Apelin = APJ endogenous ligand

APJ = former name for apelin receptor

*APLN* = human apelin peptide gene

*APLNR* = human apelin receptor gene

aplnra = zebrafish apelin receptor type a

aplnrb = zebrafish apelin receptor type b

AT<sub>1</sub> = angiotensin II type 1 receptor

AT<sub>2</sub> = angiotensin II type 2 receptor

AVP = arginine vasopressin

B<sup>0</sup>AT1 = sodium-dependent neutral amino acid transporter

B<sub>1</sub> = bradykinin receptor 1

B<sub>2</sub> = bradykinin receptor 2

B<sub>max</sub> = receptor density

BMI = body mass index

BMPR2 = bone morphogenetic protein type 2 receptor

BMPR4 = bone morphogenetic protein type 4 receptor

BPS = British Pharmacological Society

BSA = bovine serum albumin

Ca<sup>2+</sup> = calcium ion

CAB = cell assay buffer

Caco-2 = human colon carcinoma cell

Calu-3 = human lung cancer cell  
CaM = calmodulin  
cAMP = cyclic adenosine monophosphate  
CCR3 = C-C chemokine receptor type 3  
CCR5 = C-C chemokine receptor type 5  
CD = cluster of differentiation  
CD13 = aminopeptidase N  
cGMP = cyclic guanosine monophosphate  
CHO = Chinese hamster ovary cell  
CHO-APLNR = CHO-K1 cells stably expressing human apelin receptor  
CHO-K1 = subclone of CHO cell line  
CHO-WT = CHO-K1 cells left untransfected  
CITIID = Cambridge Institute of Therapeutic Immunology & Infectious Disease  
CO<sub>2</sub> = carbon dioxide  
COVID-19 = corona virus disease 2019  
CPR = cell plating reagent  
CRISPR = clustered regularly interspaced short palindromic repeats  
*CTSB* = human cathepsin B gene  
*CTSL* = human cathepsin L gene  
CXCR4 = C-X-C chemokine receptor type 4  
dACE2 = short *delta*ACE2 isoform  
DAG = diacylglycerol  
DMEM = Dulbecco's Modified Eagle Medium  
DMR = dynamic mass redistribution  
DMSO = dimethyl sulfoxide  
E8 = essential 8 media  
EA = enzyme acceptor  
EC<sub>50</sub> = concentration of drug required to elicit 50% of maximum effect  
ED = enzyme donor  
eGFP = enhanced green fluorescent protein  
ELA = shorthand for elabela/Toddler  
Elabela = epiboly late because of endoderm late  
EMA = European Medicines Agency

$E_{max}$  = maximum response elicited by a drug  
eNOS = endothelial nitric oxide synthase  
ERK = Extracellular signal-regulated kinase  
FBS = foetal bovine serum  
FDA = U.S. Food and Drug Administration  
FGF2 = fibroblast growth factor 2  
FSK = forskolin  
GFP = green fluorescent protein  
GLP-1 = glucagon-like peptide-1  
gp120 = glycoprotein 120  
GPCR = G protein-coupled receptor  
GRK = G protein-coupled Receptor Kinase  
 $G\alpha_i$  =  $G_i$  alpha subunit  
 $G\alpha_q$  =  $G_q$  alpha subunit  
H&E = haematoxylin & eosin  
HBSS = Hank's balanced salt solution  
HCoV-NL63 = human corona virus NL63  
HEK293 = human embryonic kidney 293 cells  
HEK293T = subclone of HEK293 cell line  
hESC = human embryonic stem cell  
hESC-CM = human embryonic stem cell-derived cardiomyocyte  
HGNC = HUGO Gene Nomenclature Committee  
HIV = human immunodeficiency virus  
HLV = human left ventricle  
HUGO = human genome organisation  
Huh-7 = human hepatocyte-derived carcinoma cell  
IBMX = 3-isobutyl-1-methylxanthine  
IMEM = Iscove's Modified Dulbecco's Medium  
 $IP_3$  = inositol 1,4,5-trisphosphate  
iPSC = induced pluripotent stem cell  
IUPHAR = International Union of Pharmacology  
IWR1-endo = Wnt signalling pathway inhibitor  
K16P = apelin-17<sub>(1-16)</sub>

$K_D$  = dissociation constant  
KD = knockdown  
 $K_i$  = inhibitory constant  
KKS = kinin-kallikrein system  
KLF2 = Krüppel-like Factor  
LED = light emitting diode  
Ly294002 = phosphoinositide 3-kinase inhibitor  
MAPK = mitogen-activated protein kinase  
MAS1 oncogene = MAS receptor  
MC4R = melanocortin 4 receptor  
MCT = monocrotaline  
MLCK = myosin light chain kinase  
MOI = multiplicity of infection  
mRNA = messenger RNA  
NA = numerical aperture  
NBD = no binding determined  
NCX = sodium-calcium exchanger  
NHE1 = sodium-hydrogen antiporter 1  
NHS = National Health Service (UK)  
NIHR = National Institute for Health Research  
NO = nitric oxide  
NSB = non-specific binding  
p70S6K = ribosomal protein S6 kinase beta-1  
PAH = pulmonary arterial hypertension  
PBS = phosphate buffered saline  
PCR = polymerase chain reaction  
PCSK3 = proprotein convertase subtilisin/kexin 3  
 $pD_2$  =  $-\log_{10} EC_{50}$   
PEG = polyethylene glycol  
PI3K = Phosphoinositide 3-kinase  
PKC $\epsilon$  = protein kinase C  $\epsilon$   
PLC $\beta$  = phospholipase C  $\beta$   
PolyPhen-2 = Polymorphism Phenotyping v2

PWV = peak wavelength value  
RAAS = renin-angiotensin-aldosterone system  
RLU = relative light units  
ROCKi = Rho-associated protein kinase inhibitor  
ROI = region of interest  
S protein = spike protein  
s.e.m. = standard error of the mean  
SARS-CoV = severe acute respiratory syndrome coronavirus  
SARS-CoV-2 = severe acute respiratory syndrome coronavirus 2  
SD = standard deviation  
SIFT = Sorting Intolerant From Tolerant  
SIV = simian immunodeficiency virus  
SLC6A19 = human B<sup>0</sup>AT1 gene  
t<sub>1/2</sub> = half-life  
TCID<sub>50</sub> = Median Tissue Culture Infectious Dose  
TMPRSS2 = transmembrane protease serine 2  
TNF $\alpha$  = tumour necrosis factor  $\alpha$   
U2OS = human osteosarcoma-derived cell  
VeroE6 = African green monkey kidney cell  
VSV = vesicular stomatitis virus  
VSV-G = vesicular stomatitis virus G glycoprotein  
WGA = wheat germ agglutinin  
Wnt = Wntless and Int-1 signalling pathway  
WT = wild-type

## Tables & Figures

- P40 Figure 1.1.** Schematic showing some of the proposed signalling cascades induced by apelin receptor stimulation in the cardiovascular system.
- P54 Figure 1.2.** Snake plot showing the 380 amino acid apelin receptor.
- P58 Figure 1.3.** Snake plot showing the 380 amino acid apelin receptor, with amino acids critical for internalisation (red), trafficking (green), signalling (pink), or binding (blue).
- P59 Table 1.1.** Key amino acid interactions regulating binding of a modified apelin\* ligand and ELA-11 endogenous peptide to apelin receptor.
- P86 Figure 2.1.** Representative sample traces from the dynamic mass redistribution assay.
- P88 Figure 2.2.** Schematic showing the principle behind the cAMP accumulation assay.
- P90 Figure 2.3.** Validation of the cAMP accumulation assay.
- P91 Figure 2.4.** Schematic showing the principle behind the internalisation assay.
- P104 Figure 3.1.** Amino acid (single letter code) structures of apelin based peptides used in this thesis.
- P105 Figure 3.2.** Amino acid (single letter code) structures of ELA based peptides used in this thesis.
- P106 Figure 3.3.** Validation of CHO cells stably expressing human apelin receptor (CHO-APLNR).

- P107 Figure 3.4.** Association of apelin647 in CHO-APLNR over a 90 mins time-course.
- P108 Figure 3.5.** Competition binding at apelin receptor of peptides described in this thesis, against [<sup>125</sup>I]-apelin-13 (0.1 nM) in human left ventricle tissue homogenate (1.5 mg/mL).
- P109 Figure 3.6.** Validation of peptides described in this thesis in *in vitro* functional assays.
- P110 Table 3.1.** Summary of pharmacological parameters for the peptide ligands described in this thesis.
- P111 Figure 3.7.** Representative confocal fluorescent images of human kidney cortex sections treated with the fluorescent ligands apelin488 (1 μM, left, shown in green), or ELA488 (1 μM, centre, shown in green).
- P112 Figure 3.8.** Representative high content confocal fluorescent images of human embryonic stem cell-derived cardiomyocytes – either wild-type, or with an apelin receptor knockdown (APLNR KD) – treated with 300 nM apelin647 (red) for 90 mins.
- P114 Figure 3.9.** The fluorescent ligand, apelin647, is a robust tool for exploring the pharmacology of the apelin receptor using high content imaging.
- P116 Figure 3.10.** Internalisation of fluorescent apelin647 (300 nM) in CHO-APLNR, over a 90 mins time-course.
- P121 Figure 3.11.** Schematic showing apelin receptor internalisation following stimulation with a ligand.

- P125 Figure 4.1.** Schematic showing the points at which mutation can impact on GPCR signal transduction.
- P132 Table 4.1.** Saturation radioligand binding preliminary screen performed by Ms Rhoda Kuc.
- P133 Figure 4.2.** Snake plot showing the 380 amino acid apelin receptor with the single-point substitutions and deletions identified in the BRIDGE project highlighted in colour.
- P135 Figure 4.3.** High content assessment of apelin receptor variant expression.
- P137 Figure 4.4.** Representative high content confocal fluorescent images showing fluorescent ligand binding (shown in red) at apelin receptor variants tagged at the C-terminus with eGFP (shown in green).
- P138 Figure 4.5.** Saturation binding in high content imaging. Quantification of mean whole cell fluorescence (emitted light at wavelength of 647 nm, background corrected) in CHO-K1 cells transiently expressing wild-type (WT, black) apelin receptor or apelin receptor variants V38L (blue), T89M (red), or R168H (purple) and treated with a concentration range (1 – 300 nM) of apelin647.
- P140 Figure 4.6.** [<sup>125</sup>I]-apelin-13 radioligand binding in apelin receptor variants.
- P141 Figure 4.7.** Dynamic mass redistribution GPCR functional assay response (shown as the change in peak wavelength value,  $\Delta$ PWV, from baseline) of wild-type (WT, black) apelin receptor versus the variants V38L (blue), T89M (red), or R168H (purple) following stimulation with [Pyr<sup>1</sup>]apelin-13.
- P143 Figure 4.8.** Representative high content confocal fluorescent video snapshots showing apelin647 binding and internalisation over a 90 mins time-course.

- P144 Figure 4.9.** Representative high content confocal fluorescent images of human embryonic stem cell-derived cardiomyocytes – either wild-type (WT, left column) or an R168H variant line (right column) – treated with 300 nM apelin647 (red) for 90 mins.
- P153 Figure 5.1.** Simple schematic (created in BioRender.com) showing the mechanisms SARS-CoV-2 uses to infect host cells.
- P156 Table 5.1.** Markers used in immunochemistry, with respective concentrations/dilutions used.
- P158 Table 5.2.** Summary of the protein targets and compounds used in a drug screen looking for inhibitors of SARS-CoV-2 spike protein pseudotyped viral infection.
- P160 Figure 5.2.** ACE2 and ancillary proteins used by SARS-CoV-2 are present in hESC-CMs and human left ventricle tissue.
- P161 Figure 5.3.** Schematic showing the experimental workflow for generation of hESC-CMs before plating in 96-well plates.
- P163 Figure 5.4.** SARS-CoV-2 spike pseudotyped viral infection, and pharmacological inhibition, in hESC-CMs.
- P165 Figure 5.5.** Still shots from brightfield videos of hESC-CMs treated with media containing SARS-CoV-2 spike pseudotyped virus (**a**), media containing no viral particles (**b**), or media containing vesicular stomatitis virus (VSV-G) pseudotyped lentivirus (**c**).
- P166 Fig 5.6.** Representative images (from n = 2 independent experiments) of hESC-CMs infected with isolated SARS-CoV-2, tested at several different titres (0.001-0.1 multiplicity of infection, MOI) and incubation times (24-72 hours).

- P173 Figure 6.1.** Data showing ACE2 protein (**a**) and mRNA (**b**) expression in human central and peripheral tissues from the Human Protein Atlas.
- P176 Figure 6.2.** Schematic of full-length ACE2 (left) and the short dACE2 isoform (right).
- P178 Table 6.1.** Markers used in immunochemistry, with respective concentrations/dilutions used.
- P179 Figure 6.3.** Sequence of the fluorescently tagged SARS-CoV-2 spike receptor binding motif protein monomer (spike-AF647).
- P181 Figure 6.4.** Representative examples of quantification of ACE2 fluorescence in regions of interest (ROI) of human tissue sections using ZEN software (Zeiss).
- P182 Figure 6.5.** Brightfield images of H&E stained human tissue sections used to facilitate identification of regions of interest (ROI).
- P184 Figure 6.6.** Representative slide scanner fluorescent images showing positive immunoreactivity for ACE2 protein in human tissues infected and/or damaged by SARS-CoV-2.
- P186 Figure 6.7.** Graphical data showing quantification of fluorescence intensity (mean  $\pm$  SD) for ACE2 fluorescence, measured in grayscales at a bit depth of 16, in regions of interest (ROI) in human tissue sections (n = 6 ROI, across n  $\geq$  2 tissue donors) imaged as in Fig 6.6.
- P188 Figure 6.8.** Expression of full-length ACE2 versus short dACE2 in human tissue sections (n  $\geq$  3 individual donors, stained in duplicate).
- P191 Figure 6.9.** Quantification of differential staining with *ACE2poly* and *ACE2mono* as a surrogate measure of ACE2 isoform enrichment.

**P192 Figure 6.10.** Validation of *ACE2poly* and *ACE2mono* antibodies in a CHO-K1 cell model artificially expressing ACE2.

**P194 Figure 6.11.** A SARS-CoV-2 spike receptor binding motif protein monomer (spike-AF647) binds at low levels to structures enriched with dACE2.

**P197 Table 6.2.** Summary of interacting amino acids in SARS-CoV-2 spike protein bound to ACE2 identified in structural modelling in Yan et al., 2020.

## **Chapter 1. Thesis introduction**

### **1.1. Background**

Cardiovascular disease encompasses any pathology associated with the cardiovascular system, comprising the heart and blood vessels. A great number of disorders can arise in the cardiovascular system, from coronary heart disease to cerebrovascular disease to thromboembolism, but it is critical to note that cardiovascular disease, in all its forms, accounts for ~32 % of mortality (Stewart et al., 2017; 2020), and is the leading cause of death and disability (Flora & Nayak, 2019; Nghiem et al., 2019). Many lifestyle choices, such as smoking, high fat and/or high salt diets, alcohol consumption, and lack of exercise, contribute significantly to cardiovascular disease risk, but congenital defects, co-morbidities, age, sex, and ethnic background are also critical determinants (Flora & Nayak, 2019). Whilst many cardiovascular pathologies can be mitigated through lifestyle changes, and pharmaceutical intervention (Aminde et al., 2018; Nghiem et al., 2019), including lipid-lowering statins (Taylor et al., 2013; Kazi et al., 2017) and blood-pressure lowering drugs (Rahimi et al., 2021), there are still expansive gaps in the prevention and treatment of cardiovascular disease (Flora & Nayak, 2019).

This thesis describes the exploration of two critical protein regulators of cardiovascular health and disease, the apelin receptor and angiotensin-converting enzyme 2 (ACE2). The apelin receptor (formerly known as APJ) (O'Dowd et al., 1993; Pitkin et al., 2010) is a class A G protein-coupled receptor (GPCR) that binds two endogenous peptide ligands, apelin (Tatemoto et al., 1998) and elabela/Toddler (ELA) (Chng et al., 2013; Pauli et al., 2014), to induce highly potent vasoactive and inotropic effects (Yang et al., 2015). ACE2 on the other hand, is a zinc-metalloproteinase type 1 transmembrane protein (Tipnis et al., 2000; Donoghue et al., 2000; Hamming et al., 2007) that regulates the renin-angiotensin-aldosterone system (RAAS), counteracting angiotensin II vasoconstriction and fluid retention, to lower blood pressure (Burrell et al., 2004; Hamming et al., 2007; Tikellis et al., 2011). Intriguingly, ACE2 also acts as a host cell surface receptor for viral entry of the coronaviruses, severe acute respiratory syndrome coronavirus (SARS-CoV) (Li et al., 2003; Kuhn et al., 2004) and

human corona virus NL63 (HCoV-NL63) (Hofmann et al., 2005). ACE2 subsequently emerged as the target receptor for severe acute respiratory syndrome coronavirus 2 (SARS-CoV-2), the cause of the on-going COVID-19 (corona virus disease 2019) pandemic (Hoffmann et al., 2020; Wrapp et al., 2020; Yan et al., 2020; Yang et al., 2020), attracting much attention as a potential target for COVID-19 treatment (Alexander et al., 2020; Gaziano et al., 2021). Perhaps unsurprisingly, the case fatality rate in COVID-19 patients rises from 2.3 % to 10.5 % in the presence of cardiovascular comorbidities (Kang et al., 2020; Sommerstein, 2020; Robinson et al., 2020). In a small study, nearly 28 % of patients with confirmed COVID-19 were shown to have elevated troponin T levels – a surrogate measure of myocardial injury (Guo et al., 2020). COVID-19 mortality rose from 7.62 % in otherwise normal controls to 13.33 % in patients with underlying cardiovascular morbidities, and to 69.44 % in patients with underlying cardiovascular comorbidities that also presented with elevated troponin T. Further, the mortality rates of patients taking or not taking angiotensin-converting enzyme inhibitors/angiotensin receptor blockers was 36.8 % and 21.4 % respectively, indicating higher mortality in patients on cardiovascular medicines treating an underlying condition. Additionally, viral particles with associated myocarditis has been observed in autopsy samples from COVID-19 patients (Bailey et al., 2021; Italia et al., 2021). Whether cardiac damage in COVID-19 is induced directly via ACE2, or via indirect mechanisms such as inflammation or hypoxia associated with the disease, remains to be fully elucidated, but a combination of both is probable (Italia et al., 2021).

Two overarching aims have been addressed in this thesis. The first aim was to characterise the apelin signalling axis using novel fluorescent ligands and mutational analyses (utilising apelin receptor variants identified in human patients), to explore the therapeutic potential of this GPCR target in cardiovascular disease, improving on our current knowledge of the protein and facilitating informed drug design. The second aim was to characterise the therapeutic potential of ACE2, particularly in relation to its role in SARS-CoV-2 infection, providing a strategy for development of pharmaceutical therapies combatting COVID-19.

## **1.2. Apelin receptor**

### **1.2.1. G protein-coupled receptors**

G protein-coupled receptors (GPCRs) make up the largest family of signal transducing cell membrane bound receptor proteins that are targeted by clinically approved medicines, with approximately 700 drugs (~35 % of all approved drugs) mediating their effects through GPCRs (Santos et al., 2017; Sriram & Insel, 2018). Upon engagement with an external stimulus (e.g. a ligand), the seven transmembrane domains of a GPCR may adopt a conformation that allows for interaction with intracellular proteins such as heterotrimeric G proteins or  $\beta$ -arrestins (Weis & Kobilka, 2018). Classically, ligands that promote G protein activation and subsequent second messenger signalling were thought of as agonists, with antagonists simply blocking those effects (Wisler et al., 2018). More recently, it is acknowledged that ligands can stabilise GPCRs to facilitate interaction with a select few components of that receptor's functional repertoire (Wisler et al., 2014). Ligands are now realised as potentially displaying functional selectivity, or bias, towards one receptor pathway over others, with this having important ramifications in the understanding of cell biology and drug discovery.

Of the 800 GPCRs identified in the human genome, over 400 respond to sensory stimuli (olfaction, taste, light), whilst the remaining ~350 mediate signalling through small molecule, peptide, or protein ligands (Mombaerts., 2004). The GPCR superfamily is divided into classes based on sequence homology (Alexander et al., 2019). Class A (rhodopsin-like) is the largest division, comprising 197 receptors with known ligands that typically bind to a site in the seven transmembrane domains (Basith et al., 2018). Class B (secretin receptor family) is made up of 20 receptors that bind peptide ligands at sites in the seven transmembrane or extracellular domains. Class C (metabotropic glutamate receptor family) receptors possess an extracellular Venus flytrap module ligand-binding pocket. A remaining 87 GPCRs, split between the different classes, have unknown ligands (thus are termed orphan receptors), and it is currently unknown if these will provide novel therapeutic targets (Davenport et al., 2020).

### **1.2.2. Apelin receptor overview**

The apelin receptor is a 380 amino acid long Class A GPCR (UniProt ID: P35414), identified based on its 30% sequence homology (up to 54% in the transmembrane domains) with the angiotensin II type 1 (AT<sub>1</sub>) receptor (O'Dowd et al., 1993). The apelin receptor was shown not to bind angiotensin II however, and was not paired with its first cognate ligand, apelin (APJ endogenous ligand) until five years later, when it was identified in bovine stomach extract (Tatemoto et al., 1998). The apelin gene (*APLN*) encodes a 77 amino acid preproprotein that is predicted to undergo proteolytic cleavage at dibasic residue sites to form several active apelin peptide fragments – apelin-36 (Habata et al., 1999), apelin-17 (Masri et al., 2005), apelin-13 (Tatemoto et al., 2001), and pyroglutamated [Pyr<sup>1</sup>]apelin-13 (Maguire et al., 2009).

A second endogenous apelin receptor peptide ligand was discovered independently by two groups, and was named elabela (epiboly late because of endoderm late) after the developmental phenotype induced in zebrafish (*Danio rerio*) elabela null embryos (Chng et al., 2013). The other group named the peptide 'Toddler' after absence or overproduction of the peptide was observed to reduce motility of mesendodermal cells during zebrafish gastrulation (Pauli et al., 2014). The peptide will herein be referred to as ELA. The *Apela* (zebrafish) and *APELA* (human) (where *APELA* stems from apelin receptor early endogenous ligand) genes were identified in a conserved region of the genome that was previously designated as non-coding, and encodes a 54 amino acid prepropeptide that is highly conserved between vertebrate species (Chng et al., 2013; Pauli et al., 2014). As with apelin, ELA is thought to undergo proteolytic cleavage, generating smaller active isoforms (ELA-32, ELA-22, ELA-21, and ELA-11) which share little sequence similarity (~25%) with apelin (Chng et al., 2013; Pauli et al., 2014; Xie et al., 2014; Murza et al., 2016).

### **1.2.3. Apelin receptor expression**

The apelin receptor is encoded by the *APLNR* gene, localised to chromosome 11q12, with no known receptor subtypes observed in mammals (O'Dowd et al., 1993; Katugampola et al., 2001) – although there are two receptors (*aplnra* and *aplnrb*) in zebrafish (Deshwar et al., 2016). The receptor is highly conserved among vertebrate species with the human receptor sharing 89 % and 91 % sequence homology with the

377 amino acid long rat (*Rattus norvegicus*) and mouse (*Mus musculus*) receptors respectively (Pitkin et al., 2010; Narayanan et al., 2015). Of the zebrafish receptors, aplnrb shares greater identity with the human receptor (Scott et al., 2007).

The apelin receptor is widely distributed, with mRNA expression observed in the central nervous system (including the majority of brain regions, and the spinal cord) (Medhurst et al., 2003; Pope et al., 2012), and in many peripheral tissues including the heart, lungs, spleen, kidney, and liver (Hosoya et al., 2000; O'Carroll et al., 2000; Katugampola et al., 2001; Medhurst et al., 2003; Kleinz & Davenport, 2005; Wang et al., 2015). Apelin receptor is also observed in cardiomyocytes, and vascular endothelial and smooth muscle cells (Kleinz et al., 2004). Additionally, apelin receptor expression in platelets has been shown recently (Adam et al., 2016).

#### **1.2.4. Apelin peptides**

As mentioned, the apelin receptor binds two endogenous peptide ligands, apelin and ELA, that are both proteolytically cleaved into smaller active fragments. Despite the low amino acid sequence identity (~25 %) between the peptides, there is a similarity in the positioning of hydrophobic amino acids, and both peptides dock into the same binding site in molecular dynamics simulations (Yang et al., 2017a). The precise reasons for why the receptor binds two endogenous ligands remain unclear, but raises interesting questions regarding the spatiotemporal pattern of signalling that the receptor may mediate. Additionally, the observation of two receptors in zebrafish may point to an evolutionary loss of one receptor whilst two ligands remain.

The apelin gene (*APLN*) is localised at chromosome Xq25-26.1 (Lee et al., 2000). Apelin peptide is expressed widely, and generally shares a similar distribution pattern to apelin receptor, suggesting an autocrine/paracrine mode of signalling is likely. Apelin mRNA has been observed in the central nervous system (all brain regions and spinal cord) (De Mota et al., 2000; Lee et al., 2000; Medhurst et al., 2003), and in the heart, vasculature (endothelium and smooth muscle), lungs, spleen, kidney, liver, skeletal muscle, testes, gastrointestinal tract (small intestine), and adipocytes (Habata et al., 1999; Lee et al., 2000; Kawamata et al., 2001; Medhurst et al., 2003; Kleinz et

al., 2004; Boucher et al., 2005). Apelin peptide is also expressed in platelets (Adam et al., 2016).

Following translation, the 77 amino acid preproapelin is cleaved at an N-terminal secretory sequence to generate 55 amino acid proapelin, before subsequent cleavage is predicted to form shorter isoforms (apelin-36, apelin-17, and apelin-13) (Kleinz & Davenport, 2005; Pitkin et al., 2010; Shin et al., 2013). Generation of smaller fragments may occur sequentially, but proapelin has also been shown to be directly, and specifically, cleaved to apelin-13 by proprotein convertase subtilisin/kexin 3 (PCSK3 or furin) (Shin et al., 2013). The N-terminal glutamine of apelin-13 can spontaneously cyclise to form pyroglutamated [Pyr<sup>1</sup>]apelin-13, the most abundant isoform in human cardiac tissue (Maguire et al., 2009), likely due to the protection from peptidase activity that the pyroglutamate offers (Habata et al., 1999). The C-terminal F of apelin is actually a cleavage product for ACE2 (Vickers et al., 2002; Wang et al., 2016), where resultant apelin-13<sub>(1-12)</sub> is still biologically active (Yang et al., 2017b). Further cleavage at the N-terminus to form apelin-13<sub>(1-11)</sub>, and at the C-terminus to form apelin-13<sub>(2-12)</sub> generates the two smallest fragments known to display activity (Zhang et al., 2016). Recently, [Pyr<sup>1</sup>]apelin-13<sub>(1-12)</sub>, [Pyr<sup>1</sup>]apelin-13<sub>(1-10)</sub>, and [Pyr<sup>1</sup>]apelin-13<sub>(1-6)</sub> have been identified as metabolites following [Pyr<sup>1</sup>]apelin-13 infusion in human plasma (Nyimanu et al., 2019).

### **1.2.5. ELA peptides**

The ELA gene (*APELA*) is localised at chromosome 4q32.3 (HGNC, HUGO Gene Nomenclature Committee). As a more recently discovered gene, the expression of *APELA* mRNA, and its peptide transcript, is less well defined, but it appears to be more restricted than apelin (Read et al., 2019). ELA is a critical growth factor for embryonic heart development and is abundantly secreted by human embryonic stem cells, where it promotes self-renewal and pluripotency (Ho et al., 2015). In adult human, ELA is expressed in the kidney and prostate (Chng et al., 2013; Wang et al., 2015). ELA is also present in the adult cardiovascular system, in the endothelium and plasma (at higher levels than apelin peptides), but not in cardiomyocytes (Yang et al., 2017a).

ELA is transcribed as a 54 amino acid protein containing a secretory sequence and 32 amino acid mature peptide (ELA-32), with suspected furin cleavage sites predicted to yield smaller fragments such as ELA-23, ELA-22, ELA-21, ELA-14, and ELA-11 that are active in adult mammalian systems (Chng et al., 2013; Pauli et al., 2014; Murza et al., 2016; Yang et al., 2017a).

The role of ELA as the second apelin receptor ligand was predicted prior to its definitive discovery due to discrepancies between apelin and apelin receptor knockout models, where apelin ligand knockout mice were shown to be viable, fertile, and fully developed, whilst apelin receptor knockout mice were embryonic lethal (born in a sub-Mendelian ratio), with many displaying aberrant cardiovascular development (Kuba et al., 2007; Charo et al., 2009; Kang et al., 2013). In zebrafish, the naturally occurring *grinch*<sup>s608</sup> (W85L) mutation in *aplnrb* – which prevents binding of apelin – induces a severe reduction in myocardial progenitor cells and cardiomyocytes (Scott et al., 2007; Zeng et al., 2007), resulting in poor/absent cardiac development and resembling apelin receptor knockout in mice. Zebrafish ELA mutants exhibit a similar phenotype to *grinch*<sup>s608</sup>, whilst loss of apelin peptide alone results in a less severe phenotype, suggesting ELA is the primary activator of the apelin receptor during cardiac development. Further evidence for this comes from the fact that apelin peptide is not expressed during early gastrulation whereas the apelin receptor is, and peak ELA and apelin receptor expression coincide during days five to nine of zebrafish gastrulation (Pauli et al., 2014).

Overall, the identification of ELA, a critical GPCR ligand, in a region of the genome previously classed as non-coding is an exciting discovery, and it remains to be seen if there are further uncharacterised peptide ligands to be found for remaining orphan receptors that have not been paired with their cognate ligands.

### **1.2.6. Apelin receptor signalling**

The apelin receptor mediates a multitude of physiological responses. As a GPCR, the receptor transduces signals from outside of cells (e.g. the peptide hormones apelin and ELA) to the inside, via intracellular coupling to members of the second messenger complement, such as G protein subunits and  $\beta$ -arrestin proteins. To use the apelin

receptor as a therapeutic target, the cellular signalling cascades that it interacts with need to be well characterised.

Regarding G proteins, the apelin receptor shows a degree of promiscuity coupling to  $G\alpha_{i1}$  and  $G\alpha_{i2}$  subunits, but not  $G\alpha_{i3}$ , to inhibit forskolin stimulated adenylyl cyclase dependent cAMP accumulation in a pertussis toxin sensitive manner (Habata et al., 1999; Hosoya et al., 2000; Masri et al., 2006) and  $G\alpha_q$  subunits to mediate phospholipase C  $\beta$  (PLC $\beta$ ) dependent increases in intracellular  $Ca^{2+}$  (Choe et al., 2000; Szokodi et al., 2002; Japp & Newby, 2008).  $G\alpha_i$  subunits can stimulate the MAPK/ERK and PI3K/Akt pathways, both of which may result in phosphorylation of endothelial nitric oxide synthase (eNOS) to increase nitric oxide production (Makowski et al., 2015).

Following agonist treatment, G protein-coupled Receptor Kinase (GRK) phosphorylation has been shown to facilitate recruitment of  $\beta$ -arrestin 2 to the apelin receptor (Masri et al., 2006; Murza et al., 2012; Chen et al., 2014; Pope et al., 2016). Interestingly, a mechanosensor apelin receptor stretch mediated hypertrophic response in cardiomyocytes is also  $\beta$ -arrestin dependent, and is ligand and G protein independent (Scimia et al., 2012). A summary schematic of some of the signalling pathways stimulated by apelin receptor activation can be found in Fig 1.1.

### **1.3. Apelin receptor in physiology**

Ongoing research on the apelin receptor and its endogenous peptide ligands is revealing increasingly important roles in physiology, particularly relating, but not limited to, the cardiovascular system (Folino et al., 2015).

#### ***1.3.1 Apelin receptor in cardiovascular development***

As discussed in Section 1.2.5, the apelin receptor, specifically through ELA mediated activation, is critical for proper development of the heart. This role has been observed in genetically engineered mouse models (Ishida et al., 2004; Charo et al., 2009; Kang et al., 2013), and in zebrafish, both in the naturally occurring grinch<sup>s608</sup> aplnr mutation (Scott et al., 2007) and genetic models (Pauli et al., 2014).

### **1.3.2. Apelin receptor in cardiovascular regulation**

In the adult cardiovascular system, apelin receptor stimulation with intravenously infused apelin peptides induces anti-angiotensin-like (i.e. antihypertensive) effects, mediating venous and arterial (including the coronary artery) vasodilatation (Salcedo et al., 2007; Japp et al., 2008, 2010; Maguire et al., 2009; Barnes et al., 2013; Brame et al., 2015). In anaesthetised rats, apelin-12, apelin-13, and apelin-36 peptide administration lowers mean arterial pressure in a nitric oxide dependent manner (Tatemoto et al., 2001). In isolated human splanchnic arteries, apelin-13 induced vasodilatation was shown to be, at least in part, nitric oxide dependent without contribution from prostanoids (Salcedo et al., 2007). However, [Pyr<sup>1</sup>]apelin-13, the most abundant apelin isoform in human cardiovascular tissue, induces vasodilatation via endothelium dependent mechanisms acting through prostanoids and not nitric oxide (Maguire et al., 2009). The mechanisms by which apelin mediates vasorelaxation may therefore differ between vascular beds. Interestingly, the removal of the endothelium (denudation) unmasks apelin receptor dependent vasoconstriction in *ex vivo* arterial and vein tissue preparations (Katugampola et al., 2001; Maguire et al., 2009). Contrasting effects in intact versus denuded endothelial preparations may reflect different activity of the apelin receptor on the endothelium versus vascular smooth muscle (Yang et al., 2015), where apelin has been shown to induce myosin light chain phosphorylation (critical for initiating contraction) through activation of receptors directly present on vascular smooth muscle (Hashimoto et al., 2006).

In the heart itself, apelin induces one of the most potent endogenous positive inotropic responses observed in man, mediating increased cardiac contractility and cardiac output in *in vivo* settings (Szokodi et al., 2002; Berry et al., 2004, Perjés et al., 2014) and humans (Japp et al., 2010; Barnes et al., 2013), through activation of apelin receptors present on cardiomyocytes (Kleinz et al., 2005). Apelin knockout mouse models have provided further evidence for the cardiac role of apelin signalling, displaying a progressive impairment of cardiac contractility associated with systolic dysfunction (Kuba et al., 2007).

Fig 1.1 shows a simple schematic (expanding on those shown in Yang, et al., 2015) outlining the current consensus on signalling cascades that regulate the cardiovascular system following apelin receptor stimulation. Following synthesis and release of apelin and/or ELA from endothelial cells, the peptide ligands can act in a paracrine manner at apelin receptors expressed on cardiomyocytes or vascular cells. Through classical  $G\alpha_q$  signalling, activation of phospholipase C (PLC) can stimulate inositol 1,4,5-trisphosphate ( $IP_3$ )- and diacylglycerol (DAG)-mediated activation of calmodulin (CaM) and protein kinase C  $\epsilon$  (PKC $\epsilon$ ) respectively, to activate myosin light chain kinase (MLCK). MLCK can phosphorylate the regulatory light chain of myosin II to induce contraction in cardiomyocytes and resultant positive inotropy. Note that  $G\alpha_q$  signalling can also stimulate sodium-hydrogen antiporter 1 (NHE1), which increases intracellular  $Na^+$ , driving the sodium-calcium exchanger (NCX) to further increase intracellular  $Ca^{2+}$  levels. There is also evidence that activation of extracellular signal-regulated kinases 1/2 (ERK1/2) by the apelin receptor can stimulate NHE1 (pathway not shown in schematic), although how exactly this occurs remains incompletely characterised (Yang et al., 2015; Read et al., 2019).

In the vasculature, endothelially derived apelin can act in an autocrine manner at the apelin receptor on the cell it was released from and neighbouring endothelial cells to stimulate the  $G\alpha_i$  pathway. Resultant activation of phosphatidylinositol 3-kinase (PI3K) can stimulate protein kinase B (Akt), which, in turn, stimulates endothelial nitric oxide synthase (eNOS). Canonically, eNOS drives synthesis of the small gaseous and lipophilic molecule, nitric oxide (NO), which can then diffuse to act on the underlying vascular smooth muscle to induce vasodilatation through activation of soluble guanylyl cyclase. Interestingly, there is also evidence for  $G\alpha_q$  mediated production of NO through activation of 5' adenosine monophosphate-activated protein kinase (AMPK) and Krüppel-like Factor 2 (KLF2), which can upregulate eNOS.

As discussed above, a vasoconstrictor role of apelin receptor activation is revealed in denuded vessels (i.e. stripped of endothelium) (Katugampola et al., 2001; Maguire et al., 2009). Supposed mechanisms for this contractile response are similar to those that induce positive cardiac inotropy (e.g.  $G\alpha_q$  calcium-dependent activation of MLCK),

where apelin acts directly at apelin receptors expressed on the exposed vascular smooth muscle. This effect of apelin is likely pathological and might occur in disease states where the endothelium is dysfunctional or damaged (Yang et al., 2015).

A controversial stretch mechanosensory role for the apelin receptor has also been identified in cardiomyocytes, which contributes to cardiac hypertrophy (Scimia et al., 2012; Xie et al., 2015; Lu et al., 2017). Initially, cardiac hypertrophy occurs as an adaptive compensatory response to sustained overload in heart failure, but eventually progresses to a pathological extent that can worsen symptoms. Apelin receptor knockout mice, if they survive birth, are resistant to chronic pressure overload and show reduced cardiac hypertrophy and heart failure, whilst apelin peptide knockout mice are still susceptible to hypertrophy (Scimia et al., 2012). The data from the Scimia study suggest that cardiac hypertrophy through the apelin receptor is ligand independent, and that stretch of cardiomyocytes results in apelin receptor mediated  $\beta$ -arrestin signalling to contribute to hypertrophy observed in heart failure. The group also demonstrated that  $G\alpha_i$  signalling following apelin receptor stimulation by apelin peptide was protective against stretch mediated hypertrophy. However, another group found that apelin-13 increased the diameter, volume, and protein content of H9c2 cells (derived from embryonic rat heart tissue), through phosphorylation of PI3K, Akt, and ERK1/2 to stimulate ribosomal protein S6 kinase beta-1 (p70S6K) (Xie et al., 2015). This positions  $G\alpha_i$  signalling as contributing to cardiac hypertrophy rather than protecting against it. Further work will need to be done to fully elucidate the stretch mechanosensory role of apelin in physiology, and in diseases such as heart failure.

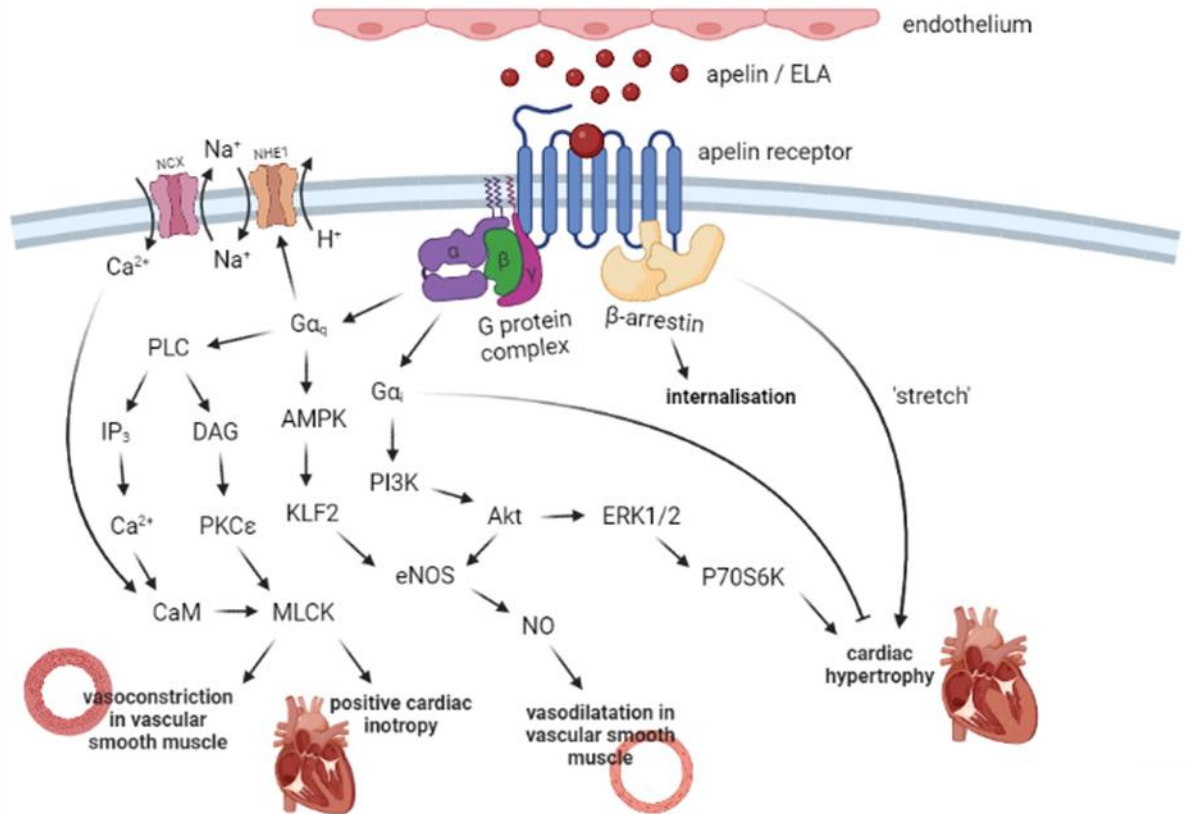


**Figure 1.1.** Schematic showing some of the proposed signalling cascades induced by apelin receptor stimulation in the cardiovascular system. Apelin and/or ELA peptide, synthesised and released from endothelial cells, acts on apelin receptor in an autocrine/paracrine manner on endothelial cells or vascular or cardiac muscle to induce physiological responses. Stretch mediated cardiac hypertrophic responses may be mediated through  $\beta$ -arrestins in a ligand independent manner, or may see contribution from  $G\alpha_i$  signalling. Note that  $\beta$ -arrestins also mediate desensitisation and internalisation of the apelin receptor. This is shown in greater detail in Fig 3.11. Schematic was designed using BioRender (<https://biorender.com/>).

### **1.3.3. Apelin receptor in angiogenesis**

Angiogenesis is the process of new blood branch development (a form of neovascularisation) from pre-existing blood vessels via sprouting, and can have beneficial or detrimental roles in biology (Wu et al., 2017). Apelin has been shown to act in a manner similar to growth factors to promote endothelial cell proliferation in isolated umbilical endothelial cells (Masri et al., 2004), and enhance proliferation, migration, and capillary-like tube formation in retinal endothelial cells (Kasai et al., 2004). Hypoxia has been shown to increase apelin expression in cultured vascular endothelial and smooth muscle cells, and in the lungs of mice exposed to hypoxia, potentially driving adaptive physiological and pathophysiological responses in low oxygen (Eyries et al., 2008). Apelin receptor signalling is also essential for embryonic angiogenesis in frogs (*Xenopus*), and, interestingly, was shown in the same study to be highly upregulated in microvascular proliferations of brain tumours (malignant gliomas) (Kälin et al., 2007).

### **1.3.4. Apelin receptor in haemostasis**

Apelin signalling also plays a role in haemostasis, with both apelin peptide and apelin receptor shown to be present in mouse and human platelets (Adam et al., 2016). Apelin-13 exerts an antithrombotic action, inhibiting *in vitro* thrombin and collagen, but not ADP or thromboxane A<sub>2</sub>, dependent platelet activation, secretion, and activation. Additionally, apelin knockout in mice reduces tail bleeding time and increases whole blood perfusion thrombosis, whilst the reverse is true for mice treated with intravenous apelin-13. The authors suggest apelin treatment might prove useful as concomitant antiplatelet therapy for patients who respond poorly to currently used clinical drugs (such as clopidogrel and aspirin) which typically target the ADP and thromboxane A<sub>2</sub> pathways. The ability of apelin to stimulate nitric oxide and cGMP production may also contribute to its antiplatelet mechanisms.

Following on from the discovery of apelin as a regulator of haemostasis and antithrombotic factor (Adam et al., 2016), the apelin receptor has been confirmed to be expressed at the platelet membrane, where it is reduced on platelet activation (Strohbach et al., 2021). This study also showed that platelet apelin receptor levels were reduced in patients with acute myocardial infarction, coinciding with a reduction

in plasma apelin-17 levels. The authors also demonstrate that apelin-17 is able to attenuate the activation of platelets by a selective thrombin receptor-activating peptide in an in vitro setting, further supporting the potential use for apelin peptides as an antithrombotic therapy.

### ***1.3.5. Apelin receptor in fluid homeostasis***

In line with its expression in the nervous system at sites coinciding with arginine vasopressin (AVP) synthesis and release, the apelin receptor is involved in fluid uptake and retention (Flahault et al., 2017). The hypothalamus, a brain structure involved in the control of drinking behaviour, contained by far the most apelin-positive nerve fibres in rats, with high levels also detected in the circumventricular organs, and the pituitary gland (Reaux et al., 2002). Apelin receptor knockout mice that survived to adulthood drink significantly less water than wild-type, yet urine volume and osmolality remained the same (Roberts et al., 2009). Additionally, 24 hour water deprivation significantly reduced urine volume and increased urine osmolality in wild-type but not apelin receptor knockout mice, suggesting an antidiuretic effect of functional apelin signalling. Central administration of [Pyr<sup>1</sup>]apelin-13 increases drinking behaviour and water intake in rats, and increases AVP release from hypothalamic regions (Taheri et al., 2002).

Considerable work has also been performed to characterise apelin-17 specifically, particularly its role in lowering blood pressure and haemostasis. It has been shown that intra-cerebroventricular administration of apelin-17 reduces plasma levels of vasopressin, and increases diuresis in lactating mice (De Mota et al., 2004). Conversely, the authors also demonstrated that water deprivation induced increases in vasopressin decrease plasma levels of apelin, suggesting counter-regulatory effects of the peptide hormones. Intriguingly, apelin and its receptor are expressed in the kidney, particularly in the glomeruli, where intravenous injection of apelin-17 induces significant diuresis, and vasorelaxation of efferent and afferent arterioles (Hus-Citharel et al., 2008). In conjunction with a central role for apelin in diuresis through inhibition of vasopressin release, intravenously administered apelin-17 acts directly in the collecting duct of the kidney to reduce insertion of apical aquaporin-2 to promote diuresis in lactating rats (Hus-Citharel et al., 2014). The imbalance of apelin to

vasopressin levels is therefore posited as a cause of water retention and resultant disease states such as syndrome of inappropriate antidiuretic hormone and chronic heart failure (Blanchard et al., 2013), with apelin agonists showing potential in treatment of these disorders.

The precise role of apelin signalling in fluid homeostasis is unclear, particularly why intracranial administration of apelin induces antidiuresis whilst systemic administration induces diuresis. The extent and significance of apelin dependent changes on fluid homeostasis and blood pressure also require further study.

### ***1.3.6. Apelin receptor in metabolism***

Apelin has been identified as an adipokine, with an expression profile seen in adipocytes that increases with obesity that coincides with hyperinsulinaemia in mouse models of obesity (Boucher et al., 2005). Conversely, a lack of insulin reduces adipocyte apelin expression. Additionally, in obese patients, plasma apelin levels are significantly higher than healthy weight controls, with insulin exerting a direct positive action on adipocyte apelin secretion. Apelin, acting as an adipokine, lowers blood glucose through increased uptake into skeletal muscle and adipose tissue in a manner additive to that of insulin (Dray et al., 2008). Apelin knockout mice present with a hyperinsulinaemic and insulin resistant phenotype, that is exacerbated by a high fat/high sugar diet, confirming a correlative relationship between apelin and insulin, and suggesting a potential insulin sensitising role of apelin (Yue et al., 2010).

## **1.4. Apelin receptor in pathophysiology**

The apelin receptor is therefore a critical regulator of numerous physiological processes, and it follows that dysregulation of the apelin signalling axis can induce pathological states. As a class A GPCR however, a family of receptor proteins targeted by 35 % of all clinically approved drugs, the apelin receptor should be exploitable as a therapeutic target in disease.

#### **1.4.1. *Apelin receptor in pulmonary arterial hypertension***

Pulmonary arterial hypertension (PAH) is a disease characterised by increased pulmonary vascular resistance (mean resting pulmonary artery pressure of  $\geq 25$  mmHg) caused by functional and structural changes in the pulmonary vasculature (Galié et al., 2009; Morrell et al., 2009; Thenappan et al., 2018). PAH patients exhibit a complex pathological phenotype. In general, an imbalance of vasodilatory and vasoconstrictive agents, inflammation, and aberrant proliferation/migration of smooth muscle cells and myofibroblasts in small precapillary pulmonary arterioles results in vascular remodelling, the formation of plexiform lesions, and reduced vessel compliance (Gan et al., 2007; Morrell et al., 2009). The stiffening of pulmonary arterioles puts upstream pressure on larger proximal arteries and the right side of the heart itself, ultimately hypertrophying the right ventricle and inducing fatal right-sided heart failure (Toshner et al., 2010). Symptoms, as outlined by the NHS, include shortness of breath, tiredness, feelings of faintness and/or dizziness, chest pain (angina), heart palpitations, and peripheral oedema, all of which often worsen during exercise. PAH is a rare disease with an estimated prevalence of 10-50 cases per million (Peacock et al., 2007; Hoeper & Gibbs, 2014), with a disproportionate 70-80% of those cases reported as female (McGoon et al., 2013), although this may reflect the fact that male patients tend to present with a more severe phenotype and die sooner (Shapiro et al., 2012). In an analysis of 2635 PAH patients, 1-, 3-, 5-, and 7-year survival rates after diagnosis were reported as 85 %, 68 %, 57 %, and 49 % respectively, indicating that over half of PAH patients die within 7 years, mostly directly due to right-sided heart failure (Benza et al., 2012). Current therapy for PAH involves targeting three main biological pathways – endothelin, nitric oxide, and prostacyclin – either individually or concomitantly (Corris & Degano, 2014). These therapies only address symptoms however and do not reverse disease progression. Additionally, many patients, particularly those with severe PAH, do not respond to the treatment, and lung transplantation becomes the only viable option for extending life. There is a clear need for better therapeutics in the treatment of PAH.

Apelin signalling is implicated in PAH and the apelin receptor is a proposed novel target for PAH therapy (Yang et al., 2015). Apelin-36 plasma levels are significantly reduced in chronic heart failure, and idiopathic pulmonary hypertension patients

versus healthy controls, with the authors concluding that apelin may prove useful as a diagnostic biomarker (Goetze et al., 2006). Human pulmonary arterial endothelial cells are also confirmed as exhibiting reduced expression of apelin in PAH patients compared to controls, and, in mice, apelin administration reverses PAH (Alastalo et al., 2011). Additionally, apelin knockout mice present with more severe pulmonary hypertension when exposed to chronic hypoxia than wild-type (Chandra et al., 2011). In the rat monocrotaline (MCT) induced model of PAH, disease symptoms, including right ventricular hypertrophy and reduced cardiac contractility, are reversed with chronic [Pyr<sup>1</sup>]apelin-13 treatment (Falcão-Pires et al., 2009). Interestingly, ELA treatment also reduces the severity of cardiopulmonary remodelling and improves cardiac function in the MCT rat model (Yang et al., 2017). Moreover, this has also been observed following chronic treatment with the G protein biased peptide MM07 in the same model, with reversal of the disease aetiology observed, supporting further development of biased compounds that have a sufficient pharmacokinetic profile (Yang et al., 2019). In PAH patients, apelin infusion during right heart catheterisation significantly increases cardiac output and decreases pulmonary vascular resistance (Brash et al., 2015). Subsequent work confirmed these findings, and showed accentuated and additive effects of apelin infusion in PAH patients receiving standard-of-care concomitant phosphodiesterase type 5 inhibitors, demonstrating the potential of the apelin signalling axis as a therapeutic target in this disease (Brash et al., 2018).

#### ***1.4.2. Apelin receptor in heart failure***

Following its role in right sided heart failure in PAH, and due to its potent positive inotropic effects, apelin signalling is also implicated in heart failure (Pitkin et al., 2010). As already outlined, plasma apelin and cardiac tissue apelin levels can change in heart failure states, implicating the peptide as a disease biomarker (Goetze et al., 2006). Left ventricular apelin mRNA levels are ~5-fold higher in chronic heart failure patients than healthy controls, whilst atrial and plasma apelin peptide levels are significantly reduced (Földes et al., 2003). Conversely, plasma apelin levels have been observed to increase in patients with left ventricular dysfunction following placement of a left ventricular assist device, and that the apelin receptor itself is significantly upregulated, confirming the presence of the GPCR as a drug target (Chen et al., 2003). Further work has confirmed that patients with chronic heart failure show reduced baseline

apelin levels in plasma, but long term cardiac resynchronisation therapy with a biventricular pacemaker induces a significant increase in plasma apelin that is comparable to healthy controls (Francia et al., 2007). Evidence suggests that apelin signalling is downregulated in heart failure states, and upregulation – whether through therapeutic targeting or secondarily following mechanical improvement of cardiac function – is beneficial through its apparent physiological antagonism of the renin-angiotensin-aldosterone system (Dalzell et al., 2015; Goidescu & Vida-Simiti, 2015). The role of the apelin receptor in cardiac hypertrophy associated with heart failure has been discussed above in Section 1.3.2.

#### ***1.4.3. Apelin receptor in HIV***

The human immunodeficiency viruses type 1 and 2 (HIV-1 and HIV-2 respectively) are species of lentivirus that result in acquired immunodeficiency syndrome (AIDS), suppressing the immune system of the infected host following depletion of CD4-positive T lymphocytes (Weiss, 1993). Entry of HIV-1 into target cells is dependent on the sequential binding of a viral envelope glycoprotein (gp120) to CD4 and a second GPCR co-receptor. Typically, chemokine receptors mediate viral entry, with beta-chemokine receptors CCR3 and CCR5, and alpha-chemokine receptor CXCR4, acting as the principle co-receptors (Choe et al., 1996; Schramm et al., 2000). However, the apelin receptor has also been identified as a co-receptor for HIV-1 and Simian immunodeficiency virus mac316 (SIVmac316), facilitating viral entry into CD4-positive cell lines (Choe et al., 1998; Edinger et al., 1998). The first 20 amino acids of the apelin receptor have been identified as important for supporting cell-cell fusion mediated by the gp120 envelope protein of HIV-1, and site-directed mutagenesis identified amino acids Y10, Y11, E20, and D23 as substantially contributing to apelin receptor co-receptor function (Zhou et al., 2003b,c). Interestingly, the high number of aromatic and acidic residues in the N-terminus of the apelin receptor is a feature shared with many of the chemokine receptors, including those used for entry by HIV (Choe et al., 1998), and it is no coincidence that CXCR4 provided the template for a 3-dimensional homology model of the apelin receptor (Gerber et al., 2015). Finally, endogenous apelin peptide treatment has been shown to block entry of HIV-1 and HIV-2 into CD4-positive cells, with longer peptide isoforms showing greater inhibitory efficiency than shorter ones, which may be due to a longer peptide N-terminus providing greater steric

hindrance (Cayabyab et al., 2000; Puffer et al., 2000; Zou et al., 2000). The synthetic compound ALX40-4C is also able to prevent HIV-1 viral entry through reported antagonism of both the apelin receptor and CXCR4 (Zhou et al. 2003a).

#### **1.4.4. Apelin receptor in immune-mediated injury**

In early work, apelin was observed to partially suppress cytokine production in mouse spleen cells in response to T cell receptor/CD3 cross-linking (Habata et al., 1999). Downregulation of apelin has also been observed in the plasma of patients with Group 1 PAH, which includes PAH associated with autoimmune disease (Goetze et al., 2006; Alastalo et al., 2011; Chandra et al., 2011; Yang et al., 2017a; Read et al., 2019). Recently, a report has identified an upregulation of apelin peptide in response to immune-mediated vasculopathy in a mouse model, and apelin treatment was shown to reduce progression of arterial occlusion (Masoud et al., 2020). *In vitro*, an apelin receptor agonist stimulated eNOS activation to promote wound repair of the endothelial monolayer, and reduced immune cell adhesion. The report points to the proangiogenic effects of apelin mediating vascular repair, and posits the apelin receptor as a potential therapeutic target for immune-mediated vascular injury. Additionally, the G protein biased apelin receptor agonist, CMF-019, has recently been shown to rescue human pulmonary artery endothelial cells from apoptosis induced by tumour necrosis factor  $\alpha$  and cycloheximide (Read et al., 2019).

#### **1.4.5. Apelin receptor in diabetes**

Apelin signalling may play a role in Type 2 diabetes mellitus, a highly prevalent metabolic disease characterised by insulin resistance and/or relative insulin insufficiency that results in chronic hyperglycaemia (Read et al., 2019). The disorder is also commonly associated with higher risk of cardiovascular disease (Balkau and Eschwège, 1999; Patel et al., 2016).

Apelin peptide is expressed in  $\alpha$  and  $\beta$  pancreatic cells, with the receptor showing expression in  $\beta$  cells (Ringström et al., 2010). In *in vitro* and *in vivo* settings, apelin treatment inhibits insulin secretion but, conversely, reduces insulin resistance leading to decreased blood glucose levels (Sorhede Winzell et al., 2005; Guo et al., 2009; Dray et al., 2008). Further, in an apelin deficient mouse model, apelin administration

reversed insulin resistance associated with the loss of native apelin (Yue et al., 2010). In rats, [Pyr<sup>1</sup>]apelin-13 treatment reduces plasma insulin and glucose levels with a concurrent decrease in blood pressure (Akçilar et al., 2015), suggesting that apelin therapy might have use in reducing chronic hyperglycaemia, as well as diabetes associated hypertension. In humans, apelin plasma levels are increased in Type 2 diabetics and patients presenting with obesity, suggesting a potential use as a biomarker (Castan-Laurell et al., 2011; Ma et al., 2014). This elevation of apelin as an anti-hyperglycaemic agent may be a compensatory mechanism to combat aberrant pancreatic function.

Diabetes is also associated with disorder of the microvasculature, which can result in diabetic nephropathy, neuropathy, and retinopathy (Read et al., 2019). Following its role in angiogenesis (see Section 1.3.3.), apelin may actually be partially causative of microvascular complications seen in disease states such as diabetes. Apelin has been shown to promote proliferation and migration of retinal pigment epithelial cells, collagen expression, and initiate retinal neovascularization to contribute to retinopathy (Wu et al., 2017). Intriguingly, one study has shown that blocking the apelin receptor with a repurposed antimalarial drug, amodiaquine, suppressed both apelin- and VEGF-induced endothelial tube formation (McAnally et al., 2018). Further, amodiaquine reduced choroidal neovascularisation in a laser-induced mouse model, providing proof-of-principle for blockade of apelin signalling being beneficial in aberrant vessel formation in retinopathy.

In summary, apelin treatment may be of benefit in Type 2 diabetics by improving insulin sensitivity, increasing cardiac output, and promoting vasodilatation. Negative effects of apelin treatment, such as neovascularisation and aberrant angiogenesis, will need to be considered. Further work will need to be done to determine how best to exploit apelin signalling to provide a novel therapeutic strategy in diabetes.

## **1.5. Apelin receptor as a therapeutic target**

The apelin signalling axis has been proposed as a new target for novel cardiovascular therapeutics, but a number of caveats will need to be addressed before any new treatments are translated into a clinical setting (Zhong et al., 2017).

### **1.5.1. G protein bias**

It has long been proposed that apelin receptor agonists exhibiting bias towards G protein pathways versus  $\beta$ -arrestin and internalisation, would offer greater clinical efficacy through induction of desired pharmacological effects whilst crucially avoiding desensitisation and loss of the target receptor from the cell surface (Yang et al., 2015). Additionally, G protein bias would be beneficial in heart failure associated with cardiac hypertrophy, if the findings by Scimia et al., 2012 are correct and pathological stretch induced hypertrophy is ligand independent, mediated by  $\beta$ -arrestin, and protected against by  $G\alpha_i$  apelin signalling. Apelin therapeutics, hypothesised as having potential use in cardiovascular diseases such as PAH and heart failure, have thus been explored for G protein bias.

### **1.5.2. Peptide therapeutics**

Owing to high target specificity and affinity, nearly 50 GPCR peptide drugs have been approved to date (Davenport et al., 2020). However, peptides are limited therapeutically, given their typically poor pharmacokinetics (short half-life, rapid degradation, and rapid clearance), and poor oral bioavailability.

Apelin peptides display an extremely short half-life of ~5 – 8 mins in plasma (Zhen et al., 2013; Murza et al., 2016), undergoing cleavage by circulating enzymes such as those mentioned in Section 1.2.4, including ACE2, where cleavage of apelin-13 and apelin-17 was shown to partially inactivate the peptides (Vickers et al., 2002; Kazemi-Bajestani et al., 2012; Wang et al., 2016). More recently however, the [Pyr<sup>1</sup>apelin-13<sub>(1-12)</sub> cleavage product was shown to be biologically active Yang et al., 2017b). Modifications to peptides, such as stapling, cyclization, and glycosylation can be introduced to extend half-life and improve oral bioavailability (Davenport et al., 2020). Liraglutide, for example, is an approved glucagon-like peptide-1 (GLP-1) analogue,

used in the treatment of type 2 diabetes and obesity, that is 97% homologous to native human GLP-1. The addition of a 16-carbon fatty acid chain facilitates binding to serum albumin in plasma to protect the peptide from enzymatic degradation, increasing the half-life from 1 – 2 mins to 13 h (Sisson, 2011).

A number of techniques have attempted to design novel peptide ligands with better duration of action and longer half-lives. A series of three cyclic analogues of apelin-12 have been developed that are bioactive and provided the groundwork for the development of more drug-like apelin peptides (Hamada et al., 2008). MM07 is a cyclised apelin ligand, the cyclisation initially designed to increase peptide half-life by protecting against peptidases, that also shows bias towards the G protein pathway, displaying a similar potency to [Pyr<sup>1</sup>]apelin-13 in G protein assays but a potency two orders of magnitude less than [Pyr<sup>1</sup>]apelin-13 in  $\beta$ -arrestin and internalisation assays (Brame et al., 2015). Systemic infusion of MM07 induces a dose-dependent increase in rat cardiac inotropy that is significantly greater than that for [Pyr<sup>1</sup>]apelin-13. Additionally, MM07 was shown to be safe and active in healthy human volunteers, and induces increased forearm blood flow that were reproducible following repeat doses, unlike [Pyr<sup>1</sup>]apelin-13. K16P (apelin-17<sub>(1-16)</sub>), a modified analogue of apelin-17 lacking the C-terminal F, is also G protein biased but is unable to decrease blood pressure, unlike apelin-17 itself (Ceraudo et al., 2014). The authors conclude that apelin receptor mediated reductions in blood pressure are  $\beta$ -arrestin dependent, although this conflicts with the subsequent findings observed for MM07 – this may be due to the fact that K16P vasoactivity was investigated in rat glomerular afferent arterioles preconstructed with angiotensin II. Generation of a novel series of macrocyclic apelin-13 analogues led to the identification of four further G protein biased peptides that show high affinity for the apelin receptor, although these are yet to be fully characterised *in vivo* (Murza et al., 2017).

The conjugation of a 40 kDa polyethylene glycol (PEG) to the N-terminus of apelin-36 (PEG-apelin-36) was shown to enhance the duration of action on increased cardiac ejection fraction versus unmodified apelin-36 following intravenous infusion in rats (Jia et al., 2012). PEG-apelin-36 showed comparable binding affinity and G protein activation to apelin-36 in *in vitro* assays. Following development of a series of apelin-

36 variants, modified apelin-36(L28A) incorporating an L28A substitution, and apelin-36-[L28C(30kDa-PEG)] incorporating an L28C substitution and conjugation of a 30 kDa PEG linker to the Cys side-chain, were shown to significantly lower blood glucose and improve glucose tolerance in obese rats but had no effect on blood pressure (Galon-Tilleman et al., 2017). The authors concluded that the peptides function independently of the apelin receptor. Further assessment however revealed that both apelin-36(L28A) and apelin-36-[L28C(30kDa-PEG)] bind to rat and human apelin receptor with similar affinities to apelin-36, and are active in G protein assays, but show less potency in  $\beta$ -arrestin assays (Nyimanu et al., 2019). The peptides are therefore G protein biased ligands of the apelin receptor.

One group aimed to identify metabolically stable apelin-17 analogs and designed LIT01-196 by adding a fluorocarbon chain to the N-terminus of the peptide (Gerhier et al., 2017). This modification extends the half-life from 4.6 mins to over 24 hours whilst retaining the pharmacology of the peptide. Intra-cerebroventricular administration of LIT01-196 into water-deprived mice significantly reduces systemic vasopressin release, and is 160-fold more effective than the native apelin-17 peptide. Intravenously administered LIT01-196 also increases urine output and decreases arterial blood pressure in normotensive rats over a sustained duration. The LIT01-196 has been used subsequently to decrease vasopressin antidiuretic effects and improve hyponatremia in a rat model (Flahault et al., 2021a), and normalises arterial blood pressure in conscious hypertensive DOCA-salt rats over a 7 hour window (Flahault et al., 2021b). Apelin-17 is now known to be a target of the human plasma kallikrein enzyme, which cleaves the three N-terminal (KFR) amino acids of the peptide, exposing an R amino acid at the N-terminus and resulting in significantly reduced biological activity and abolished blood pressure lowering effects (Fischer et al., 2019). Addition of palmitic acid or polyethylene glycol (PEG) to the N-terminus of apelin-17 protects against kallikrein cleavage whilst retaining good pharmacological activity at the apelin receptor, extends plasma half-life, and restores the blood pressure lowering effects of the peptide. A subsequent study also showed that the incorporation of non-natural cyclohexylalanine and homoarginine amino acids extended the plasma half-life of [Pyr1]apelin-13 and apelin-17 by 40-fold and 340-fold respectively, with the modified apelin-17 peptide showing pronounced blood pressure lowering effects

(Fernandez et al., 2021). In summary, reducing peptidase metabolism of apelin-17 to extend the plasma half-life may be a novel therapeutic strategy to treat diseases characterised by inappropriate antidiuresis.

Alternative strategies have involved conjugating a lipid to apelin-12 to form a lipopeptide that retains high affinity for the apelin receptor but has an extended duration of action and increased intracellular access (McKeown et al., 2014). The addition of an anti-serum albumin domain antibody (AlbudAb) via a [PEG4] linker to a modified apelin peptide incorporating an M to norleucine substitution at position 11 and an F to 3,4,5-trifluorophenylalanine at position 13 resulted in identification of MM202-AlbudAb (Read et al., 2020). This peptide binds to human apelin receptor with similar affinity to the endogenous peptides [Pyr<sup>1</sup>]apelin-13 and apelin-17; is active in G protein and  $\beta$ -arrestin assays; binds with high affinity to immobilised human serum albumin; and induces haemodynamic and cardiovascular effects in rats providing proof-of-concept for conjugation of AlbudAb to peptide ligands as a potential novel therapeutic strategy.

### **1.5.3. Small molecule therapeutics**

The development of orally bioavailable, efficacious, and safe small molecules targeting the apelin receptor is an attractive prospect. E339-3D6 was initially identified as a peptidomimetic (nonpeptidic but with high molecular weight) ligand that showed high affinity for the apelin receptor and partial agonism in G protein assays, full agonism in internalisation assays, and induced vasorelaxation of preconstructed rat aorta (Iturrioz et al., 2010a). However, E339-3D6 is now known to have been a mixture of polymethylated species (Margathe et al., 2014). Solid-phase purification was used to identify the major component of E339-3D6, and the resultant compound was used as the basis for a series of derivatives that show varying degrees of agonist activity at the apelin receptor and high stability in mouse plasma (half-life of more than 10 hours). ML233, a small molecule exhibiting a degree of specificity for the apelin receptor, was identified in the Molecular Libraries Small Molecule Repository high throughput screen of ~330,600 compounds, and showed good potency in *in vitro* assays (Khan et al., 2011). Screening of a small drug library of ~100 compounds that share structural features common amongst AT<sub>1</sub> receptor ligands led to the discovery of a drug-like

small molecule low affinity agonist of the apelin receptor (Narayanan et al., 2016). After modifying the side chains of the initial pyrazole based compound, a second was synthesised that showed a 27-fold enhancement in potency, demonstrating the potential of the initial compound as a scaffold for apelin receptor ligand discovery. Subsequent systematic structural modifications of the pyrazole core and side chain of the second compound resulted in a further 8-fold increase in potency (Narayanan et al., 2020).

CMF-019 is a small molecule based on a benzimidazole scaffold structure from Sanofi (Hachtel et al., 2014; Read et al., 2016). The compound binds to human, rat, and mouse apelin receptor with high affinity, and shows strong bias towards G protein signalling over  $\beta$ -arrestin and internalisation pathways. CMF-019 induces significant increases in cardiac contractility in rats, and is relatively stable in rat plasma versus [Pyr<sup>1</sup>]apelin-13. Interestingly, CMF-019 did not decrease blood pressure like [Pyr<sup>1</sup>]apelin-13, which may corroborate findings from Ceraudo et al., 2014, who suggest blood pressure responses mediated via the apelin receptor are  $\beta$ -arrestin dependent. Alternatively, the discrepancy between CMF-019 and [Pyr<sup>1</sup>]apelin-13 on blood pressure may be due to the limited solubility of the small molecule, or that a higher concentration may be required. Additionally, CMF-019 was, however, disease modifying in endothelial apoptosis *in vitro* and induced vasodilatation without desensitisation *in vivo* (Read et al., 2021). To summarise, CMF-019 provides proof-of-concept for the generation of biased small molecule apelin receptor ligands that target the receptor without inducing loss of the target from the cell surface following  $\beta$ -arrestin dependent desensitisation and internalisation. A number of other compounds based on the Sanofi structure have been assessed. For example, CMF-087 resulted from the introduction of an additional nitrogen atom into the benzimidazole ring, whilst side-chain modifications resulted in the design of MM239 and MM240, but these have not been fully experimentally characterised.

## 1.6. Apelin receptor structure

A number of studies have attempted to resolve the structure of the apelin receptor in order to characterise its interactions with endogenous and exogenous ligands, providing a useful scaffold for informed drug design, particularly by considering amino acids that regulate G protein signalling and bias. A snake plot showing the amino acid sequence of the apelin receptor is shown in Fig 1.2.

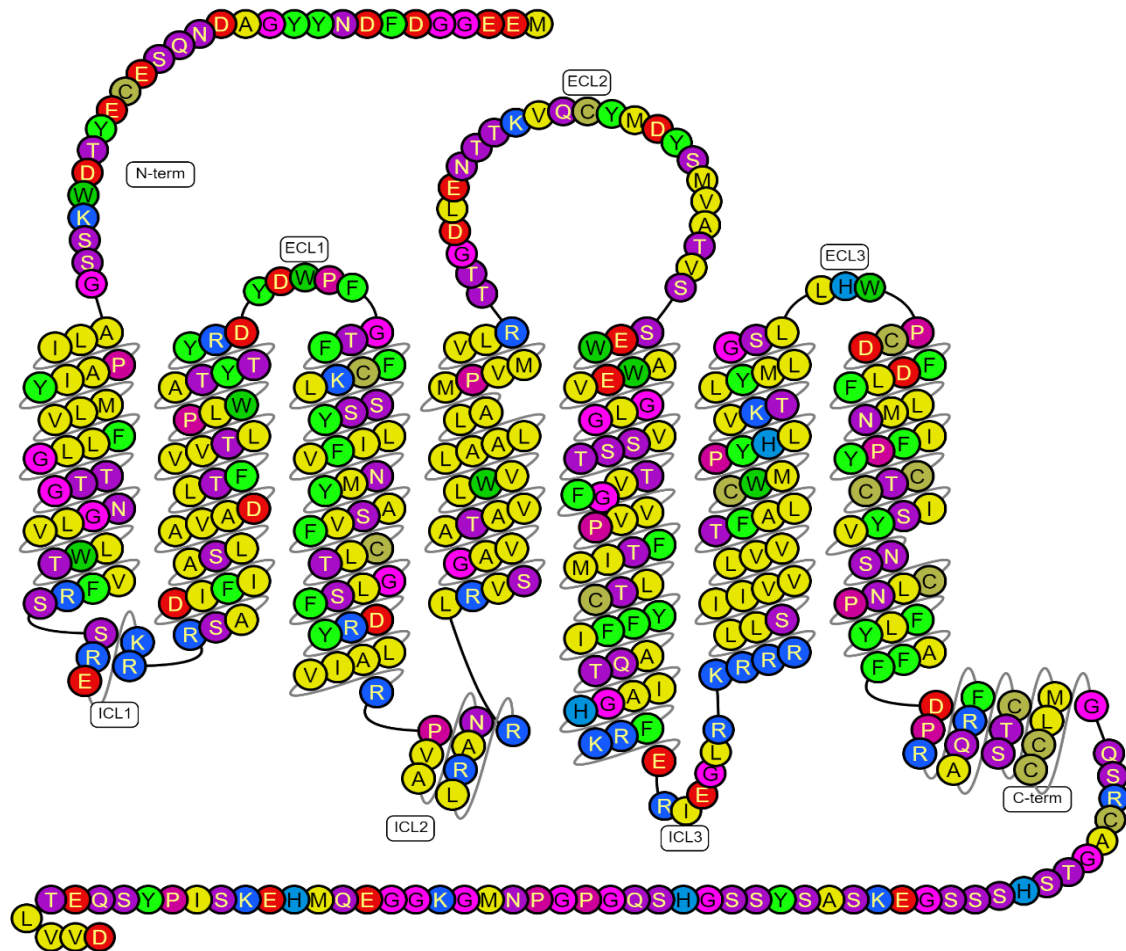


**Figure 1.2.** Snake plot showing the 380 amino acid apelin receptor. The plot shows the typical 7 transmembrane domains, extracellular and intracellular loops, and the N- and C-termini. Positively charged amino acids are shown in blue, negatively charged in red, hydrophobic in yellow, polar uncharged in purple, phenylalanine and tyrosine in green, cysteine in gold, proline in pink, and histidine in light blue. Figure was generated using GPCRdb (<https://gpcrdb.org/>, Kooistra et al., 2021).

Homology 3-dimensional (3D) models of the apelin receptor, based on the validated cholecystinin receptor-1 3D model or  $\beta$ 2 adrenergic receptor and C-X-C chemokine receptor type 4 (CXCR4) receptor X-ray crystal structure templates, docked to [Pyr<sup>1</sup>]apelin-13, have identified residues that are critical for ligand binding and receptor signalling. A conserved hydrophobic cavity comprising amino acids D92, E172, and D282 interacts with K8, R2, and R4 of the [Pyr<sup>1</sup>]apelin-13 ligand (Gerbier et al., 2015). Computational docking of ligands in a 2.5 Å resolution human CXCR4 receptor apelin receptor homology model demonstrated an interaction between Y88 and R168 of the receptor with the small molecule G protein biased agonist, CMF-019, that is predicted to bind at the same site as the SHK region of apelin-13 (Read et al., 2016). This homology model has also been used to show strong overlap in the calculated binding poses of apelin-13, ELA-11, and a G protein biased peptide agonist MM07 in molecular dynamics simulations (Brame et al., 2015; Yang et al., 2017a).

Mutational studies have identified key residues in the apelin receptor. After identifying phosphorylation sites, an artificial single point substitution, S348A, at the conserved S348 site, demonstrated reduced receptor phosphorylation by GRK, reducing recruitment of  $\beta$ -arrestin, extracellular signal-related kinase (ERK) signalling, and internalisation following exposure to apelin-13 (Chen et al., 2014). The S348 site showed no involvement in apelin receptor G protein signalling. A systematic mutational investigation of amino acids in the orthosteric binding site identified I109A as a single point substitution that results in the receptor adopting a G protein biased conformation, that shows defective engagement with G protein receptor kinases (GRKs) and  $\beta$ -arrestin (Ban et al., 2018). F255 and W259 in helix VI of the rat apelin receptor (corresponding to F257 and W261 in the human receptor) were also shown to be critical for internalisation following interaction with the C-terminal F of apelin-17, which docks into another hydrophobic cavity comprised of the above helix VI residues and W152 in helix IV of the cholecystinin receptor-1 3D model (Iturrioz et al., 2010b). The F255 and W259 sites also played no role in G protein signalling. Nuclear magnetic resonance spectroscopy and homology model based techniques allowed for the resolution of the first 55 amino acids of the apelin receptor, making the N-terminus and first transmembrane domain (Langelaan et al., 2013). E20 and D23 forms an extracellular anionic face that interacted with lipid head groups in molecular dynamics

simulations, suggesting binding of cationic apelin peptides is membrane catalysed. Full length receptor mutagenesis of amino acids in the first 55 amino acid long segment indicate G42, G45, and N46 as critical for proper trafficking of the apelin receptor.

A 2.6 Å atomic-resolution structure of the apelin receptor in complex with a conformationally restrained 17 amino acid apelin peptide mimetic (AMG3054) has recently been published (Ma et al., 2017). The study identified a distinct two-site binding mode of the ligand that had not been previously observed for the apelin receptor, or any other peptide-binding GPCR. The first site is made up of groove 1 (D172, E174, D184, and E194 in extracellular loop 2) and groove 2 (D282 and surrounding residues), whilst the second site is formed of the N-terminal loop that is conformationally restricted by a disulphide bond between C19 and C281. A second disulphide bridge was identified between C102 and C181. The C-terminal end of AMG3054 binds deeply into the canonical binding pocket that lies approximately perpendicular to the membrane plane, with the C-terminal F (4-Cl-Phe17) interacting with a hydrophobic cavity comprising Y35, W85, Y88, Y93, and Y299 that also line site 1. P16 and 4-Cl-Phe17 of the AMG3054 ligand both interact with R168. The lactam ring formed by the sidechains of E10 and K13 in AMG3054 induce a perpendicular kink in the peptide that allows the N-terminus to slide into site 2 at the extracellular surface of the receptor, in parallel with the membrane plane. Interestingly, the authors demonstrated that 17 amino acid dynorphin A peptide binds to the κ opioid receptor via a similar two-site binding mode, indicating this may be common amongst GPCRs.

Alanine scanning mutagenesis of the sites in groove 1 showed no impact on binding of apelin-13. It was concluded that shorter apelin isoforms may not interact with the acidic amino acids in groove 1 whilst longer isoforms such as apelin-36, that contain many positively charged amino acids. This may provide an explanation for longer lasting actions of apelin-36, although this was not experimentally determined. Further mutagenesis showed that many of the amino acids (e.g. Y35, W85, and R168) in sites 1 and 2 critical for binding of AMG3054, were also critical for [<sup>125</sup>I]-apelin-13 radioligand binding and G protein signalling.

The structural insights from Ma et al., 2017 need to be interpreted carefully, as the apelin receptor structure was heavily modified to improve protein yield and the thermostability of the receptor, and facilitate crystallisation. Both termini were truncated with amino acids 1-6 removed from the N-terminus and amino acids 331-380 from the C-terminus. An eight amino acid tag sequence was incorporated at the N-terminus, and rubredoxin (54 amino acids long) was incorporated between A229 and R243, replacing most of intracellular loop 3. Two further mutations in the C-terminus (C325L and C326M) were made to remove palmitoylation sites, and a mutation in the second extracellular loop (T177N) removed an N-glycosylation site. Finally, V117A and W261K mutations were introduced to further improve receptor yield and stability. Note that the peptide, AMG3054, also contains modifications not present in apelin-17, including a E10 to K13 lactam ring and non-naturally occurring amino acids at positions 8, 14, 15, and 17.

A snake plot showing key residues identified in the modelling and mutational studies discussed above is shown in Fig 1.3. Note, in general, that amino acids forming the binding pocket of the receptor are located at the extracellular ends of transmembrane domains I, II, IV, V, and VII, and in extracellular loops 1 and 2 themselves, where ligands bind to the receptor from the extracellular side.

Binding of ELA to the apelin receptor has also been explored recently in docking and binding studies (Trân et al., 2020). Key findings by the authors show that the F residue at position 10 of the ELA-11 peptide binds to a groove distinct from that of the C-terminal F of apelin-13, and the C-terminal P residue of ELA-11 may bind to the F13 apelin-13 pocket. G protein and  $\beta$ -arrestin assays revealed the necessity of a P or F aromatic residue at the C-terminal end of the peptides for receptor activation. A summary of the critical interaction sites between a modified apelin peptide ligand (AMG3054; from Ma et al., 2017) and ELA-11 (from Trân et al., 2020) with the receptor are displayed in Table 1.1.



<b>Apelin receptor</b>	<b>Apelin*</b>	<b>ELA-11</b>
Y264, K268	F13	-
W85, Y88, T89, Y93, Y299	F13	-
R168	P12	P11
W24, Y93	P12	P11
W24, K268, Y271, F291	M11	F10
L173, E198	P10	P9
Y271	G9	V8
Y21, S275, D284	K8	R7
E174	H7	S6
Y21	S6	H5
E174	S6	H5
E20, T22	L5	L4
D23	R4	-
T22, D23	P3	M2
K25, D92	pQ1	-

**Table 1.1.** Key amino acid interactions regulating binding of a modified apelin\* ligand and ELA-11 endogenous peptide to apelin receptor. Determined by docking and binding studies in Ma et al., 2017 and Trân et al., 2020 for apelin\* and ELA-11 respectively.

## **1.7. Apelin receptor mutations**

Whilst the above mutational studies have assessed artificial mutation at the apelin receptor, the identification and characterisation of naturally occurring mutations at this GPCR remain poorly explored and understood. In zebrafish, the naturally occurring grinch<sup>s608</sup> mutation has been identified in *aplnr*b (see Section 1.2.5; Scott et al., 2007; Zeng et al., 2007), comprising a W85L amino acid substitution that abolishes responses to apelin, but naturally occurring mutations in human apelin receptor have not been reported.

### **1.7.1. GPCR mutation**

GPCRs are susceptible to mutation, where variations in the amino acid sequence can induce changes in the protein structure, potentially impacting the ability of the receptor to perform its physiological functions. Reduced, or even wholly abolished receptor function, can occur as the result of loss-of-function mutations, but receptor efficiency can also be enhanced by mutations in gain-of-function mutations (Thompson et al., 2014; Stoy & Gurevich, 2015). To date, just more than 2350 mutations, identified in 55 GPCRs, have been associated with 66 human diseases, 14 of which are associated with gain-of-function mutations (Schöneberg & Liebscher, 2021).

Three naturally occurring mutations in the endothelin B receptor, for example, have been well characterised (Fuchs et al., 2001). Identified in patients with Hirschsprung's disease, the G57S and R319W bound the peptide ligand, endothelin-1, and induced Ca<sup>2+</sup> signalling, but did not inhibit adenylyl cyclase. In fact, the G75S mutation stimulated cAMP accumulation. Additionally, a P383L mutation resulted in clustering of the receptor in perinuclear regions, and absence at the membrane.

Identified in a patient with congenital nephrogenic diabetes insipidus, a deletion mutation shifts the reading frame from position 247 and introduces a premature stop codon from position 270 in the vasopressin V2 receptor, resulting in loss of the entire C-terminal third of the receptor (Rosenthal et al., 1992). Shortly after, the naturally occurring R137H mutation was also identified in a patient with congenital nephrogenic diabetes insipidus, and the mutated receptor was characterised *in vitro*. Data showed

good expression and binding with vasopressin, but failed coupling to  $G\alpha_s$  and stimulation of adenylyl cyclase (Rosenthal et al., 1993). The authors suggest the findings offered biochemical proof that the mutant receptor was causative of the disease pathology.

More recently, 61 variants of the melanocortin 4 receptor (MC4R), identified in a screen of 0.5 million people recruited in the UK Biobank, were characterised *in vitro* (Lotta et al., 2019). Intriguingly, several of the variants demonstrated gain-of-function in recruitment of  $\beta$ -arrestin, and this was associated with significantly lower body mass index (BMI), and lower odds of obesity, type 2 diabetes, and coronary heart disease. This study shows a protective effect of mutation in a human protein, and the results indicate that the design of biased ligands selective for  $\beta$ -arrestin pathways at MC4R could be an effective therapeutic strategy at this receptor in a number of metabolic disorders.

### ***1.7.2. The NIHR BioResource Rare Diseases BRIDGE consortium sequencing project***

The NIHR BioResource Rare Diseases BRIDGE consortium sequencing project (herein referred to as the BRIDGE project), is a collaboration between 13 rare disease projects that aim to discover the genetic sequence variants underlying unresolved inherited disorders and to improve identification of already identified high penetrance variants, as a prospective component of the Genomics England 100,000 Genomes Project (Turnbull et al., 2018). The BRIDGE project covers a variety of rare disease research areas including cardiovascular, infection and immunity, and neuroscience. As one example of its success, whole-genome sequencing of 1038 pulmonary arterial hypertension (PAH) index cases and 6385 PAH-negative control subjects, with subsequent case-control analysis, identified significant overrepresentation of rare variants in several proteins, revealing missing heritability of PAH not caused by variation in bone morphogenetic protein type 2 receptor (BMP2) (Gräf et al., 2018). In its association with the NIHR BioResource, the BRIDGE project is highly valuable to researchers for the capacity to provide phenotypic information for recruited participants, and the opportunity to recall participants for further assessment.

## **1.8. Aims for the apelin receptor**

As a highly important regulator of human cardiovascular physiology and disease, the apelin receptor GPCR is an attractive target in translatable pharmaceutical research. In this thesis, the apelin receptor will be explored using a variety of binding and functional assays, including the use of four novel fluorescent ligands based on apelin and ELA peptide agonists, described in-depth in Chapter 3. These were hypothesised to function as versatile experimental tools for studying apelin receptor pharmacology in response to apelin and ELA based ligands. Data showed that these fluorescent ligands were highly suitable for studying the apelin receptor, and were subsequently used in the work outlined in Chapter 4. This Chapter aimed to characterise the pharmacological consequences of apelin receptor mutation, exploring apelin receptor variants identified in patients recruited to the BRIDGE project. The variants were selected for their rarity and predicted harmfulness, and were thus hypothesised to show pronounced effects on the pharmacology of the receptor. Data identified three apelin receptor variants, incorporating V38L, T89M, and R168H single point substitutions that substantially altered ligand binding, signalling, and/or membrane localisation of the receptor.

## **1.9. ACE2**

### **1.9.1. ACE2 overview**

The human *ACE2* gene is mapped to chromosomal locus Xp22.2, and encodes angiotensin-converting enzyme 2 (ACE2, UniProt ID: Q9BYF1) (Turner et al., 2002). The ACE2 protein is an 805 amino acid zinc-metalloproteinase type 1 transmembrane protein (Tipnis et al., 2000; Donoghue et al., 2000; Hamming et al., 2007; Badawi & Ali, 2021). During the COVID-19 pandemic, ACE2 attracted much attention, following its identification as the cell surface receptor that the severe acute respiratory syndrome coronavirus 2 (SARS-CoV-2) exploits to infect host cells (Hoffmann et al., 2020; Wrapp et al., 2020; Yan et al., 2020; Yang et al., 2021). This follows on from its earlier identification as the receptor for other human coronaviruses – severe acute respiratory syndrome coronavirus (SARS-CoV) and human corona virus NL63 (HCoV-NL63) Li et al., 2003; Kuhn et al., 2004; Hofmann et al., 2005; Hamming et al., 2007). Despite the negative role ACE2 plays in viral infection, the protein is also a critical regulator of the cardiovascular system, where it mediates beneficial antihypertensive effects as a component of the renin-angiotensin-aldosterone system (RAAS) (Burrell et al., 2004; Hamming et al., 2007; Tikellis et al., 2011; Samavati & Uhal, 2020). Intriguingly, ACE2 also interacts with the apelin signalling axis, where the enzyme cleaves the C-terminal F of [Pyr<sup>1</sup>]apelin-13 to form [Pyr<sup>1</sup>]apelin-13<sub>(1-12)</sub>, which is expressed and retains its biological functional as a potent vasoactive agent and positive cardiac inotrope in the cardiovascular system (Yang et al., 2017b).

### **1.9.2. ACE2 expression**

Assessment of ACE2 mRNA expression has shown a relatively wide distribution, potentially owing to its endothelial localisation, with mRNA expression detected at particularly high levels in the kidney, testis, gastrointestinal tract (predominantly intestinal), and heart (Tipnis et al., 2000; Donoghue et al., 2000; Harmer et al., 2002; Hamming et al., 2004; Reich et al., 2008). In the heart itself, mRNA has been observed in the vascular endothelium and smooth muscle, myofibroblasts, and cardiomyocytes (Burrell et al., 2005; Guy et al., 2008). When looking at ACE2 protein, endothelial and vascular smooth muscle localisation has been observed, but localisation to lung epithelial cells (sinonasal cavity and alveolar type II cells), renal tubules, intestinal

enterocytes, and cardiomyocytes is also reported (Hamming et al., 2004; Reich et al., 2008; Hikmet et al., 2020; Ortiz et al., 2020; Zhao et al., 2020).

## **1.10. ACE2 in physiology**

### ***1.10.1. Renin angiotensin aldosterone system***

The highly complex RAAS tightly regulates cardiovascular physiology through control of vascular tone and fluid homeostasis, amongst other mechanisms (Ocaranza et al., 2020). Renin enzyme was discovered in kidney extract and was described as displaying hypertensive properties (Tigerstedt & Bergman, 1898; Karnik et al., 2015). Renin is secreted into the circulation by juxtaglomerular cells in the kidney, in response to response to several stimuli, including renal sympathetic activity (through  $\beta$ -adrenergic receptors), decreased intrarenal blood pressure, and/or decreased delivery of salt (chloride ions) to the macula densa (Persson, 2003). The enzyme catalytically cleaves angiotensinogen, produced in the liver, to form angiotensin I, a 10 amino acid peptide that displays no biological activity on its own (Karnik et al., 2015; Lu et al., 2016). Angiotensin I however, is a precursor for angiotensin II, an 8 amino acid peptide hormone produced following catalytic cleavage of the two last amino acids at the C-terminus by angiotensin-converting enzyme (ACE). ACE is also a zinc-metalloproteinase that shares 42 % identity with ACE2 in the catalytic domain (Donoghue et al., 2000). Angiotensin II can act directly on angiotensin II type 1 (AT<sub>1</sub>) and type 2 (AT<sub>2</sub>) receptors, GPCRs that mediate the effects of the RAAS. The AT<sub>1</sub> receptor has two subtypes, AT<sub>1a</sub> and AT<sub>1b</sub> that share 95 % sequence identity, but show different patterns of expression, with AT<sub>1a</sub> receptor expressed in most cardiovascular tissues, whilst AT<sub>1b</sub> is more restricted to endocrine tissues (Kakar et al., 1992; Ito et al., 1995; Sugaya et al., 1995; Chen et al., 1997; de Gasparo et al., 2000; Karnik et al., 2015). Angiotensin II stimulation of AT<sub>1</sub> receptors induces hypertension through vasoconstriction, and increased blood volume through stimulation of aldosterone (increases renal salt retention) from the adrenal gland (Aguilera et al., 1992) and vasopressin (a vasoconstrictor that also mediates renal reabsorption of water) from the hypothalamus (Qadri et al., 1993).

### **1.10.2. ACE2 counter-regulates the renin angiotensin aldosterone system**

ACE2 can cleave both angiotensin I and angiotensin II peptides to generate angiotensin 1-9 and angiotensin 1-7 as part of the counter-regulatory arm of the RAAS (Oudit et al., 2003; Forrester et al., 2018; Ocaranza et al., 2020). Angiotensin 1-9 acts at AT<sub>2</sub> receptors to induce natriuresis, lowering blood volume (Padia et al., 2008), and stimulates production of the vasodilator, nitric oxide (Ocaranza et al., 2014). Angiotensin 1-7 also exerts antihypertensive effects, possibly through targeting the MAS1 oncogene (MAS receptor) (Sato et al., 2013), a GPCR shown to induce natriuresis (DelliPizzi et al., 1994) and vasodilatation through nitric oxide production (Li et al., 1997) (Ocaranza et al., 2020).

### **1.10.3. ACE2 substrates outside the RAAS**

In its role as a carboxypeptidase that cleaves single C-terminal amino acids from peptides (Hamming et al., 2007), ACE2 has a wide substrate specificity, outside the angiotensin peptides of the RAAS. In a panel of 126 biological peptides, 11 were hydrolysed by ACE2, with particularly high efficiency observed for C-terminal catalysis of des-Arg(9)-bradykinin, dynorphin A-(1–13), and apelin-13 (Vickers et al., 2002).

The kinin-kallikrein system (KKS), like the RAAS, comprises a precursor, kininogen, and kallikrein enzymes that produce the effector peptides bradykinin and des-Arg(9)-bradykinin (Sodhi et al., 2018). The effector peptides in the KKS also target GPCRs – the bradykinin receptor 1 (B<sub>1</sub>) and bradykinin receptor 2 (B<sub>2</sub>). Both receptors mediate proinflammatory responses in the vasculature, including vasodilatation and increased vascular permeabilisation (Marceau et al., 2020). Strangely, ACE and ACE2 work in tandem to suppress the KKS, metabolising bradykinin and des-Arg(9)-bradykinin respectively into inactive metabolites, both reducing kinin mediated vasodilatation (Hamming et al., 2007). The KKS and role of ACE2 in this setting, remains poorly characterised however.

### **1.10.4. ACE2 and the apelin signalling axis**

There is considerable crosstalk between ACE2 and the apelin signalling axis (Chen et al., 2015; Chatterjee et al., 2020). As discussed previously, apelin peptides are substrates for ACE2, with the enzyme removing the C-terminal F residue (Vickers et

al., 2002). The [Pyr<sup>1</sup>]apelin-13<sub>(1-12)</sub> metabolite of ACE2 cleavage is expressed in human cardiovascular tissue, and was shown to be biologically active both *in vitro* and *in vivo* (Yang et al., 2017b), suggesting that ACE2 does not necessarily 'switch off' apelin signalling like it does des-Arg(9)-bradykinin in the KKS (Hamming et al., 2007). However, other findings demonstrate ACE2 mediated cleavage of [Pyr<sup>1</sup>]apelin-13 and apelin<sub>17</sub> partially inactivates the peptides in an *in vitro* setting, and abolished cardioprotective effects *in vivo* in mice (Wang et al., 2016). Additionally, when ACE2 was knocked out or pharmacologically inhibited in mice, hypotensive effects of apelin peptides were potentiated and prolonged.

Both ACE2 and apelin have been hypothesised as novel targets for therapeutics in heart failure and other cardiovascular diseases (Kazemi-Bajestani et al., 2012). ACE2 mRNA and protein was downregulated in the heart and aorta of aged apelin knockout mice, as was the apelin receptor itself (Sato et al., 2013). Consistent with previous reports showing impaired contractility and cardiac hypertrophy in apelin knockout mice, the authors go on to demonstrate rescue of this aberrant phenotype via inhibition of the AT<sub>1</sub> receptor, and by treatment with angiotensin 1-7. Additionally, apelin treatment increased ACE2 promoter activity *in vitro* and stimulated increased ACE2 expression in the failing heart *in vivo*. Finally, the study also showed that apelin increased ACE2, and cardiac contractility, in AT<sub>1</sub> receptor knockout mice. The data suggest that a component of beneficial cardiovascular apelin signalling is mediated through its upregulation of ACE2 and subsequent negative control of the RAAS (Sato et al., 2013).

The role of the second apelin receptor ligand, ELA, has also been studied for interaction with ACE2. ELA was shown to downregulate ACE, but had no significant impact on ACE2 expression, in contrast with apelin (Sato et al., 2017). Regardless, ELA treatment blocked angiotensin II mediated hypertension and cardiac hypertrophy *in vivo* in mice. In another study, ELA peptide, shown to be expressed in the collecting duct of the kidney, antagonised the RAAS within the kidney to lower blood pressure and protect against renal injury in mice (Xu et al., 2020). Exogenous ELA treatment downregulated prorenin and renin protein, and ELA-32 infusion reversed high salt

induced upregulation of prorenin and renin in rats, whilst significantly lowering blood pressure. It is currently unreported whether ELA acts as a substrate for ACE2.

The interplay with ACE2 provides further evidence for discrepancies in the mechanistic effects of apelin versus ELA at the apelin receptor. It remains to be seen how best to exploit the counter-regulation of the RAAS by the apelin receptor signalling axis as a therapeutic strategy.

#### ***1.10.5. ACE2 in the gastrointestinal tract***

ACE2 is highly expressed in the gastrointestinal tract, particularly the enterocytes lining the small intestine (Zhang et al., 2020). The digestion of proteins into their constituent amino acids is facilitated by a number of peptidases, of which ACE and ACE2 are included, localised at the brush-border, before subsequent absorption through transporter proteins (Bai, 1993; Kowalczyk et al., 2008). The neutral amino acid transporter, B<sup>0</sup>AT1 (encoded by the *SLC6A19* gene in humans), was shown to be co-expressed with ACE2, where ACE2 significantly increased the expression of B<sup>0</sup>AT1 at the cell surface in heterologous systems (Kowalczyk et al., 2008; Camargo et al., 2009). A complex formed from the interaction of ACE2 with B<sup>0</sup>AT1 has been identified in immunoprecipitation experiments, and confirmed the requirement of the ACE2 for appropriate surface expression of the amino acid transporter (Fairweather et al., 2012). The role of ACE2 in the gastrointestinal, particularly in gastrointestinal disease, will be discussed below, in Section 1.11.2.

### **1.11. ACE2 in pathophysiology**

#### ***1.11.1. ACE2 in cardiovascular disease***

Owing to its role in the RAAS, ACE2 is associated with various cardiovascular risks and diseases (Ramchand & Burrell, 2020). A soluble form of ACE2 is shed from the membrane following proteolytic cleavage by ADAM17 (A disintegrin and metalloprotease 17), reducing the protection afforded by ACE2 in tissue RAAS (Jia et al., 2009; Wang et al., 2020). Additionally, increased levels of the soluble ACE2 circulating in plasma is a predictor for adverse cardiovascular outcomes in patients with coronary heart disease and heart failure, suggesting that ACE2 could be used as a biomarker

for cardiovascular disease and adverse events (Ramchand & Burrell, 2020). A large scale study, looking at over 10,000 participants showed increased circulating ACE2 was associated with a higher risk of heart failure, myocardial infarction, stroke, and diabetes, and also with increased risk of death in patients with cardiovascular morbidities (Narula et al., 2020). Targeting ACE2, pharmacologically or genetically, is hypothesised as an alternative strategy to ACE inhibitors or AT<sub>1</sub> receptor blockers for suppressing the RAAS in various cardiovascular disease states (Robles et al., 2014), but it remains to be seen if this will be an effective approach in the development of new treatment options.

### **1.11.2. ACE2 in Hartnup disease**

Intriguingly, ACE2 potentially plays an indirect role in the pathology of the genetic metabolic Hartnup disease. The disorder is characterised by increased excretion of neutral amino acids from both the intestinal tract and the kidney (Scriver, 1965), and patients can present with a pellagra-like rash (where pellagra is a disease caused by lack of niacin or tryptophan), and cerebellar ataxia amongst other neurological or psychiatric aberrations (Seow et al., 2004). Hartnup disease is causally linked to mutations (Seow et al., 2004) in the *SLC6A19* gene encoding the B<sup>0</sup>AT1 protein that forms a complex with ACE2 as described in Section 1.10.4. A study assessing the R240Q mutation identified in a patient with Hartnup disease, showed that the B<sup>0</sup>AT1 protein was no longer able to associate with ACE2 and the renal paralogue of ACE2, called collectrin, resulting in reduced membrane expression in cells lining the intestine and kidney tubules (Kowalczyk et al, 2008). An subsequent study demonstrated that the D173N and P265L mutants of B<sup>0</sup>AT1 were able to interact with ACE2 but not collectrin, whilst the A69T and R240Q mutants were functional in neutral amino acid transport, but were both unable to form complexes with ACE2 or collectrin, confirming that the R240Q disease pathology is intrinsically linked to the inability to form complexes with ACE2 (Camargo et al., 2009).

### **1.11.3 ACE2 as a viral entry receptor**

Alongside its cardiovascular role in the RAAS, ACE2 has attracted attention for its exploitation by human coronaviruses, giving the typically beneficial protein a so-called 'double-edge' (Wang et al., 2020; Gheblawi et al., 2020).

Initially, the S1 domain of spike (S) proteins decorating the outer layer of SARS-CoV viral capsules were shown to bind to ACE2 with high affinity, that could be displaced by inclusion of high concentrations of soluble ACE2, and SARS-CoV virus replicated only in heterologous cells expressing an ACE2 construct but not mock-transfected cells (Li et al., 2003). In mice, SARS-CoV myocardial infection was shown to be ACE2 dependent, and corresponded with a marked decrease in ACE2 expression (Oudit et al., 2009). Further, the authors demonstrated that SARS-CoV induced myocardial inflammation and damage observed in SARS-CoV infected patients may be associated with downregulation of ACE2. ACE2 is also critical for binding of human coronavirus NL63 (HCoV-NL63) spike protein (Hofmann et al., 2005; Li et al., 2007). The COVID-19 pandemic continues to put great strain on global health care, wellbeing, and the economy. SARS-CoV-2, the viral cause of the pandemic, also binds and infects host cells through interaction of its spike S1 domain with ACE2 (Hoffmann et al., 2020; Wrapp et al., 2020; Yan et al., 2020; Yang et al., 2020). The organs critically affected (e.g. infected and/or damaged) by SARS-CoV-2 are those that typically express ACE2, such as the epithelial cells of the nasopharyngeal tracts, lungs, gastrointestinal tract, kidney, and heart. In line with its role as the viral entry receptor, ACE2 was quickly recognised as a potential pharmacological therapeutic target in the treatment of COVID-19, particularly in individuals where vaccination is contraindicated or might show less efficacy (e.g. in the immunosuppressed) (Alexander et al., 2020). Additionally, a large-scale study (> 7500 COVID-19 patients) used Mendelian randomisation to strategically explore drug repurposing strategies to combat SARS-CoV-2 infection, and shows that increased expression of ACE2 correlates with increased risk of hospitalisation in COVID-19 (Gaziano et al., 2021).

SARS-CoV-2 spike was shown to bind to ACE2 with high affinity (~15 nM), but mutations in the viral spike protein, such as the D614G variant, can enhance the strength of the interaction (Ozono et al., 2021). Importantly, a number of other host cell proteins are involved in the viral infection and/or replication stages of SARS-CoV-2. Transmembrane protease serine 2 (TMPRSS2) has been shown to be crucial for priming of the SARS-CoV-2 spike protein through cleavage of S1/S2 and S2' sites at the host cell surface, and cells were significantly more permissive to viral infection

when TMPRSS2 was co-expressed with ACE2 (Shang et al., 2020; Hoffman et al., 2020). The intracellular proteases, furin and cathepsin, were shown to catalytically cleave S1/S2 spike sites, and mediate endosomal processing of the viral particle respectively (Cheng et al., 2020; Liu et al., 2020). Furin inhibitors were shown to suppress viral production and infection of neighbouring cells, reducing cytotoxicity (Cheng et al., 2020). The cathepsin L isoform predominantly, has demonstrated a key role in enhancing SARS-CoV-2 infection *in vitro*, and drugs that inhibit cathepsins, such as amantadine (Zhao et al., 2021) and E64d (Hoffman et al., 2020) have exhibited SARS-CoV-2 spike protein anti-viral properties.

A dimer-of-heterodimers complex formed between ACE2 and B<sup>0</sup>AT1 (as described in Sections 1.10.4 and 1.11.2) can intriguingly bind two SARS-CoV-2 spike proteins simultaneously, reportedly with higher affinity than ACE2 alone (Yan et al., 2020; Stevens et al., 2021). Further, B<sup>0</sup>AT1 in the complex may have an impact on the engagement of ACE2 with TMPRSS2, although this needs further characterisation (Stevens et al., 2020).

Owing to the complex interactions between ACE2 and the apelin signalling axis discussed in Section 1.10.3, it has been hypothesised that the apelin receptor is also a potential target in the treatment of COVID-19 and/or its symptoms (Saravi & Beer, 2020). In an analysis of RNA-sequencing datasets from cardiomyocytes infected with SARS-CoV-2, and from cardiovascular tissues from COVID-19 patients, both apelin and ACE2 were shown to be downregulated, possibly contributing to the cardiorenal injury observed in COVID-19 (Li et al., 2021), as was observed in the myocardium of patients infected with SARS-CoV (Oudit et al., 2009). Additionally, the APEL-COVID clinical trial (ClinicalTrials.gov Identifier: NCT04632732), completed in October 2021 but with results yet to be disclosed, aimed to assess apelin and ACE2 as biomarkers for alveolar capillary permeability in COVID-19. Nevertheless, the experimental exploration of apelin in SARS-CoV-2 remains to be conducted.

## **1.12. ACE2 structure**

As discussed, ACE2 is an 805 amino acid (~120 kDa) zinc-metalloproteinase type 1 transmembrane protein that shares high sequence homology with ACE (Tipnis et al., 2000; Donoghue et al., 2000; Hamming et al., 2007; Badawi & Ali, 2021). Modelling studies revealed structural differences in the active site of ACE versus ACE2, conferring specificity for different substrates (Guy et al., 2003). Surprisingly, the C-terminal portion of ACE2 shares high sequence homology (~48 %) with the renal protein, collectrin, that is also mapped to chromosome Xp22 (Zhang et al., 2001; Danilczyk et al., 2006; Malakauskas et al., 2007). Collectrin has been shown to act as a chaperone for B<sup>0</sup>AT1 membrane expression in the kidney (Danilczyk et al., 2006; Malakauskas et al., 2007), and it is through the 'collectrin-like domain' (comprising amino acids 616 – 805) that ACE2 protein also performs this role, particularly in the intestine where collectrin is not expressed (described in Section 1.11.2). ADAM17 cleaves ACE2 to generate a soluble form of the protein (555 amino acids long) that is shed from the membrane (Jia et al., 2009).

Additionally, six different transcript variants of the human receptor have been identified, corresponding to four ACE2 isoforms that are shorter than the full-length protein (Badawi & Ali, 2021). One isoform encodes a protein only slightly shorter than the full-length ACE2, lacking the last 18 amino acids at the C-terminus but otherwise showing 100 % sequence identity. Another is comprised of 694 amino acids that shares ~95 % identity. A novel transcript variant has been recently identified in three independent reports, encoding a short isoform comprising amino acids 357-805 of the full-length ACE2 protein, and possessing a unique 10 amino acid cap at the N-terminus (Ng et al., 2020; Onabajo et al., 2020; Blume et al., 2021). This transcriptionally independent isoform is upregulated in response to interferon stimulation and rhinovirus infection, unlike the full-length ACE2 protein, but is not upregulated by SARS-CoV-2 (Ng et al., 2020; Onabajo et al., 2020; Blume et al., 2021). Intriguingly, the isoform lacks both fully functional enzymatic activity, and loses the high affinity SARS-CoV-2 spike protein binding sites seen in full-length ACE2. A schematic showing the structure of full-length ACE2 versus the short isoform can be found in Chapter 6 (see Fig 6.2). Whilst mRNA of the short isoform is expressed in

airway epithelia and squamous tumours of the respiratory, gastrointestinal, and urogenital tracts, expression at the protein level remains uncharacterised. Work discussed in Chapter 6 of this thesis aims to address the dearth of information on the tissue distribution, and potential role in COVID-19, of the short ACE2 isoform.

### **1.13. Aims for ACE2**

ACE2 is a crucial component of the RAAS in the cardiovascular system, but has recently drawn attention as a target for infection by human coronaviruses, including SARS-CoV-2, which is the cause of the COVID-19 pandemic. In this thesis, it was hypothesised that ACE2, along with other host cell proteins implicated in SARS-CoV-2 infection, would be expressed in hESC-CMs, a clinically relevant model where SARS-CoV-2 has been causally linked to cardiac damage in infected patients. A high-throughput drug screening platform, using this cell model, was developed to identify novel inhibitors of viral infection, and is discussed in-depth in Chapter 5. The emergence of an ACE2 isoform, truncated at the N-terminus and thus lacking SARS-CoV-2 binding sites, is poorly characterised in relation to its protein expression and distribution. Work described in Chapter 6 aims to identify the organs and tissue beds that this short isoform is present in, and uses a novel fluorescently tagged SARS-CoV-2 spike receptor binding motif protein monomer, that was hypothesised not to bind to dACE2, to explore the potential role of this isoform in COVID-19.

## **Chapter 2. Materials & Methods**

### **2.1. Overview**

The Materials & Methods chapter of this thesis will describe the basic outlines and principles of the techniques used in this work, including in-house validation where appropriate. In-depth methodological procedures can then be found in the relevant Results chapters.

### **2.2. COVID-19 statement**

During the COVID-19 pandemic, the UK government coronavirus lockdowns in 2020 and 2021 were necessary precautions, but severely impacted on the ability to continue work, particularly in a hospital environment. Approximately four months (March – June 2020) of laboratory time was lost, but Professor Davenport was subsequently able to secure permission to conduct research on projects directly associated with the SARS-CoV-2 virus, meaning work on the apelin receptor was temporarily halted. Additionally, access to facilities for training, cell culture, and use of experimental equipment was strictly limited. Work that had been conducted at Sosei Heptares, as part of the ORBIT (Opportunities in Receptor Biology for Industrial Translation) collaboration was unable to continue under the UK government COVID-19 restrictions.

### **2.3. Materials**

All reagents used in this thesis were from Sigma-Aldrich (now Merck), unless specified as otherwise. All antibodies used in this thesis were from Abcam, unless specified otherwise. HEK293T cells (# CRL-3216) and CHO-K1 cells (# CCL-61) were from ATCC. H9 human embryonic stem cells (hESCs) (WA09) were from WiCell. These pluripotent cells are derived from a female human blastocyst (Thomson et al., 1998). Surgical samples of human tissue were obtained with informed consent, and ethical approval (05/Q104/142) held by Professor Anthony Davenport.

## **2.4. Cell culture**

All cells were maintained in incubators at 37 °C, 5 % CO<sub>2</sub>, humidified.

### **2.4.1. General cell culture**

Prior to the COVID-19 pandemic, HEK293T cells were cultured by the author at Sosei Heptares. During restrictions, culturing was instead performed by Mr Jason Brown. Cells were maintained in 20 – 25 mL Dulbecco's Modified Eagle Medium (DMEM, ThermoFisher Scientific) supplemented with 10 % foetal bovine serum (FBS, ThermoFisher Scientific) in T175 cell culture flasks (Corning). CHO-K1 cells were cultured in-house. Cells were maintained in 20- 25 mL DMEM/F-12 (1:1) nutrient mix + L-glutamine (ThermoFisher Scientific), supplemented with 10 % FBS (ThermoFisher Scientific) in the presence of 0.1 mg/mL Normocin antibiotic formulation (InvivoGen) in T175 cell culture flasks (Corning). Cells were grown to confluency before washing with sterile phosphate buffered saline (PBS, ThermoFisher Scientific), and subsequent passaging with 3 mL porcine trypsin for 3 mins. Trypsin dissociation was neutralised with 7 mL culture media, before cell suspensions were spun in a centrifuge at 300 xg for 5 mins. Media was aspirated before cell pellets were resuspended in 10 mL media for replating in flasks or experimental plates. For determination of cell numbers, 3 mL of the cell suspension was diluted 1:10 in media, and 10 µL of the resulting suspension counted using a haemocytometer.

### **2.4.2. Generation of apelin receptor plasmid DNA**

Wild-type apelin receptor plasmid DNA constructs were generated in collaboration with Dr Heather Currinn at Sosei Heptares. In brief, wild-type apelin receptor templates were PCR cloned into a pcDNA3.1 mammalian expression vector (Invitrogen) at NheI/NotI restriction sites using Phusion Hot Start II DNA polymerase (ThermoFisher Scientific), in accordance with the manufacturer's instructions. Wild-type and variant apelin receptor cDNA templates tagged C-terminally with eGFP were cloned in the same manner. Cloned plasmid vectors were transformed in DH5α competent *E. coli*, before isolation using a QIAprep Spin Miniprep Kit (Qiagen), in accordance with the manufacturer's instructions. DNA concentration was determined using a NanoDrop One (ThermoFisher Scientific). The plasmid constructs also harboured a G418 genetic

resistance gene. A CHO-K1 cell line, stably expressing the apelin receptor (herein referred to as CHO-APLNR), were a kind gift from Mr Jason Brown at Sosei Heptares, generated by selecting colonies that survived 500 µg/mL G418 genetic antibiotic selection.

#### **2.4.3. Transfection of cells with apelin receptor DNA**

HEK293T were grown to ~60 % confluency in 20 mL DMEM supplemented with 10% foetal bovine serum in T175 cell culture flasks, before incubation with 6 ng/mL wild-type or variant apelin receptor plasmid DNA in the pcDNA3.1 mammalian expression vector. Transfection reagent was comprised of a mix of 3 µL Novagen GeneJuice Transfection Reagent (Merck) added into 100 µL Opti-MEM reduced serum medium (ThermoFisher Scientific), incubated for 5 mins at room temperature, before addition of plasmid DNA to give the final 6 ng/mL concentration for a further 15 mins to allow complexes to form. Plasmid DNA was added to cells in transfection reagent, before incubation for 24 h at 37 °C, 5 % CO<sub>2</sub>, humidified. The following day, cells were dissociated with TrypLE reagent for subsequent preparation and use in experiments.

CHO-K1 cell transfection was performed in-house. Cells were seeded in CellCarrier-96 Ultra Plates (PerkinElmer) at a density of 10 k/well and returned to an incubator (37 °C, 5 % CO<sub>2</sub>, humidified) for 24 h. Cells were then transiently transfected with wild-type or variant apelin receptor plasmid DNA using a TransIT-CHO Transfection Kit (MIR 2174; Mirus Bio), in accordance with the manufacturer's instructions. In brief, 0.05 µL CHO MoJo reagent was added to 0.3 µL TransIT-CHO reagent in 9 µL Opti-MEM reduced serum medium, and plasmid DNA added to make a 10 ng/mL working solution per well to be infected. Complexes were allowed to form for 30 mins at room temperature, before a 10 µL addition of the transfection solution into 90 µL DMEM/F-12 media in each well, to give a final DNA concentration of 1 ng/mL. Cells were incubated for 24 h at 37 °C, 5 % CO<sub>2</sub>, humidified before subsequent experimentation.

#### **2.4.4. hESC cell culture**

Owing to restrictions on the grounds of COVID-19, training and access to facilities for the culturing of H9 hESC cells was not permitted. Culturing and differentiation was instead performed by Ms Robyn Macrae and Dr Maria Colzani in the Wellcome-MRC

Cambridge Stem Cell Institute, using a protocol adapted from Cheung et al., 2014. In brief, undifferentiated H9 hESCs were maintained in CDM-BSA media, comprised of Iscove's Modified Dulbecco's Medium (IMDM)/F-12 (1:1) nutrient mix, supplemented with 15 µg/mL transferrin (R&D Systems), 7 µg/mL insulin, 450 mM monothioglycerol, 1 % chemically defined concentrated lipids (ThermoFisher Scientific), 5 mg/mL bovine serum albumin (Europa Bio Products), 100 U/mL penicillin-streptomycin (ThermoFisher Scientific), 12 ng/mL fibroblast growth factor 2 (FGF2, Qkine Ltd), and 10 ng/mL activin-A (Qkine Ltd). Cells were grown in 6-well plates (Corning) coated with 0.1 % gelatin in sterile PBS. Media was changed every day. Cells were grown to confluency before washing with sterile PBS, and subsequent passaging with collagenase IV (ThermoFisher Scientific) for 3 mins. Collagenase dissociation was neutralised with media, before cells were scraped and triturated for collection into collection tubes. Cells were allowed to settle at the bottom of the tubes before aspiration of the media and subsequent resuspension of cells in fresh media for replating.

#### **2.4.5. hESC differentiation to cardiomyocytes**

Dissociated H9 hESCs were collected as a triturated suspension. A 10 µL volume of cell suspension was mixed 1:1 with 0.4 % trypan blue solution (ThermoFisher Scientific) for counting in a Countess Automated Cell Counter (Invitrogen). Remaining cells were spun in a centrifuge at 300 xg for 3 mins, before resuspending in CDM-BSA media, supplemented with 12 ng/mL FGF2, 30 ng/mL activin-A, and 10 µM Rho-associated protein kinase inhibitor (ROCKi, Insight Biotech) to give a final cell concentration of 80 k/well in 6-well plates coated with Matrigel (Corning). After incubation for 4 h, mesoderm induction was performed by aspirating media and replacing with 2 mL/well CDM-BSA media, supplemented with 20 ng/mL FGF2, 50 ng/mL activin-A, 10 µM phosphoinositide 3-kinase inhibitor (Ly294002, Stratech), and 10 ng/mL bone morphogenetic protein 4 (BMP4, R&D Systems).

After a further incubation for 42 h, media was aspirated, and cells washed with sterile PBS. Cells were then covered with CDM-BSA media, supplemented with 8 ng/mL FGF2, 10 ng/mL BMP4, 1 µM retinoic acid, and 1 ng/mL Wnt signalling pathway inhibitor (IWR1-endo, Tocris). Cells were then refed with this media every 48 h, for 4

days, before swapping to CDM-BSA media, supplemented with 8 ng/mL FGF2 and 10 ng/mL BMP4. Cells were refreshed with media every other day, until spontaneous beating of differentiated cardiomyocytes (herein referred to as hESC-CMs) was observed.

After  $\geq 14$  days, media was aspirated, and cells were washed with sterile PBS. Cells were subsequently dissociated with TrypLE Express (ThermoFisher Scientific) for 10 mins, before neutralising with CDM-BSA media, supplemented with 5  $\mu$ g/mL DNase I (New England BioLabs) to prevent cell clumping. Cells were collected into tubes and spun in a centrifuge at 300 xg for 3 minutes. Media was aspirated off cell pellets before resuspension in CDM-BSA, supplemented with 10  $\mu$ M ROCKi and plating in 6-well plates coated with Matrigel. Cells were incubated overnight. Next, media was removed and replaced with a lactate selection media, comprised of DMEM no glucose, no pyruvate (ThermoFisher Scientific), supplemented with 1X MEM non-essential amino acids (ThermoFisher Scientific), and 4 mM sodium L-lactate solution in HEPES buffer.

#### **2.4.6. Generation of *shRNA apelin receptor knockdown hESC-CMs***

A tetracycline inducible, short hairpin RNA apelin receptor knockdown system was designed using the single-step optimised inducible knockdown system (sOPTiKD) described in Bertero et al., 2016. The authors outline a pAAV-Puro\_siKD vector targeting the *AAVS1* locus for transgene expression, and carrying the short hairpin RNA and tetracycline response expression cassettes, and a puromycin resistance gene. The pAAV-Puro\_siKD vector was a kind gift from Professor Ludovic Vallier (Addgene plasmid #86695; <http://n2t.net/addgene:86695>; RRID:Addgene\_86695).

H9 hESCs, cultured in 6-well plates coated with 0.1 % gelatin, were aspirated of media, and washed with sterile PBS, before incubation with 1 mL Opti-MEM reduced serum media. Two transfection mixtures were made. Mixture A was comprised of 10  $\mu$ L Lipofectamine 2000 Transfection Reagent (Thermofisher Scientific) in 240  $\mu$ L Opti-MEM per well to be transfected. Mixture A was incubated for 5 mins. Mixture B was comprised of 2  $\mu$ g shRNA vector and 2  $\mu$ g of 2 *AAVS1* zinc finger nuclease plasmids (also described in Bertero et al., 2016) in 250  $\mu$ L Opti-MEM per well to be transfected. Mixture A and Mixture B were added 1:1 and incubated for 20 mins at room

temperature to allow complexes to form. Subsequently, 500  $\mu$ L of the complex solution was added to each well to be transfected. Cells were incubated for 24 h at 37 °C, 5 % CO<sub>2</sub>, humidified. Cells were then aspirated and washed with sterile PBS and maintained in CDM-BSA media, refreshed daily, until ~80 % confluency was observed. Cells were swapped to CDM-BSA media containing 1  $\mu$ g/mL puromycin, refreshed daily, to select for colonies that had successfully taken up the construct. Colonies were manually isolated using a pipette, and expanded in colonies before undergoing the cardiomyocyte differentiation protocol outlined in Section 2.4.5.

#### **2.4.7. Generation of R168H variant apelin receptor cardiomyocytes**

Base editing is a form of CRISPR/Cas technology that induces precise genetic changes in a target of interest. In brief, using protocols adapted from Komor et al., 2016 and Koblan et al., 2018, a cytosine base editor was used in conjunction with custom guide RNA (gRNA) to induce a G-C to A-T substitution in the apelin receptor gene (*APLNR*), resulting in an amino acid substitution (R168H) at the protein level. To induce the substitution, the gRNA vector and a BE4max base editor plasmid were nucleofected into H9 hESCs (WiCell) using the Amaxa 4D Nucleofector (Lonza) and P3 Primary Cell 4D-Nucleofector X Kit, in accordance with the manufacturer's instructions. The gRNA vector also carries a puromycin resistance gene, and cells that had taken up the plasmid were selected for using puromycin (1  $\mu$ g/mL) selection for 48 h. Subsequently, successfully nucleofected cells were manually isolated using a pipette, and expanded in colonies before undergoing the cardiomyocyte differentiation protocol outlined in Section 2.4.5.

## **2.5. Cell infection with virus in SARS-CoV-2 studies**

### **2.5.1. Pseudotyped virus production**

Owing to tight restrictions during the UK government imposed lockdowns, and the training required for access and use of Biological Safety Containment Level 2 facilities, pseudotyped virus production was instead carried out by Mr Stuart Bloor and Mr Jun Ru Zhan in the Cambridge Institute of Therapeutic Immunology & Infectious Disease (CITIID).

Plasmid pCG1-SARS-CoV-2  $\Delta$ 19 D614G HA, encoded the SARS-CoV-2 spike protein, carrying the D614G mutation that increases the affinity for ACE2 and an HA tag that replaces the last 19 amino acids at the C-terminus. The plasmid was generated using the pCG1-SARS-2-S construct, kindly gifted by M. Hoffman and described in Hoffman et al., 2020, by PCR (Phusion polymerase (New England Biolabs)) using the primer pairs:

(1) CoV2optFor(TTGTATCGGATCCACCATGTT CGTGTTTCTGGTGCTGCTG) with CoV2D614Gr(CAGTTCACGcCCTGGTACAGCAC TGCCAC)

(2) CoV2D614Gf(GTACCAGGgCGTGAAGTGTACCGAAGTGCC) with CoV2optD19HArev(ATCCCGATCTAGATCAAGCGTAATCTGGAACATCGTATGGG T AACTTCCGCAGCAGCTGCCACAGCTACA)

This generated overlapping amplification products, that were gel purified and combined as a template in a second PCR reaction using primer pair; CoV2optFor and CoV2optD19HArev. The final amplification product was digested and re-cloned into the pCG1 vector using BamHI-XbaI sites. The HIV-1 based GFP-expressing lentiviral vector pHRSIN CSGW eGFP was a kind gift from Y. Ikeda. Pseudotyped lentiviral supernatants were generated following co-transfection of HEK293T cells with pHRSIN CSGW eGFP plus the packaging plasmid pCMV $\Delta$ R8.91 and either pMD.G (VSV-G) or pCG1-SARS-CoV-2  $\Delta$ 19 D614G HA spike plasmid, using TransIT-293 transfection reagent (MIR 2704; Mirus Bio), in accordance with the manufacturer's protocol. Viral supernatants were harvested 48 h post transfection and cell debris was removed with a 0.45  $\mu$ m syringe filter, prior to concentrating up (approximately 10-fold) using a Vivaspin 20 MWCO 100 kDa centrifugal concentrator (Sartorius), in accordance with the manufacturer's instructions.

### **2.5.2. Pseudotyped viral infection of hESC-CMs**

For infection of hESC-CMs, cells in CellCarrier-96 Ultra Plates (PerkinElmer) were incubated for 4 h with pseudotyped viral stock at the desired multiplicity of infection (MOI) in media. In drug screens, cells were pre-treated for 1 h before infection with either camostat, benztropine, or E64d at a final concentration of 30  $\mu$ M; DX600 at a

final concentration of 10  $\mu$ M; ACE2 antibody (AF933; R&D Systems) at 20  $\mu$ g/mL; a mix of camostat + E64d at a final concentration of 30  $\mu$ M each; or DMSO at 0.6% (equivalent of the highest concentration included in drug dilutions). Cells were then washed 3x with PBS to remove infectious lentivirus particles, before replenishment with the media outlined above, maintained in the presence of the respective drug treatments for 4-5 days. Viral infection was monitored using an EVOS Cell Imaging System to look for the enhanced green fluorescent protein (eGFP) reporter of viral presence in cells.

### **2.5.3. SARS-CoV-2 viral infection of hESC-CMs**

Owing to the inability to get training in the Biological Safety Containment Level 3 facilities required for handling SARS-CoV-2 viral isolates, infection of hESC-CMs with this virus was instead performed by Dr Edward Greenwood in the Cambridge Institute of Therapeutic Immunology & Infectious Disease (CITIID). The SARS-CoV-2 virus described in this thesis is the "SARSCoV2/human/Liverpool/REMRQ0001/2020"<sup>30,31</sup> clinical isolate. Viral stock was passaged 3x in VeroE6 cells, 1x in Caco-2 cells, and 1x in Calu-3 cells. Viral stock titre was calculated using the TCID<sub>50</sub> (Median Tissue Culture Infectious Dose) observed in Huh-7 cells transfected with an ACE2 expression vector. For SARS-CoV-2 immunostaining, infected cells were fixed in 2% formaldehyde for 30 mins and permeabilized with BD Perm/Wash buffer (BD Biosciences, 554723). The primary antibody used was a sheep anti-SARS-CoV-2 nucleocapsid antibody (DA114, MRC-PPU), which was visualised with AF488 conjugated donkey anti-sheep antibody (#713-545-147; Jackson ImmunoResearch).

## **2.6. Protein preparation**

### **2.6.1. Cell membrane preparation**

Cell membrane preparations (HEK293T and CHO-K1 cells) were made by dissociating cells grown to confluency in T175 flasks using 3 mL trypsin or TrypLE Express for 3 mins. Dissociating reagent was neutralised with 7 mL respective cell media (see Section 2.4.1). Cell suspensions were transferred to tubes and spun in a centrifuge at 1000 xg for 10 mins at 4 °C. Pellets were resuspended in ice-cold TRIS wash buffer (50 mM TRIS-HCl in deionised water, pH balanced to 7.4 at room temperature, as

used during wash steps of subsequent radioligand binding experiments), and triturated, to induce complete hypotonic lysis of cells. Cells were spun a second time in a centrifuge at 21,000 xg for 20 mins at 4 °C, to obtain a crude membrane fraction. Supernatant was discarded and membrane preparations resuspended in TRIS wash buffer. Cell membrane preparations were stored at -70 °C until use in experiments.

### **2.6.2. Tissue homogenisation**

Surgical samples of human left ventricle (HLV) tissue were obtained with informed consent and ethical approval (05/Q104/142). Tissues were snap frozen in liquid nitrogen before storage at -80 °C. On the day of preparation, tissue was chopped finely with a razor blade on ice, before subsequent homogenisation using a Polytron Homogenizer (Thomas Scientific), in homogenisation buffer (50 mM Tris-HCl, 5 mM MgCl<sub>2</sub>, 5 mM EDTA, 1 mM EGTA, 1:500 protease inhibitor cocktail containing aprotinin and amastatin, balanced at pH 7.4) at 4 °C. The resulting homogenate was subsequently spun in a centrifuge at 1000 xg for 2 mins at 4 °C. Supernatant was transferred to another set of tubes (pellet discarded) for a high speed spin in a centrifuge at 40,000 xg, for 30 mins at 4 °C. Supernatant was then discarded, and the remaining pellet resuspended in 2.5 mL/g of homogenisation buffer, before a second high speed spin at 40,000 xg, for 30 mins at 4 °C. The supernatant was discarded, and the remaining pellet was resuspended in HEPES buffer (50 mM HEPES, balanced at pH 7.4 at room temperature) and stored in the freezer at -70 °C until use in assays.

### **2.6.3. Protein assay**

Protein concentration of protein preparations (cell based or homogenised tissue), was determined using a DC Protein Assay (Bio-Rad), in accordance with the manufacturer's instructions. The kit makes use of the established colorimetric Lowry method, tracking the colour change that occurs when peptide bonds in proteins react with an alkaline copper tartrate solution to reduce an added folin reagent. In brief, the solubilising buffer provided in the kit was warmed on top of a water bath heated to 80 °C to prevent precipitation of buffer components. Frozen protein samples were thawed and mixed 1:1 (typically 100 µL) with the solubilising buffer. The mix was heated in the 80 °C water bath for 30 mins. Samples were then spun in a centrifuge at 11,000 xg for 5 mins. 50 µL of supernatant was serially diluted with 50 µL solubilising buffer down

to 1:128. A bovine serum albumin (BSA) standard at 1.5 mg/mL in solubilising buffer was prepared and diluted down to 0.1875 mg/mL to produce a standard curve in the assay. After adding 5  $\mu$ L blank controls (solubilising buffer), BSA standard, or sample supernatant dilutions to a clear-bottomed 96 well plate, kit reagents A' (alkaline copper tartrate solution) and B (dilute folin reagent) were added at 25 and 200  $\mu$ L respectively. After incubating for 5 mins at room temperature, absorbance at 450 nm was measured using a FLUOstar Omega microplate reader (BMG LABTECH). The BSA standard curve was plotted, and concentrations of the protein samples interpolated.

## **2.7. Radioligand binding**

Radioligand binding was performed using the [Glp<sup>65</sup>,Nle<sup>75</sup>,Tyr<sup>77</sup>][<sup>125</sup>I]-apelin-13 radiolabel (PerkinElmer), herein referred to as [<sup>125</sup>I]-apelin-13, using protocols adapted from Katugampola et al., 2001; Maguire et al., 2012; Yang et al., 2017a. The radiolabel has a specific activity of 2200 Ci/mmol.

Binding buffer was comprised of 50 mM TRIS-HCl and 5 mM MgCl<sub>2</sub>, balanced to pH 7.4 at room temperature. Wash buffer was the same but with no MgCl<sub>2</sub>.

Protein samples were diluted in binding buffer to give final assay concentrations of 1 mg/mL or 1.5 mg/mL for cell preparations or homogenised tissue respectively.

Plasticware used in radioligand binding experiments were coated with Sigmacote, a siliconizing reagent that forms a covalent film that reduces sticking of the radiolabel.

### ***2.7.1. Fixed concentration binding***

Protein sample was mixed 1:1 (typically 50 or 100  $\mu$ L) with 0.15 nM [<sup>125</sup>I]-apelin-13 (diluted in binding buffer), and incubated for 90 mins at room temperature to reach equilibrium. Non-specific binding was determined in the presence of 5  $\mu$ M [Pyr<sup>1</sup>]apelin-13 (Severn Biotech). At the end-point, samples were spun in a centrifuge at 20,000 xg for 10 mins at 4 °C to terminate equilibrium. Supernatant was aspirated, and pellets were resuspended and triturated in 500  $\mu$ L ice-cold wash buffer all over ice. Samples were spun a second time at 20,000 xg for 10 mins at 4 °C, before aspiration of the

supernatant. Radioactivity in pellets was counted using a Cobra II model 5003 gamma counter (Packard).

### **2.7.2. Saturation binding**

Protein sample was mixed 1:1 (typically 50 or 100  $\mu\text{L}$ ) with a concentration range (2 pM – 1 nM) of [ $^{125}\text{I}$ ]-apelin-13 (diluted in binding buffer), and incubated for 90 mins at room temperature to reach equilibrium. Non-specific binding was determined in the presence of 5  $\mu\text{M}$  [Pyr<sup>1</sup>]apelin-13. At the end-point, samples were spun in a centrifuge at 20,000 xg for 10 mins at 4 °C to terminate equilibrium. Supernatant was aspirated, and pellets were resuspended and triturated in 500  $\mu\text{L}$  ice-cold wash buffer all over ice. Samples were spun a second time at 20,000 xg for 10 mins at 4 °C, before aspiration of the supernatant. Radioactivity in pellets was counted using a Cobra II model 5003 gamma counter (Packard).

### **2.7.3. Competition binding**

Competition binding was performed to assess the displacement of [ $^{125}\text{I}$ ]-apelin-13 at apelin receptor by other ligands. Protein sample was mixed 1:1:1 with 0.1 nM [ $^{125}\text{I}$ ]-apelin-13, and a concentration range (1 pM – 1  $\mu\text{M}$ ) of competing ligand, diluted in binding buffer. Total binding was determined in the absence of competing ligand. Non-specific binding was determined in the presence of 5  $\mu\text{M}$  [Pyr<sup>1</sup>]apelin-13. At the end-point, samples were spun in a centrifuge at 20,000 xg for 10 mins at 4 °C to terminate equilibrium. Supernatant was aspirated, and pellets were resuspended and triturated in 500  $\mu\text{L}$  ice-cold wash buffer all over ice. Samples were spun a second time at 20,000 xg for 10 mins at 4 °C, before aspiration of the supernatant. Radioactivity in pellets was counted using a Cobra II model 5003 gamma counter (Packard).

### **2.7.4. Radioligand binding data analysis**

Saturation binding data were analysed using the EBDA and LIGAND components of the KELL (Kinetic, EBDA, Ligand, Lowry) software package (Biosoft), described in McPherson, 1985. The software uses co-analysed iterative curve fitting. EBDA performs a Scatchard plot linearised analysis to generate initial estimates of receptor affinity ( $K_D$ ) and receptor density ( $B_{\text{max}}$ ). These estimates are subsequently entered into LIGAND, which uses weighted, nonlinear curve fitting to more accurately calculate

$K_D$  and  $B_{max}$  values.  $B_{max}$  values, in fmol/mg, are calculated from the known specific activity of the radiolabel and concentration of protein used. Additionally, a runs test determines if points are randomly distributed around the fitted line. LIGAND also accounts for receptor occupancy and ligand depletion, as total binding, non-specific binding, total radioactivity added, and the dissociation constant (in this instance, 0.076 nM) and specific activity (2200 Ci/mmol) of the radiolabel are input into the software. Saturation data were presented using the nonlinear one site specific binding with Hill slope model fitted by GraphPad Prism version 6.07 for Windows (GraphPad Software).

Competition binding data were presented using the nonlinear one site Fit  $K_i$  [2] model fitted by GraphPad Prism version 6.07, with constraints for the radiolabel concentration (0.1 nM) and  $K_D$  (0.076 nM) input. The software was also used to calculate binding affinities ( $K_i$  values) of competing ligands using the Cheng-Prusoff equation:

$$K_i = IC_{50} / (1 + [L] / K_D)$$

where  $K_i$  is the absolute inhibitor constant, the concentration of competing ligand that produces half-maximal inhibition of binding;  $IC_{50}$  is the half-maximal inhibitory concentration determined from the competition curve generated in the given assay;  $[L]$  is the concentration of the radiolabel; and  $K_D$  is the affinity constant of the radiolabel (0.076 nM).

## **2.8. In vitro assays**

### **2.8.1. Dynamic mass redistribution assay**

BIND technology (SRU Biosystems) provides a plate based label-free assay format that can measure cellular responses to receptor-ligand interactions, generally used as a screening platform. The proprietary 96-well biosensor plates use a nanostructured optical grating that reflects a single wavelength of light following illumination from underneath with broad spectrum light that is dependent on the index of refraction, that is in turn dependent on the material attached to the biosensor surface. The more material (i.e. cells) that is in contact with the biosensor surface, the higher the peak wavelength value (PWV) of the returned light signal, and vice versa. The change in material at the biosensor surface can be measured over time using the shift in PWV observed. In cell based assays, the number of cells adherent to the biosensor surface, and/or the extent of adherence and spreading – often influenced by downstream effectors following receptor-ligand interaction – induces observable shifts in PWV. Detected shifts in PWV fall exponentially up to distances of ~200 nm above the biosensor surface. Fig 2.1 shows representative sample traces of the response to a concentration range (0.1 nM – 1  $\mu$ M) of the fluorescent apelin receptor ligand, apelin488. Traces show responses ( $\Delta$ PWV from a pre-established baseline taken 5 mins after the drug addition, which can then be used to plot concentration response curves. Note, wild-type CHO cells (i.e. untransfected) treated with 1  $\mu$ M apelin488 showed no response, confirming that the presence of fluorescence does not induce signal in this light based assay.

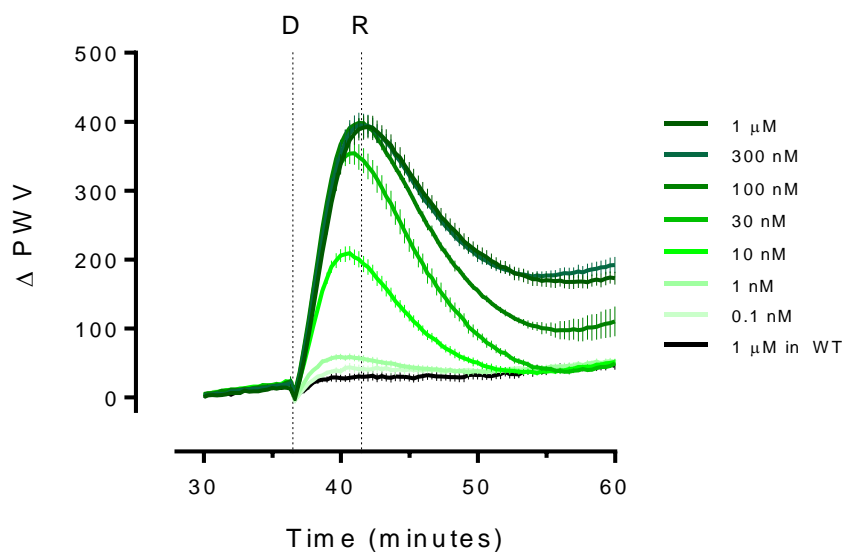


**Figure 2.1.** Representative sample traces from the dynamic mass redistribution assay. A baseline peak wavelength value (PWV) reading is taken over a 30 mins period before the start of the experiment, allowing cells in the biosensor plate to acclimatise to the experimental environment. After T30, any deviation in PWV is recorded to give responses in  $\Delta$ PWV. At  $\sim$ T37 mins, a concentration range (0.1 nM – 1  $\mu$ M) of drug (D, in this case the fluorescent ligand, apelin488) was added to CHO-APLNR cells. The response (R), was taken as the  $\Delta$ PWV from the initial baseline 5 mins after the drug addition, at  $\sim$ T42 mins. Note, black trace shows the response of 1  $\mu$ M apelin488 in wild-type (WT) CHO cells (i.e. untransfected).

### 2.8.2. cAMP accumulation assay

$G_{\alpha i}$  G protein signalling at the apelin receptor was determined using an *in vitro* cAMP Hunter eXpress GPCR Assay (DiscoverRx, now Eurofins). The manufacturer's protocol was modified in accordance with previous in-house optimisation. All reagents were provided in the assay kit. Note that [Pyr<sup>1</sup>]apelin-13 is used as a reference agonist in this assay.

The assay allows for sensitive monitoring of GPCR activation using enzyme fragmentation complementarity to induce chemiluminescent signal that is directly proportional to the concentration of cAMP present in the CHO-K1 cells expressing apelin receptor provided with the kit (see Fig 2.2). The  $\beta$ -galactosidase enzyme is split

into two fragments, the enzyme donor (ED) and enzyme acceptor (EA) with the donor labelling cAMP in the kit. ED labelled cAMP and cellular cAMP compete for an anti-cAMP antibody (anti-cAMP Ab) binding, where ED labelled cAMP bound to antibody will no longer be able to fuse with the EA. When cellular levels of cAMP are high, there is more competition for binding with the anti-cAMP antibody which leaves more ED labelled cAMP free to fuse with the EA to allow for hydrolysis of the chemiluminescent substrate by complete  $\beta$ -galactosidase to give signal.

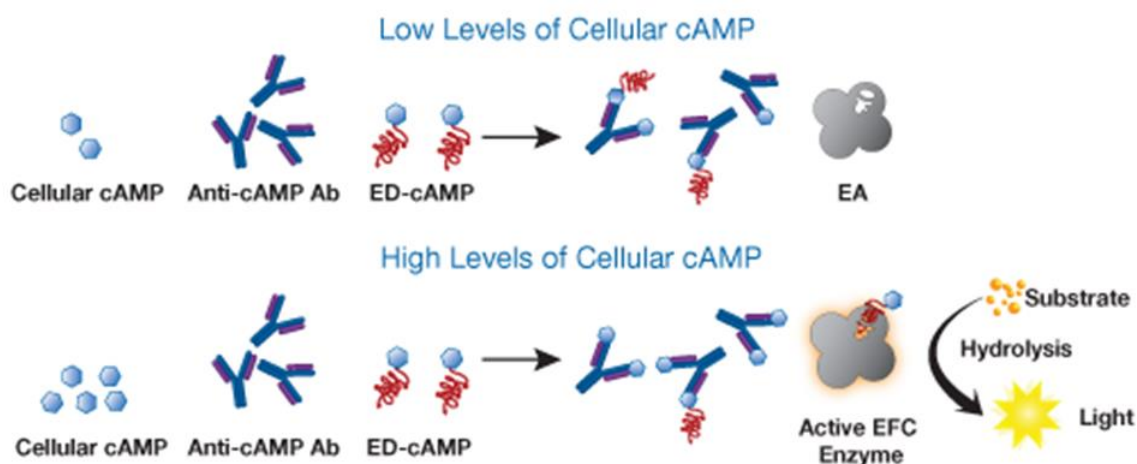


**Figure 2.2.** Schematic showing the principle behind the cAMP accumulation assay. Cellular and kit components required for detection of chemiluminescent signal (light) in the cAMP Hunter eXpress GPCR Assay. In low level cellular cAMP conditions (i.e.  $G_{\alpha i}$  inhibition of forskolin stimulated adenylyl cyclase), the anti-cAMP antibody is able to mop up the cAMP labelled with the enzyme donor, also supplied in the kit, preventing fusing of the donor with the enzyme acceptor and a lack of chemiluminescent signal. In high level cellular cAMP conditions (i.e. no  $G_{\alpha i}$  inhibition of forskolin stimulated adenylyl cyclase), the cellular cAMP saturates the anti-cAMP antibody, leaving cAMP labelled with the enzyme free to fuse with the enzyme acceptor and generate chemiluminescent signal. Image from [www.discoverx.com](http://www.discoverx.com).

CHO-K1 cells overexpressing human apelin receptor (AGTRL1) were seeded in cell plating reagent (CPR) into 96-well plates and incubated for 24 h at 37 °C, 5 % CO<sub>2</sub>, humidified. Cell Plating Reagent was aspirated and replaced with Cell Assay Buffer containing cAMP Antibody Reagent. To investigate novel compounds for agonist activity, wells were treated with test compounds over an 8 point concentration range minimum, in the presence of 15 μM forskolin (to stimulate cAMP production, see Fig 2.2). Cells were then incubated for 30 mins at 37°C, 5 % CO<sub>2</sub>, humidified. Cells were subsequently treated with Working Detection Solution (cAMP Lysis Buffer, Substrate Reagent 1, Substrate Reagent 2, and cAMP Solution D), containing 3-isobutyl-1-methylxanthine (IBMX; a non-selective phosphodiesterase inhibitor) and incubated for 1 h at room temperature, protected from light. Cells were then treated with cAMP solution A and incubated for 3 h at room temperature, protected from light. Plates were

read in a chemiluminescence detecting LumiLITE Microplate Reader (DiscoverX). Responses measured in Relative Light Units (RLU) were fitted to four parameter logistic concentration response curves in GraphPad Prism version 6.07 for Windows (GraphPad Software) to determine compound concentrations inducing half maximal response ( $EC_{50}$ ), and  $pD_2$  values ( $-\log_{10} EC_{50}$ ) were calculated. Data were expressed in a normalised manner as the percentage of forskolin response (% inhibition (FSK)) at the lowest concentration of [Pyr<sup>1</sup>]apelin-13.

The cAMP accumulation assay was validated extensively in-house (see Fig 2.3). A forskolin concentration response curve (Fig 2.3a) demonstrated that the 15  $\mu$ M concentration recommended for use in the assay was sub  $EC_{50}$ . The fact that the recommended concentration falls on the linear part of the concentration response curve may provide some evidence for variability observed for forskolin baseline responses. Whilst a higher concentration of forskolin may therefore have been more appropriate, experiments were conducted using 15  $\mu$ M, as per the manufacturer's recommendations. A cAMP standard (provided in the kit) concentration response curve (Fig 2.3b), showed that the levels of cAMP determined experimentally fit well within the upper and lower detection limits of the assay and plate reader. The response for 15  $\mu$ M forskolin (~63,000 RLU) was nearly 4-fold lower than the maximum cAMP response detectable (~230,000 RLU). The inhibition of 15  $\mu$ M forskolin induced cAMP accumulation by a concentration range of [Pyr<sup>1</sup>]apelin-13 (Fig 2.3c) shows that the highest concentration used is able to fully inhibit the forskolin response ( $\leq 0$  %). A  $pD_2$  value of  $8.97 \pm 0.08$  was determined for [Pyr<sup>1</sup>]apelin-13 in this experiment.

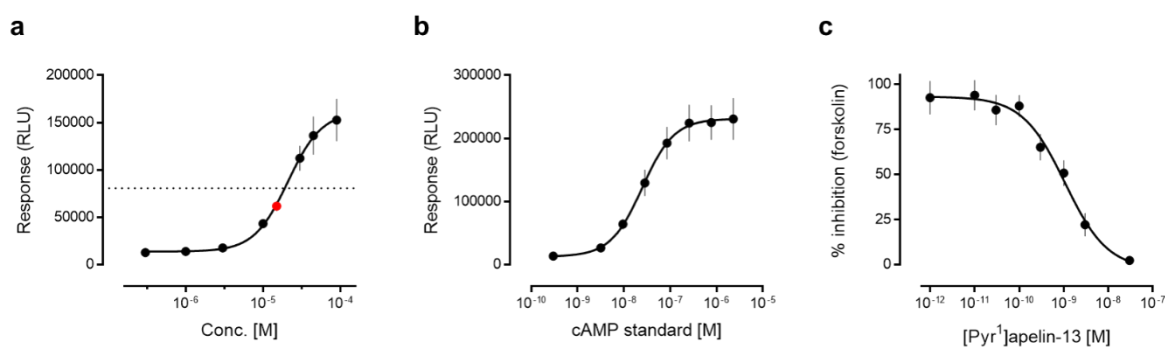


**Figure 2.3.** Validation of the cAMP accumulation assay. All data show mean  $\pm$  SD. **a** Accumulation of cAMP induced by forskolin, measured as relative light units (RLU) on detection of chemiluminescent signal. The 15  $\mu$ M concentration (shown in red), recommended for use as the final assay concentration by the manufacturer, falls just under the half-maximal response (shown by the dotted line), indicating that 15  $\mu$ M is just sub  $EC_{50}$ . **b** A cAMP standard control curve shows that cAMP levels in the assay fall within the detectable range. The cAMP standard  $E_{max}$  was slightly higher than that for forskolin, and the response for 15  $\mu$ M forskolin falls well within the detectable range. **c** Inhibition of 15  $\mu$ M forskolin response (expressed as % inhibition of the maximum 15  $\mu$ M forskolin response) by [Pyr<sup>1</sup>]apelin-13. In all instances,  $n = 3$  independent experiments performed in triplicate.

### 2.8.3. Internalisation assay

Internalisation of apelin receptor following ligand treatment was determined using an *in vitro* PathHunter GPCR Internalization Assay (DiscoverRx). The manufacturer's protocol was modified in accordance with previous in-house optimisation. All reagents were provided in the assay kit.

This assay also uses enzyme fragmentation complementarity. The apelin receptor GPCR is fused with a ProLink tag (PK; a small fragment of the enzyme donor, ED), while the enzyme acceptor (EA) is localised to endosomes in the U2OS cells used (see Fig 2.4). Any ligands that stimulate receptor internalization forces the PK tag and EA in the endosome into proximity, where a now functional  $\beta$ -galactosidase enzyme can hydrolyse the chemiluminescent signal to produce light signal. Signal is directly proportional to the extent of GPCR and endosome interaction.

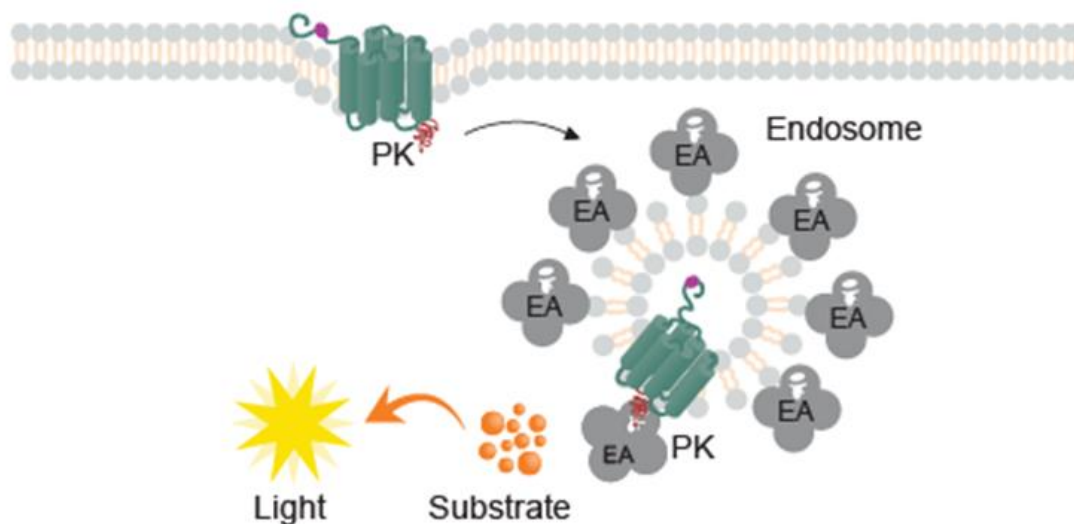


**Figure 2.4.** Schematic showing the principle behind the internalisation assay. Cellular and kit components required for detection of chemiluminescent signal (light) in the PathHunter GPCR Internalization Assay. Following stimulation of the receptor by a ligand, and subsequent engagement of internalisation mechanisms, internalised receptor tagged with the ProLink (PK) tag is brought into proximity with the enzyme acceptor (EA) localised in endosomes. Chemiluminescent signal produced by the complete  $\beta$ -galactosidase enzyme is directly proportional to the extent of the interaction between the receptor and endosomal compartment. Image taken from [www.discoverx.com](http://www.discoverx.com).

U2OS cells overexpressing human apelin receptor (AGTRL1) were seeded in cell plating reagent into 96-well plates and incubated for 48 h at 37°C, 5 % CO<sub>2</sub>, humidified. To test novel compounds for agonist activity, wells were treated with test compounds over a concentration range in Cell Plating Reagent to generate an 8-point concentration-response curve. Cells were then incubated for 90 mins at 37°C, 5 % CO<sub>2</sub>, humidified before treatment with Working Detection Solution (Cell Assay Buffer, Substrate Reagent 1, Substrate Reagent 2), and incubation for 2 h at room temperature, protected from light. Plates were read in a chemiluminescence detecting LumiLITE Microplate Reader (DiscoverX, Fremont, CA, USA). Responses measured in Relative Light Units (RLU) were fitted to four parameter logistic

concentration response curves in GraphPad Prism version 6.07 for Windows (GraphPad Software) to determine compound concentrations inducing half maximal response ( $EC_{50}$ ), and  $pD_2$  values ( $-\log_{10} EC_{50}$ ) were calculated. Data were expressed in a normalised manner as the percentage of forskolin response (% FSK) at the lowest concentration of [Pyr<sup>1</sup>]apelin-13.

## **2.9. Imaging**

A number of fluorescent imaging studies, using a number of fluorescent markers from antibodies to protein reporters to fluorescent ligands, are described in this thesis. An overview of the fluorescent markers and techniques will be provided here, with further details described in respective Chapters. Imaging was performed in the Metabolic Research Laboratories (MRL) imaging hub, following relevant training conducted by the hub manager, Mr Gregory Strachan.

### **2.9.1. Fluorescent markers**

In multiple settings, cells and tissue sections were stained with Hoechst 33342 nuclear marker (H3570; Invitrogen), a cell permeant nuclear counterstain that is maximally excited by 350 nm wavelength light and emits maximally at 461 nm, and wheat germ agglutinin conjugated to Alexa Fluor 555 (herein referred to as WGA-555; W32464; Invitrogen), a lectin that binds to sialic acid and N-acetylglucosaminyl residues present in cell membranes, with the fluorophore maximally excited by 555 nm wavelength light and maximally emitting at 580 nm. Both markers were typically made up at 10  $\mu\text{g/mL}$  in clear buffers used throughout the respective cell and tissue experiments.

Four novel fluorescent apelin receptor ligands were used in this thesis, and are characterised in depth in Chapter 3. Two apelin peptides conjugated to dyes structurally identical to Alexa Fluor 488 and Alexa Fluor 647, with max excitation/emission of 490/525 and 650/665 respectively, and two ELA peptides conjugated to the same dyes were used in the work in this thesis. Additionally, a fluorescently tagged SARS-CoV-2 spike receptor binding motif protein monomer conjugated to the dye structurally identical to Alexa Fluor 647 was also used, and is discussed in Chapter 6. All fluorescently tagged peptides were designed by Professor

Davenport and custom synthesised by Cambridge Research Biochemicals. Fluorescent apelin peptides were designed following the success of MM02-AlbudAb, which successfully utilised a [PEG4] linker and incorporated M to norleucine (position 11) and F to 3,4,5-trifluorophenylalanine (position 13) substitutions that are also present in the [<sup>125</sup>I]-apelin-13 radiolabel and have been shown to improve binding (Murza et al., 2012; Read et al., 2020).

Immunostaining was performed in multiple instances to identify proteins of interest. Antibodies used and all essential details will be provided in relevant Chapters.

Enhanced green fluorescent protein (eGFP) reporter was used in two instances. In CHO-K1 cells transfected with wild-type and variant apelin receptor, constructs were C-terminally tagged with eGFP to identify expression and localisation of the receptor. In pseudotyped viral studies, the viral DNA package incorporated an eGFP reporter as a marker for successful infection. The eGFP protein is maximally excited at 488 nm wavelength light, and emits maximally at 509 nm.

### ***2.9.2. Opera Phenix High Content Screening System***

The Opera Phenix High Content Screening System (PerkinElmer), herein referred to as the Opera Phenix, is a highly sensitive high throughput (accommodating 96-well and 384-well plates) laser spinning disk confocal fluorescent imaging platform. The closed-box system uses dual optics and dual cameras to visualise and acquire images extremely quickly, whilst requiring low laser intensity, to minimise spectral overlap, and reduce fade and phototoxicity of fluorophores. Additionally, the dual optics allow for the visualisation of up to five different fluorophores in a single experiment, along with digital phase contrast. The Opera Phenix works in tandem with Harmony software (PerkinElmer), which provides a workflow based user interface that handles set-up of fluorescent channels, focusing, acquisition, post-processing, segmentation, and complex analyses at subcellular levels.

### ***2.9.3. Opera Phenix acquisition***

Cells in CellCarrier-96 Ultra Plates (PerkinElmer) which have optimised optical density for the device, were imaged using a 40x/NA1.1 water immersion objective. The device

was set to measure an image field within each well, where the field is made up of a 4 x 4 or 5 x 5 grid of imaging regions (where each region is 250 x 250  $\mu\text{m}$  in area). After using Z stacking to find an appropriate focal plane, cells were visualised and imaged at a focal depth of 0.5  $\mu\text{m}$  above the bottom of the plate in all experiments. In the work outlined in this thesis, a profile with four fluorescent channels was used; a first channel (blue), with excitation of 405 nm and emission filter of 435-480 nm for Hoechst 33342 nuclear marker; a second channel (green), with excitation of 488 nm and emission filter of 500-550 nm for Alexa Fluor 488 or eGFP; a third channel (yellow), with excitation of 561 nm and emission filter of 570-630 nm for Alexa Fluor 555; and a fourth channel (red), with excitation of 631 nm for Alexa Fluor 647. In all instances, excitation laser intensity was set at 50 % of the Opera Phenix maximum, with a short 50 ms exposure time. In all experiments, cells were also imaged using digital phase contrast, an optical method that translates phase shifts in light passing through cell matter in the plates to changes in brightness. Digital phase contrast images were used alongside fluorescent nuclear and membrane markers to identify and segment cells.

#### **2.9.4. Opera Phenix analysis**

Following image acquisition, several cell parameters were quantified using the in-built Harmony software. Full descriptions of analysis workflows for cellular identification and segmentation into subcellular compartments are described in relevant Chapters.

### **2.9.5. Zeiss Axio Scan Z1 slide scanner**

The Zeiss Axio Scan Z1 slide scanner (Zeiss), herein referred to as the slide scanner, is an automated fluorescent microscope system that offers imaging of up to four fluorescent channels and brightfield in a single experiment, and can image full sections of mounted tissue on up to 100 slides. The slide scanner allows for rapid but high resolution acquisition of whole tissue section images, where short exposure times reduce fade of fluorophores in samples. Additionally, the LED-Module light sources used in the closed-box device provide a more consistent illumination than lasers, ensuring reliable and reproducible excitation across the whole sample.

In the work described in this thesis, automated fluorescent images (16 bit, 0.325 x 0.325  $\mu\text{m}$  scaling per pixel) of fixed and mounted human tissue stained with fluorescent markers were acquired in the slide scanner with a Plan-Apochromat 20x/NA0.8 M27 objective lens connected to a Hamamatsu Orca Flash camera. An initial brightfield scan was performed to visualise tissue on slides, and a spline contour tool was used to outline the tissue to minimise the total region imaged. A profile with three fluorescent channels was used; a first channel (blue), with an LED-Module 385 nm light source set at 10 % intensity and 10 ms exposure time at a depth of focus of 1.45  $\mu\text{m}$  for Hoechst 33342 nuclear marker; a second channel (green), with an LED-Module 475 nm light source set at 40 % intensity and 20 ms exposure time at a depth of focus of 1.64  $\mu\text{m}$  for Alexa Fluor 488; and a third channel (yellow/orange), an LED-Module 567 nm light source set at 80% intensity and 30 ms exposure time at a depth of focus of 1.88  $\mu\text{m}$  for Alexa Fluor 555. Focal depths were determined by the slide scanner's in-built Z stacking autofocusing. Haematoxylin and eosin (H&E) stained tissue sections were imaged on mounted slides using the brightfield setting. All acquired images were saved and visualised using ZEN software (Zeiss) and/or Orbit Image Analysis (ORBIT) software.

### **2.9.6. Zeiss LSM 510 Meta Inverted Confocal Microscope**

During the first year of study, the Metabolic Research Laboratories (MRL) imaging hub used a Zeiss LSM 510 Meta Inverted Confocal Microscope. Tissue sections mounted on slides were imaged using a 40x oil immersion objective lens. Lasers illuminating at 405 nm and 488 nm wavelengths were used to excite the Hoechst nuclear marker

(blue) and fluorescent ligands (green) respectively. Image analysis was performed using Fiji (imagej.net) software.

### **2.9.7. Multiphoton Microscope Leica TCS SP8 MP**

Owing to a technical issue with far-red excitation and emission in the slide scanner, a Multiphoton Microscope Leica TCS SP8 MP microscope (Leica Microsystems), herein referred to as the Leica SP8, was used to visualise human tissue sections treated with fluorescently tagged SARS-CoV-2 spike receptor binding motif protein monomer conjugated to a dye structurally identical to Alexa Fluor 647 (discussed in Chapter 6), alongside other fluorophores. Confocal fluorescent images were acquired using an HC PL APO CS2 63x/NA1.40 oil immersion objective lens. A profile with three fluorescent channels was used; a first channel (blue), with a 405 nm wavelength excitation set at a gain of 702.5 V, a second channel (green), with a 488 nm wavelength excitation set at a gain of 702.6 V; and a third channel (red), with a 633 nm wavelength excitation set at a gain of 672.4 V. Emission filters for wavelengths of 410-480 nm, 500-550 nm, and 650-700 nm were used for the blue, green, and red channels respectively. Microscope image acquisition (512 x 512 pixels) was performed using Leica Application Suite X (LAS X) software before subsequent analysis using Fiji (imagej.net) software.

### **2.9.8. Data analysis and statistics**

Where applicable, quantitative data are represented as mean  $\pm$  SD. Statistical tests used to determine significant differences in results will be described in relevant figure legends. A p value of  $< 0.05$  was deemed statistically significant. Data were tested for normality using the Shapiro-Wilk test for normality and qualitatively using Q-Q plots. Non-parametric statistical tests were used where data did not pass the criteria for normality. Raw data were handled using Microsoft Excel for Windows (Microsoft). Graphical presentation and statistical tests were performed using GraphPad Prism version 6.07 for Windows (GraphPad Software).

## Chapter 3. Design and characterisation of novel fluorescent peptide ligands at the apelin receptor

### 3.1. Introduction

As a GPCR with promising therapeutic potential in cardiovascular diseases and other, successfully targeting the apelin receptor with drugs that exhibit good pharmacokinetic and pharmacodynamic profiles will require an in-depth understanding of the receptor's pharmacology (Yang et al., 2015; Read et al., 2016; Davenport et al., 2020).

Fluorescently labelled ligands are an evolving, and increasingly important, experimental tool for exploring GPCR pharmacology that can be used in a wide range of settings, from flow cytometry to simple *in vitro* binding and kinetic assays, to high-throughput plate-based platforms and high content screening (Soave et al., 2017). Major improvements in the brightness and stability of fluorescent dyes, conjugation techniques, and optical equipment and quantification, have meant fluorescent ligands are emerging as safer, easier, and more versatile tools than other classical techniques such as radioligand binding (Vernall et al., 2014; Stoddart et al., 2015, 2016). Additionally, the localisation of fluorescent ligands at both the cell and subcellular level can be visualised in real-time, with colocalisation of multiple other markers in a single biological system.

As examples, directly labelled fluorescent ligands have been used successfully to probe the pharmacology of the adenosine A<sub>1</sub> receptor in an artificially expressing cell line (Baker et al., 2010). The adenosine A<sub>2A</sub> receptor has also been visualised and characterised in both artificially expressing and endogenously expressing cell systems using a fluorescent antagonist (Stoddart et al., 2020). The pharmacology of the fluorescent ligands themselves must also be carefully approached and validated. The study assessing adenosine A<sub>1</sub> receptor showed that both the fluorophore used, and linker length used to conjugate the fluorophore to an agonist or antagonist, has critical effects on the behaviour of the fluorescent ligands in terms of potency and affinity (Baker et al., 2010). A further study reports conversion of a non-selective adenosine receptor antagonist into a highly selective, high affinity adenosine A<sub>3</sub> receptor

fluorescent probe following conjugation of the fluorophore to the pharmacophore via a dipeptide linker (Vernall et al., 2013). A fluorescent ligand designed to probe endogenous cannabinoid CB<sub>2</sub> receptors (Sexton et al., 2011) retained good selectivity and binding compared to unlabelled ligands, as did a chemokine receptor CXCR4 fluorescent antagonist (Oishi et al., 2010), suggesting that the pharmacology of ligands is not necessarily perturbed by the inclusion of fluorophores.

The apelin receptor has not been extensively explored using fluorescent ligands. One group has successfully used modified apelin-13 peptides, conjugated to the red lissamine rhodamine dye (El Messari et al., 2004; Iturrioz et al., 2007, 2010) or a far-red dye (Margathe et al., 2016) to qualitatively study apelin receptor internalisation in artificially expressing cells, but the full range of advantages that fluorescent ligands offer has not been tapped. This thesis outlines four directly labelled novel fluorescent peptide ligands targeting the apelin receptor, designed by Professor Davenport with custom syntheses carried out by Cambridge Research Biochemicals. Two fluorescent apelin ligands (Fig 3.1a,b) were based on a modified apelin-13 peptide that shows high affinity for the apelin receptor (Murza et al., 2012; Shin et al., 2017), and has been used successfully as the basis of the [<sup>125</sup>I]-apelin-13 radioligand (Fig 3.1c), carrying several minor changes from endogenous [Pyr<sup>1</sup>]apelin-13 (Fig 3.1d). Two fluorescent ELA ligands (Fig 3.2a,b) were also designed, based on the ELA-14 (Fig 3.2c) isoform of the second endogenous apelin receptor ligand. Professor Davenport has attempted to design radioactive ELA ligands, tagged at the C-terminus with [<sup>125</sup>I], in the past, but they did not function experimentally. Fluorescent ELA ligands would provide a useful alternative to this.

The work in this thesis aimed to characterise the pharmacology of these fluorescently peptides at the apelin receptor using binding studies and *in vitro* assays. The fluorescent peptides were subsequently used to visualise apelin receptor binding in human kidney sections, and in a clinically relevant hESC-CM model. Finally, apelin647, the most promising candidate identified in validation assays, was used to explore apelin receptor visualisation, binding, and near real-time internalisation in an artificially expressing CHO-K1 cell line, in conjunction with a high content screening system.

The data in this thesis show that the four fluorescent peptides retained their pharmacology at the apelin receptor, including the two ELA based ligands, which are the first such ligands to be reported. The data also confirmed the suitability of fluorescent apelin receptor ligands in high-throughput platforms that carry minimal risks to safety and offer many more measurable parameters than radioligand binding alone.

## **3.2. Methods**

### ***3.2.1. Design of four novel fluorescent apelin receptor ligands***

The four novel fluorescent ligands designed by Professor Davenport are based on either a modified apelin-13 peptide agonist that shows very high affinity at the apelin receptor and forms the basis for the [<sup>125</sup>I]-apelin-13 radiolabel, or the endogenous ELA-14 agonist peptide. The structures of the peptides described in this thesis are shown in Fig 3.1 and Fig 3.2. Fluorophores structurally identical to Alexa Fluor 488 or 647 were conjugated to the peptide in custom syntheses carried out by Cambridge Research Biochemicals via a pegylated linker at the N-terminus of the peptides. Powdered peptides were reconstituted in DMSO to a concentration of 10 mM before subsequent experimentation.

### ***3.2.2. Radioligand binding assays***

CHO-APLNR cells were generated and cultured as described in Section 2.4. CHO-APLNR cell membrane preparations and human left ventricle (HLV) heart tissue homogenates were prepared as described in Section 2.6.1 and Section 2.6.2, and were used at final concentrations of 1 mg/mL and 1.5 mg/mL respectively in radioligand binding assays. Protein concentrations were determined using the DC Protein Assay (Bio-Rad), described in Section 2.6.3.

Fixed concentration binding (described in Section 2.7.1) was used to validate apelin receptor binding in CHO-APLNR versus untransfected wild-type CHO cells (CHO-WT). Total binding was determined using a final concentration of 0.15 nM [<sup>125</sup>I]-apelin-13. Non-specific binding was determined in the presence of 5 μM [Pyr<sup>1</sup>]apelin-13.

Competition binding (described in Section 2.7.3) was used to validate binding of the four novel fluorescent ligands to native apelin receptor in HLV tissue. Concentration ranges of 1 pM – 1  $\mu$ M of the competing ligands were tested against 0.1 nM [<sup>125</sup>I]-apelin-13.

### **3.2.3. *In vitro* GPCR assays**

Further functional validation of the four novel fluorescent ligands was performed using several *in vitro* GPCR assays. Firstly, a dynamic mass redistribution assay (described in Section 2.8.1) was used to assess cellular responses to a concentration range covering 10 pM – 1  $\mu$ M of endogenous [Pyr<sup>1</sup>]apelin-13 and ELA-14 peptides versus the four novel fluorescent ligands in CHO-APLNR cells. Secondly, a commercially available cAMP accumulation assay (described in Section 2.8.2) was used to assess apelin receptor G $\alpha_i$  inhibition of 15  $\mu$ M forskolin-stimulated cAMP following exposure to a concentration range covering 30 pM – 3  $\mu$ M of [Pyr<sup>1</sup>]apelin-13 and ELA-14 versus the four novel fluorescent ligands in CHO-K1 cells overexpressing human apelin receptor (provided in the kit). Buffer treated wells showed no response. Lastly, a commercially available internalisation assay (described in Section 2.8.3) was used to assess apelin receptor internalisation following exposure to a concentration range covering 10 pM – 10  $\mu$ M of [Pyr<sup>1</sup>]apelin-13 and ELA-14 versus the four novel fluorescent ligands in U2OS cells overexpressing human apelin receptor (provided in the kit). Buffer treated wells showed no response. Note that, where curves were incomplete, i.e. ELA-14 in the cAMP assay, and red fluorescent apelin in the internalisation assay, non-linear fits were constrained to bottom of curve = 0, Hill slope = -1, and bottom of curve = 0, Hill slope = 1 respectively to derive  $pD_2$  values.

### **3.2.4. *Human tissue***

Surgical samples of human kidney tissue were obtained with informed consent and ethical approval (05/Q104/142). Tissues were snap frozen in liquid nitrogen before storage at -80 °C. Tissue samples from humans (n  $\geq$  3 individuals) were cut, using a cryostat (-20 °C to -30 °C), into 10  $\mu$ m sections and thaw mounted onto slides before return to storage at -80 °C. On the day of experimentation, frozen tissue sections were

thawed for 20 mins at room temperature (21 °C), encircled with a hydrophobic pen, and rehydrated with PBS.

### ***3.2.5. Fluorescent ligand binding in human kidney tissue***

Human kidney tissue sections were washed with HBSS before being treated with 1  $\mu$ M green fluorescent apelin or ELA, made up in HBSS, for 90 mins in the dark at room temperature. Non-specific binding was determined in the presence of 10  $\mu$ M [Pyr<sup>1</sup>]apelin-13. Slides were washed with HBSS before fixation with 4 % formaldehyde for 20 mins. Slides were washed with HBSS before treatment with Hoechst 33342 nuclear marker prepared at 10  $\mu$ g/mL in HBSS for 15 mins. After a final HBSS wash, slides were blotted dry with lint-free tissue, mounted with ProLong Gold Antifade Mountant, covered with a cover slip, and left at room temperature in the dark to set ( $\geq$  48 h).

### ***3.2.6. Zeiss LSM 510 Meta Inverted Confocal Microscope***

To visualise fluorescent ligand binding in human kidney, tissue sections were imaged using a Zeiss LSM 510 Meta Inverted Confocal Microscope using the blue and green channels described in Section 2.9.6.

### ***3.2.7. Fluorescent ligand binding in cells***

Several studies were performed using red fluorescent apelin in cell-based experiments. hESC culturing and differentiation to cardiomyocytes (hESC-CMs) was performed as described in Section 2.4.4 and Section 2.4.5. Additionally, generation of an apelin receptor knockdown hESC-CM line was carried out as described in Section 2.4.6.

For fluorescent ligand binding in hESC-CMs, cells were seeded in CellCarrier-96 Ultra Plates (PerkinElmer) at a density of  $\sim$ 40 k/well. After a wash with HBSS, hESC-CMs were treated with 300 nM red fluorescent apelin, made up in HBSS, for 90 mins in the dark at room temperature. Non-specific binding was determined in the presence of 10  $\mu$ M [Pyr<sup>1</sup>]apelin-13. hESC-CMs were then washed with HBSS before fixation with 4 % formaldehyde for 3 mins. hESC-CMs were washed with HBSS before treatment with

Hoechst 33342 nuclear marker prepared at 10 µg/mL in HBSS for 15 mins. After a final HBSS wash, hESC-CMs were maintained in 100 µL HBSS for imaging.

For fluorescent ligand binding in CHO-APLNR, cells were seeded in CellCarrier-96 Ultra Plates at a density of ~10 k/well. After a wash with HBSS, CHO-APLNR cells were treated with red fluorescent apelin. For time-course experiments, CHO-APLNR were treated with 300 nM of the fluorescent ligand for 0 – 90 mins, in the dark at room temperature. For saturation binding experiments, CHO-APLNR were treated with a concentration range covering 1 – 300 nM of the fluorescent ligand for 90 mins, in the dark at room temperature. Non-specific binding was determined in the presence of 10 µM [Pyr<sup>1</sup>]apelin-13. Untransfected CHO-WT cells were also used as controls. For competition binding experiments, a concentration range covering 10 pM – 10 µM of [Pyr<sup>1</sup>]apelin-13 was used to compete against a 30 nM concentration of the red fluorescent apelin ligand. At the end-points of the above experiments, CHO-APLNR were washed with HBSS before fixation with 4 % formaldehyde. CHO-APLNR were washed with HBSS before treatment with Hoechst 33342 nuclear marker prepared at 10 µg/mL in HBSS for 15 mins. For internalisation experiments, CHO-APLNR were treated with WGA-555 (10 µg/mL) and Hoechst 33342 nuclear marker (10 µg/mL) in HBSS for 15 mins, before a wash and subsequent treatment with 300 nM red fluorescent apelin ligand for 5 mins. After a final wash with HBSS, cells were imaged in near real-time at 37 °C and 5 % CO<sub>2</sub> using the Opera Phenix. For cells pre-treated with either CMF-019 (10 µM) or [Pyr<sup>1</sup>]apelin-13 (1 µM), compounds were added for 1 h before a 1 h wash and subsequent treatment with fluorescent ligand (300 nM).

### **3.2.8. Opera Phenix High Content Screening**

The Opera Phenix was used to image hESC-CMs and CHO-APLNR cells as described in Section 2.9.2. Scale bars are as indicated in figures.

### **3.2.9. Data analysis and statistics**

Quantitative data are expressed as mean ± SD. Raw data were handled using Microsoft Excel for Windows (Microsoft). Graphical presentation and statistical tests were performed using GraphPad Prism version 6.07 for Windows (GraphPad Software). For radioligand competition binding experiments, K<sub>i</sub> values were

determined using Cheng-Prusoff methodology (described in Section 2.7.3). For *in vitro* GPCR assays,  $EC_{50}$ ,  $pD_2$ , and  $E_{max}$  values were calculated using GraphPad Prism version 6.07 for Windows. Statistical tests are indicated in figure legends where used. A p value of  $< 0.05$  was determined as significant.

### **3.3. Results**

#### **3.3.1. Design of the four novel fluorescent ligands**

Novel fluorescent ligands were based on the parent endogenous peptides [Pyr<sup>1</sup>]apelin-13 or ELA-14. Apelin488 and apelin647 peptide sequences (Fig 3.1) include non-natural amino acids norleucine and tyrosine-O-benzene at positions 11 and 13. The norleucine residue replaces a methionine that can otherwise oxidise during labelling processes (Hosoya et al., 2000; Medhurst et al., 2003; Murza et al., 2012; Read et al., 2019), whilst the tyrosine replacing phenylalanine allows for the addition of iodine-125 to make the high-affinity radioligand used in this thesis. A short 4 unit polyethylene glycol linker, commonly used for conjugation due to their good solubility and lack of toxicity, was used to conjugate the fluorescent dye to the amine group at the N-terminus of the apelin based peptides and ELA based peptides (Fig 3.2). Note ELA488 and ELA647 peptide sequences does not contain any non-natural amino acids. Cambridge Research Biochemicals ensured a purity  $> 95\%$  and a net peptide content  $> 80\%$  for all fluorescent ligands used in this thesis.

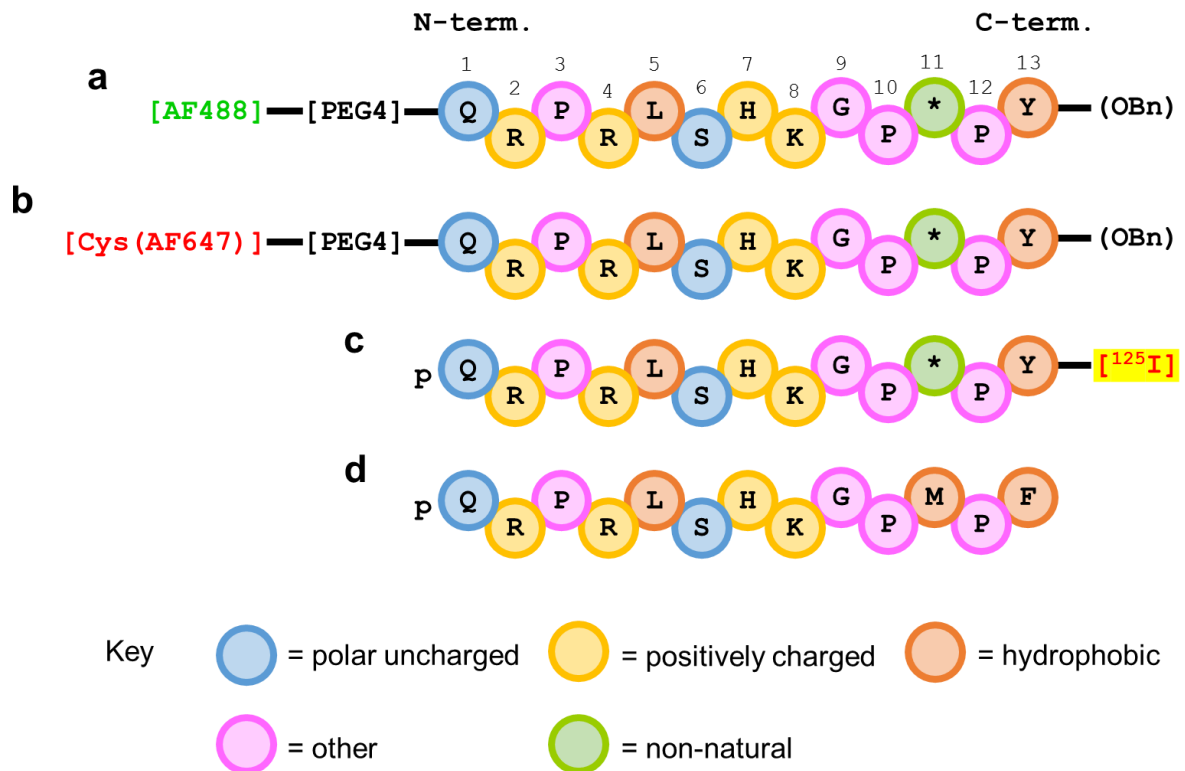


**Figure 3.1.** Amino acid (single letter code) structures of apelin based peptides used in this thesis. **a** Apelin488 fluorescent peptide conjugated to the fluorescent dye ([AF488]) structurally identical to Alexa Fluor 488, via a 4 unit polyethylene glycol ([PEG4]) linker at the N-terminus. \* indicates substitution of methionine with the non-natural amino acid norleucine (Nle). (OBn) indicates O-benzene. **b** Apelin647 fluorescent peptide conjugated to the fluorescent dye ([Cys(AF647)]) structurally identical to Alexa Fluor 647, via a [PEG4] linker at the N-terminus. **c** [Glp65,Nle75,Tyr77][<sup>125</sup>I]-apelin-13 (referred to as [<sup>125</sup>I]-apelin-13), with an irradiated [<sup>125</sup>I] tyrosine at position 13. **d** The endogenous peptide, [Pyr<sup>1</sup>]apelin-13, that the labelled peptides are based on.

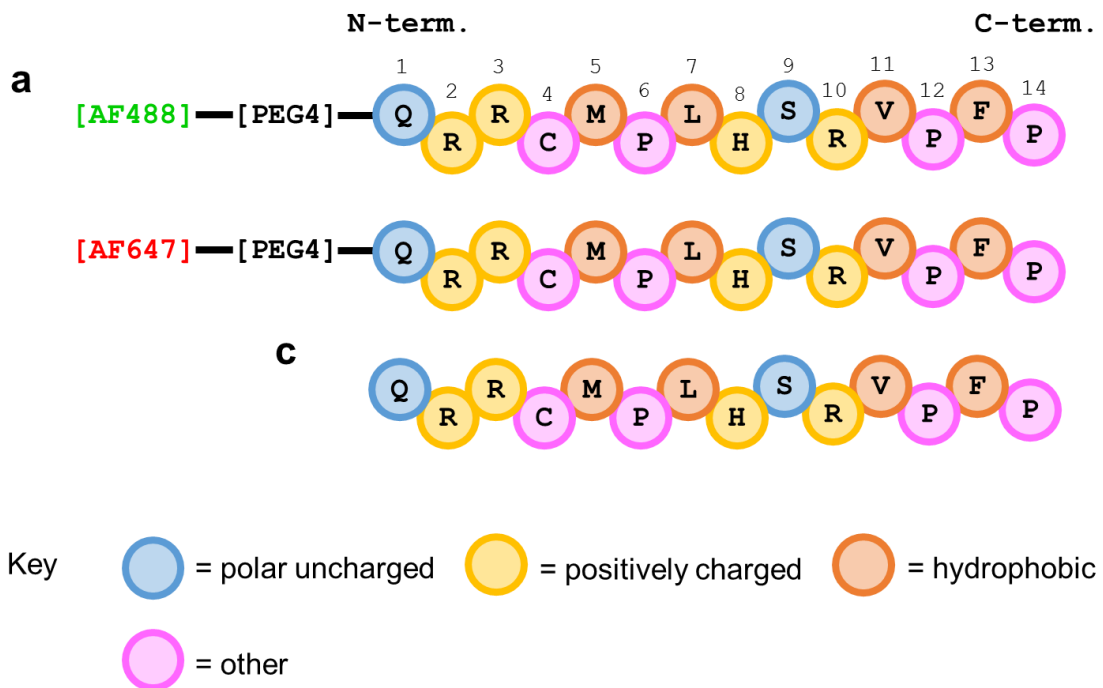


**Figure 3.2.** Amino acid (single letter code) structures of ELA based peptides used in this thesis. **a** ELA488 fluorescent peptide conjugated to the fluorescent dye ([AF488]) structurally identical to Alexa Fluor 488, via a 4 unit polyethylene glycol ([PEG4]) linker at the N-terminus. **b** ELA647 fluorescent peptide conjugated to the fluorescent dye ([AF647]) structurally identical to Alexa Fluor 647, via a [PEG4] linker at the N-terminus. **c** The endogenous peptide, ELA-14, that the labelled peptides are based on.

When comparing the endogenous [Pyr<sup>1</sup>]apelin-13 (Fig 3.1d) and ELA-14 (Fig 3.2c) peptides, it is interesting to note that there is little sequence similarity between them, but there is overlap in the class of side chain associated with amino acids at certain positions (Yang et al., 2015).

### 3.3.2. Validation of apelin receptor binding in CHO-APLNR

Apelin receptor binding was first validated in CHO-APLNR cells using fixed concentration radioligand binding (Fig 3.3). Total binding equalling  $1148.10 \pm 256.9$  disintegrations per minute (DPM) in 1 mg/mL preparations of CHO-APLNR was significantly higher than the non-specific binding of  $74.21 \pm 10.91$  DPM. For comparison, total binding in 1.5 mg/mL preparations of human left ventricle (HLV)

equalled  $2712.07 \pm 515.5$  DPM, also significantly higher than the non-specific binding of  $491.46 \pm 239.1$  DPM. Specific binding for [ $^{125}$ I]-apelin-13 in HLV was therefore 2220.61 DPM, which is somewhat comparable to 1610.84 DPM determined in CHO-APLNR when adjusted for protein concentration. The data demonstrated that artificial expression of apelin receptor in CHO-APLNR was consistent with expression in native tissue. Untransfected CHO-WT were tested as controls and exhibited a total binding ( $53.72 \pm 40.23$  DPM), which was not significantly different from non-specific binding ( $73.10 \pm 30.32$  DPM). This confirmed that binding of [ $^{125}$ I]-apelin-13 in CHO cells was dependent on the expression of the apelin receptor construct.

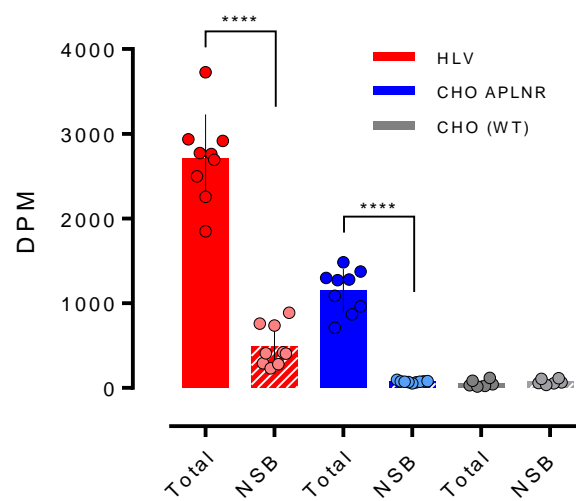


**Figure 3.3.** Validation of CHO cells stably expressing human apelin receptor (CHO-APLNR). Graph shows Total binding, measured as disintegrations per minute (DPM) of 0.15 nM [ $^{125}$ I]-apelin-13 in human left ventricle tissue homogenate (HLV), CHO-APLNR, and wild-type CHO cells (CHO-WT) that do not artificially express the apelin receptor. Non-specific binding (NSB) was determined in the presence of 5  $\mu$ M [Pyr $^1$ ]apelin-13. The difference between Total and NSB indicates specific binding of [ $^{125}$ I]-apelin-13 to apelin receptor. Both HLV and CHO-APLNR showed Total binding that was significantly (\*\*\*\* =  $p < 0.001$ ) higher than NSB, determined using an unpaired Student's T test. CHO-WT cells showed no significant Total binding above the NSB. Note that protein concentrations used were 1.5 mg/mL final for HLV, and 1 mg/mL final for CHO-APLNR and CHO-WT.  $n = 3$  independent experiments performed in triplicate for each condition. CHO-APLNR were prepared by Mr Jason Brown.

Using high content imaging, a time-course showed that mean whole cell fluorescence in the 647 nm channel increased with the time that CHO-APLNR cells were incubated with 300 nM apelin647 (Fig 3.4). After 90 mins, a maximum fluorescence intensity of  $185.73 \pm 23.4$  was observed, that showed a tendency towards saturation. A half-life ( $t_{1/2}$ ) of ~24 mins was calculated for the apelin647 binding observed in CHO-APLNR.

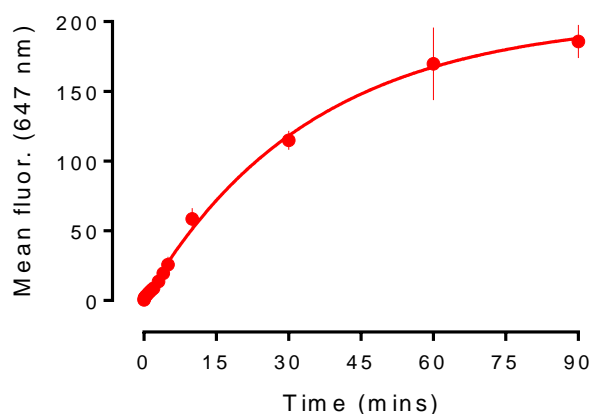


**Figure 3.4.** Association of apelin647 in CHO-APLNR over a 90 mins time-course. Cells were incubated with 300 nM apelin647 for 0 – 90 mins before fixation with 4 % formaldehyde and subsequent imaging and quantification using high content imaging. Graph shows mean whole cell fluorescence (emitted light at wavelength of 647 nm, background corrected)  $\pm$  SD.  $n = 3$  independent experiments performed in triplicate.

### 3.3.3. Validation of the four novel fluorescent ligands in competition binding

Specific binding of the four novel fluorescent ligands, apelin647, apelin488, ELA647, and ELA488 at the apelin receptor was determined using competition binding in HLV tissue homogenate. Apelin647 and apelin488 were less potent than their parent endogenous peptide, [Pyr<sup>1</sup>]apelin-13, but were still able to displace 0.1 nM [<sup>125</sup>I]-apelin-13 (Fig 3.5a). Equally, ELA647 and ELA488, were less potent than ELA-11, but displacement of the radioligand was still observed (Fig 3.5b). See Table 3.1 for  $pK_i$  values of the ligands. Overall, the data suggested that, whilst inclusion of the [PEG4] linker and fluorescent dyes seems to reduce affinity versus the endogenous peptides, binding to the apelin receptor still occurs with high affinity, comparable with other validated ligands. Note that apelin488 showed lower affinity than apelin647, whilst ELA647 and ELA488 were essentially equipotent.

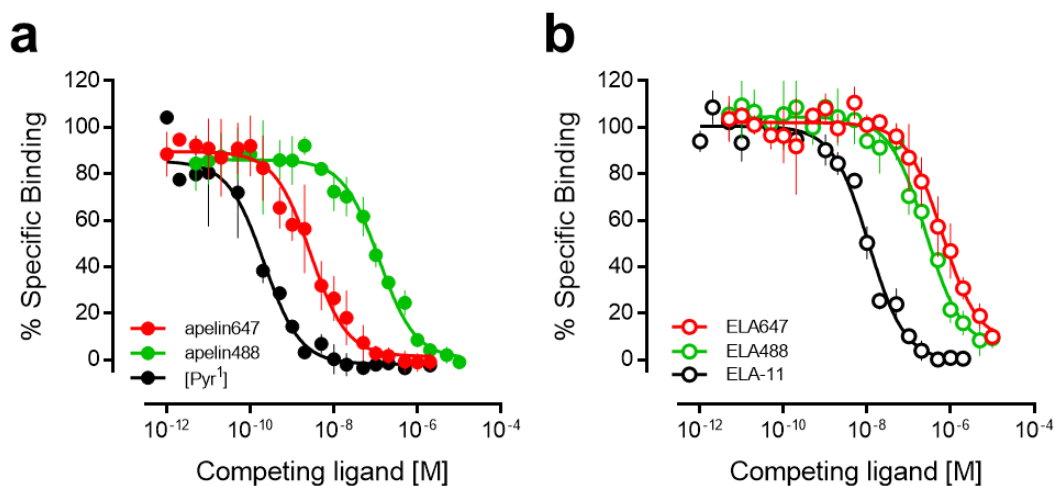


**Figure 3.5.** Competition binding at apelin receptor of peptides described in this thesis, against [ $^{125}$ I]-apelin-13 (0.1 nM) in human left ventricle tissue homogenate (1.5 mg/mL). Competition curves for: **a** the fluorescent apelin peptides, apelin647 (red) and apelin488 (green), and the endogenous parent peptide, [Pyr<sup>1</sup>]apelin-13 (black); **b** the fluorescent ELA peptides, ELA647 (red) and ELA488 (green), and the endogenous parent peptide, ELA-11. In all instances, n = 1 independent experiment performed in triplicate.

### 3.3.4. Validation of the four novel fluorescent peptides in *in vitro* GPCR assays

Pharmacological activity of the four novel fluorescent peptides was assessed in several functional *in vitro* assays (Fig 3.6). In all platforms, fluorescent ligands exhibited activity, with a trend towards being less potent than the parent endogenous peptides. However, it is interesting to note that apelin647, whilst less potent and displaying a lower  $E_{max}$  than [Pyr<sup>1</sup>]apelin-13 in the dynamic mass redistribution assay (Fig 3.6a), was more potent than [Pyr<sup>1</sup>]apelin-13 in the cAMP inhibition assay (Fig 3.6b) and approximately equipotent in the internalisation assay (Fig 3.6c). ELA488 and ELA647 showed consistently lower potency in all platforms versus ELA-14. Summaries of ligand  $pD_2$  values and  $E_{max}$ , can be seen in Table 3.1. Overall, the data suggested that, whilst modification of peptides to include the [PEG4] linker and fluorescent dyes does have nuanced effects on pharmacological parameters, the novel fluorescent ligands all showed function at the apelin receptor.

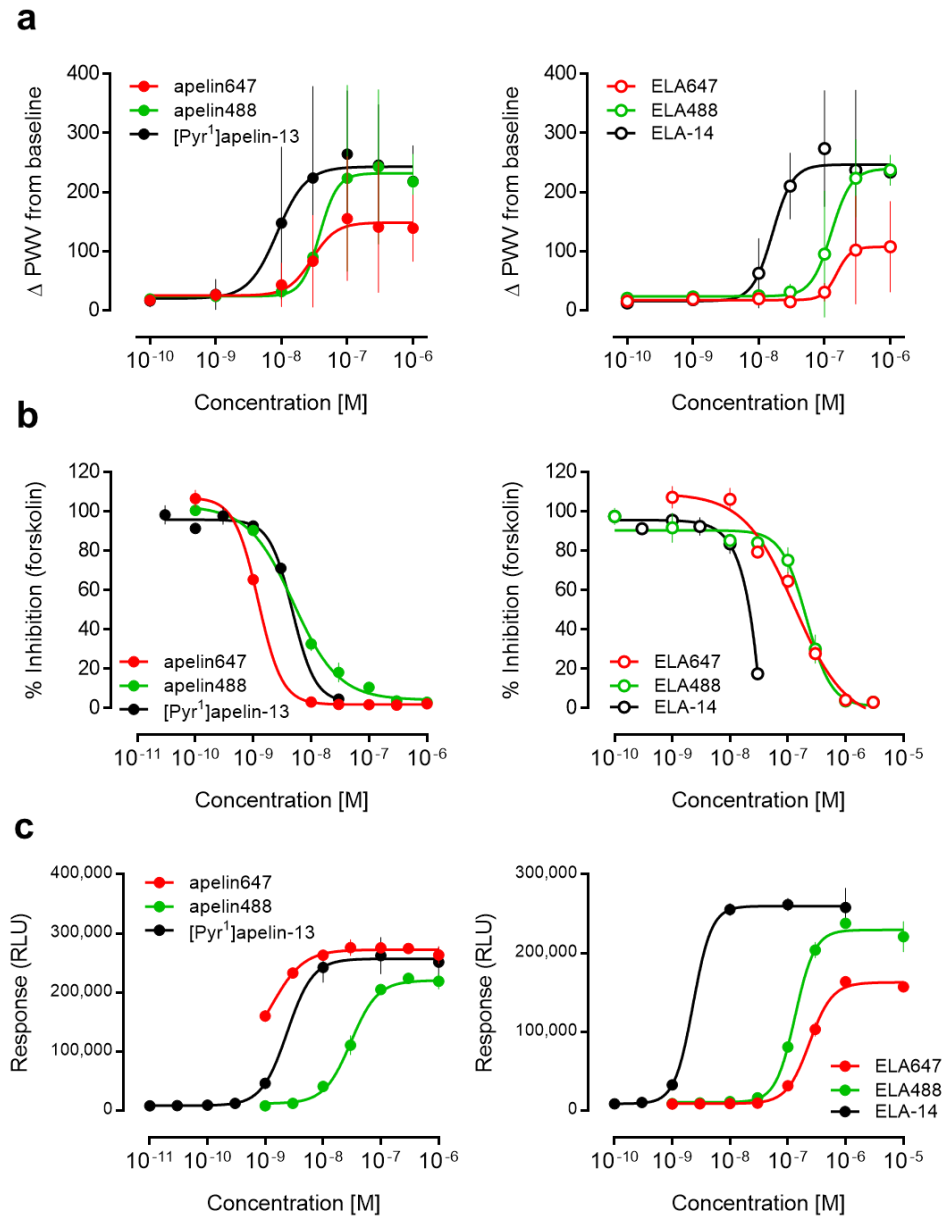


**Figure 3.6.** Validation of peptides described in this thesis in *in vitro* functional assays. Apelin647, apelin488, and [Pyr<sup>1</sup>]apelin-13 (left column), and ELA647, ELA488, and ELA-14 (right column) were tested in; **a** A dynamic mass redistribution GPCR functional assay (response shown as the change in peak wavelength value,  $\Delta$ PWV, from baseline), n = 3 independent experiments performed in triplicate; **b** An assay assessing inhibition of forskolin stimulated cAMP (response shown as % Inhibition versus forskolin alone), n= 1 independent experiment performed in triplicate; **c** An assay assessing internalisation (response in relative light units, RLU), n = 1 independent experiment performed in triplicate.

Assay	Binding	DMR		cAMP accum.		Internalisation	
Parameter	$pK_i$	$pD_2$	$E_{max}$	$pD_2$	% inhib.	$pD_2$	$E_{max}$
[Pyr <sup>1</sup> ]apelin-13	10.05 $\pm$ 0.19	8.07 $\pm$ 0.35	242.9 $\pm$ 46.96	8.32 $\pm$ 0.19	2.94 $\pm$ 9.91	8.62 $\pm$ 0.17	257,117 $\pm$ 13001
apelin488	7.29 $\pm$ 0.12	7.42 $\pm$ 0.28	231.8 $\pm$ 43.37	8.31 $\pm$ 0.09	4.18 $\pm$ 2.27	7.52 $\pm$ 0.05	220,503 $\pm$ 6816
apelin647	8.92 $\pm$ 0.09	7.54 $\pm$ 0.35	148.5 $\pm$ 39.63	8.91 $\pm$ 0.03	1.84 $\pm$ 0.80	8.88 $\pm$ 0.97	272,476 $\pm$ 6208
ELA-11	8.33 $\pm$ 0.09	7.79 $\pm$ 0.19	246.4 $\pm$ 32.56	7.63 $\pm$ 0.22	-	8.64 $\pm$ 0.17	259,787 $\pm$ 7219
ELA488	6.96 $\pm$ 0.12	6.90 $\pm$ 0.17	239.6 $\pm$ 50.07	6.68 $\pm$ 0.09	-6.69 $\pm$ 14.57	6.87 $\pm$ 0.05	229,625 $\pm$ 7939
ELA647	6.57 $\pm$ 0.14	6.81 $\pm$ 0.42	107.6 $\pm$ 31.44	6.88 $\pm$ 0.16	0.83 $\pm$ 7.57	6.63 $\pm$ 0.03	162,951 $\pm$ 5179

**Table 3.1.** Summary of pharmacological parameters for the peptide ligands described in this thesis. Data shows the parameter of interest for each assay expressed as mean $\pm$ SD for each of the peptides. DMR = dynamic mass redistribution assay. Note that for the cAMP accumulation assay, % inhibition is shown, indicating the lowest cAMP levels achieved by the highest concentration of compound, expressed as a percentage of the maximum cAMP achieved by the standard forskolin concentration (i.e. 15  $\mu$ M) in the assay. Units for  $E_{max}$  values for the DMR assay and internalisation assay are as indicated in Fig 3.6a and c.

### 3.3.4. Fluorescent ligands are suitable tools for visualisation of apelin receptor in native tissue

A critical advantage of using fluorescent ligands is the ability to visualise binding to the receptor of interest using fluorescent imaging techniques. In human kidney tissue sections, apelin488 and ELA488 were used to assess apelin receptor binding and localisation in renal tubules of the cortex (Fig 3.7). Data confirmed that both fluorescent ligands (at a concentration of 1  $\mu$ M) were observed in the tissue, with the apelin488 ligand exhibiting particularly intense fluorescence. Binding of the fluorescent ligand was likely specific, demonstrated by the near total loss of apelin488 signal in the presence of a saturating 10  $\mu$ M concentration of unlabelled [Pyr<sup>1</sup>]apelin-13.

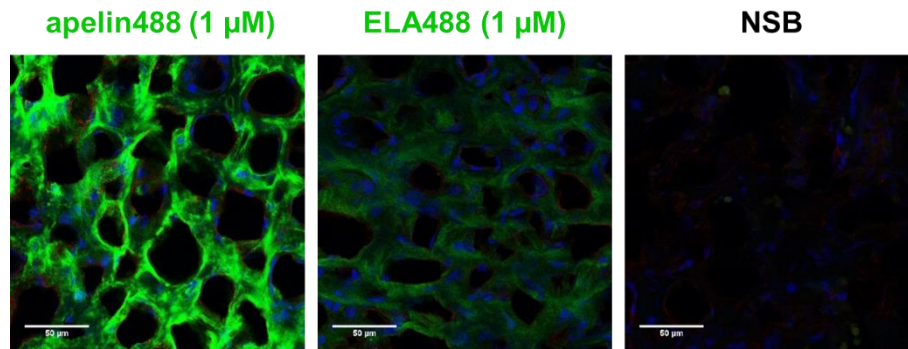


**Figure 3.7.** Representative confocal fluorescent images of human kidney cortex sections treated with the fluorescent ligands apelin488 (1  $\mu$ M, left, shown in green), or ELA488 (1  $\mu$ M, centre, shown in green). Non-specific binding (NSB, right) shows section treated with 1  $\mu$ M apelin488 in the presence of a saturating concentration (10  $\mu$ M) [Pyr<sup>1</sup>]apelin-13. Scale bars as indicated in figure. Hoechst nuclear marker shown in blue.

A clinically relevant hESC-CM cell model was also used to visualise fluorescent apelin receptor ligand binding. Apelin647 was selected as the ligand of choice due to the high affinity and potency observed in previous binding and functional assays (see Fig 3.5a and Fig 3.6a-c respectively). Additionally, the far-red fluorescent dye could be visualised using high content imaging, and would allow for inclusion of other fluorophores such as GFP in subsequent studies that will be outlined later in this thesis (Section 4.3.3). Data here showed that apelin647 (300 nM) bound to wild-type hESC-CMs, but no fluorescent signal was observed in a population of hESC-CMs with apelin receptor knockdown (Fig 3.8). Additionally, 10  $\mu$ M [Pyr<sup>1</sup>]apelin-13 was again able to outcompete apelin647 for binding at the apelin receptor in wild-type hESC-CMs. Data confirm that apelin647 binding can be visualised in a cell model that recapitulates a native phenotype.

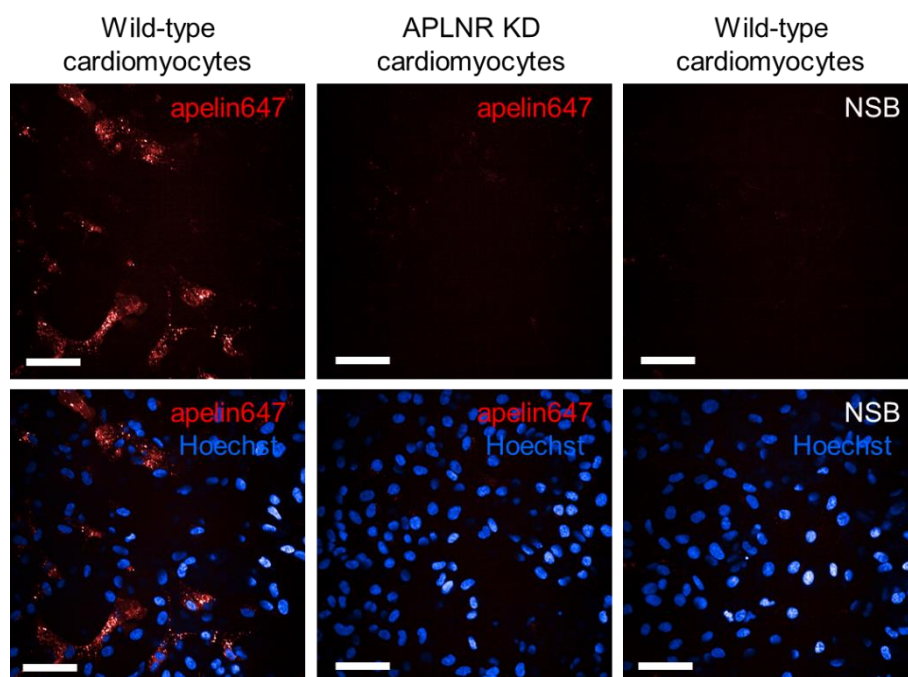


**Figure 3.8.** Representative high content confocal fluorescent images of human embryonic stem cell-derived cardiomyocytes – either wild-type, or with an apelin receptor knockdown (APLNR KD) – treated with 300 nM apelin647 (red) for 90 mins. Non-specific binding (NSB) was determined in the presence of a saturating concentration (10  $\mu$ M) [Pyr<sup>1</sup>]apelin-13. n = 4 independent experiments performed in triplicate. Bottom row shows merged images with Hoechst nuclear marker (blue) included. Scale bars show 50  $\mu$ m. Cardiomyocytes were cultured by Ms Robyn Macrae

### **3.3.5. Apelin647 is a versatile tool for exploring apelin receptor pharmacology**

Following the successful validation of the four novel fluorescent ligands, particularly apelin647, the work in this thesis aimed to use the far-red apelin peptide as a safe, easy-to-use alternative to a radioligand that could be used in a high-throughput format.

CHO-APLNR cells were treated with a concentration range of apelin647 (1 – 300 nM) that was visualised using high content imaging (Fig 3.9a). Fluorescence was visibly brighter at higher concentrations than lower. Specificity of apelin647 binding to apelin receptor was demonstrated (Fig 3.9b and c) using 10  $\mu$ M [Pyr<sup>1</sup>]apelin-13 to displace the fluorescent ligand, and, additionally, untransfected CHO-WT did not bind apelin647. Maximum background-corrected whole cell fluorescence (i.e. total binding

with 300 nM apelin647), equalling  $209.80 \pm 42.50$ , was significantly higher than the non-specific binding, equalling  $2.76 \pm 0.38$ . Total binding in CHO-WT was  $0.70 \pm 0.45$ .

Quantification of high content images provided a curve for the 1 – 300 nM concentration range of apelin647 in CHO-APNLR that saturated at the top concentration (Fig 3.9d). A  $K_D$  of  $85.35 \pm 9.00$  nM was determined for apelin647 in this platform. Additionally, a competition binding experiment was performed using a concentration range covering 0.01 nM – 10  $\mu$ M of [ $\text{Pyr}^1$ ]apelin-13 to compete against a sub- $K_D$  30 nM concentration of apelin647 (Fig 3.9e). A  $K_i$  of  $23.24 \pm 2.34$  nM was determined for [ $\text{Pyr}^1$ ]apelin-13 against the fluorescent ligand. In summary, the data provided evidence that apelin647 can be used to characterise parameters typically assessed in radioligand binding studies, whilst also allowing for visualisation of the labelled ligand.

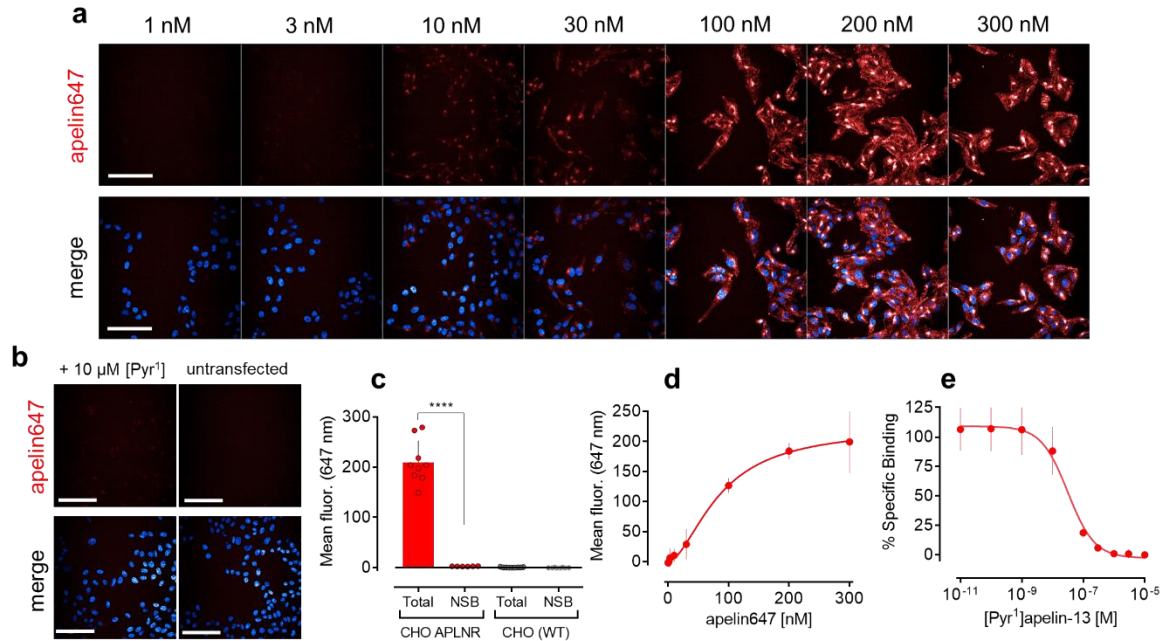


**Figure 3.9.** The fluorescent ligand, apelin647, is a robust tool for exploring the pharmacology of the apelin receptor using high content imaging. **a** Representative high content confocal fluorescent images of CHO cells stably expressing human apelin receptor (CHO-APLNR) treated with a concentration range (1 – 300 nM) of apelin647 (top row, visualised in red), as indicated in figure. Hoechst nuclear marker (visualised in blue) is included in the merge (bottom row). Scale bars show 100 μm. **b** Control images showing CHO-APLNR treated with 300 nM apelin647 in the presence of 10 μM [Pyr<sup>1</sup>]apelin-13 (left column), or CHO-WT treated with 300 nM apelin647 (right column). Scale bars show 100 μm. **c** Quantification of mean whole cell fluorescence (emitted light at wavelength of 647 nm) in CHO-APLNR or CHO-WT treated with 300 nM apelin647 in the absence (Total) or presence (NSB) of 10 μM [Pyr<sup>1</sup>]apelin-13. Total fluorescence was significantly higher (\*\*\*\* =  $p < 0.001$ ) than NSB in CHO-APLNR, determined using an unpaired Student's T test. **d** Saturation binding using high content imaging. Quantification of mean whole cell fluorescence (emitted light at wavelength of 647 nm, background corrected) in CHO-APLNR treated with a concentration range (1 – 300 nM) of apelin647. The curve demonstrates saturability of binding of the apelin647 ligand in this platform. **e** Competition binding using high content imaging. Displacement of specific binding of apelin647 (30 nM) with increasing concentrations of [Pyr<sup>1</sup>]apelin-13. In all instances,  $n = 4$  independent experiments performed in triplicate. CHO-APLNR were provided by Mr Jason Brown.

### **3.3.6. Apelin647 allows for visualisation of apelin receptor internalisation**

After data demonstrated that apelin647 induced apelin receptor internalisation in an *in vitro* assay (see Fig 3.6c and Table 3.1), it was assessed whether fluorescent ligand internalisation could be viewed in near real-time.

CHO-APLNR were treated with Hoechst nuclear marker and WGA-555 membrane marker before treatment with 300 nM apelin647 for 5 mins before a rapid wash and subsequent high content imaging. Cells were then imaged from the start point (5 mins) to the end point (90 mins) every 30 secs (Fig 3.10). Visually, apelin receptor localised at the membrane at the earlier time-points, showing could colocalisation with the WGA-555 at the cellular edge (Fig 3.10a and b). As the time-course progressed, staining with apelin647 at the membrane became less pronounced, whilst intracellular fluorescence became more apparent at later time-points, particularly in perinuclear locations (Fig 3.10a). Apelin647, bound to apelin receptor, internalised with the WGA-555 membrane marker, as seen for the 90 mins time-point in Fig 3.10b, suggesting that the internalisation may occur through endocytosis of membrane-bound receptor. Quantification of internalised apelin647 (Fig 3.10c), confirmed the reduction in membrane 647 nm fluorescence over the 90 mins time-course, with a  $t_{1/2}$  of ~12 mins.

Quantification of internalised apelin647 (Fig 3.10c), expressed as a ratio of the apelin647 fluorescence at the membrane versus total cell fluorescence, confirmed that apelin647 was lost at the membrane over the 90 mins time-course, with a half-life of 7.15 mins. Intriguingly, cells pre-treated with CMF-019 (10  $\mu$ M), a G protein-biased small molecule apelin receptor agonist for 1 h, before a 1 h wash and treatment with apelin647, were able to bind apelin647 and internalise ( $t_{1/2}$  of ~6 mins) in a manner similar to cells treated with apelin647 alone. Conversely, cells pre-treated with [Pyr<sup>1</sup>]apelin-13 for 1 h, before a 1 h wash and treatment with apelin647, bound apelin647 to a lesser extent at the start of the time-course, and, additionally, the apelin647 that was able to bind did not internalise.

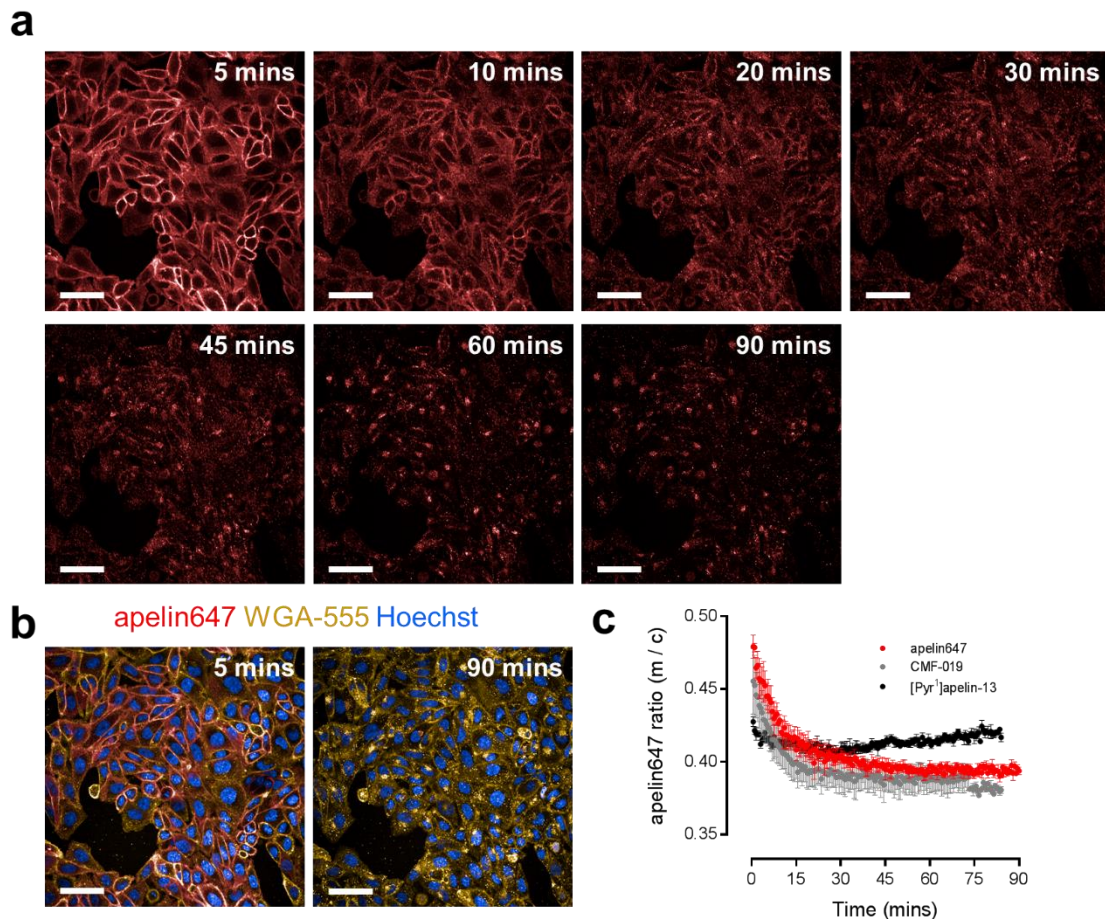


**Figure 3.10.** Internalisation of fluorescent apelin647 (300 nM) in CHO-APLNR, over a 90 mins time-course. **a** Representative high content confocal fluorescent images show snapshots of apelin647 (shown in red) bound to apelin receptor in live CHO-APLNR cells at the time points indicated in the figure. Scale bars show 50  $\mu$ m. For a compiled video of apelin647 internalisation, see associated video file. **b** Merged representative high content confocal fluorescent images show the snapshots of CHO-APLNR taken at the start (5 mins) and end (90 mins) points with the wheat germ agglutinin-AF555 membrane marker (gold) and Hoechst nuclear marker (blue) included. Scale bars show 50  $\mu$ m. **c** Quantified data shows apelin647 fluorescence as a ratio of the signal observed at the cell membrane out of the total cell signal (m / c) over a 90 mins time-course. Graph shows data for apelin647 treated cells alone (red) or apelin647 treated cells after a pre-treatment for 1 h with CMF-019 (10  $\mu$ M) or [Pyr<sup>1</sup>]apelin-13 and wash. n = 3 independent experiments. CHO-APLNR were provided by Mr Jason Brown.

### **3.4. Discussion**

#### **3.4.1. Novel fluorescent ligands bind and activate the apelin receptor**

Ensuring fluorescent ligands retain their pharmacological properties, in terms of binding, and function if agonists, is a critical step in their use as experimental tools (Soave et al., 2020). Here, data showed that four novel fluorescent ligands, apelin488 and apelin647 (Fig 3.1), based on the endogenous apelin receptor peptide agonist [Pyr<sup>1</sup>]apelin-13, and ELA488 and ELA647 (Fig 3.2) based on the second endogenous apelin receptor ligand, ELA-14, were all able to bind to their native target receptor in human left ventricle homogenate (Fig 3.5). Note that apelin488 and apelin647 included non-natural amino acids – norleucine in place of methionine at position 11 and tyrosine-O-benzene in place of phenylalanine at position 13. The norleucine residue prevents oxidation of the methionine that can occur during labelling procedures, and tyrosine allows for the addition of iodine-125, hence their inclusion in the [<sup>125</sup>I]-apelin-13 radioligand (Fig 3.1, Hosoya et al., 2000; Medhurst et al., 2003; Read et al., 2019). A peptide with these modifications showed very high affinity in an apelin receptor binding assay (Murza et al., 2012).

In competition binding assays against [<sup>125</sup>I]-apelin-13, apelin647 bound with the highest affinity of the novel ligands ( $pK_i$  of  $8.92 \pm 0.05$ ), which was lower than that observed for [Pyr<sup>1</sup>]apelin-13 ( $pK_i = 10.05 \pm 0.11$ ) but higher than that for the other endogenous peptide, ELA-14 ( $pK_i = 8.33 \pm 0.05$ ). A  $pK_i$  of  $8.83 \pm 0.06$  has been reported for [Pyr<sup>1</sup>]apelin-13 against the radioligand in human heart previously (Yang et al., 2017), lower than reported here, but very similar to the  $pK_i$  determined for apelin647. Intriguingly, apelin488 bound with lower affinity ( $pK_i = 7.29 \pm 0.07$ ) than apelin647, despite the fact that the only difference between the peptides is the fluorophore itself at the C-terminus of the peptide. A previous report in the literature have shown however, that different fluorescent dyes were able to influence the pharmacology of fluorescent adenosine A<sub>1</sub> receptor ligands (Baker et al., 2010). ELA488 and ELA647 were also able to outcompete the radioligand, although with low affinity, displaying  $pK_i$  values of  $6.96 \pm 0.07$  and  $6.57 \pm 0.08$ .

Once binding was confirmed, fluorescent ligands were assessed for function at the apelin receptor in several *in vitro* GPCR assays (Fig 3.6). A dynamic mass redistribution assay (Fig 3.6a), showed that apelin488 ( $pD_2 = 7.42 \pm 0.16$ ) and apelin647 ( $pD_2 = 7.54 \pm 0.20$ ) induced cellular responses, but were less potent than [Pyr<sup>1</sup>]apelin-13 ( $pD_2 = 8.07 \pm 0.20$ ). Consistent with results in binding, ELA-14 ( $pD_2 = 7.79 \pm 0.11$ ) was slightly less potent than [Pyr<sup>1</sup>]apelin-13 in the assay, and ELA488 and ELA647 were less potent again ( $pD_2 = 6.90 \pm 0.10$  and  $6.81 \pm 0.24$  respectively). Apelin647 and ELA647 showed lower  $E_{max}$  values than both their respective endogenous parent ligands in this assay, and apelin488 and ELA488 (see Table 3.1), although reasons for this are unclear.

The dynamic mass redistribution assay typically assesses GPCR dependent changes in cells, but provides little information on signalling pathways without the inclusion of highly toxic inhibitors of downstream effectors. Instead, assays directly measuring apelin receptor  $G\alpha_i$  inhibition of forskolin-stimulated cAMP production, and internalisation, were used to characterise the fluorescent ligands. Apelin ligands showed relatively similar potencies in the cAMP assay (Fig 3.6b), with  $pK_i$  values of  $8.32 \pm 0.11$ ,  $8.31 \pm 0.05$ ,  $8.91 \pm 0.02$  determined for [Pyr<sup>1</sup>]apelin-13, apelin488, and apelin647 respectively. ELA-14 showed a trend for very potent inhibition of cAMP production, but a full curve was not determined. ELA488 and ELA647 were less potent in this assay, displaying  $pD_2$  values of  $6.68 \pm 0.05$  and  $6.88 \pm 0.09$  respectively. In the internalisation assay, [Pyr<sup>1</sup>]apelin-13 and apelin647 showed relatively similar potencies ( $pD_2 = 8.62 \pm 0.10$  and  $8.88 \pm 0.56$ ), whilst apelin488 was less potent ( $pD_2 = 7.52 \pm 0.03$ ). ELA-14 exhibited a  $pD_2$  value of  $8.64 \pm 0.10$ , but ELA488 and ELA647 were, again, considerably less potent ( $pD_2 = 6.87 \pm 0.03$  and  $6.63 \pm 0.02$  respectively). Additionally, ELA647 also showed a reduced  $E_{max}$  value versus other peptides in this assay (see Table 3.1). The consistently lower potency of ELA488 and ELA647 may be due to their low affinity binding as observed in the competition assay. The data suggest that ELA peptides appear to have been more perturbed by the inclusion of the linker and fluorophores. Note that a methionine residue at position 5 has not been replaced by norleucine in ELA488 or ELA647, and this may undergo oxidation during the labelling step, although this is unlikely to affect binding.

Overall, however, data show that all four novel apelin receptor ligands used in this thesis are able to bind the apelin receptor, and display agonist activity, providing evidence for their suitability as pharmacological tools for exploring this GPCR target.

#### **3.4.2. Apelin488 and apelin647 bind to apelin receptor in the kidney**

To confirm whether the fluorescent ligands could be visualised binding to the apelin receptor in endogenously expressing systems, apelin488 and ELA488 were used to treat human kidney sections. Note that these ligands were chosen at this step as the Zeiss LSM 510 microscope used to image the sections was unable to visualise far-red 647 nm wavelength fluorophores. Apelin488 (1  $\mu$ M) was visualised in tubules of the renal cortex (Fig 3.7), in a manner that is likely apelin receptor specific, as signal was lost in the presence of a competing concentration of 10  $\mu$ M unlabelled [Pyr<sup>1</sup>]apelin-13. ELA488 (1  $\mu$ M) was also visualised in the cortical tubules, but was considerably less bright than apelin488. Again, this may reflect the lower binding that ELA488 exhibited in the human heart. The kidney is widely reported as expressing apelin receptor mRNA and protein (Chapman et al., 2021), and is used frequently in-house as positive controls for [<sup>125</sup>I]-apelin-13 due to apelin receptor expression in cortical regions and glomeruli (Katugampola et al., 2001; Kleinz et al., 2004). It would be interesting to see if the fluorescent ligands can be used as quick (30 mins incubation), easy, and consistent replacements for antibodies (typically requiring 24 – 48 h incubation) or autoradiography (typically requiring several weeks to perform) to identify apelin receptor in other tissues.

#### **3.4.3. Apelin647 binds to apelin receptor in human embryonic stem cell-derived cardiomyocytes**

A well-established hESC-CM cell model was used to confirm binding of apelin647 to apelin receptor in a native setting, rather than in an artificially expressing system such as CHO-APLNR cells. High content imaging showed apelin647 bound to hESC-CMs (Fig 3.8) in a manner likely to be dependent on the presence of apelin receptor as, again, no signal was observed in the presence of 10  $\mu$ M [Pyr<sup>1</sup>]apelin-13. Additionally, an hESC-CM line incorporating apelin receptor knockdown was unable to bind the apelin647 ligand. This knockdown line has been well validated by Ms Robyn Macrae.

The data provide further evidence that apelin647 fluorescent ligand can be used to visualise apelin receptor, even when the protein is present at physiological levels.

#### **3.4.4. Exploration of apelin receptor pharmacology using apelin647**

The apelin647 far-red fluorescent ligand was used to explore apelin receptor pharmacology using CHO-APLNR cells in conjunction with high content imaging. After confirming that binding of apelin647 reached an equilibrium after 90 mins (Fig 3.4), a concentration range (1 – 300 nM) was incubated in CHO-APLNR for 90 mins before fixation and imaging (Fig 3.9a). Apelin647 binding was saturable at 300 nM (Fig 3.9d), and a  $K_D$  value of  $85.35 \pm 9.00$  nM was determined. Controls confirmed that apelin647 binding in CHO-APLNR was dependent on the presence of the apelin receptor construct, and could be blocked in the presence of 10  $\mu$ M [Pyr<sup>1</sup>]apelin-13 (Fig 3.9b). Further, a full competition binding curve was established for [Pyr<sup>1</sup>]apelin-13 ( $K_i = 23.24 \pm 2.34$  nM) against a 30 nM concentration of apelin647 (Fig 3.9e).

The data provide proof-of-principle for the use of apelin647 as a tool for the exploration of apelin receptor pharmacology that could supplement, or even replace, radioligand binding. The platform outlined in this thesis allows for an easy, very robust, high-throughput approach that could be used to identify novel compounds that might compete with apelin647 for binding at the apelin receptor. Additionally, far fewer safety concerns are raised when using a fluorescent ligand versus a radioligand.

#### **3.4.5. Observation of apelin receptor internalisation in near real-time**

Canonical GPCR internalisation (see Fig 3.11 for a schematic) is a complex multi-step process that involves many accessory proteins to shuttle the receptor from the cell surface to intracellular compartments (Calebiro & Godbole, 2018). With respect to the apelin receptor, agonist stimulation can result in phosphorylation by G protein-coupled receptor kinase (GRK), which has been shown to facilitate recruitment of  $\beta$ -arrestin proteins (Reaux et al., 2001; Zhou et al., 2003; Masri et al., 2006; Murza et al., 2012; Chen et al., 2014; Pope et al., 2016). Subsequent  $\beta$ -arrestin dependent apelin receptor internalisation following stimulation with [Pyr<sup>1</sup>]apelin-13 has been confirmed previously (Pope et al., 2016).

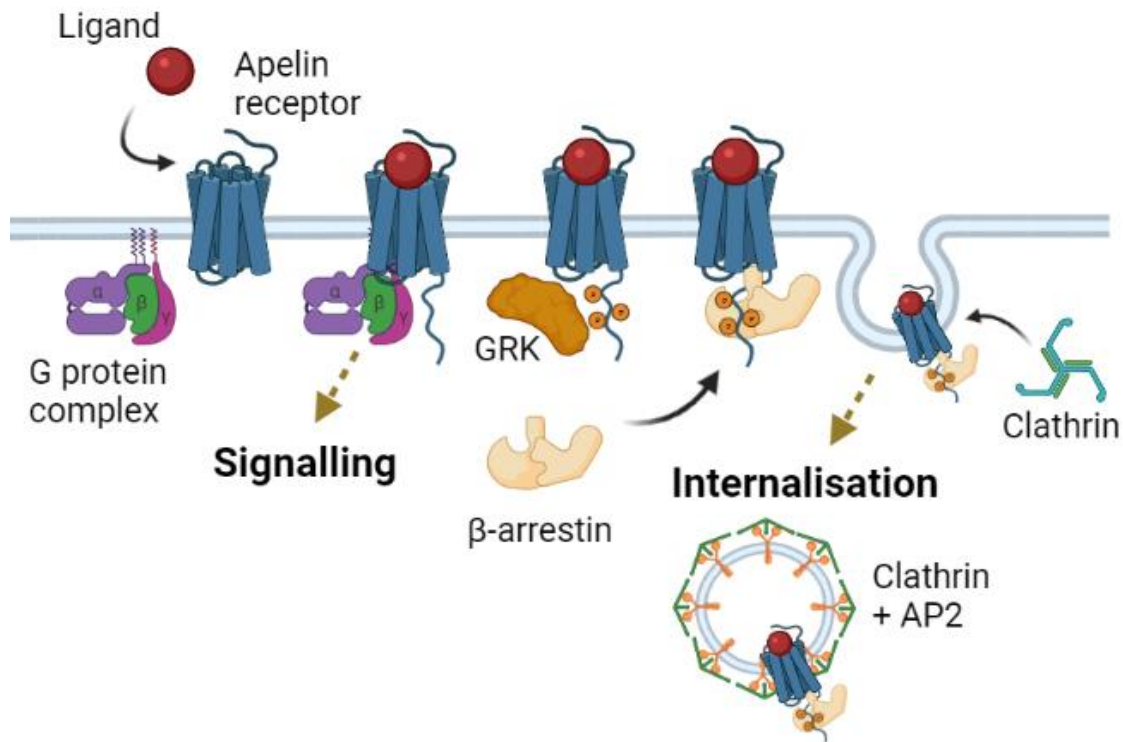


**Figure 3.11.** Schematic showing apelin receptor internalisation following stimulation with a ligand. Following binding of a ligand that displays agonist activity, the receptor can recruit the heterotrimeric G protein complex, which can lead to downstream G protein dependent signalling. Subsequently, G protein-coupled receptor kinase (GRK) can phosphorylate the receptor which can result in recruitment and association of  $\beta$ -arrestin proteins. This can facilitate recruitment of clathrin and adaptin AP2 protein complexes to the budding vesicle, which can then internalise as an endosomal package with the receptor-ligand complex. Schematic was designed using BioRender (<https://biorender.com/>).

An additional benefit of using apelin647 versus a radioligand is the ability to track subcellular localisation of the fluorescent ligand in near real-time. CHO-APLNR were treated with a 300 nM concentration of apelin647 for 5 mins before cells were rapidly washed before subsequent high content imaging over a 90 minute time-course (Fig 3.10a). Intriguingly, apelin647 fluorescence observed at the membrane at earlier time-points (e.g. 5 – 10 mins), appeared to become more intracellular by later time points (e.g. 20 – 90 mins). A WGA-555 membrane marker showed good colocalisation with apelin647 (Fig 3.10b), visualised at the membrane at 5 mins but at perinuclear locations at 90 mins. Compiling the images, captured every 30 seconds, into a video

(see associated Fig 3.10 video file) shows the movement of apelin647 from the membrane to intracellular compartments very clearly.

Quantification of the imaging data (Fig 3.10c), confirmed the loss of apelin647 from the membrane over the time-course. Data were expressed as the ratio of apelin647 fluorescence at the membrane versus total cell fluorescence to account for any changes in fluorescence between compartments that might occur due to factors other than internalisation, such as fading of the fluorophore or moving in/out of the focal plane. The data showed that apelin647 fluorescence proportionally decreased at the membrane, with a non-linear one phase decay regression determining a  $t_{1/2}$  of ~7 mins (i.e. proportion of apelin647 fluorescence at the membrane halves every ~7 mins). Internalisation plateaued by the end-point (90 mins), in accordance with findings from Pope et al., 2016 that show a plateau in apelin receptor internalisation at  $\geq 2$  h following stimulation with 100 nM [Pyr<sup>1</sup>]apelin-13. Pre-treatment of cells with [Pyr<sup>1</sup>]apelin-13 here, prior to a wash and treatment with apelin647, led to reduced apelin647 binding at the membrane, and no change in internalisation over time. This may be reflective of loss of apelin647 binding due to internalisation of the apelin receptor during the [Pyr<sup>1</sup>]apelin-13 pre-treatment. Intriguingly, pre-treatment with CMF-019, a G protein-biased small molecule apelin receptor agonist that shows little activity in  $\beta$ -arrestin or internalisation assays (Read et al., 2016), had little effect on apelin647 binding and internalisation ( $t_{1/2}$  of ~6 mins). Overall, the data show that pre-treatment with CMF-019 followed by washout, allows for subsequent apelin647 binding and internalisation, whereas pre-treatment with [Pyr<sup>1</sup>]apelin-13 does not. This provides evidence that apelin receptor may not have substantially internalised during the CMF-019 pre-treatment and was still available for apelin647 binding following washout of the small molecule agonist.

In summary, internalisation is a highly interesting physiological parameter to measure, particularly considering that avoiding apelin receptor internalisation is hypothesised to be a beneficial therapeutic strategy when designing novel drugs by reducing loss of the target protein from the cell surface (Yang et al., 2015; Read et al., 2016). Apelin647 could be used to more thoroughly characterise mechanisms of apelin receptor

internalisation using additional markers and inhibitors/knockdown of accessory proteins, such as GRKs and  $\beta$ -arrestins in future imaging studies.

### **3.5. Conclusions**

The data in this thesis have shown successful design and validation of four novel fluorescent ligands that bind and activate the apelin receptor in artificial and endogenous cellular and human tissue systems.

The apelin647 ligand was successfully used to assess apelin receptor pharmacology, providing similar outputs to radioligand binding (e.g. affinity constants and competing ligand  $K_i$  values), but in a platform that can be used more safely, and that allows for many more replicates and experiments to be performed over the same time-frame. The data provide proof-of-principle for the use of apelin647 as a tool to screen other compounds designed to hit the apelin receptor.

Additionally, apelin647 was used to qualitatively and quantitatively visualise internalisation of the apelin receptor in near real-time (images captured every 30 secs). Apelin647 in this platform could be used to characterise mechanisms by which the apelin receptor internalises, in theory, in any cell based system that expresses the protein. This could also facilitate drug design at the apelin receptor, where an emphasis on G protein biased compounds that avoid internalisation are hypothesised to be of greater benefit.

## Chapter 4. Characterisation of apelin receptor variants identified in a patient cohort in the NIHR BRIDGE project

### 4.1. Introduction

Of the ~20,000 proteins that the human genome encodes (Ezkurdia et al., 2014), just over 800 (~4 %) are GPCRs (Lv et al., 2016; Alexander et al., 2019). The expansive physiological roles of membrane bound GPCRs in transducing a plethora of extracellular signals to the intracellular environment, has positioned these proteins as targets for ~34 % of all approved pharmaceuticals (Hauser et al., 2017; Schöneberg & Liebscher, 2021).

As genetically encoded proteins, GPCRs are susceptible to mutation, where changes in the protein structure of a GPCR can impact its ability to transduce signals (see Fig 4.1 for a schematic), either decreasing or increasing their efficiency through loss-of-function or gain-of-function mutations (Thompson et al., 2014; Stoy & Gurevich, 2015). So far, over 2350 mutations, across 55 GPCRs, have been causally linked to 66 human disease phenotypes, with approximately 14 of these diseases caused by gain-of-function mutations (Schöneberg & Liebscher, 2021). As examples of loss-of-function mutations in GPCRs, two mutations, G57S, R319W, in the endothelin B receptor, associated with Hirschsprung's disease, were identified as retaining  $G\alpha_q$  G protein subunit coupling, but defective  $G\alpha_i$  signalling, with G57S actually demonstrating coupling to  $G\alpha_s$ . A third mutation, P383L, showed significantly lower membrane expression versus the wild-type receptor (Fuchs et al., 2001). A deletion mutation that induces a frame-shift at position 247, subsequently introducing a premature stop codon at position 270, results in a V2 vasopressin receptor variant lacking the entire C-terminal third that is associated with congenital nephrogenic diabetes insipidus (Rosenthal et al., 1992). Surprisingly, variants of the melanocortin 4 receptor (MC4R), that exhibited gain-of-function in relation to  $\beta$ -arrestin signalling, were associated with significantly lower body mass index and protection against obesity, type 2 diabetes, and coronary artery disease (Lotta et al., 2019). These data show that mutations can be beneficial and provide evidence for targeting MC4R with  $\beta$ -arrestin biased therapeutics as an anti-obesity strategy.

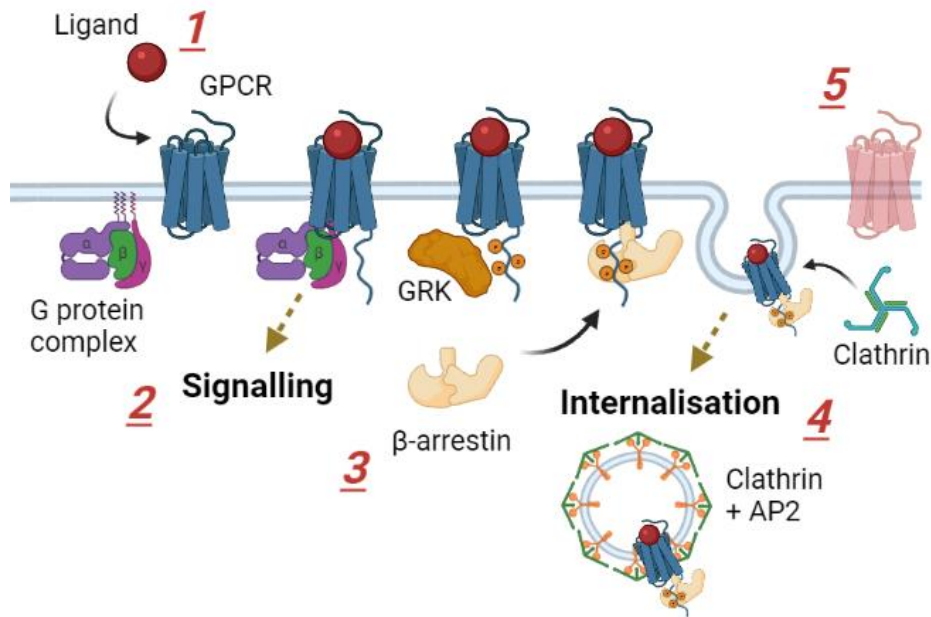


**Figure 4.1.** Schematic showing the points at which mutation can impact on GPCR signal transduction. **1** Binding of ligands to GPCRs requires specific protein sequences that can be mutated, either decreasing or increasing the affinity, efficacy, and kinetics of the ligand at the receptor. **2** G protein recruitment to the receptor, and subsequent signalling, requires precise conformational changes in the receptor that can be perturbed by mutation. Additionally, mutations can lock GPCRs in an active state, inducing signalling even in the absence of an external stimulus. **3** Receptor phosphorylation and recruitment of  $\beta$ -arrestin. Mutations can modify the sites in the GPCR that regulate phosphorylation by G protein-coupled receptor kinases (GRKs), which can in turn alter the efficiency of  $\beta$ -arrestin recruitment. Mutations may also directly impact on the association of  $\beta$ -arrestin with the receptor. **4** Whilst  $\beta$ -arrestin is important for signalling in its own right, the protein is canonically required in GPCR internalisation. Mutations that impact  $\beta$ -arrestin recruitment can, therefore, also alter the extent to which the GPCR is internalised and shuttled between the cell surface and endosomal compartments. **5** Another important facet to GPCR mutation is the impact of changes to the protein structure on the stability of the receptor at the membrane. Mutations can alter the signal peptide sequences of GPCRs, potentially impacting on delivery of the receptor to the cell surface; send the protein down degradational pathways; or induce misfolding. Schematic was designed using BioRender (<https://biorender.com/>).

As discussed in detail in Section 1.7, the apelin receptor has been explored in several mutational studies. Mutagenesis has previously been based on experimental findings, such as the S348 position in the C-terminus being identified as a site of receptor phosphorylation, and the artificial S348A substitution mutation subsequently confirming impaired recruitment of GRK, reducing receptor phosphorylation, recruitment of  $\beta$ -arrestin, and internalisation in response to apelin-13 (Chen et al., 2014). Additionally, systematic alanine scanning mutagenesis, identified I109A, in transmembrane domain III, as single point substitution that converts the receptor to a G protein biased conformation, that shows defective engagement with GRK and  $\beta$ -arrestin (Ban et al., 2018). The Ma et al., 2017 study, performed extensive systematic mutational analysis, and showed single point substitutions, C325L and C326M, removed palmitoylation sites, whilst T177N removed an N-glycosylation site. These, combined with V117A and W261K mutations, greatly improved the protein yield and stability. The authors then further demonstrated that D23A and K268A reduced binding affinity of [<sup>125</sup>I]-apelin-13, whilst Y35A, W85A, R168A, and Y271A completely abolished binding of the radioligand, and were non-functional in a cAMP assay (Ma et al., 2017).

In zebrafish, the naturally occurring grinch<sup>s608</sup> (W85L) mutation in *Aplnr*b, the zebrafish receptor homologous with mammalian apelin receptor, was shown to prevent binding of apelin, inducing a severe reduction in myocardial progenitor cells and cardiomyocytes, resulting in poor/absent cardiac development (Scott et al., 2007; Zeng et al., 2007). The mutation provided key evidence for the role of the apelin receptor in cardiac development. However, naturally occurring mutations in humans have been poorly identified, let alone characterised pharmacologically.

The NIHR BioResource Rare Diseases BRIDGE consortium sequencing project (herein referred to as the BRIDGE project), is a collaboration between 13 rare disease projects that aim to discover the genetic sequence variants underlying unresolved inherited disorders and to improve identification of already identified high penetrance variants, as a prospective component of the Genomics England 100,000 Genomes Project (Turnbull et al., 2018). The BRIDGE project covers a variety of rare disease research areas including cardiovascular, infection and immunity, and neuroscience.

As one example of its success, whole-genome sequencing of 1038 pulmonary arterial hypertension (PAH) index cases and 6385 PAH-negative control subjects, with subsequent case-control analysis, identified significant overrepresentation of rare variants in several proteins, revealing missing heritability of PAH not caused by variation in bone morphogenetic protein type 2 receptor (BMP2) (Gräf et al., 2018). In its association with the NIHR BioResource, the BRIDGE project is highly valuable to researchers for the capacity to provide phenotypic information for recruited participants, and the opportunity to recall participants for further assessment.

From the participants screened in the BRIDGE project, 50 apelin receptor variants were identified, that were associated with, but not necessarily causative of, rare cardiovascular and immune diseases. Pre-determined exclusion criteria were applied to select only those variants that were:

- Rare (displaying a frequency of < 1 in 10,000)
- Mutated at sites conserved across 29 vertebrate species
- Mutated at sites predicted to be deleterious using both SIFT (Sorting Intolerant From Tolerant, Sim et al., 2012) and PolyPhen-2 (Polymorphism Phenotyping v2, Adzhubei et al., 2010)
- Mutated at sites predicted to impact receptor binding and/or function when compared to corresponding sites in other, similar GPCRs using GPCRdb (<https://gpcrdb.org/>, Kooistra et al., 2021).

These criteria would select for variants that occur at amino acid sites that are highly evolutionarily conserved in the apelin receptor, and would thus likely impact on the pharmacology of the receptor if substituted or deleted.

The work in this thesis aimed to characterise 11 apelin receptor variants that were identified in participants in the BRIDGE project and selected for using the exclusion criteria outlined above, as part of the ORBIT (Opportunities in Receptor Biology for Industrial Translation) collaboration with Sosei Heptares. Following an initial screen using [<sup>125</sup>I]-apelin-13 radioligand binding, the V38L, T89M, and R168H apelin receptor variants were identified as particularly attractive for further assessment and pharmacological characterisation. High content imaging was used to assess

expression and membrane localisation of the apelin receptor variants, and additional binding studies were performed using the fluorescent ligands apelin647 and ELA647. Variants were also assessed for pharmacological function in a dynamic mass redistribution assay. Finally, the R168H variant was visualised in a clinically relevant human embryonic stem cell-derived cardiomyocyte (hESC-CM) model, using a base edited variant line, in conjunction with apelin647.

## **4.2. Methods**

### **4.2.1. Cell culture**

HEK293T, CHO-K1, and hESC cell culture was performed as described in Section 2.4. Additionally, genetic manipulation of HEK293T and CHO-K1 cells, from generation of wild-type and apelin receptor variant plasmid constructs, to transfection procedures, is outlined in Section 2.4.2 and Section 2.4.3. The generation of a differentiated hESC-CM (Section 2.4.5) cell line carrying the R168H apelin receptor variant using base editing is described in Section 2.4.7.

### **4.2.2. Radioligand binding assays**

HEK293T and CHO-K1 cell membrane preparations were made as described in Section 2.6.1, and used at a final concentration of 1 mg/mL (concentration determined using a DC Protein Assay from Bio-Rad, as described in Section 2.6.3).

Saturation binding (described in Section 2.7.2), to determine wild-type and variant apelin receptor affinity and density, was performed by incubating membrane preparations with a concentration range (2 pM – 1 nM) of [<sup>125</sup>I]-apelin-13 for 90 mins at room temperature. Non-specific binding was determined in the presence of 5 μM [Pyr<sup>1</sup>]apelin-13.

Competition binding (described in Section 2.7.3) was used to assess binding of a concentration range (1 pM – 1 μM) of ELA-14 against 0.1 nM [<sup>125</sup>I]-apelin-13 in wild-type or T89M variant apelin receptor expressed in HEK293T cell membrane preparations.

### **4.2.3. Assessment of apelin receptor expression, membrane localisation, and fluorescent ligand binding**

Wild-type and variant apelin receptor constructs transiently expressed in CHO-K1 cells were tagged at the C-terminus with eGFP. To assess expression and membrane localisation, cells were washed with HBSS, before fixation with 4 % formaldehyde for 5 mins. After another wash with HBSS, cells were treated with WGA-555 membrane marker (10 μg/mL) and Hoechst 33342 nuclear marker (10 μg/mL) in HBSS for 15

mins. After a final wash with HBSS, cells were maintained in HBSS before high content imaging. To assess binding of apelin647 and ELA647 fluorescent ligands, cells were washed with HBSS, before treatment with 300 nM apelin647 or ELA647 for 90 mins in the dark at room temperature. Non-specific binding was determined in the presence of 10  $\mu$ M [Pyr<sup>1</sup>]apelin-13. A full saturation curve was also performed for apelin647 in wild-type and variant apelin receptor by treating cells with a concentration range (1 – 300 nM) of the fluorescent ligand for 90 mins in the dark at room temperature. At the end-point, cells were fixed with 4 % formaldehyde for 5 mins. After another wash with HBSS, cells were treated with WGA-555 membrane marker (10  $\mu$ g/mL) and Hoechst 33342 nuclear marker (10  $\mu$ g/mL) in HBSS for 15 mins. After a final wash with HBSS, cells were maintained in HBSS before high content imaging. For internalisation experiments, CHO-K1 cells transiently expressing wild-type or V38L variant apelin receptor were treated with WGA-555 (10  $\mu$ g/mL) and Hoechst 33342 nuclear marker (10  $\mu$ g/mL) in HBSS for 15 mins, before a wash and subsequent treatment with 300 nM apelin647 for 5 mins. After a final wash with HBSS, cells were imaged in near real-time at 37 °C and 5 % CO<sub>2</sub>. Apelin647 binding was also assessed in the R168H apelin receptor variant hESC-CM line. Differentiated cardiomyocytes, plated in CellCarrier-96 Ultra Plates (PerkinElmer) at a density of 80 k/well, were washed with HBSS, before treatment with 300 nM apelin647 for 90 mins in the dark at room temperature. At the end-point, cells were fixed with 4 % formaldehyde for 5 mins. After another wash with HBSS, cells were treated with Hoechst 33342 nuclear marker (10  $\mu$ g/mL) in HBSS for 15 mins. After a final wash with HBSS, cells were maintained in HBSS before high content imaging.

#### **4.2.4. Opera Phenix High Content Screening**

CHO-K1 cells transfected with wild-type or variant apelin receptor, and treated as described in Section 4.2.3, were imaged using the Opera Phenix (described in Section 2.9.2).

#### **4.2.5. In vitro GPCR assay**

Wild-type and variant apelin receptor function was assessed in a dynamic mass redistribution assay (described in Section 2.8.1), measuring cellular responses to a

concentration range (0.1 nM – 300 nM) of [Pyr<sup>1</sup>]apelin-13 in transiently transfected CHO-K1 cells. Buffer treated wells showed no response.

#### **4.2.6. Data analysis and statistics**

Quantitative data are expressed as mean  $\pm$  SD. Raw data were handled using Microsoft Excel for Windows (Microsoft). Graphical presentation and statistical tests were performed using GraphPad Prism version 6.07 for Windows (GraphPad Software). For saturation radioligand binding experiments, data were analysed using the EBDA and LIGAND components of the KELL (Kinetic, EBDA, Ligand, Lowry) software package (Biosoft) (described in Section 2.7.4). For competition binding experiments,  $K_i$  values were determined using Cheng-Prusoff methodology (described in Section 2.7.3). For *in vitro* GPCR assays,  $EC_{50}$ ,  $pD_2$ , and  $E_{max}$  values were calculated using GraphPad Prism version 6.07 for Windows. Statistical tests are indicated in figure legends where used. A p value of  $< 0.05$  was determined as significant.

### **4.3. Results**

#### **4.3.1. Several apelin receptor variants identified in the BRIDGE project show perturbed binding in a preliminary screen**

Following selection of 11 apelin receptor variants using the exclusion criteria outlined in section 4.1, [<sup>125</sup>I]-apelin-13 radioligand binding was performed by Ms Rhoda E. Kuc in a preliminary screen using HEK293T cell membrane preparations. Table 4.1 shows that wild-type (WT) apelin receptor exhibited a  $K_D$  of  $2.14 \pm 0.36$  nM for the radioligand and a receptor density ( $B_{max}$ ) of  $813 \pm 133$  fmol/mg of protein. A Hill slope of  $1.03 \pm 0.04$  indicates a one site binding mode. Over the study, 3 of the 11 variants were deemed to be of particular interest – V38L, T89M, and R168H – and will be the focus of this chapter. V38L exhibited a  $K_D$  of  $2.35 \pm 0.85$  nM, similar to WT, but a  $B_{max}$  of  $175 \pm 91$  fmol/mg, significantly lower than WT. This might suggest an effect of the V38L single point substitution on receptor expression or stability at the membrane. T89M also bound the radioligand, with a  $K_D$  of  $5.63 \pm 4.00$  nM, and had a high  $B_{max}$  of  $4920 \pm 3520$  fmol/mg, but also showed high error around the mean. R168H showed no detectable binding of [<sup>125</sup>I]-apelin-13, indicating a potentially substantial effect of this

single point substitution on ligand interaction. Note, G45X and T227X, that also showed no detectable binding, are single amino acid deletions inducing frame-shift of the protein sequence that will likely highly alter apelin receptor expression and/or pharmacology.

Condition	K <sub>D</sub> (nM)	B <sub>max</sub> (fmol/mg)	Hill slope ( <i>nH</i> )
Untrans.	NBD	NBD	NBD
WT	2.14 $\pm$ 0.36	813 $\pm$ 133	1.03 $\pm$ 0.04
V38L	2.35 $\pm$ 0.85	175 $\pm$ 91*	1.03 $\pm$ 0.02
G45X	NBD	NBD	NBD
D65V	1.64 $\pm$ 0.56	445 $\pm$ 106	1.06 $\pm$ 0.05
V79M	5.33 $\pm$ 3.20	1630 $\pm$ 325	1.08 $\pm$ 0.07
T89M	5.63 $\pm$ 4.00	4920 $\pm$ 3520	1.15 $\pm$ 0.07
R127H	1.61 $\pm$ 0.35	562 $\pm$ 250	0.99 $\pm$ 0.06
R139W	1.37 $\pm$ 0.76	64.3 $\pm$ 19.4**	0.95 $\pm$ 0.03
R168H	NBD	NBD	NBD
T227X	NBD	NBD	NBD
R243W	3.57 $\pm$ 1.93	1340 $\pm$ 775	1.04 $\pm$ 0.04
T269M	3.48 $\pm$ 1.81	1370 $\pm$ 351	1.02 $\pm$ 0.03

**Table 4.1.** Saturation radioligand binding preliminary screen performed by Ms Rhoda Kuc. HEK293T cell membranes artificially expressing wild-type (WT) apelin receptor, the variants identified in patients in the BRIDGE project, or left untransfected (Untrans.) were assessed for binding of [<sup>125</sup>I]-apelin-13 in a preliminary screen. Table shows effects of amino acid substitutions and deletions on receptor affinity (K<sub>D</sub>) and receptor density (B<sub>max</sub>). The Hill slope (*nH*) was approximately 1 in all instances where binding was detected, suggesting a one site binding mode. NBD = no binding detected. Statistically significant differences versus WT were determined using an unpaired Student's T test. \* = p < 0.05, \*\* = p < 0.01. Experiments performed by Ms Rhoda Kuc

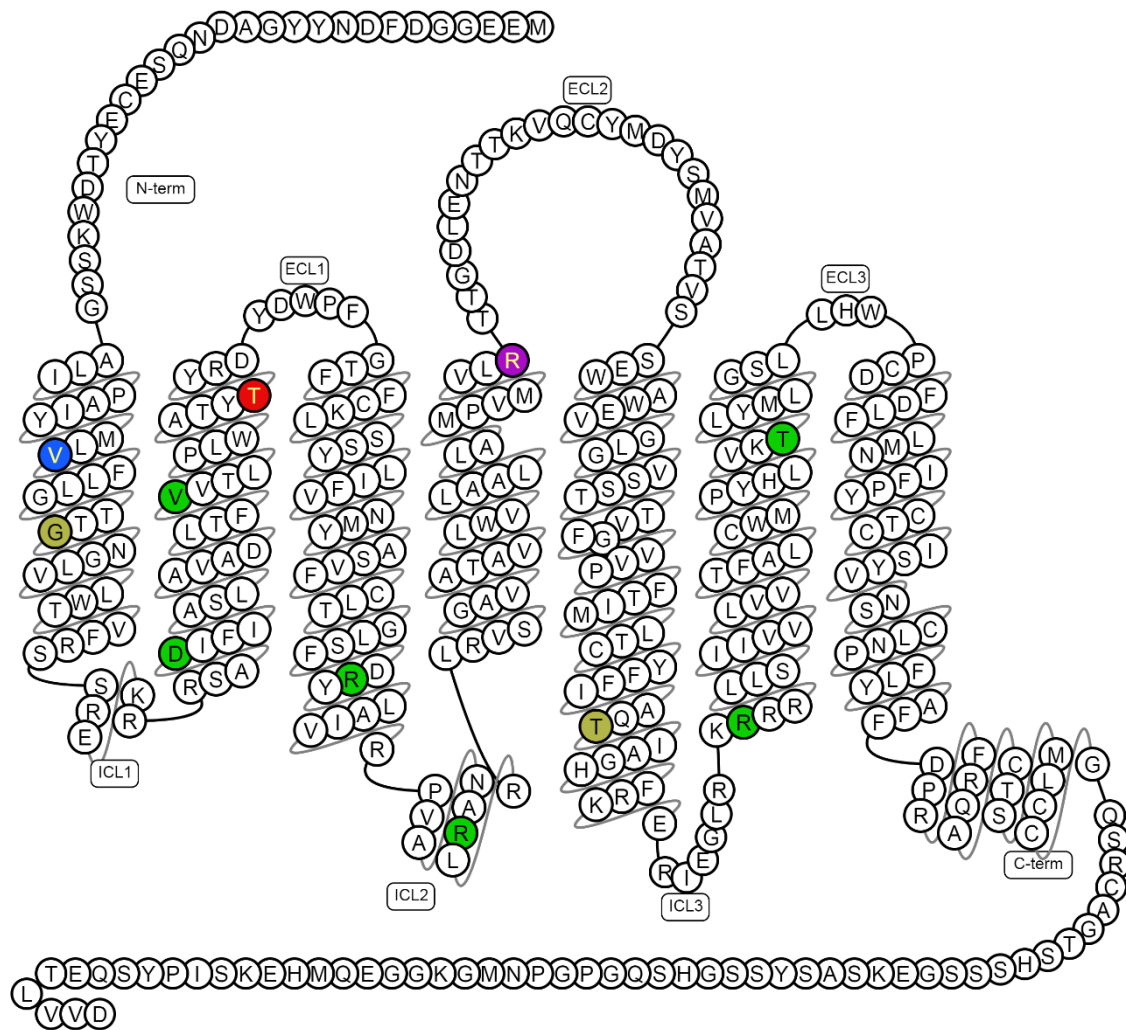


**Figure 4.2.** Snake plot showing the 380 amino acid apelin receptor with the single-point substitutions and deletions identified in the BRIDGE project highlighted in colour. Amino acids of particular interest are V38 (blue, substituted with L), T89 (red, substituted with M), and R168 (purple, substituted with H). All other single-point substitutions are shown in green, and deletions are shown in gold. Figure was generated using GPCRdb (<https://gpcrdb.org/>, Kooistra et al., 2021).

For clarity, Figure 4.2 shows a snake plot of the apelin receptor indicating the positions of the amino acid changes identified in the BRIDGE project. Variants of particular interest, V38L (blue), T89M (red), and R168H (purple), occur in transmembrane helices I, II, and IV respectively. Intriguingly, T89 and R168 have been shown

previously to make up part of the apelin receptor binding pocket, where R168 forms a critical ionic interaction with the G protein biased small molecule agonist CMF-019 (Read et al., 2016).

#### **4.3.2. Apelin receptor variants can impact receptor expression at the membrane**

Following the preliminary binding screen, it was crucial to establish whether differences in binding for apelin receptor variants versus wild-type were due to direct effects on the binding site itself, or receptor expression at the cell surface.

Data in Figure 4.3 show the artificial expression of wild-type apelin receptor and variants in CHO-K1 cells, co-stained with a wheat germ agglutinin membrane marker conjugated to Alexa Fluor 555 (WGA-555). Qualitative assessment (Fig 4.3a) confirmed cellular expression of wild-type receptor, and the V38L, T89M, and R168H variants, determined via visualisation of the C-terminal eGFP reporter. Untransfected cells (treated with transfection reagent in the absence of DNA) showed no eGFP expression.

Visually, it is very difficult to accurately assess expression of the receptor at the membrane specifically. However, quantification (Fig 4.3b) demonstrated that, when looking at only those cells that are eGFP positive, wild-type receptor exhibited a relative membrane expression (i.e. eGFP signal that occurred in the membrane segment determined by WGA-555, normalised to that signal observed in untransfected control cells) of  $1.63 \pm 0.28$ . Relative membrane expression for the V38L variant,  $1.11 \pm 0.11$ , was significantly lower than wild-type ( $p < 0.001$ ), and was not significantly higher than untransfected cells, providing evidence that V38L may reduce membrane localisation of the apelin receptor. T89M exhibited a relative membrane expression of  $1.65 \pm 0.34$ , which was not significantly different to wild-type, suggesting that this variant does not impact receptor expression at the membrane in this platform. Crucially, R168H also showed a relative membrane expression of  $1.71 \pm 0.30$  that was not significantly different to wild-type. This provides evidence that loss of detectable binding observed in the preliminary screen is not due to reduced receptor density or membrane localisation, but is likely a perturbation of the ability of the receptor to interact with the radioligand.

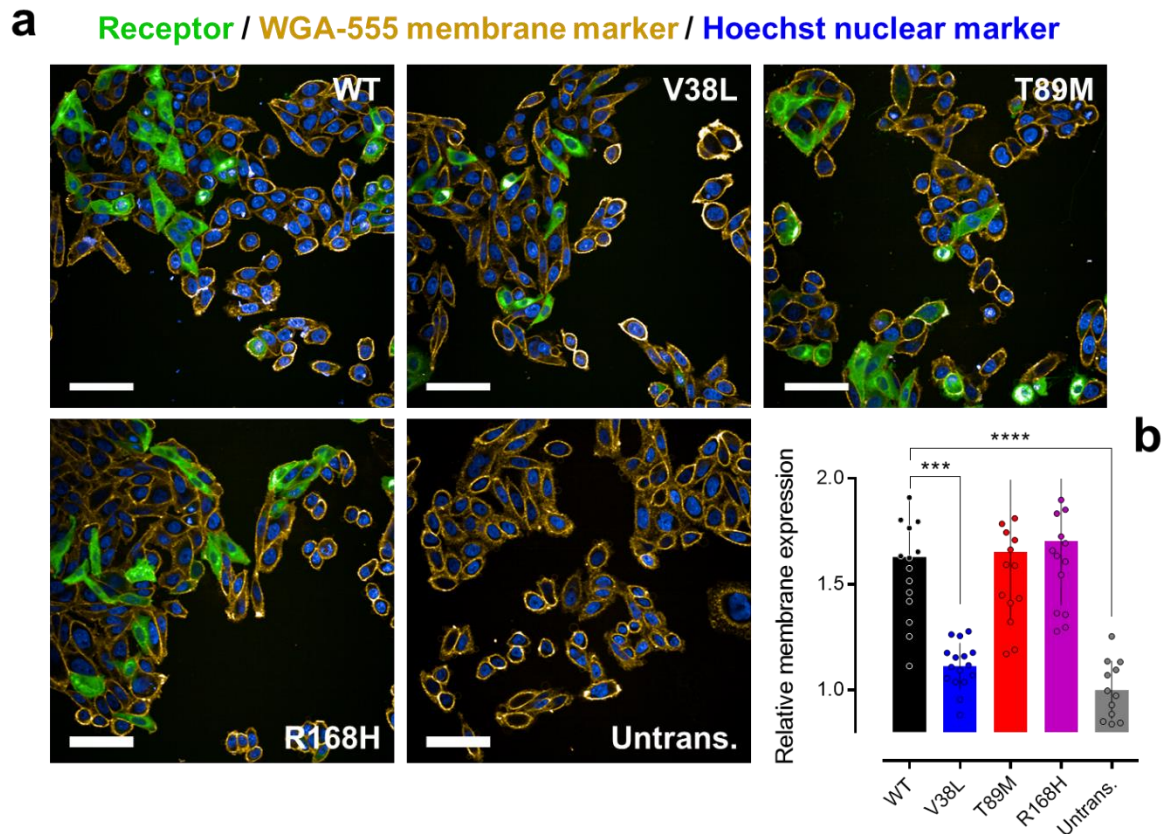


**Figure 4.3.** High content assessment of apelin receptor variant expression. **a** Representative confocal fluorescent images of CHO-K1 transiently expressing wild-type (WT) apelin receptor, or the V38L, T89M, or R168H variant, or untransfected (Untrans.). Images show the receptor tagged at the C-terminus with eGFP in green, cell membranes stained with WGA-555 marker in gold, and nuclei stained with Hoechst nuclear marker in blue. Scale bars show 50  $\mu\text{m}$ .  $n = 4$  independent experiments performed in at least triplicate. **b** Quantified high content data showing relative membrane expression of eGFP tagged receptor in eGFP positive cells normalised to signal observed in untransfected cells. Data pooled from  $n = 4$  independent experiments performed in at least triplicate. Statistical significance was determined using a Kruskal-Wallis test on non-normal data, with Dunn's correction for multiple comparisons looking for differences between (WT) apelin receptor and receptor variants or untransfected cells. \*\*\* =  $p < 0.001$ , \*\*\*\* =  $p < 0.0001$ . Cells were transfected with DNA provided by Dr Heather Currinn.

### **4.3.3. Fluorescent ligands identify further effects of apelin receptor variants on binding**

To further characterise apelin receptor variant ligand binding, fluorescent apelin647 and ELA647, were used in high content imaging studies looking at CHO-K1 cells transfected with receptor constructs. Imaging (Fig 4.4a) demonstrated good binding of both ligands to wild-type apelin receptor following incubation for 90 mins. Of note, V38L was also able to bind both ligands, despite showing low receptor density in Table 4.1 and low receptor membrane expression in Fig 4.3. Surprisingly, T89M appeared to be able to bind the apelin647 ligand to a similar extent as the wild-type receptor, but showed little to no binding of the ELA647 ligand. R168H showed little to no binding with either ligand. Controls (Fig 4.4b) confirmed that binding of apelin647 and ELA647 to wild-type apelin receptor was specific, determined by inclusion of 10  $\mu$ M [Pyr<sup>1</sup>]apelin-13 during the 90 mins incubation.

Quantification shows total mean fluorescence (background subtracted) calculated for the apelin647 (Fig 4.4c) and ELA647 (Fig 4.4d) ligands in the transfected CHO-K1 cells. In eGFP positive cells, wild-type receptor bound apelin647 with a mean fluorescence of  $141.71 \pm 8.85$ . Both V38L and T89M bound apelin647 to a similar extent (mean fluorescence of  $137.18 \pm 10.03$  and  $125.45 \pm 2.69$ ), matching the qualitative assessment in Fig 4.4a. Crucially, the quantitative data also confirmed a lack of binding of apelin647 in R168H, where a mean fluorescence of  $3.56 \pm 0.69$  was significantly lower than wild-type ( $p < 0.0001$ ) but no different from the NSB control. Results demonstrated that mean fluorescence of ELA647 was lower in general ( $36.88 \pm 6.22$  in wild-type), likely due to the lower affinity of this ligand as shown in Section 3.3.2 and 3.3.3, and/or inter-batch variation in the quantum yield of the fluorescent dye itself (a phenomenon that the manufacturer, Cambridge Research Biochemicals, confirmed as being possible). As with apelin647, V38L bound ELA647 ( $46.82 \pm 3.23$ ) in a manner similar to wild-type. However, T89M bound ELA647 ( $17.06 \pm 3.22$ ) to a significantly lower extent than wild-type ( $p < 0.01$ ), but fluorescence was significantly higher than in NSB controls ( $p < 0.05$ ). R168H mean fluorescence for ELA647 ( $10.81 \pm 7.14$ ) was significantly lower than wild-type, but no different to NSB controls, suggesting a complete loss of binding for the ELA-based ligand as well.

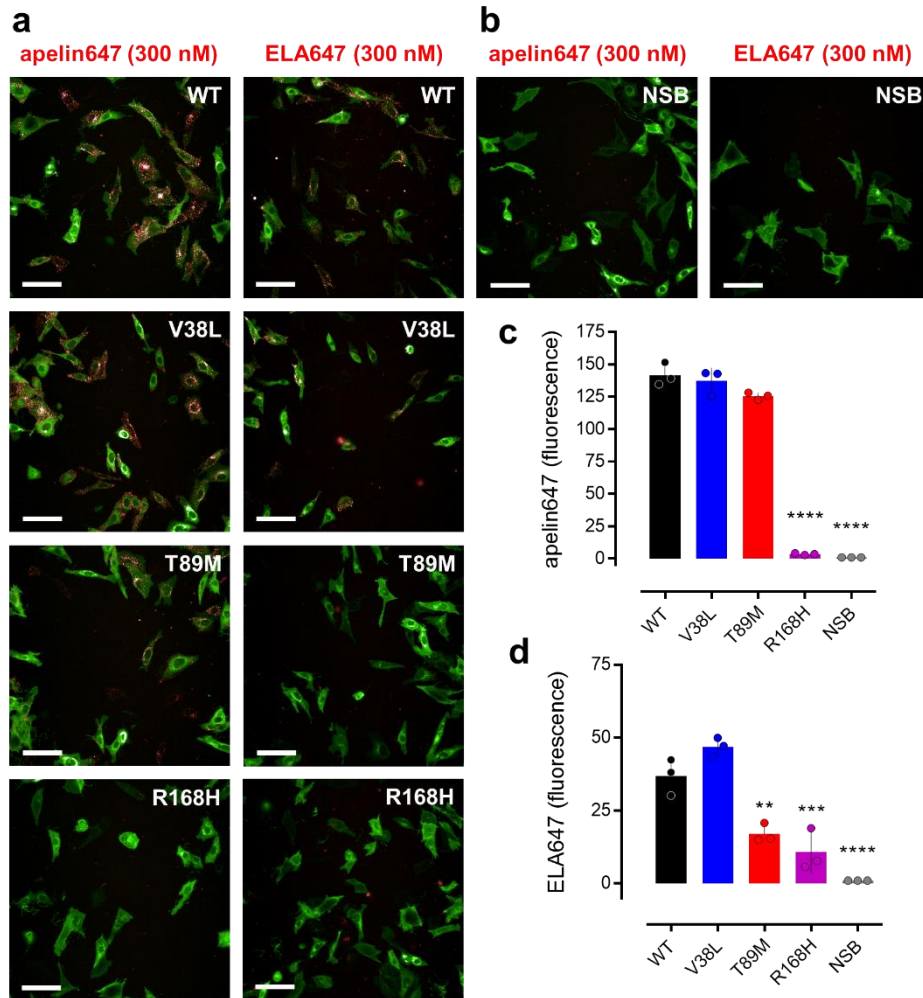


**Figure 4.4.** Representative high content confocal fluorescent images showing fluorescent ligand binding (shown in red) at apelin receptor variants tagged at the C-terminus with eGFP (shown in green). **a** CHO-K1 cells expressing wild-type (WT) apelin receptor or variants (V38L, T89M, or R168H) treated with 300 nM apelin647 (left column) or ELA647 (right column) for 90 mins. **b** CHO-K1 cells expressing wild-type apelin receptor treated with 300 nM apelin647 (left column) or ELA647 (right column) for 90 mins in the presence of 10  $\mu$ M [Pyr<sup>1</sup>]apelin-13 to determine non-specific binding (NSB). Graphical data shows quantification of apelin647 (**c**) or ELA647 (**d**) mean fluorescence in eGFP positive cells. Statistical significance was determined using a one way ANOVA, with Tukey's correction for multiple comparisons looking for differences between (WT) apelin receptor and receptor variants or NSB treated cells. \*\* =  $p < 0.01$ , \*\*\* =  $p < 0.001$ , \*\*\*\* =  $p < 0.0001$ .  $n = 1$  independent experiment performed in triplicate. Cells were transfected with DNA provided by Dr Heather Currinn.

Full saturation binding curves were generated using high content quantification for wild-type apelin receptor and variants treated with a concentration range (1 – 300 nM) of apelin647 (Fig 4.5). Wild-type receptor showed good, saturable binding, with a  $K_D$  value of  $54.97 \pm 20.48$  nM determined. Surprisingly, V38L also showed saturable binding, but with a lower  $K_D$  value of  $15.80 \pm 3.96$  nM determined versus wild-type. T89M binding may not have saturated at the highest concentration tested, and the  $K_D$  value of  $163.7 \pm 10.73$  nM was higher than that observed for wild-type. Note that mean fluorescence of apelin647 at 300 nM was lower in general here than in Fig 4.4c, which may be due to the fact that a different batch of the fluorescent ligand was used between experiments, and inter-batch variation in quantum yield may have occurred. Finally, though, R168H was unable to bind apelin647 in a saturable manner, and no  $K_D$  value was determined, falling in line with the previous results, and its reported role in the receptor binding pocket (Read et al., 2016).

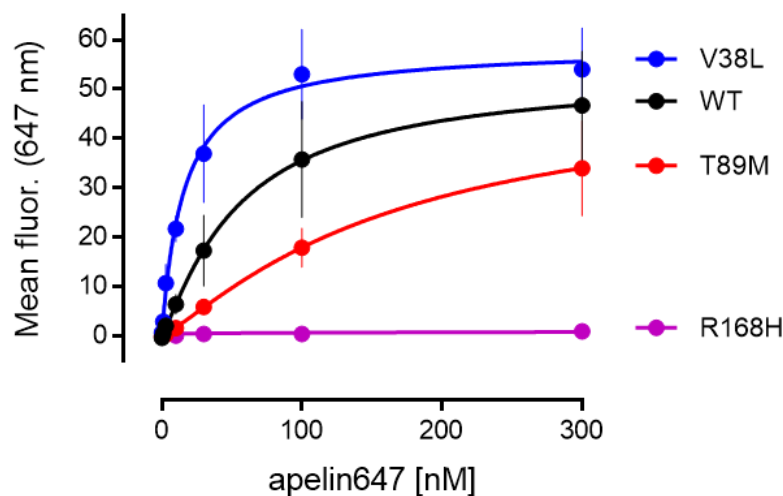


**Figure 4.5.** Saturation binding in high content imaging. Quantification of mean whole cell fluorescence (emitted light at wavelength of 647 nm, background corrected) in CHO-K1 cells transiently expressing wild-type (WT, black) apelin receptor or apelin receptor variants V38L (blue), T89M (red), or R168H (purple) and treated with a concentration range (1 – 300 nM) of apelin647.  $n = 2$  independent experiments performed in duplicate. Cells were transfected with DNA provided by Dr Heather Currinn.

#### **4.3.4. Further binding studies confirm the impact of the T89M variant on binding of ELA ligands**

Following the findings in high content imaging studies that the T89M variant bound ELA647 to a significantly lesser extent than wild-type, saturation radioligand binding was revisited along with competition binding, to confirm the effect of T89M on the ability of the apelin receptor to bind ELA based ligands. Additionally, further radioligand binding data would add weight to the results garnered in the preliminary screen.

Saturation binding with [<sup>125</sup>I]-apelin-13 was performed in HEK293T cell membrane preparations previously transfected with wild-type apelin receptor or variant constructs (Fig 4.6a). Saturable binding at wild-type receptor provided a  $K_D$  value of  $0.40 \pm 0.07$  nM, indicating high binding affinity, with a  $B_{max}$  value of  $263.7 \pm 37.7$  fmol/mg. A binding curve for V38L was able to be determined, where binding of the radioligand occurred with very high affinity ( $K_D$  value of  $0.13 \pm 0.02$  nM) despite a very low receptor density ( $B_{max}$  value of 23.5 fmol/mg). The T89M variant bound with an affinity ( $K_D$  value of  $0.48 \pm 0.11$  nM) similar to wild-type, but the receptor density was higher ( $B_{max}$  of 405.5 fmol/mg). R168H showed no detectable binding. The data closely matched the trends seen in the preliminary screen for the V38L, T89M, and R168H variants (see Table 4.1).

In competition binding (Fig 4.6b), 0.1 nM [<sup>125</sup>I]-apelin-13 was displaced by ELA-11 with a  $pK_i$  value of  $7.80 \pm 0.07$  at wild-type apelin receptor. However, for the T89M variant, a  $pK_i$  value of  $6.36 \pm 0.06$  was determined for ELA-11, indicating an approximate 28-fold increase in the concentration of ELA-11 required to displace the radioligand versus the wild-type. The data suggest that, whilst T89 has been shown to reside in the apelin receptor binding pocket (Read et al., 2016), this site may have more influence over the binding of the alternate ligand, ELA, compared to apelin, given that substitution to methionine has consistently perturbed binding of ELA peptides in two different platforms.

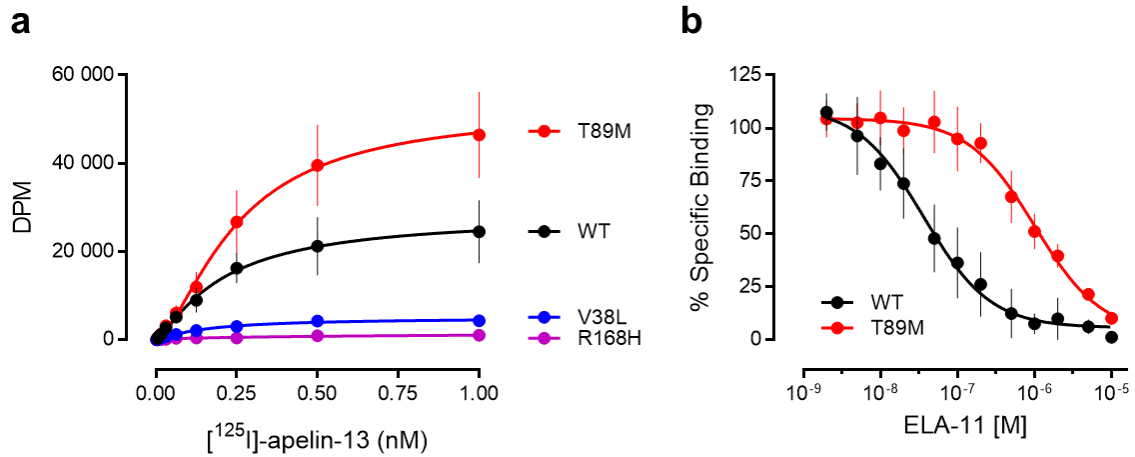


**Figure 4.6.**  $[^{125}\text{I}]$ -apelin-13 radioligand binding in apelin receptor variants. **a** Saturation radioligand binding in HEK293T cells transfected with wild-type (WT) apelin receptor (black), the V38L variant (blue), T89M variant (red), or the R168H variant (purple). Data show specific binding (total binding minus non-specific binding determined in the presence of 5  $\mu\text{M}$   $[\text{Pyr}^1]$ apelin-13), expressed as mean  $\pm$  SD.  $n = 3$  independent experiments performed in at least duplicate. **b** Competition binding of ELA-11 peptide against  $[^{125}\text{I}]$ -apelin-13 (0.1 nM) in HEK293T cells transfected with wild-type (WT) apelin receptor (black) or the T89M variant (red). Data show % specific binding (% of total binding in the absence of ELA-11 minus non-specific binding determined in the presence of 5  $\mu\text{M}$   $[\text{Pyr}^1]$ apelin-13), expressed as mean  $\pm$  SD.  $n = 3$  independent experiments performed in triplicate. Cells were transfected with DNA provided by Dr Heather Currinn.

#### 4.3.5. Assessment of apelin receptor variants on GPCR function

Concomitant with binding studies, it was critical to assess the functional effects of amino acid substitution on apelin receptor pharmacology. A dynamic mass redistribution assay (Fig 4.7) was used to assess cellular responses to a concentration range covering 0.1 nM – 300 nM of [Pyr<sup>1</sup>]apelin-13, in CHO-K1 cells. Wild-type apelin receptor, as well as the V38L and T89M variants, were active in this assay displaying similar E<sub>max</sub> values of 39.48 ± 3.93, 42.55 ± 15.16, and 50.06 ± 8.32 ΔPWV from baseline. However, the receptor variants were slightly less potent (approximately 4-fold lower), with pD<sub>2</sub> values of 7.67 ± 0.48 and 7.71 ± 0.21, versus wild-type (pD<sub>2</sub> value of 8.32 ± 0.24). Crucially, the R168H variant appeared non-functional in response to [Pyr<sup>1</sup>]apelin-13, giving an E<sub>max</sub> value of 5.49 ± 6.42. Untransfected control cells gave an E<sub>max</sub> value of 0.21 ± 7.07.

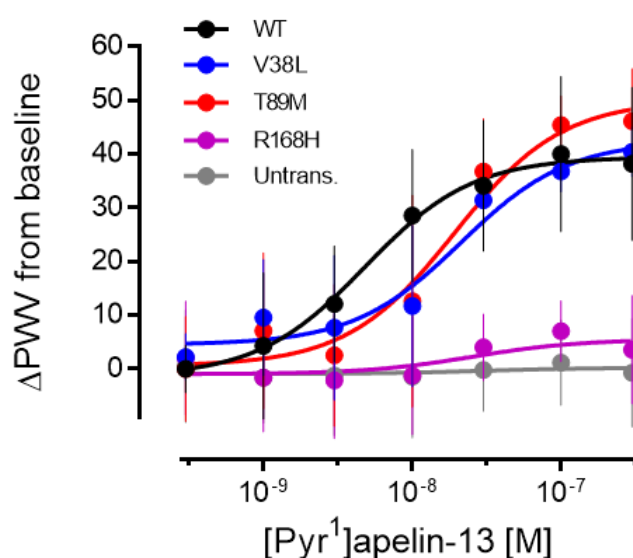


**Figure 4.7.** Dynamic mass redistribution GPCR functional assay response (shown as the change in peak wavelength value, ΔPWV, from baseline) of wild-type (WT, black) apelin receptor versus the variants V38L (blue), T89M (red), or R168H (purple) following stimulation with [Pyr<sup>1</sup>]apelin-13. Untransfected cell response shown in grey. n = 4 (WT) or 3 (variants) independent experiments performed in duplicate. Data show mean ± SD. Cells were transfected with DNA provided by Dr Heather Currinn.

Next, internalisation of apelin647 was visualised in near real-time. CHO-K1 cells expressing either wild-type (Fig 4.8a) apelin receptor or the V38L variant (Fig 4.8b) were treated with 300 nM apelin647 for 5 mins before a rapid wash and subsequent high content imaging. Cells were then imaged from the start point (T5, 5 mins) to the end point (T90, 90 mins) every 30 secs.

Qualitative observation of cells demonstrated good binding of apelin647 at wild-type apelin receptor at the start of imaging (T5), with punctate fluorescence observed at the whole cell level, and, to a large extent, at the membrane. By the end-point (T90) however, much of the apelin647 fluorescence moved into the intracellular compartment, with considerable loss from the membrane. This phenomenon is particularly clear when focussing on the video compilation (See Fig 4.8 associated video file) that shows distinct puncta accumulating at the membrane before moving intracellularly. Despite the low receptor density for the V38L variant identified in radioligand binding (Table 4.1 and Fig 4.6a), and low membrane expression in high content images (Fig 4.3), the variant was able to bind apelin647 at the membrane, consistent with data in Fig 4.4 and Fig 4.5). Interestingly, intense apelin647 fluorescence at the membrane at T5 appears not to be lost to the same extent as was observed for wild-type. In the associated video file, distinct puncta can again be seen accumulating at the membrane and moving intracellularly, but a noticeable portion of the fluorescence remains at the membrane at T90 for the V38L variant when compared to wild-type receptor. In the snapshots, the outline of cells can still be seen when looking only at the apelin647 fluorescence for the V38L variant (Fig 4.8b), but this is much less clear for the wild-type (Fig 4.8a). The data provide evidence that V38L may impact apelin receptor internalisation, although considerable further work needs to be performed to confirm this.

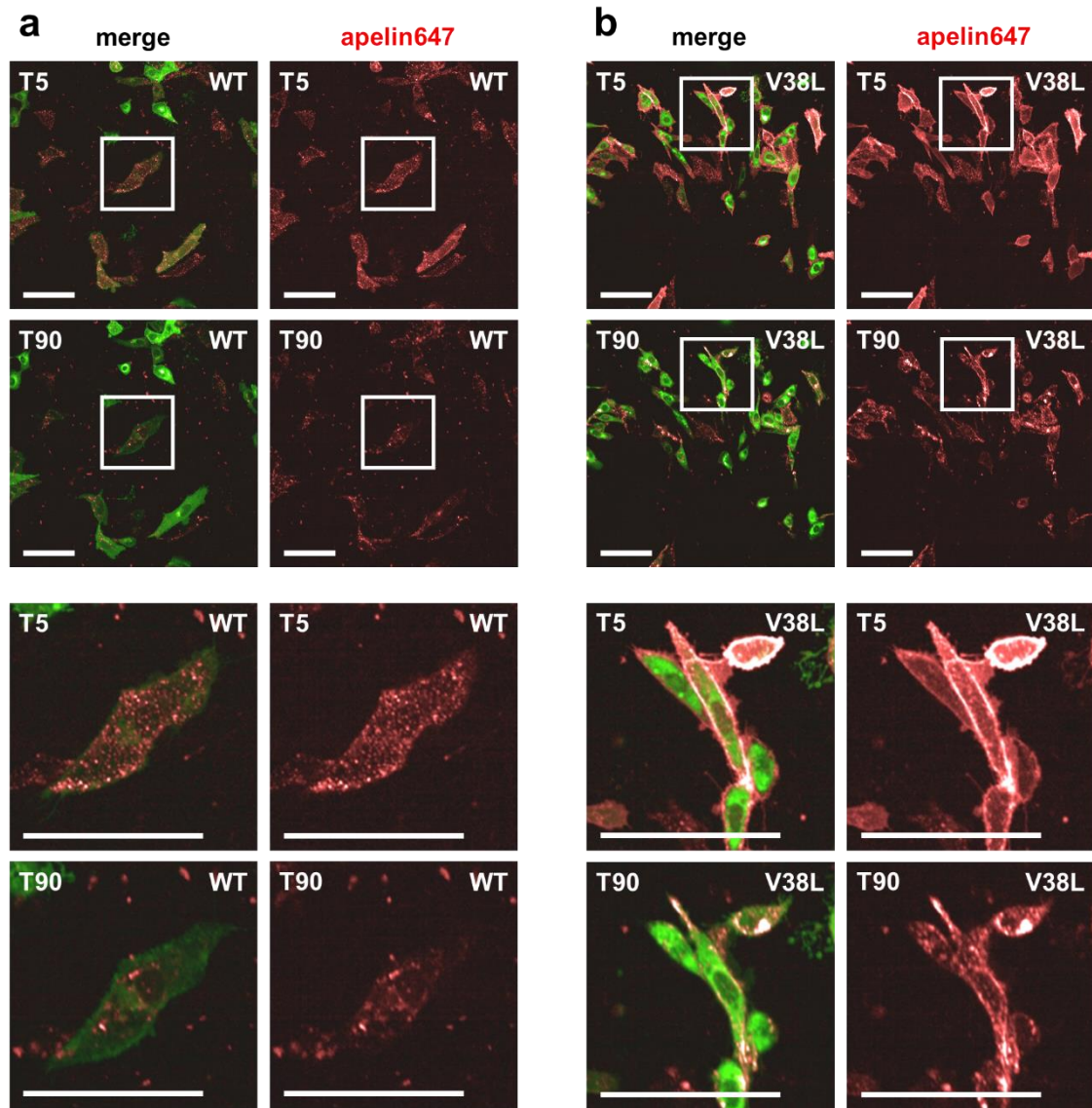


**Figure 4.8.** Representative high content confocal fluorescent video snapshots showing apelin647 binding and internalisation over a 90 mins time-course. **a** (Upper) CHO-K1 cells transfected with wild-type (WT) apelin receptor (green) and treated with apelin647 (300 nM, red) at T0 and T90 mins. (Lower) Cells in white box shown at increased zoom. **b** (Upper) CHO-K1 cells transfected with the V38L apelin receptor variant (green) and treated with apelin647 (300 nM, red) at T0 and T90 mins. (Lower) Cells in white box shown at increased zoom. In all instances, left column (merge) shows receptor and apelin647 together, right column shows apelin647 in isolation. Scale bars show 50 μm. See corresponding attached video files for footage of the 90 mins time-course (images captured every 30 seconds) for WT and V38L receptor. Cells were transfected with DNA provided by Dr Heather Currinn.

#### ***4.3.6. R168H is unable to bind apelin647 in a clinically relevant cardiomyocyte model***

The apelin647 fluorescent ligand was used to look for binding in a human embryonic stem cell (hESC) line incorporating an heterozygous R168H apelin receptor variant generated using cytosine base editing CRISPR/Cas9 technology as described in Section 4.2.4. After differentiation of the hESCs to cardiomyocytes, the binding of apelin647 to wild-type cells naturally expressing apelin receptor (Fig 4.9) was not observed in the R168H variant line. The data indicate, for the first time, loss of binding at the R168H variant in a clinically relevant cell model.

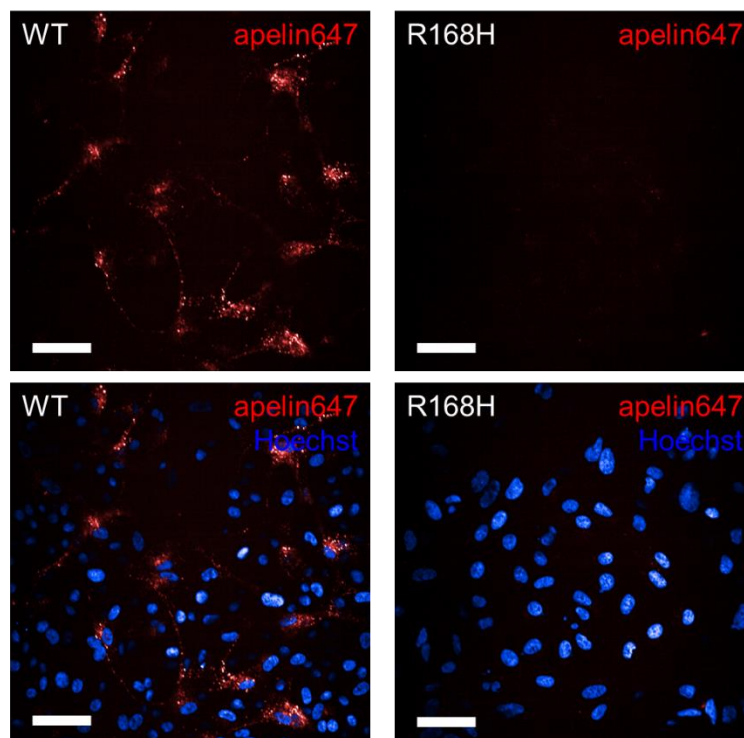


**Figure 4.9.** Representative high content confocal fluorescent images of human embryonic stem cell-derived cardiomyocytes – either wild-type (WT, left column) or an R168H variant line (right column) – treated with 300 nM apelin647 (red) for 90 mins. Bottom row shows merged images with Hoechst nuclear marker (blue) included. Scale bars show 50  $\mu$ m. n = 4 independent experiments performed in triplicate. Cardiomyocytes were cultured by Ms Robyn Macrae.

## **4.4. Discussion**

### ***4.4.1. Apelin receptor variants identified in the BRIDGE project impact on ligand binding, receptor density, and receptor expression***

The selected 11 apelin receptor variants, identified in human participants in the BRIDGE project, were assessed for [<sup>125</sup>I]-apelin-13 radioligand binding in a preliminary screen (Table 4.1), and several showed changes in receptor affinity and density. Compared to wild-type, V38L showed a similar  $K_D$  value but also demonstrated a significantly lower receptor density ( $B_{max}$ ) in the HEK293T membrane preparations. G45X and T227X are single amino acid deletions that result in frame-shift of the entire receptor after the site, and consequently, are expected to have pronounced impact on receptor expression and function. No binding was detected at these variants. Although T89 is reported to make up part of the apelin receptor binding pocket (Read et al., 2016), the T89M substitution showed a similar  $K_D$  value for the radioligand as the wild-type, and  $B_{max}$  was not significantly different either, although a trend for higher receptor density was observed. R168H was a critical variant in this project. Also forming part of the binding pocket, previous reports show a critical ionic interaction between the R168 site and the G protein biased small molecule agonist CMF-019 (Read et al., 2016). Additionally, mutational studies in the apelin receptor show that alanine mutation at this site (R168A), results in loss of radioligand binding, and function in a cAMP assay (Ma et al., 2017). Here, the naturally occurring R168H substitution results in a variant that also abolishes [<sup>125</sup>I]-apelin-13 binding. Note that the V38L and T89M mutations were identified in a subset of patients presenting with primary immune disease (PID), whilst the R168H mutation was identified in an individual in the bleeding and platelet disorder (BPD) branch of the NIHR BRIDGE project. It is unknown what disease phenotype exactly these patients exhibited, nor is it known if the apelin receptor mutations they possess are causative of the disease states. Regarding the R168H mutation, it is important to consider that the apelin receptor is highly implicated in bleeding and platelet disorders with anti-thrombotic effects observed in two independent studies (see Section 1.3.4.).

Whilst radioligand binding is a very useful technique for characterising several parameters of receptor binding (Maguire et al., 2012), in mutational studies where

binding is lost, it cannot definitively define whether changes in binding are due to changes to the binding pocket directly, or due to loss of receptor expression or membrane localisation. High content imaging was used to delineate the mechanisms for reduced or abolished binding in the apelin receptor variants. Data in Fig 4.3 show that wild-type apelin receptor artificially expressed in CHO-K1 cells is expressed at the membrane. The V38L variant signal at the membrane was significantly lower, matching findings in the preliminary binding screen where reduced  $B_{max}$  was observed. The T89M variant showed membrane localisation that was no different to the wild-type receptor. Critically, R168H also shows membrane localisation comparable to wild-type, suggesting that the abolished binding observed in the preliminary screen was due to a direct impact on ligand binding, and not expression of the variant receptor at the cell surface.

#### ***4.4.2. Discrepancies in apelin and ELA binding at the T89M apelin receptor variant***

Following successful visualisation of apelin receptor variants tagged with eGFP in the high content imaging, fluorescent apelin647 and ELA647 were used to further assess ligand interactions in CHO-K1 cells (Fig 4.4). Wild-type apelin receptor was able to bind apelin647 well, showing high fluorescent signal in cells transfected with the protein. ELA647 binding was also detected, but signal was considerably lower – this is likely due to differences in the affinities of the fluorescent ligands (validated in Section 3.3.2), and in the brightness of the fluorescent dye itself. The V38L variant showed binding of both fluorescent ligands that was comparable to the wild-type receptor. Intriguingly, the T89M variant was able to bind apelin647 to a similar extent as the wild-type receptor, but ELA647 fluorescence was significantly lower. This provides evidence that the T89 site, forming part of the apelin receptor binding pocket (Read et al., 2016), may have different roles in mediating binding of the endogenous peptide ligands, with the T89M substitution significantly perturbing binding of an ELA-based ligand but not an apelin-based ligand. It is interesting to note that ELA peptides show little sequence similarity with apelin peptides (Yang et al., 2015), and a recent report has extensively explored distinctions in the downstream effects of ELA versus apelin isoforms (Jiang et al., 2021). Finally, another report has shown that apelin and ELA bind differently to the human apelin receptor, and that an artificial D284 mutation

reduced apelin binding and function, but had little impact on ELA (Couvineau et al., 2020). In accordance with radioligand binding, the R168H variant did not bind apelin647 or ELA647.

Saturation binding with a concentration range (1 – 300 nM) of apelin647 (Fig 4.5) was also performed. In contrast to the preliminary radioligand binding screen, a full curve for V38L was observed, that reached a plateau similar to wild-type and showed a  $K_D$  value nearly 3.5-fold lower than wild-type. The T89M variant exhibited a  $K_D$  value nearly 3-fold higher than wild-type in this experiment. The R168H variant however, showed no binding, which was consistent with all previous findings.

Saturation radioligand binding was performed with the wild-type apelin receptor, and V38L, T89M, and R168H variants (Fig 4.6a) to provide more robust data with a higher number of replicates. In accordance with the preliminary screen, binding at the V38L variant showed high affinity ( $K_D$  value of  $0.13 \pm 0.02$  nM, slightly lower than the wild-type  $K_D$  value of  $0.40 \pm 0.07$  nM), but a reduced density ( $B_{max}$  value of 23.5 fmol/mg), that was more than 10-fold lower than the wild-type receptor density ( $B_{max}$  value of  $263.7 \pm 37.7$  fmol/mg). The T89M variant also showed similar affinity ( $K_D$  value of  $0.48 \pm 0.11$  nM) similar to wild-type, but the receptor density was over 1.5-fold higher ( $B_{max}$  of 405.5 fmol/mg), suggesting that the trend for higher  $B_{max}$  observed in the preliminary screen for this variant may be a real phenomenon in the HEK293T cells. No binding was detected for the R168H variant.

To explore the potential role of amino acid T89 in ELA ligand binding, competition radioligand binding was performed looking for displacement of 0.1 nM [ $^{125}$ I]-apelin-13 by ELA-11 at the T89M variant versus wild-type receptor (Fig 4.6b). The data showed that ELA-11 competed with the radioligand with a  $pK_i$  value of  $7.80 \pm 0.07$  at wild-type apelin receptor, but with a  $pK_i$  value of  $6.36 \pm 0.06$ , ~28-fold higher, at the T89M variant. This provides further evidence for the T89M substitution affecting binding specifically of ELA-based ligands, whilst showing a similar level of binding for the apelin radioligand and apelin647 fluorescent ligand.

#### **4.4.3. The R168H variant shows abolished function**

To characterise the impact of single point substitutions on apelin receptor pharmacological function, V38L, T89M, and R168H variants were assessed for cellular responses to [Pyr<sup>1</sup>]apelin-13 versus wild-type in a dynamic mass redistribution assay (Fig 4.7). Whilst the V38L and T89M variants were able to respond to [Pyr<sup>1</sup>]apelin-13, displaying a similar E<sub>max</sub> to wild-type, albeit with lower potency, R168H was, critically, essentially unresponsive following exposure to the ligand.

#### **4.4.4. The V38L variant shows good binding, but little internalisation, of apelin647**

In the wake of the interesting results garnered for the V38L variant, showing low receptor density in HEK293T binding (Table 4.1 and Fig 4.6a), low membrane localisation (Fig 4.3), but apelin647 binding that was comparable, if not better, than wild-type (Fig 4.4 and Fig 4.5), experiments looking at apelin647 internalisation were performed (Fig 4.8). Punctate apelin647 binding was observed at the membrane for both wild-type and V38L apelin receptor in the first 5 mins, but this was lost by 90 mins for the wild-type, where puncta could be seen moving into the intracellular compartment and clustering at perinuclear locations. Conversely, apelin647 bound to V38L and remained at the membrane to a greater extent by the 90 mins end-point, with the outline of cells more clearly defined by apelin647 fluorescence. The data suggest that V38L binds apelin647 well, and may not internalise to the same extent as wild-type receptor following stimulation with an agonist.

#### **4.4.5. The R168H variant does not bind apelin647 in cardiomyocytes**

A crucial step in this project was to show that the R168H variant, non-functional in binding and pharmacological assays, displayed a similar loss of function in a clinically relevant cell line. Following the generation of human embryonic stem cell-derived cardiomyocyte (hESC-CM) line carrying an heterozygous R168H apelin receptor variant, apelin647 was shown not to bind to these cells (Fig 4.9). Wild-type hESC-CMs were able to bind apelin647, that has been shown previously to be specific using a saturating 10 µM concentration of [Pyr<sup>1</sup>]apelin-13 (see Fig 3.8 in Section 3.3.4). The data show the loss of binding of an apelin ligand at a naturally occurring apelin receptor variant in the hESC-CM model.

## **4.5. Interpretation of results**

Interpretation of the results generated in this project was approached with caution due to the cross-platform nature of the experiments, and potential discrepancies in the biological systems used. However, key findings are discussed below.

### ***4.5.1. Summary of the V38L variant***

The V38L variant exhibited similar affinity for the [<sup>125</sup>I]-apelin-13 radioligand as wild-type, but low receptor density in the HEK293T membrane preparations. Additionally, the variant was able to bind the apelin647 ligand in live CHO-K1 cells, despite showing low membrane localisation in high content imaging studies. The high-affinity binding of apelin647 is hard to reconcile with this low membrane expression, but the consistently low  $K_D$  values determined at this variant provide some evidence that any V38L receptor that does make it to the membrane will likely bind ligands with high affinity. Discrepancies between the radioligand and fluorescent ligand studies may be reflective of the membrane preparation versus live cell settings, and/or the HEK293T cells versus CHO-K1 cells used respectively, where the cells may exhibit differential expression of the variant constructs. The V38L variant showed function in a dynamic mass redistribution assay in response to [Pyr<sup>1</sup>]apelin-13, suggesting G protein engagement and signalling. In an internalisation study, V38L appeared to show less internalisation than wild-type following exposure to apelin647, and it could be speculated that, whilst not much V38L makes it to the membrane, it may be resistant to internalisation mechanisms once at the cell surface. Future studies should explore V38L internalisation and whether the variant impacts GRK phosphorylation,  $\beta$ -arrestin recruitment, and endocytosis.

### ***4.5.2. Summary of the T89M variant***

The T89M variant showed good concordance between radioligand and fluorescent ligand studies, displaying a similar  $K_D$  value to wild-type receptor and a trend for higher receptor density. Additionally, the dynamic mass redistribution confirmed function of this variant in response to [Pyr<sup>1</sup>]apelin-13. Fascinatingly, T89M was less able to bind ELA647, and higher concentrations of ELA-14 were required to displace [<sup>125</sup>I]-apelin-13, suggesting that the T89 residue, forming part of the apelin receptor binding pocket,

mediates binding of ELA ligands but may not necessarily be involved in apelin ligand binding. This provides novel evidence for a site regulating the different binding modes observed previously for the binding modes of the two endogenous ligands. Future work should prioritise the response of the T89M mutation to ELA peptides versus apelin peptides, in pharmacological assays such as the dynamic mass redistribution assay.

#### **4.5.3. Summary of the R168H variant**

Finally, the R168H variant was consistently non-functional across the platforms described in this thesis, despite showing good membrane expression. The data agree with previous findings that highlight R168 as a site involved in binding of CMF-019 as part of the apelin receptor binding pocket and possibly G protein signalling (Read et al., 2016), and the reported loss of function in an R168A artificial mutation (Ma et al., 2017). Additionally, data from Sosei Heptares show that R168 interacts with the proline residue at position 12 and 11 of apelin-13 and ELA-11 respectively. The data in this Chapter show for the first time, the naturally occurring R168H single point substitution was sufficient to abolish binding and function in artificially expressing HEK293T and CHO-K1 cells. Additionally, apelin647 was unable to bind at the R168H variant in a clinically relevant hESC-CM line.

The R168H variant was identified in the BPD branch of the BRIDGE project that recruited patients suffering from Bleeding, Thrombotic & Platelet Disorders. The apelin receptor has been shown previously to mediate an antithrombotic effect through inhibition of thrombin- and collagen-mediated platelet activation (Adam et al., 2016). It is unclear whether R168H is directly causative of the disorder the patient presented with, but if the patient could be recalled, it would be intriguing to see if apelin infusion induced responses in assays such as plethysmography, as has been done safely in humans before (Japp et al., 2008, 2010; Brash et al., 2018).

## Chapter 5. ACE2 as the SARS-CoV-2 entry receptor in cardiomyocytes

### 5.1. Introduction

The work described in this chapter is published in Williams et al., 2021a.

The *ACE2* gene, mapped to chromosome locus Xp22.2, encodes the angiotensin-converting enzyme 2 (ACE2, UniProt ID: Q9BYF1) – an 805 amino acid long (~120 kDa) zinc-metalloproteinase type 1 transmembrane protein (Tipnis et al., 2000; Donoghue et al., 2000; Hamming et al., 2007; Badawi & Ali., 2021). In the cardiovascular system, ACE2 is a critical regulator of the renin-angiotensin-aldosterone system (RAAS), where it counteracts increases in blood pressure brought about by ACE dependent production of the vasoconstrictor and fluid retaining agent, angiotensin II (Burrell et al., 2004; Hamming et al., 2007; Tikellis et al., 2011). Additionally, ACE2 also converts [Pyr<sup>1</sup>]apelin-13 to [Pyr<sup>1</sup>]apelin-13<sub>(1-12)</sub>, which is expressed and biologically functional as a potent vasoactive agent and positive cardiac inotrope in the cardiovascular system (Yang et al., 2017b). Further, apelin treatment increased ACE2 promoter activity *in vitro* and stimulated increased ACE2 expression in the failing heart *in vivo*, also increasing ACE2, and cardiac contractility, in AT<sub>1</sub> receptor knockout mice (Sato et al., 2013). The data suggest that a component of beneficial cardiovascular apelin signalling is mediated through its upregulation of ACE2 and subsequent negative control of the RAAS (Sato et al., 2013). For more detail on the interaction between ACE2 and apelin signalling see Section 1.10.4.

Intriguingly, ACE2 acts as a host cell surface receptor for entry of viruses such as the severe acute respiratory syndrome coronavirus (SARS-CoV) and human corona virus NL63 (HCoV-NL63), where ACE2 binds the S1 domain of coronavirus spike (S) proteins with high affinity (Li et al., 2003; Kuhn et al., 2004; Hofmann et al., 2005; Hamming et al., 2007). Additionally, SARS-CoV-2, the cause of the COVID-19 pandemic that has put huge strain on global health and economy, utilises ACE2 as its entry receptor, where SARS-CoV-2 spike protein binds with an affinity of ~15 nM (Hoffmann et al., 2020; Wrapp et al., 2020; Yan et al., 2020; Yang et al., 2020). Targeting ACE2 pharmacologically is hypothesised as a potential therapeutic strategy

in combatting SARS-CoV-2 infection, particularly in individuals where the COVID-19 vaccines are contraindicated (Alexander et al., 2020).

Several other host protein components are implicated in SARS-CoV-2 infection. For an overview of these proteins, see Fig 5.1. Transmembrane protease, serine 2 (TMPRSS2), also expressed at the cell surface, primes the viral spike protein through cleavage of S1/S2 and S2' sites (Shang et al., 2020; Hoffman et al., 2020). The endosomal proteases, furin and cathepsins, are involved in S1/S2 cleavage and endosomal processing respectively (Cheng et al., 2020; Liu et al., 2020). B<sup>0</sup>AT1 (SLC6A19) is a neutral amino acid transporter that forms a dimer-of-heterodimers complex with ACE2 at the cell membrane, with ACE2 acting as a chaperone that improves B<sup>0</sup>AT1 expression and stability. Interestingly, the ACE2:B<sup>0</sup>AT1 complex binds two SARS-CoV-2 spike proteins simultaneously with reportedly higher affinity than ACE2 alone (Yan et al., 2020; Stevens et al., 2021). Additionally, the B<sup>0</sup>AT1 component may have an impact on the engagement of ACE2 with TMPRSS2 (Stevens et al., 2020). In its role as an amino acid transporter, B<sup>0</sup>AT1 is expressed highly in small intestine villus epithelial cell apical brush border membranes (Stevens et al., 1984), in complex with ACE2 (Fairweather et al., 2012). Of note, approximately half of COVID-19 patients present with gastrointestinal symptoms that can persist with Long COVID, and viral particles are observed shed in faeces (Parasa et al., 2020). The Stevens group speculate that the extent of B<sup>0</sup>AT1:ACE2 expression in the gut will likely influence the susceptibility of COVID-19 patients to gastrointestinal symptoms. Other symptoms seen in SARS-CoV-2 infection, such as fatigue and brain fog, may also occur through reduced amino acid transport as B<sup>0</sup>AT1 is internalised with virus-bound ACE2.

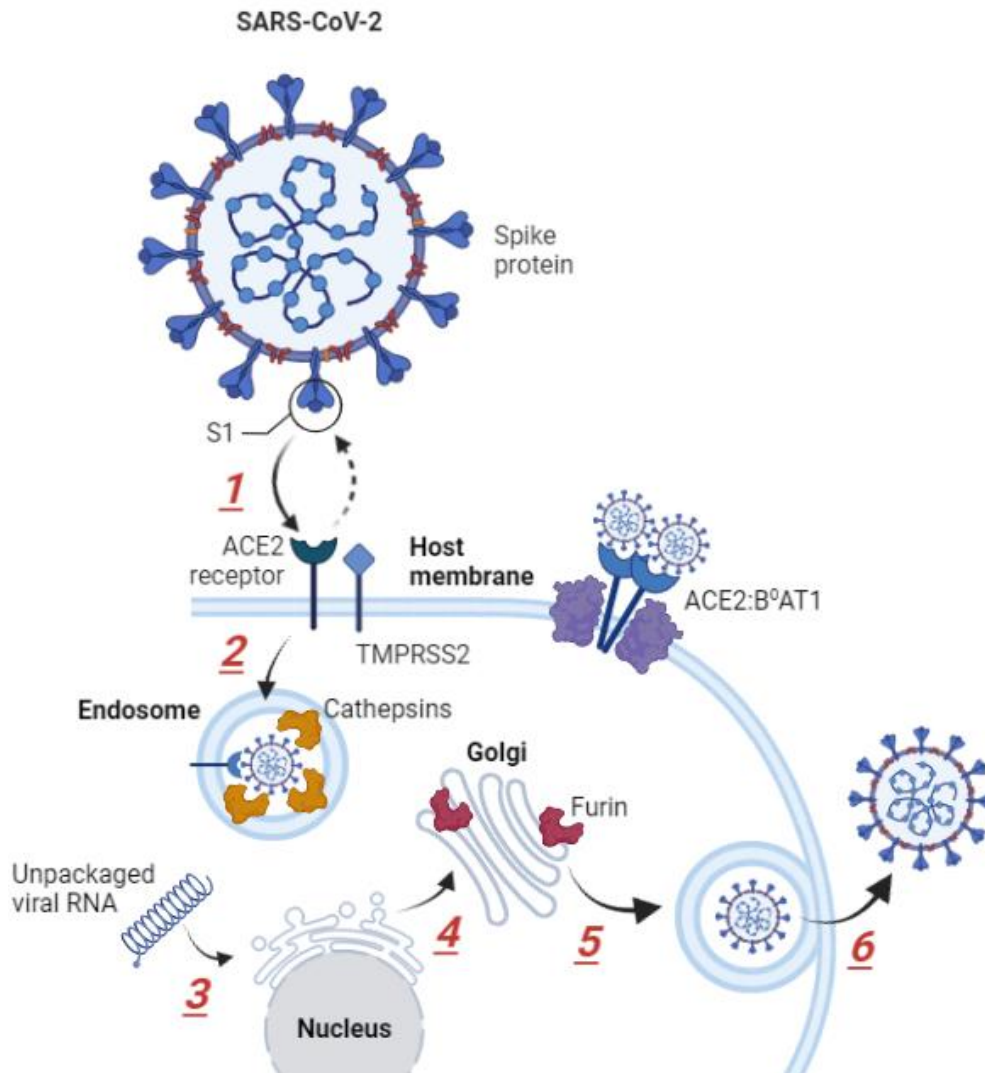


**Figure 5.1.** Simple schematic (created in BioRender.com) showing the mechanisms SARS-CoV-2 uses to infect host cells. **Step 1:** The S1 domain of the SARS-CoV-2 viral spike protein, embedded in the viral envelope, binds to the ACE2 receptor at the host membrane. TMPRSS2, also located in the host membrane, cleaves S1/S2 and S2' sites to prime the viral spike protein and facilitate the fusion of the viral membrane to the host membrane. Note also, the potential presence of the ACE2:B<sup>0</sup>AT1 dimer-of-heterodimers complex at the host membrane that can bind two SARS-CoV-2 viral particles and may have an impact on the interaction of ACE2 with TMPRSS2. **Step 2:** The viral particle enters the host cell via endocytosis, with ACE2 simultaneously internalised. Cathepsins in the endosome can also prime viral spike to further mediate fusion of the viral membrane to the endosomal membrane and facilitate release of the viral RNA. **Step 3:** The unpackaged viral RNA undergoes replication and translation,

before assembly at the endoplasmic reticulum. **Step 4:** Further assembly and processing of viral proteins occurs at the golgi apparatus, which is enriched with furin protein. A furin cleavage site in viral spike protein may also allow for spike priming, which may enhance the infectivity of any released viral particles (virions). **Step 5:** Replicated viral components are packaged into the nucleocapsid to form new virions inside exosomal compartments. **Step 6:** The exosome membrane fuses with the host membrane to facilitate the extracellular release via exocytosis of virions, which can go on to infect other cells. Schematic was designed using BioRender (<https://biorender.com/>).

The complex effects of SARS-CoV-2 infection on the heart are incompletely understood, but the case fatality rate in COVID-19 patients rises from 2.3 % to 10.5 % in the presence of cardiovascular comorbidities (Watkins, 2020; Sommerstein, 2020; Robinson et al., 2020). Transmission electron microscopy has confirmed the presence of SARS-CoV-2 viral particles in human cardiomyocytes infected *in vitro* with the virus (Bojkova et al., 2020; Bailey et al., 2021), or in autopsy samples from patients that tested positive for SARS-CoV-2 (Bailey et al., 2021). Further, SARS-CoV-2 infection in induced pluripotent stem cell (iPSC)-derived cardiomyocytes induces morphological and cytotoxic effects, and sarcomeric disruption in autopsy samples is observed, suggesting SARS-CoV-2 directly damages cardiac tissue (Bojkova et al., 2020; Bulfamante et al., 2020; Pérez-Bermejo et al., 2021).

Work in this thesis aimed to confirm the protein expression of the host cell components implicated in SARS-CoV-2 infection using surgical samples of left ventricle – the chamber of the heart responsible for pumping blood around the body. We then also aimed to determine whether a clinically relevant human embryonic stem cell-derived cardiomyocyte (hESC-CM) model expressed the same repertoire of recognition, processing, and ancillary genes (and corresponding proteins) as observed in adult cardiomyocytes, and demonstrate viral entry of SARS-CoV-2 in this model. Human stem cell lines used to generate cardiomyocytes are widely acknowledged for their utility in cardiovascular research, and will be crucial in understanding the recognised pathology of SARS-CoV-2 in cardiac tissue, alongside potentially providing a suitable model for drug screening (Khan et al., 2013; Yiangou et al., 2020). As our final aim

therefore, we looked to confirm infection of hESC-CMs using high content imaging in conjunction with a pseudotyped HIV-1 based lentivirus adorned with the SARS-CoV-2 spike protein that can be handled in lower levels of biological safety containment than the SARS-CoV-2 virus itself. Previous authors have outlined the potential of such a platform (Yang et al., 2020), but this study is the first to our knowledge to screen effective compounds that reduce SARS-CoV-2 spike dependent viral entry in a clinically relevant derived cardiomyocyte cell line.

## **5.2. Methods**

### **5.2.1 Cell culture**

Culturing of hESCs was performed as described in Section 2.4. Differentiation of hESC to hESC-CMs was conducted as described in Section 2.4.5.

### **5.2.2. Opera Phenix High Content Screening**

For immunocytochemistry, hESC-CMs in CellCarrier-96 Ultra Plates (PerkinElmer) were washed in PBS before fixation with 4 % formaldehyde solution (20 mins). Non-specific staining was blocked with PBS + 10 % donkey sera for 2 h. Cells were then aspirated and treated with antibodies raised against ACE2, TMPRSS2, B<sup>0</sup>AT1, cathepsin B, cathepsin L, and furin, all prepared in PBS + 1 % donkey sera + 0.1 % Tween-20 + 3.3 mg/mL bovine serum albumin (see Table 5.1 for details on antibodies used). After 24 h, cells were washed with PBS before incubation with the respective secondary polyclonal antibodies for 1 h. Cells were washed with PBS before treatment with 10 µg/mL Hoechst 33342 nuclear stain (H3570; Invitrogen) for 15 mins before a final wash step and maintenance in PBS. For viral infection experiments, pseudotyped virus treated hESC-CMs, maintained in the presence or absence of drugs (see Table 5.2 for details on drugs used), were washed with PBS before fixation with 4 % formaldehyde solution (20 mins). Cells were washed with PBS before treatment with 10 µg/mL Hoechst 33342 nuclear stain (H3570; Invitrogen) for 15 mins before a final wash step and maintenance in PBS.

<u>Protein/target</u>	<u>Manufacturer</u>	<u>Catalogue #</u>	<u>Species</u>	<u>Concentration</u>
ACE2	R&D	AF933	Goat	20 µg/mL
TMPRSS2	Abcam	ab92323	Rabbit	1:500
B <sup>0</sup> AT1	Abcam	ab180516	Rabbit	1:300
Cathepsin B	Abcam	ab125067	Rabbit	1:100
Cathepsin L	Abcam	ab203028	Rabbit	1:100
Furin	Abcam	ab3467	Rabbit	1:500
<i>Anti-goat IgG AF555</i>	<i>Abcam</i>	<i>ab150130</i>	<i>Donkey</i>	<i>1:200</i>
<i>Anti-rabbit IgG AF555</i>	<i>Abcam</i>	<i>ab150066</i>	<i>Donkey</i>	<i>1:200</i>
Hoechst nuclear stain	Invitrogen	H3570	n/a	10 µg/mL

**Table 5.1.** Markers used in immunochemistry, with respective concentrations/dilutions used. Secondary antibodies shown in italic.

Fluorescent confocal images were captured using the Opera Phenix High Content Screening System microscope with a 40x/NA1.1 water immersion objective, as described in Section 2.9.3.

In-built high content quantification was performed using Harmony High-Content Imaging and Analysis Software (PerkinElmer), based on methods described in Section 2.9.5. For analysis, images were filtered, and the contrast of the Hoechst nuclear blue channel was increased 5-fold to ensure cells were distinguished from background and digital phase contrast used to assist in finding the outer limits of individual cells. Fluorescence intensities were then calculated for every observed cell in the selected population and were deemed positive where whole cell fluorescence (averaged over individual cell area) was  $\geq 130$  fluorescent units, where background was determined as 113 fluorescent units based on negative control wells.

### **5.2.3. Immunohistochemistry and slide scanner imaging**

Surgical samples of human tissue were obtained with informed consent and ethical approval (05/Q104/142). Tissues were snap frozen in liquid nitrogen before storage at -80 °C. Tissue samples from humans (n = 6 individuals) were cut, using a cryostat (-

30 °C), into 10 µm sections and thaw mounted onto slides before return to storage at -80 °C.

Slides were thawed and tissue encircled with hydrophobic ink before rehydration with PBS. Tissues were fixed with 4 % formaldehyde solution (20 mins). Fixed tissue sections were then treated as hESC-CM cells were in immunocytochemistry experiments (see 5.2.2). Following a further 3x washes with PBS, slides were incubated for 1 h at room temperature in the dark with a cardiac troponin T antibody conjugated to APC (130-120-543; Miltenyi Biotec) prepared at a 1:100 dilution in PBS. After a final 3x washes with PBS, slides were blotted dry with lint-free tissue, mounted with ProLong Gold Antifade Mountant (P36930; Invitrogen), covered with a cover slip, and left overnight at room temperature in the dark to dry.

Automated fluorescent images (16 bit, 0.325 x 0.325 µm scaling per pixel) were acquired using a Slide Scanner Axio Scan.Z1 (Zeiss) microscope with a Plan-Apochromat 20x/NA0.8 M27 objective lens, as described in Section 2.9.5.

#### **5.2.4. Pseudotyped virus production and infection of hESC-CMs**

Generation of a pseudotyped lentivirus ‘decorated’ with SARS-CoV-2 spike protein was conducted as described in Section 2.5.1. Subsequent infection of hESC-CMs was conducted as described in Section 2.5.2.

For infection of hESC-CMs, cells in CellCarrier-96 Ultra Plates (PerkinElmer) were incubated for 4 h with pseudotyped viral stock at the desired multiplicity of infection (MOI) in media. In drug screens, cells were pre-treated for 1 h before infection with either camostat, benztropine, or E64d at a final concentration of 30 µM; DX600 at a final concentration of 10 µM; ACE2 antibody (AF933; R&D Systems) at 20 µg/mL; a mix of camostat + E64d at a final concentration of 30 µM each; or DMSO at 0.6% (equivalent of the highest concentration included in drug dilutions). See Table 5.2 for a summary of drugs used in the screen. Cells were then washed 3x with PBS to remove infectious lentivirus particles, before replenishment with the media outlined above, maintained in the presence of the respective drug treatments for 4-5 days. Viral

infection was monitored using an EVOS Cell Imaging System to look for green fluorescence protein (GFP) as a marker of viral presence in cells.

<u>Target</u>	<u>Compound</u>	<u>Class</u>	<u>Action</u>	<u>pIC<sub>50</sub></u>	<u>Approved</u>
TMPRSS2	Camostat	Synthetic organic	Inhibitor	6.0	Yes
B <sup>0</sup> AT1	Benztropine	Synthetic organic	Inhibitor	4.4	Yes
Cathepsins	E64d	Synthetic organic	Inhibitor	6.0 (?)	No
ACE2	DX600	Peptide	Inhibitor	8.6	No
ACE2	ACE2 antibody	Antibody	n/a	n/a	No

**Table 5.2.** Summary of the protein targets and compounds used in a drug screen looking for inhibitors of SARS-CoV-2 spike protein pseudotyped viral infection. Table shows the class of compound, mode of action, pIC<sub>50</sub> values at the respective protein target, and whether the compounds are approved. Information was provided by the IUPHAR/BPS Guide to PHARMACOLOGY. Note, camostat is not approved by the EMA or FDA, but is licensed in Japan for clinical treatment of chronic pancreatitis. Benztropine is approved by the FDA for clinical treatment of Parkinsonism.

### **5.2.5. SARS-CoV-2 infection in hESC-CMs**

Infection and imaging of hESC-CMs with SARS-CoV-2 viral isolate was performed as described in Section 2.5.3. For SARS-CoV-2 immunostaining, infected cells were fixed in 2% formaldehyde for 30 mins and permeabilized with BD Perm/Wash buffer (BD Biosciences, 554723). The primary antibody used was sheep anti-SARS-CoV-2 nucleocapsid antibody (DA114, MRC-PPU), which was visualised with AF488 conjugated donkey anti-sheep antibody (Jackson ImmunoResearch #713-545-147).

### **5.2.6. Data analysis and statistics**

Quantitative data are expressed as mean ± SD. Raw data were handled using Microsoft Excel for Windows (Microsoft). Graphical presentation and statistical tests were performed using GraphPad Prism version 6.07 for Windows (GraphPad Software). Statistical tests are indicated in figure legends where used. A p value of < 0.05 was determined as significant.

### **5.3. Results**

#### ***5.3.1 Human left ventricle and hESC-CMs express ACE2 and ancillary proteins utilised by SARS-CoV-2 to infect host cells***

Both native human left ventricle tissue and the cultured hESC-CM model express ACE2 and ancillary proteins exploited by SARS-CoV-2 virus to infect host cells (Fig 5.2a-f). Quantification of fluorescence in hESC-CMs confirmed that > 90 % of the cell population stained positive for ACE2, TMPRSS2, cathepsin L, and furin (Fig 5.2h), with  $55.6 \pm 22.2$  % of cells staining positive for B<sup>0</sup>AT1. Interestingly, no significant immunoreactivity was observed for cathepsin B ( $6.3 \pm 5.6$  %) above background ( $4.1 \pm 3.9$  % of cells). The proteins were also expressed in the human left ventricle tissue sections, barring cathepsin B, which again displayed little to no immunoreactivity. Expression of the corresponding genes (mRNA) for the proteins of interest were also identified in hESC-CMs and human left ventricle (Fig 5.2i). Interestingly, cathepsin B mRNA was not identified in left ventricle tissue. RNA extraction, processing, and sequencing was kindly performed by Dr Emma L. Robinson (School of Medicine, Division of Cardiology, University of Colorado Denver, Anschutz Medical Campus, Aurora, U.S.A.).

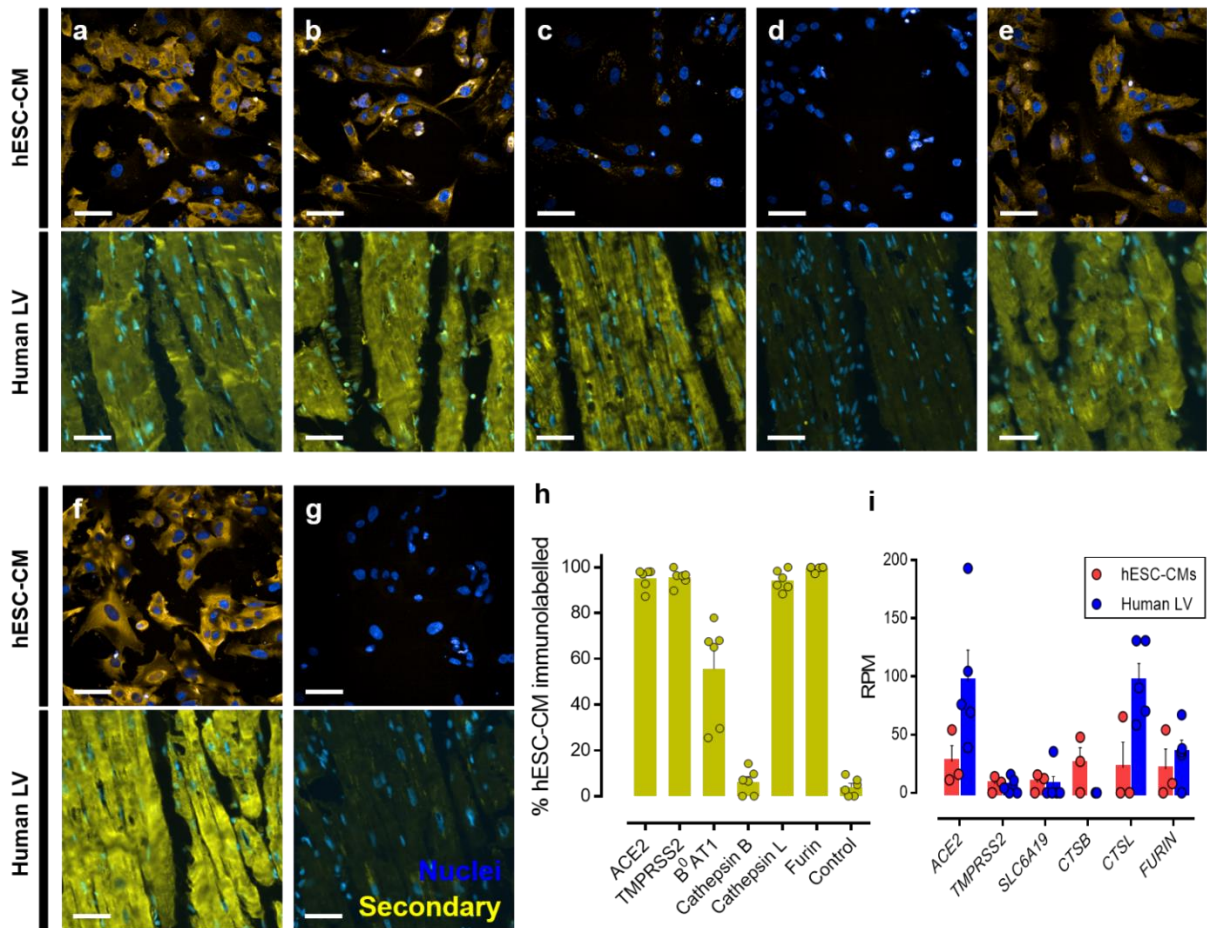


**Figure 5.2.** ACE2 and ancillary proteins used by SARS-CoV-2 are present in hESC-CMs and human left ventricle tissue. Scale bars show 50  $\mu$ m. **a-f** Representative fluorescent confocal images of hESC-CMs ( $n = 3$  independent experiments from 3 distinct differentiations performed in duplicate) and representative fluorescent images of human left ventricle (LV,  $n = 6$  from 6 independent donors). Nuclei are coloured blue and proteins of interest are visualised using a yellow secondary antibody. Both cells and tissue were treated with primary antibodies raised against ACE2 (**a**), TMPRSS2 (**b**), B0AT1 (**c**), cathepsin B (**d**), cathepsin L (**e**), and furin (**f**), before visualisation with a secondary antibody conjugated to Alexa Fluor 555 (shown in yellow) and Hoechst 33342 nuclear marker (shown in blue). Control cells and tissue were treated in the absence of primary antibody (**g**). Scale bars show 50  $\mu$ m. **h** Graphical data showing the percentage of the observed hESC-CM population positively immunolabelled with primary antibodies raised against the outlined protein targets.  $n = 2$  independent experiments with 2 distinct differentiations performed in duplicate. **i** Graphical data showing the reads per million (RPM)  $\pm$  SEM for expression of viral entry and

processing mRNA in hESC-CMs (n = 3 replicates across 3 distinct differentiations) and human left ventricle (n = 5 individuals). RPM values  $\geq 1.0$  were deemed to be above the noise. Benjamini-Hochberg correction for multiple testing was used with a false discovery rate of 5 %. *SLC6A19*, *CTSB*, and *CTSL* are the genes that encode B<sup>0</sup>AT1, cathepsin B, and cathepsin L, respectively. All graphical data are mean  $\pm$  SEM, with individual data points indicated. hESC-CMs were cultured by Dr Maria Colzani. RNAseq data were analysed by Dr Emma Robinson.

### 5.3.2. Infection of hESC-CMs with SARS-CoV-2 spike pseudotyped virus, and identification of novel inhibitors of infection

The clinically relevant hESC-CM model were infected with a SARS-CoV-2 spike pseudotyped GFP-expressing lentivirus, in the presence or absence of drugs hypothesised to reduce SARS-CoV-2 infection. See Fig 5.3 for a schematic outlining the experimental procedure.

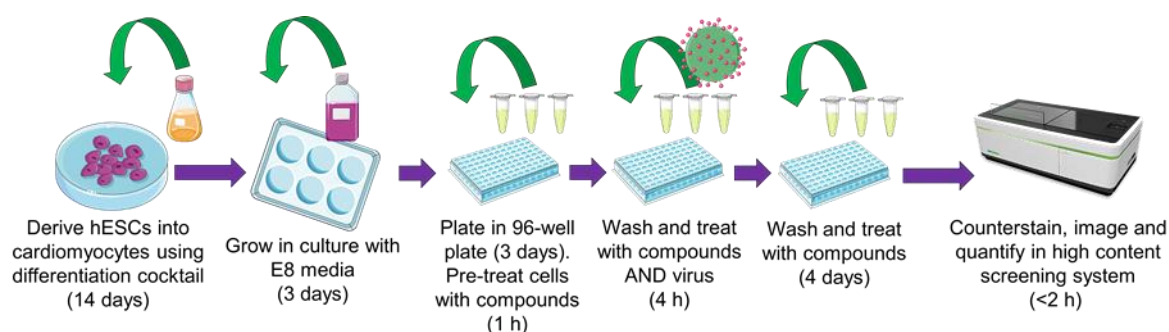


**Figure 5.3.** Schematic showing the experimental workflow for generation of hESC-CMs before plating in 96-well plates. Cells were subsequently pre-treated with compounds hypothesised to reduce SARS-CoV-2 infection or DMSO control, before a wash step and then treatment with the SARS-CoV-2 spike pseudotyped virus in the presence or absence of drug for 4 hours. Cells were then maintained in the presence of drugs for 4 days before fixation with 4 % formaldehyde, and counterstaining with Hoechst 33342 nuclear marker. Plates were then imaged using high content imaging and fluorescence qualitatively and quantitatively assessed. Schematic was generated using templates from Servier Medical Art.

High content visualisation of pseudotyped viral expression of GFP in infected hESC-CMs (Fig 5.4a-c) showed that in media and DMSO (0.6 %) treated cells,  $64.9 \pm 10.2$  % and  $61.8 \pm 14.1$  % of the cell populations were positive for GFP. Uninfected cells were treated with media that contained no viral particles and showed little to no GFP fluorescence. The compounds included in the drug screen reduced levels of infection observed in the hESC-CMs. An ACE2 antibody, shown previously to neutralize pseudotyped virus and SARS-CoV-2 infection (Hoffman et al., 2020), significantly reduced infection to  $2.9 \pm 1.0$  % of the cell population used in this study. It is important to note that the ACE2 antibody did not significantly reduce infection observed with a control vesicular stomatitis virus (VSV-G) pseudotyped lentivirus (Fig 5.4b,c), suggesting that the infection with SARS-CoV-2 spike pseudotyped lentivirus is ACE2 dependent. Interestingly, DX600, an ACE2 peptide antagonist, also lowered infection, to  $27.4 \pm 19.9$  % of the cell population.

Camostat and E64d, an inhibitor of TMPRSS2 and a pan cathepsin inhibitor respectively, both significantly reduced infection to  $20.5 \pm 15.8$  % and  $7.8 \pm 4.1$  %. A combination of camostat and E64d effectively reduced infection as well ( $6.5 \pm 3.6$  %) but this was not significantly different to E64d treatment alone. Interestingly, benztropine, a small molecule inhibitor of the B<sup>0</sup>AT1 protein that forms part of the dimer-of-heterodimers complex with ACE2, also successfully reduced pseudotyped virus infection levels to  $28.9 \pm 21.6$  %.

Cell counts (Fig 5.4d), determined using the Hoechst nuclear stain in high content imaging, provided some evidence that the drug treatments were not inherently toxic as there were no significant differences in number of cells. The pseudotyped virus infection itself was also not toxic, indicated in Fig 5.4d, and video footage (Fig 5.5 associated video file) showed beating of hESC-CMs was maintained.

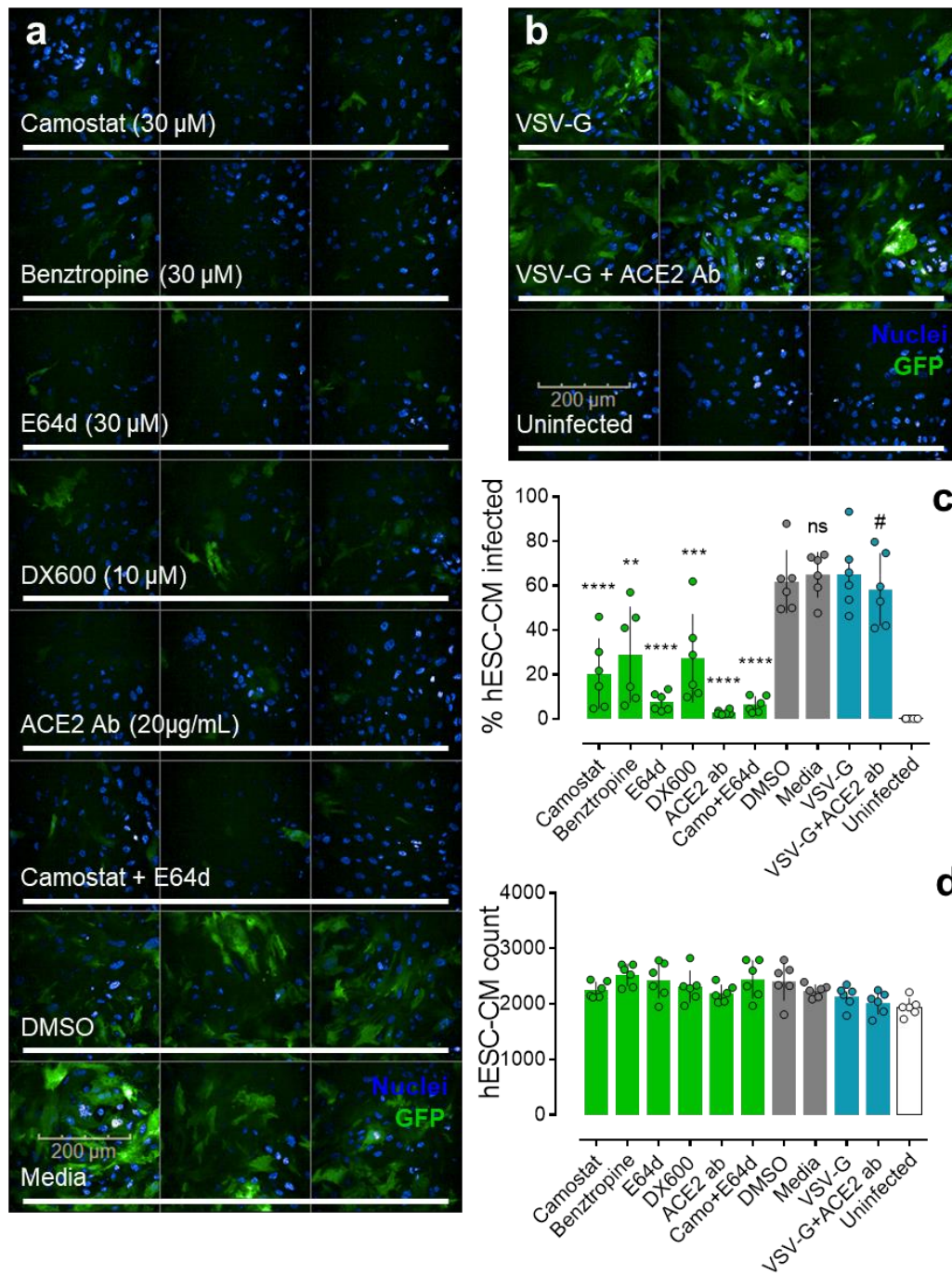


**Figure 5.4.** SARS-CoV-2 spike pseudotyped viral infection, and pharmacological inhibition, in hESC-CMs. Representative fluorescent confocal images of hESC-CMs ( $n = 2$  independent experiments from 2 distinct differentiations performed in triplicate) infected with SARS-CoV-2 spike pseudotyped lentivirus infected and treated with compounds (as indicated in figure), DMSO (0.6 %) or media (**a**). Further control hESC-CMs infected with VSG-G pseudotyped lentivirus in the absence or presence of a neutralising ACE2 antibody, or left uninfected with viral particles were also imaged (**b**). Scale bars show 200  $\mu$ m. **c** Quantified data showing the percentage of hESC-CMs

infected (GFP positive) with pseudotyped virus in the presence or absence of compounds as indicated. Uninfected cells were left untreated with viral particles. \*\* =  $p < 0.005$ ; \*\*\* =  $p < 0.0005$ ; \*\*\*\* =  $p < 0.00005$ ; and ns = no significant difference (as determined by one-way ANOVA) for each condition versus the DMSO treated control cells. ● = no significant difference for condition versus the VSV-G control. **d** Quantified cell counts of observed hESC-CMs for each condition, as indicated. No condition showed a count significantly different (as determined by one-way ANOVA) from the DMSO treated control cells. All graphical data are expressed as mean  $\pm$  SEM. hESC-CMs were cultured and treated by Dr Maria Colzani. Pseudotyped virus was provided by Mr Stuart Bloor and Mr Jun Ru Zhan.

Videos (Fig 5.5a-c and associated video files) of beating hESC-CMs, in the presence or absence of the SARS-CoV-2 pseudotyped virus, were recorded to qualitatively assess cell density and whether viral infection had an impact on contraction. Contraction was maintained in the presence of the pseudotyped virus (Fig 5.5a associated video file), at rate of ~186 beats per minute, which was comparable to the contractions observed in controls (Fig 5.5b associated video file) that were not exposed to viral particles and exhibited ~174 beats per minute. In cells treated with the vesicular stomatitis virus (VSV-G) pseudotyped lentivirus control (Fig 5.5c associated video file), contractions were also estimated at ~186 beats per minute. Whilst these data are limited and provide no information on the force of contraction or fractional shortening, the videos do at least confirm that spontaneous beating, characteristic of hESC-CMs, was visible following treatment with viral particles.

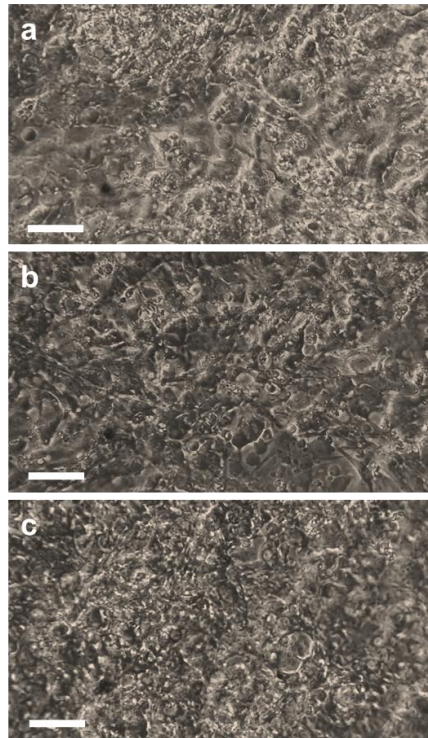


**Figure 5.5.** Still shots from brightfield videos of hESC-CMs treated with media containing SARS-CoV-2 spike pseudotyped virus (**a**), media containing no viral particles (**b**), or media containing vesicular stomatitis virus (VSV-G) pseudotyped lentivirus (**c**). Scale bars show 50  $\mu\text{m}$ . See corresponding attached video files for footage of the beating cells. hESC-CMs were cultured by Dr Maria Colzani.

Finally, it was important to establish that the hESC-CMs used in this study were susceptible to infection with SARS-CoV-2 (Fig 5.6). Imaging data confirmed infection in the cardiomyocytes that was titre- and time-dependent.

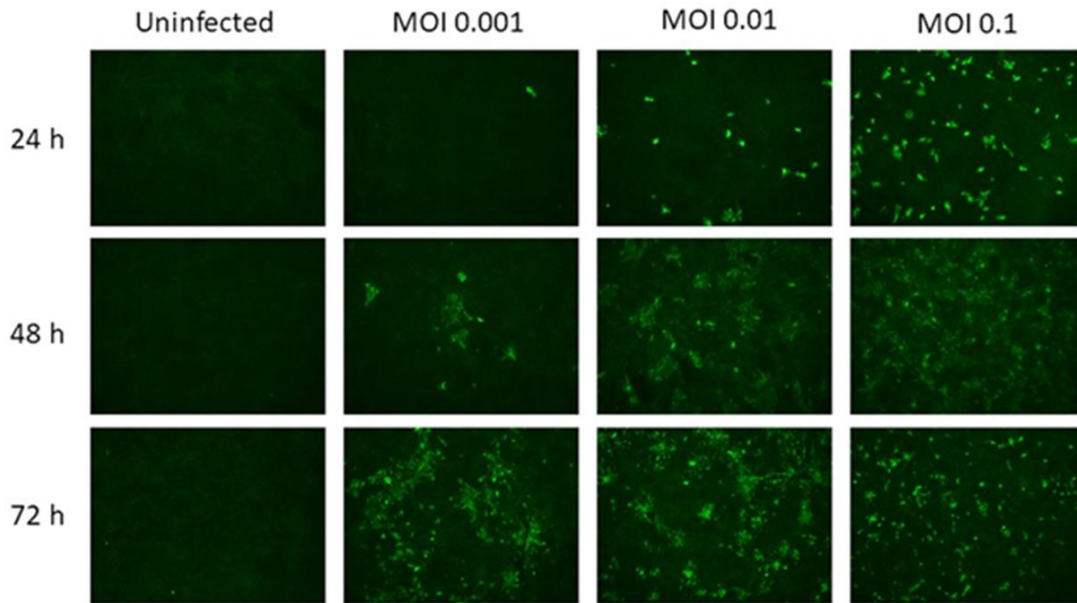


**Figure 5.6.** Representative images (from n = 2 independent experiments) of hESC-CMs infected with isolated SARS-CoV-2, tested at several different titres (0.001-0.1 multiplicity of infection, MOI) and incubation times (24-72 hours). At the end point, cells were fixed and permeabilised before immunolabelling with a primary anti-SARS-CoV-2 nucleocapsid antibody. Cells were visualised using a secondary antibody conjugated to Alexa Fluor 488 (shown in green). hESC-CMs were cultured by Dr Maria Colzani. Infection was performed by Dr Edward Greenwood.

## **5.4. Discussion**

### ***5.4.1. Cardiomyocytes express ACE2 and the ancillary protein machinery necessary for SARS-CoV-2 infection***

The hESC-CMs used in this study were shown qualitatively (Fig 5.2a-f) and quantitatively (Fig 5.2h) to express ACE2 protein, the entry receptor used by SARS-CoV-2 to infect cells, along with TMPRSS2, B<sup>0</sup>AT1, cathepsin L, and furin, that all play roles in the infection process. Quantification confirms staining with ACE2, TMPRSS2, cathepsin L, and furin was homogenous across the cell population (> 90 % of cells positive), whilst B<sup>0</sup>AT1 was only present in ~56 % of cells. Human left ventricle tissue sections expressed the same protein complement (Fig 5.2a-f), suggesting that the hESC-CM model recapitulates the native tissue. Genetic data (Fig 5.2i) also confirmed the expression of mRNA for the corresponding proteins in both the hESC-CMs and

left ventricle tissue, with an absence of cathepsin B (*CTSB*) mRNA observed in the native tissue. Interestingly, *CTSB* mRNA was detected in the hESC-CMs, and it has been shown previously that a human induced pluripotent stem cell derived cardiomyocyte line also expresses *CTSB* mRNA (Bojkova et al., 2020), indicating there may be discrepancies in protein versus mRNA expression.

#### **5.4.2. hESC-CMs provide a model for SARS-CoV-2 spike protein pseudotyped viral infection and screen for novel inhibitors**

A SARS-CoV-2 spike pseudotyped GFP-expressing lentivirus (Hoffman et al., 2020) was used to infect the clinically relevant hESC-CM model in 96-well plates, visualised using high content, which provides robust imaging and quantified outputs.

Data showed that incubation of hESC-CMs with the pseudotyped virus in the presence of DMSO or media resulted in ~62-65 % of the cell population becoming infected (Fig 5.4a,c), determined by expression of the viral GFP reporter. In the drug screen, pre-treatment and maintenance with several compounds significantly reduced levels of infection. The ACE2 antibody, used at 20 µg/mL in immunochemical experiments, has also been shown previously to 'neutralise' SARS-CoV-2 spike protein pseudotyped viral infection in the Vero E6 cell line (Hoffman et al., 2020). Here, the neutralising effect of the antibody was confirmed in hESC-CMs, reducing infection to ~3 %. Importantly, the ACE2 antibody did not significantly affect levels of infection with the VSV-G pseudotyped lentivirus control, indicating that spike protein pseudotyped viral infection is likely dependent on ACE2.

DX600 (10 µM), a peptide antagonist that binds irreversibly to ACE2 with high affinity significantly reduced infection to ~27 % of the observed hESC-CM population. Note that DX600 was ~9 fold less effective than the ACE2 antibody in terms of reducing infection, which may reflect the differences in concentrations of the two compounds, but may also result from the different mechanisms of action. DX600 binds to the catalytic site in the peptide domain of ACE2 (that lies outside of the spike protein binding domains) with a  $K_i$  of ~2.8 nM (Huang et al., 2003), but may sterically hinder binding of spike protein to ACE2 or induce a conformational change in ACE2 that prevents binding. Further work will need to be done to fully elucidate the mechanisms

by which DX600 reduces spike dependent viral infection, but a novel peptide that binds to ACE2 with high affinity and specificity has also recently been shown to block the interaction of the SARS-CoV-2 receptor binding domain with ACE2 (Adhikary et al., 2021), confirming proof-of-principle. The polyclonal ACE2 antibody meanwhile will be considerably larger than DX600 and binds to multiple epitopes of the ACE2 protein, likely blocking access to spike protein binding sites by the virus. Nevertheless, the work in this Chapter shows anti-viral activity of a peptide ligand at the ACE2 receptor.

Camostat, a small molecule inhibitor of TMPRSS2, was also shown in Hoffman et al., 2020 and 2021 to reduce pseudotyped infection. Here, a similar concentration of camostat (30  $\mu$ M) was effective in significantly reducing infection in hESC-CMs to ~21 %. The current consensus posits that TMPRSS2 is necessary for SARS-CoV-2 spike protein priming and subsequent infection (Shang et al., 2020; Hoffman et al., 2020). Camostat is therefore a promising therapeutic for COVID-19, particularly given that it is already clinically approved in Japan where it is used safely and effectively to treat chronic pancreatitis (Ota et al., 2016; Uno, 2020).

E64d (also known as aloxistatin), is a small molecule non-selective inhibitor of cysteine proteases, including cathepsins B and L, where a 10  $\mu$ M concentration of the compound has been shown to rapidly inactivate the enzymes (Barrett et al., 1982). E64d has also been used previously to reduce pseudotyped virus infection in VeroE6 cells (Hoffman et al., 2020), presumably through block of cathepsin mediated spike protein priming. E64d (30  $\mu$ M) inhibition was confirmed in hESC-CMs, significantly reducing infection to ~8 % – a marked effect. Data showed that cathepsin B levels were low to absent in the hESC-CMs, suggesting that E64d worked through inhibition of cathepsin L and/or alternative cathepsins that may be expressed in hESC-CMs but were not characterised in this project. A combination of 30  $\mu$ M camostat and 30  $\mu$ M E64d was tested here (providing a reduction of infection to ~7 %), in accordance with the Hoffman et al., 2020 study, but given that the effect of E64d alone was so substantial, no further significant additive effect of camostat was detectable. In future studies, it would be interesting to explore whether a combination of the two compounds at lower concentrations provides usable reductions in infection.

B<sup>0</sup>AT1 is a neutral amino acid transporter protein, expression of which is dependent on its interaction with the membrane peptidases aminopeptidase N (CD13) or ACE2 (Kowalczyk et al., 2008; Fairweather et al., 2012). B<sup>0</sup>AT1 has therefore been proposed as a potential therapeutic target in COVID-19 (Alexander et al., 2020). Interestingly, the data in this thesis show that benztropine, a small molecule inhibitor of B<sup>0</sup>AT1, was also able to reduce levels of infection (~29 %) in hESC-CMs. Importantly, benztropine is used clinically as an adjuvant to mitigate side effects of antipsychotic drugs, and in Parkinsonism for its anticholinergic/antihistaminergic effects, but has only more recently been identified as an inhibitor of B<sup>0</sup>AT1 (Chen et al., 2017). Precisely how benztropine mediates antiviral effects in hESC-CMs remains to be characterised, particularly given that the drug is a weak inhibitor of B<sup>0</sup>AT1 ( $pIC_{50}$  value of 4.4) and only 55.6 % of hESC-CMs expressed the protein target. Note that a highest dose of 30  $\mu$ M benztropine (slightly below the  $pIC_{50}$ ) was used in this study to ensure full solubility of the compound in DMSO, and to ensure that the DMSO did not exceed 1 % in assay to minimise toxicity.

#### **5.4.3. Drug treatments and pseudotyped virus were not toxic in cardiomyocytes**

Cell counts of SARS-CoV-2 spike protein pseudotyped infected hESC-CMs in high content imaging (Fig 5.4d) demonstrated that none of the drug treatments, including DMSO at the highest concentration used (0.6 %), significantly reduced mean cell number versus media only controls. Additionally, VSV-G pseudotyped lentivirus treated cells, and cells untreated with virus particles, were present in similar numbers as observed for media treated spike protein pseudotyped infected cells. The data provide evidence that neither the drug treatments or viral infections were inherently toxic, confirming that reductions in infection observed for drugs was not due to reduced cell number.

Video footage of beating hESC-CMs (Fig 5.5 associated video file) was also captured to qualitatively assess functional effects of viral infection. In the presence of SARS-CoV-2 spike protein pseudotyped virus (Fig 5.5a associated video file), media treated controls (Fig 5.5b associated video file), and VSV-G pseudotyped lentivirus controls (Fig 5.5c associated video file), spontaneous contraction of hESC-CMs was

maintained. This further suggested viral infections were not inherently toxic at this level.

#### **5.4.4. Cardiomyocytes are susceptible to SARS-CoV-2 virus**

To fully validate the hESC-CM model and SARS-CoV-2 spike protein pseudotyped virus described above in this thesis, it was crucial to confirm that the cells were susceptible to infection with isolates of the actual SARS-CoV-2 virus.

Infection of hESC-CMs with viral isolate was visualised using an anti-SARS-CoV-2 nucleocapsid antibody (Fig 5.6), and was shown to be titre- and time-dependent. This falls in agreement with other studies that show SARS-CoV-2 viral particles in left ventricle heart autopsy samples from COVID-19 myocarditis patients (Bailey et al., 2021) and beating cardiomyocyte samples infected with SARS-CoV-2 *in vitro* (Bojkova et al., 2020; Bailey et al., 2021). Additionally, infection has been observed in induced pluripotent stem cell (iPSC)-derived cardiomyocytes (Bojkova et al., 2020; Bulfamante et al., 2020; Pérez-Bermejo et al., 2021), which are similar but not identical to hESC-CMs.

An obvious future study for this work will be the assessment of drugs that showed inhibitory effects on viral infection in the pseudotyped viral experiments in hESC-CMs treated with the actual SARS-CoV-2 isolate.

### **5.5. Conclusions**

The data in this Chapter shows high levels of expression of ACE2, the viral entry receptor for SARS-CoV-2, and several ancillary proteins critical for infection, in native human left ventricle cardiomyocytes and a well-established hESC-CM model. The data match previous findings in the literature that show marked levels of infection and damage in the heart in COVID-19.

Using a validated SARS-CoV-2 spike pseudotyped virus, a high throughput drug screening platform was developed that incorporates the clinically relevant hESC-CM cell line in a 96-well format. Additionally, the pseudotyped virus can be handled in

intermediate biosafety facilities (Category 2), unlike studies using actual SARS-CoV-2 isolates that require higher containment levels (Category 3). The platform developed as work in this thesis therefore has great scope for translation to industrial settings, and has already successfully identified two novel inhibitors of SARS-CoV-2 spike dependent infection – DX600 and benztropine, targeting ACE2 and B<sup>0</sup>AT1 respectively. Discovery of drugs blocking SARS-CoV-2 infection may be of great importance in helping individuals where vaccination is contraindicated, or if new viral variants that escape vaccine therapy become more prevalent.

Finally, the data demonstrate that the hESC-CM model is susceptible to infection with SARS-CoV-2 isolates, solidifying the suitability of these cells in viral studies and drug screens. Further work will need to be done to confirm that DX600 and benztropine are effective in blocking SARS-CoV-2 itself in the hESC-CMs and other cells/tissues.

## **Chapter 6. Tissue distribution of ACE2 and a novel short ACE2 isoform – implications in COVID-19**

### **6.1. Introduction**

The work described in this chapter is published in Williams et al., 2021b.

Since its discovery, the tissue distribution of ACE2 in human has been shown to be relatively wide, with mRNA expression detected at particularly high levels in the kidney, testis, gastrointestinal tract (predominantly intestinal), and heart (Tipnis et al., 2000; Donoghue et al., 2000; Harmer et al., 2002). In the heart, ACE2 mRNA is localised to the vascular endothelium and smooth muscle, myofibroblasts, and the cardiomyocytes themselves (Burrell et al., 2005; Guy et al., 2008).

ACE2 protein is expressed in the endothelium and vascular smooth muscle, lung epithelial cells (sinonasal cavity and alveolar type II cells), renal tubules, intestinal enterocytes, and cardiomyocytes (Hamming et al., 2004; Hikmet et al., 2020; Ortiz et al., 2020; Zhao et al., 2020). The presence of ACE2 protein in nasopharyngeal, lung, and gastrointestinal tract epithelial cells correlates with the known entry routes for SARS-CoV-2 infection (Li et al., 2020; Lukassen et al., 2020; Ortiz et al., 2020; Sugnak et al., 2020). Note that expression of ACE2 may reflect localisation of the protein to the endothelia of vascularised tissues, and interpretation should consider this. ACE2 protein and mRNA expression in human tissue is summarised in Fig 6.1., showing data collated by the Human Protein Atlas (Human Protein Atlas [proteinatlas.org](https://www.proteinatlas.org)) (Uhlén et al., 2015). It is noteworthy that, given ACE2 is localised to the X chromosome, females show higher overall expression or ‘gene dosing’ of the protein, and that this may surprisingly confer reduced susceptibility to SARS-CoV-2 morbidity and mortality versus males (Scully et al., 2020; Viveiros et al., 2021).

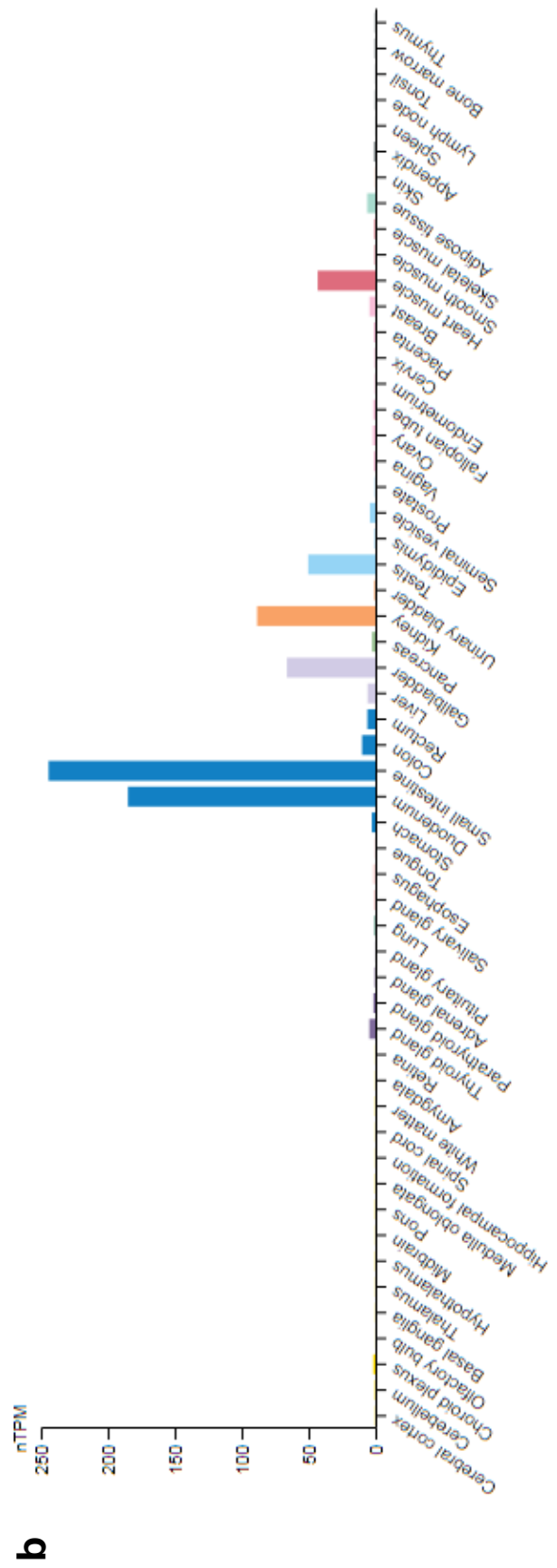
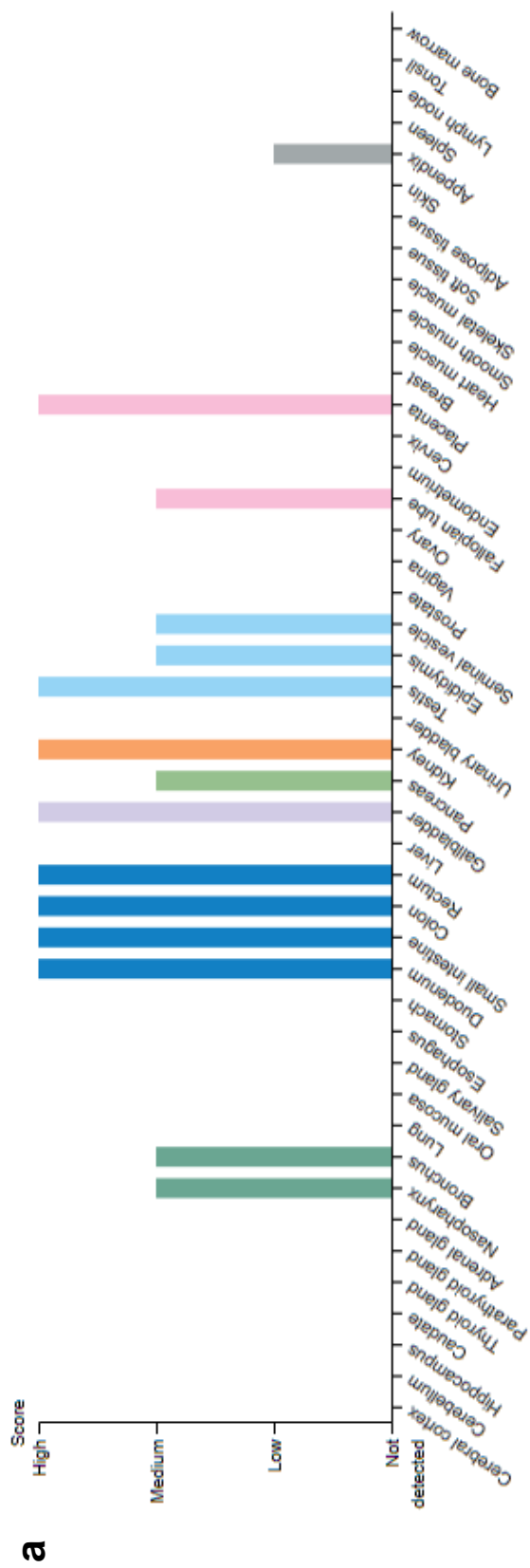


**Figure 6.1.** Data showing ACE2 protein (a) and mRNA (b) expression in human central and peripheral tissues from the Human Protein Atlas. Tissue expression was determined using immunohistochemistry in samples from surgical material from 144 individuals corresponding to 44 different normal tissue types, where normal is defined as non-neoplastic and morphologically normal. Annotation of protein expression scores were based on evaluation of staining intensity (negative, weak, moderate or strong), percentage cells stained in tissue (< 25 %, 25 – 75 % or > 75 %), and subcellular localisation (nuclear versus cytoplasmic versus membrane). For mRNA, 52 human tissue samples from consenting patients were analysed using RNA-sequencing to estimate transcript abundance of the gene encoding the protein of interest. Data are expressed as normalised transcripts per million (nTPM).

Recently, three independent reports published in Nature Genetics have provided insight into the spectrum of documented responses to infection by SARS-CoV-2, ranging from individuals who are asymptomatic to those with severe illness and ‘Long COVID’ that can have serious cardiovascular consequences. The reports outline the discovery of a novel short isoform of ACE2 (*delta*ACE2, herein referred to as dACE2), that comprises amino acids 357-805 of the full-length ACE2 protein, and possessing a unique 10 amino acid cap at the N-terminus (Ng et al., 2020; Onabajo et al., 2020; Blume et al., 2021). The protein is transcriptionally independent – i.e. it is not simply a cleavage product of ACE2 by ADAM17. For a schematic showing the different structures of dACE2 versus full-length ACE2, see Fig 6.2. Interestingly, the dACE2 protein lacks fully functional enzymatic activity, and loses the high affinity SARS-CoV-2 spike protein binding sites seen in the full-length protein. The short isoform is upregulated at the genetic level in airway epithelia and squamous tumours of the respiratory, gastrointestinal, and urogenital tracts, with the authors suggesting that dACE2 is unlikely to confer host susceptibility to SARS-CoV-2 due to its inability to bind spike protein. Whilst the focus of these reports was on dACE2 mRNA, the tissue distribution of dACE2 protein has not been characterised.

In this thesis, it was hypothesised that the tissue distribution of the non-infective dACE2 protein versus full-length ACE2 would be distinct between different tissue

beds, and that this may contribute in part to the inter-individual variation in susceptibility to SARS-CoV-2 infection. The work aimed to delineate different patterns of immunostaining using antibodies directed against different epitopes of ACE2 in human tissue sections from the major organs infected and/or damaged by SARS-CoV-2. Further, a fluorescently tagged SARS-CoV-2 spike receptor binding motif protein monomer (spike-AF647, see Fig 6.3 for structure), designed by Professor Anthony P. Davenport in collaboration with Cambridge Research Biochemicals, was used to confirm the distribution of full-length ACE2 and dACE2, and validate previous findings that dACE2 does not bind SARS-CoV-2 spike.

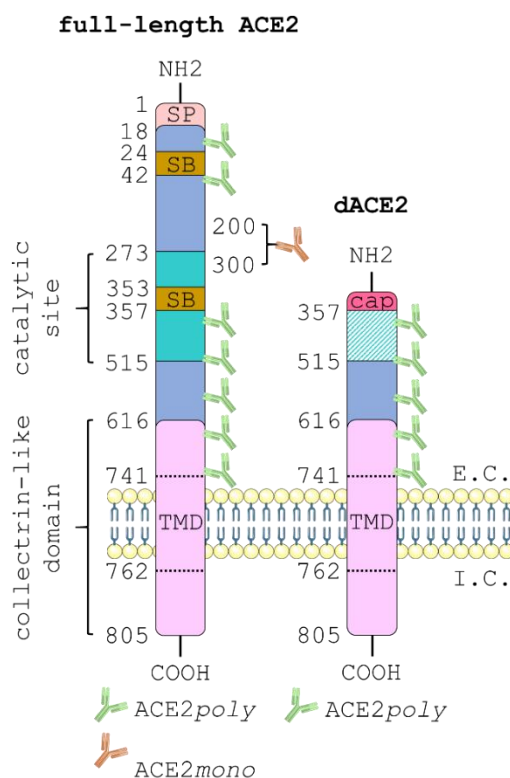


**Figure 6.2.** Schematic of full-length ACE2 (left) and the short dACE2 isoform (right). The full-length protein is 805 amino acids long, and comprises an extracellular domain (1-740), a transmembrane domain (TMD, 741-762), and an intracellular domain (763-805). A signal peptide (SP) caps the N-terminus at positions 1-18. The catalytic domain resides in positions 272-515, and the two spike protein binding sites (SB) reside at positions 24-42 and 353-357. The portion of the protein between positions 616-805 forms the collectrin-like domain. Note for dACE2, the protein lacks amino acids 1-356, losing functionality in the catalytic domain, and the ability to bind spike protein. The dACE2 isoform possesses a unique 10 amino acid at the N-terminus. The schematic also highlights the epitopes that the two antibodies used in experiments bind to. The polyclonal ACE2poly antibody (shown in green) is raised against an immunogen comprising sites 18-740 (extracellular domain) of the protein, whilst monoclonal ACE2mono antibody (shown in orange) binds to a proprietary binding site between positions 200-300 in the N-terminus. If full-length ACE2 is present, both green and orange fluorescent signal should be observed in immunological staining studies. If dACE2 is present, green fluorescent signal will be observed with an absence of orange signal. The schematic was generated using templates from Servier Medical Art (smart.servier.com).

## **6.2. Methods**

### ***6.2.1. Immunohistochemistry and slide scanner imaging***

Surgical samples of human tissue were obtained with informed consent and ethical approval (05/Q104/142). Tissues were snap frozen in liquid nitrogen before storage at -80 °C. For each tissue type, samples from at least 3 independent donors were cut, using a cryostat (-30 °C), into 10 µm sections and thaw mounted onto slides before return to storage at -80 °C.

Hydrated tissue sections were washed with PBS. In experiments using spike-AF647, sections were treated with a 1 µM concentration of the fluorescently tagged monomer in PBS for 30 mins in the dark at room temperature. Slides were fixed with 4 % formaldehyde for 20 mins, and non-specific staining was blocked with PBS + 10 % donkey sera for 2 h. After tipping solution off, sections were then incubated at 4 °C, overnight, with a primary goat polyclonal ACE2 antibody (*ACE2poly*; R&D, AF933) and/or a primary rabbit monoclonal antibody targeting the N-terminus of ACE2 (*ACE2mono*; Abcam, ab108252). Control sections were treated with buffer (see below) in the absence of primary antibodies. Sections were washed with PBS before incubating with secondary polyclonal antibodies conjugated to Alexa Fluor 488 or 555 (Abcam, ab150129 and Abcam, ab150066) for 1 h. Tissue sections were washed with PBS before treatment with Hoechst 33342 nuclear marker (Invitrogen, H3570) prepared at 10 µg/mL in PBS for 15 mins. After a final PBS wash, slides were blotted dry with lint-free tissue, mounted with ProLong Gold Antifade Mountant (Invitrogen, P36930), covered with a cover slip, and left at room temperature in the dark to set (≥ 48 h). Note, all antibodies were prepared in a buffer of PBS with 1% donkey sera, 0.1% Tween-20, and 3.3 mg/mL bovine serum albumin. See Table 6.1 for a summary of the antibodies and markers used, and their respective concentrations. Experiments and incubations were performed in low light/dark to minimise fading of fluorescent dyes.

Automated fluorescent images (16 bit, 0.325 x 0.325 µm scaling per pixel) were acquired using a Slide Scanner Axio Scan.Z1 (Zeiss) microscope with a Plan-Apochromat 20x/NA0.8 M27 objective lens, as described in Section 2.9.5.

### 6.2.2. Immunocytochemistry – ACE2 antibody validation

To validate the ACE2 antibodies used in this thesis, a CHO-K1 cell line transiently expressing an ACE2 construct was used in conjunction with immunocytochemistry. CHO-K1 cells were seeded in CellCarrier-96 Ultra Plates (PerkinElmer) at a density of 10 k/well and returned to an incubator (37 °C, 5 % CO<sub>2</sub>) for 24 h. Cells were then transiently transfected with a commercial Human angiotensin I converting enzyme (peptidyl-dipeptidase A) 2 (ACE2) tagged with GFP cDNA clone (RG208442; OriGene; 10 ng/uL final) using a TransIT-CHO Transfection Kit (MIR 2174; Mirus Bio) as per the manufacturer's instructions. Following a further 24 h incubation, cells were fixed and stained using the same protocol as described for human tissue sections in Section 6.2.1, with HBSS in place of PBS. Note also, that a donkey anti-goat secondary antibody conjugated to Alexa Fluor 555 and donkey anti-rabbit secondary antibody conjugated to Alexa Fluor 555 were used to visualise ACE2<sub>poly</sub> and ACE2<sub>mono</sub> in respective wells. See Table 6.1 for a summary of antibodies and markers used in this thesis.

<u>Protein/target</u>	<u>Manufacturer</u>	<u>Catalogue #</u>	<u>Species</u>	<u>Concentration</u>
ACE2	R&D	AF933	Goat	20 µg/mL
ACE2	Abcam	ab108252	Rabbit	1:100
<i>Anti-goat IgG AF488</i>	<i>Abcam</i>	<i>ab150129</i>	<i>Donkey</i>	<i>1:200</i>
<i>Anti-goat IgG AF555</i>	<i>Abcam</i>	<i>ab150130</i>	<i>Donkey</i>	<i>1:200</i>
<i>Anti-rabbit IgG AF555</i>	<i>Abcam</i>	<i>ab150066</i>	<i>Donkey</i>	<i>1:200</i>
Hoechst nuclear stain	Invitrogen	H3570	n/a	10 µg/mL
Spike-AF647	CRB	custom	n/a	1 µM

**Table 6.1.** Markers used in immunochemistry, with respective concentrations/dilutions used. Secondary antibodies are shown in italic.

[AF647]-[Azhx]-YLYRLFRKSNLKPFFERDISTEIYQAGSTPCNGVEGFNC-  
YFPLQSYGFQPTNGVGYQPYPYR-acid

**Figure 6.3.** Sequence of the fluorescently tagged SARS-CoV-2 spike receptor binding motif protein monomer (spike-AF647). AF647 is a dye structurally identical to Alexa Fluor 647, Azhx is 6-azidohexanoic acid, C represents cysteine residues across which a disulphide bridge is formed, and acid denotes the carboxy C-terminus.

### **6.2.3. H&E staining**

Haematoxylin and eosin (H&E) staining of tissue sections adjacent to those used in immunohistochemistry (Section 6.2.1) was kindly performed by Ms Rhoda Kuc. Slides were air dried for 20 mins at room temperature before incubation with haematoxylin solution (Sigma; Hematoxylin Solution, Harris Modified; HHS128) for 5 mins. Slides were then washed in running tap water until water ran clear. Slides were then incubated in Scott's Tap Water (NaHCO<sub>3</sub>, 3.5g/L; MgSO<sub>4</sub>, 20g/L in distilled water) for 1 min. Slides were washed in running tap water a second time. Slides were next incubated with eosin solution (Sigma; Eosin Y Solution, Aqueous; HT110280) for 10 mins. A final wash was performed in running tap water until water ran clear. Slides were sequentially dehydrated (2 mins at each step) through an alcohol series (30 %, 70%, and 100 % ethanol). Slides were then cleared with xylene for 1 h before mounting with DePeX mounting medium (Serva) and being covered with a cover slip. Slides were then left to cure overnight.

### **6.2.4. Slide Scanner quantification**

Qualitative assessment of imaged human tissues sections was performed in collaboration with Dr Anna Paterson (Department of Pathology) who provided expertise in identification of anatomical structures.

Fluorescent tissue section images were quantified post-hoc using ZEN software (Zeiss). Regions of interest (ROI, Fig 6.4), such as tubules in the renal cortex, glomeruli, airway epithelia, and bile duct epithelia were identified, and a spline contour

tool was used to encircle sample regions in fluorescent images. Brightfield images of H&E stained tissue sections (Fig 6.5) were used to facilitate identification of ROI. In fluorescent images, mean fluorescence intensities for respective antibodies in ROI were provided by ZEN software. Owing to inherent differences in the brightness of each antibody and the fact that polyclonal antibodies bind to multiple epitopes, mean fluorescence intensities were normalised for each antibody relative to their own respective brightness in regions of studied tissues where signal was deemed to be low (e.g. renal medulla, respiratory connective tissue, liver hepatocytes), and presented as mean fold change from these regions  $\pm$  SD.

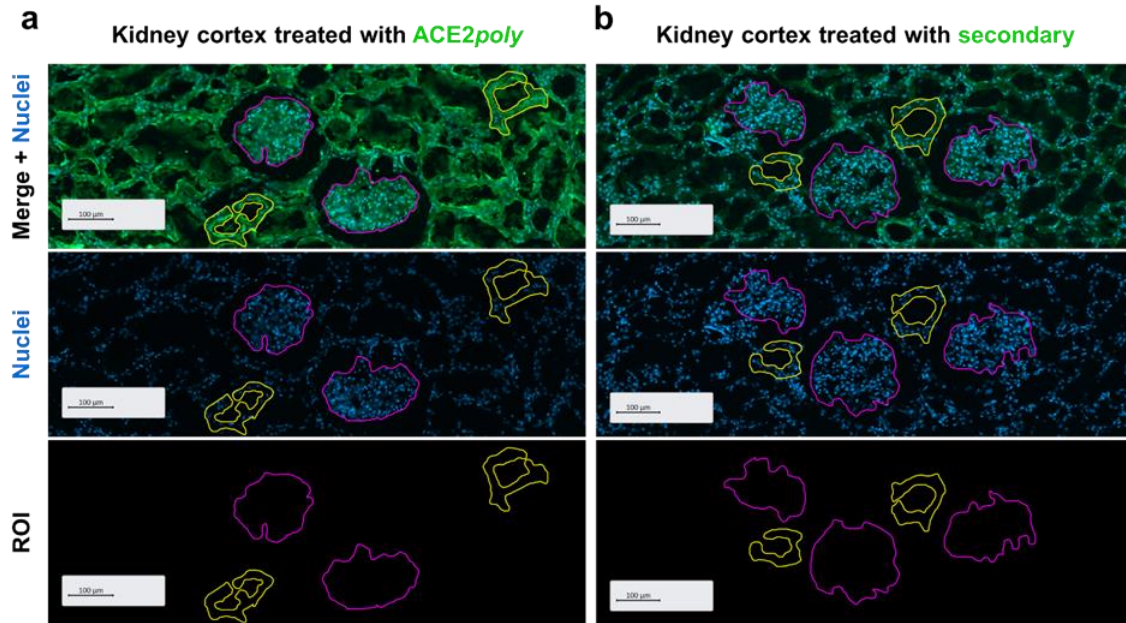


**Figure 6.4.** Representative examples of quantification of ACE2 fluorescence in regions of interest (ROI) of human tissue sections using ZEN software (Zeiss). Scale bars as indicated in figure. Nuclei shown in blue. **a** Positive staining (left column) for ACE2 with the ACE2poly antibody, visualised with a secondary antibody conjugated to Alexa Fluor 488 (shown in green). A free-hand drawing tool was used to isolate glomeruli (magenta) and tubules of the renal cortex (yellow) as ROI. Note the dense clustering of nuclei in glomeruli that allowed for their identification. Mean fluorescence intensity, measured in grayscales at a bit depth of 16, was provided by ZEN for each ROI. Note that the lumen of tubular structures are discounted from the analyses to prevent inaccurate averaging of fluorescence intensity. **b** Control staining (right column) in human kidney cortex treated with the secondary antibody in the absence of ACE2poly. Control tissue showed visibly lower levels of staining. Again, glomeruli are isolated in magenta and tubules in yellow, and mean fluorescence intensities in these ROI were provided by ZEN.

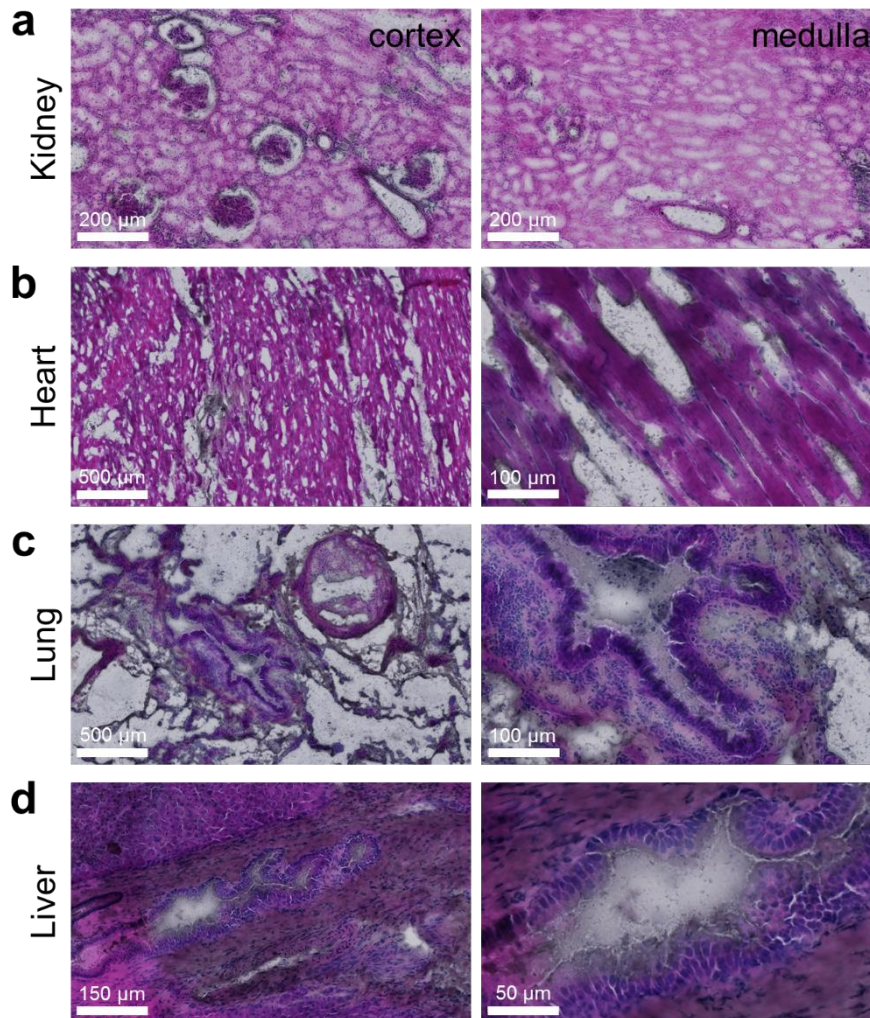


**Figure 6.5.** Brightfield images of H&E stained human tissue sections used to facilitate identification of regions of interest (ROI). Scale bars as indicated in figure. **a** Kidney sections showing renal cortex (left column) with a relatively high abundance of glomeruli visible (with dense nuclear clustering) in the image, and renal medulla (right column) with a relatively low/absent abundance of glomeruli. **b** Left ventricle tissue section from human heart showing a large view of cardiac tissue (left column), and individual cardiomyocytes (right column) that make up the bulk of the tissue. **c** Lung tissue with a visible airway structure showing the epithelium, and a large blood vessel. The right-hand column shows the airway epithelium at a higher magnification. **d** Liver tissue showing an intra-hepatic section of bile duct. Again, the right-hand column shows the structure at a higher magnification, with the epithelial cells visible in the image.

### **6.2.5. Opera Phenix High Content Screening**

Fluorescent confocal images of CHO-K1 cells prepared as described in Section 6.2.2 were captured using the Opera Phenix High Content Screening System microscope with a 40x/NA1.1 water immersion objective, as described in Section 2.9.3.

### **6.2.6. Multiphoton Microscope Leica TCS SP8 MP imaging**

To visualise far-red fluorescence (647 nm) in experiments using 1  $\mu$ M spike-AF647, tissue sections were imaged using a Leica TCS SP8 multiphoton confocal fluorescent microscope (Leica Microsystems), as described in Section 2.9.7.

## **6.3. Results**

### **6.3.1. Tissues and organs targeted by SARS-CoV-2 express ACE2**

Using immunohistochemistry with the *ACE2poly* antibody, ACE2 protein was visualised in several of the human tissue sections that are known to be targeted by SARS-CoV-2 (Fig 6.6). In the kidney (Fig 6.6a), immunoreactivity (shown in green) shows strong positive signal in the renal cortex, with less signal observed in the glomeruli and renal medulla. Kidney sections are shown as controls (Fig 6.6b), where very low levels of fluorescence were observed when using the same imaging settings but treating tissue with secondary antibody alone, indicating the dependency on the primary *ACE2poly* antibody for immunoreactivity and signal.

In the left ventricle of the heart (Fig 6.6c), positive immunoreactivity was observed at a similar level across the cardiomyocyte population. Lung tissue (Fig 6.6d), widely acknowledged as one of the primary sites for SARS-CoV-2 infection, show strong positive immunoreactivity throughout the section, but with particularly bright signal observed in the respiratory epithelia. In the liver (Fig 6.6e), hepatocytes showed relatively low positive immunoreactivity across the population, but signal was visibly brighter in the bile duct epithelium. Lastly, positive staining was detected in hepatic artery sections (Fig 6.6f), particularly at the endothelial edge.

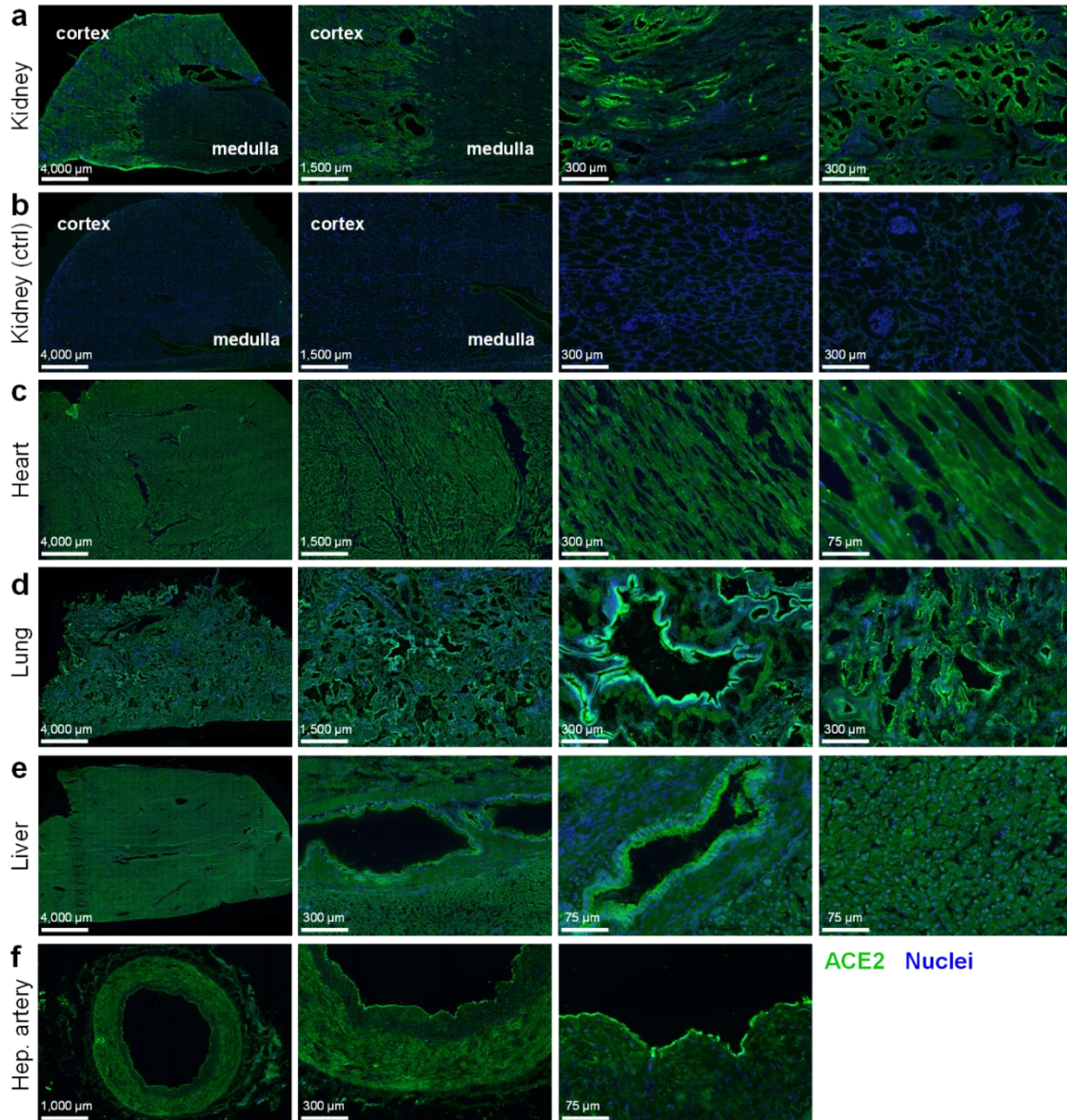


**Figure 6.6.** Representative slide scanner fluorescent images showing positive immunoreactivity for ACE2 protein in human tissues infected and/or damaged by SARS-CoV-2. Fixed tissue sections ( $n \geq 3$  individual donors, stained in duplicate) were stained with ACE2 $poly$  antibody (visualised in green) and Hoechst nuclear marker (visualised in blue). Scale bars as indicated in figure. **a** Kidney sections showed distinct regions of the cortex and medulla (as indicated in figure). Glomeruli can also be clearly seen in the far-right panel. **b** Control kidney sections were treated with secondary antibody in the absence of the primary ACE2 $poly$  antibody. Very low fluorescence was observed in the relevant green channel. **c** Cardiomyocytes in the left ventricle of the heart showed positive immunoreactivity that is homogenous across

the population. **d** Lung tissue showed positive immunoreactivity that is particularly bright in respiratory epithelia (centre-right and far-right panels). **e** Liver tissue sections showed positive immunoreactivity that was homogenous across the hepatocyte population, but was visibly brighter in bile duct epithelia (centre-right panel). **f** Hepatic artery showed positive immunoreactivity that was particularly bright at the endothelial edge.

Quantification of fluorescent images including the representative examples in Fig 6.6, confirmed that *ACE2poly* fluorescence was significantly higher than secondary antibody fluorescence in the absence of *ACE2poly*, indicating that signal is dependent on the inclusion of *ACE2poly* antibody (Fig 6.7). Comparative immunoreactivity in ROI across all tissue sections examined is also shown in Fig 6.7.

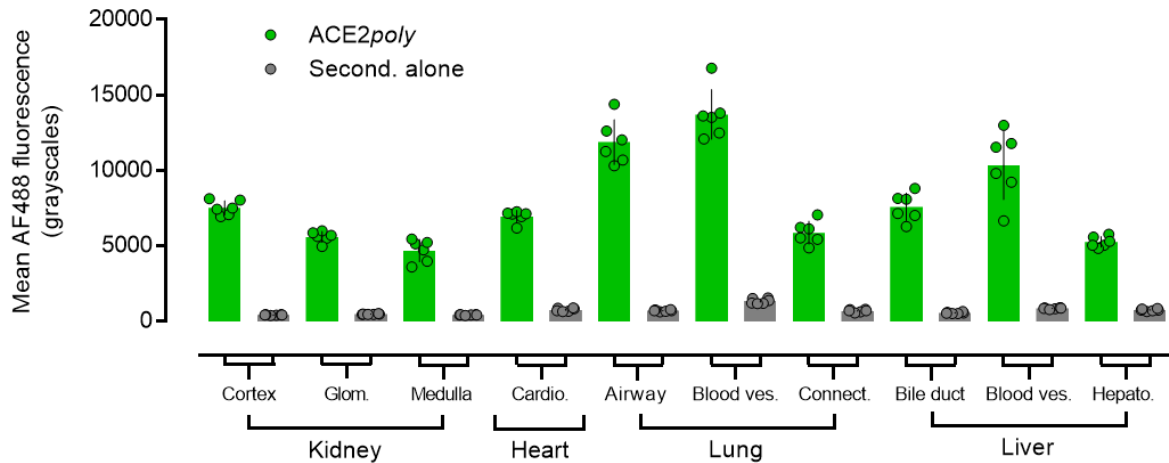


**Figure 6.7.** Graphical data showing quantification of fluorescence intensity (mean  $\pm$  SD) for ACE2 fluorescence, measured in grayscales at a bit depth of 16, in regions of interest (ROI) in human tissue sections (n = 6 ROI, across n  $\geq$  2 tissue donors) imaged as in Fig 6.6. ROI were identified as described in Fig 6.4. In all tissue types, staining with ACE2poly was significantly higher than in tissue sections treated with the secondary antibody alone. Significance (p < 0.05) was determined using a one-way ANOVA with Tukey's correction for multiple comparisons. For clarification, Glom. = glomeruli; Cardio. = cardiomyocytes; Blood ves. = blood vessels; Hepato. = hepatocytes.

### 6.3.2. The short dACE2 isoform localises to epithelial cells in lung and liver but is not enriched in the kidney or heart

Owing to the fact that ACE2poly binds to multiple epitopes of ACE2 whilst ACE2mono binds to a single epitope in the N-terminus (summarised in Fig 6.2), dual antibody staining was used to distinguish between full-length ACE2 and short dACE2 in human tissue sections, where reduced ACE2mono staining in the presence of ACE2poly suggests the presence of dACE2 (Fig 6.8).

In kidney sections, both antibodies showed strong immunoreactivity. ACE2poly and ACE2mono were visualised as colocalising in the epithelial cells lining tubules in the renal cortex (Fig 6.8a). Less staining for both antibodies was observed in the glomeruli (Fig 6.8a), and epithelial cells lining tubules in the renal medulla (Fig 6.8b). Overall, staining in the kidney suggested that ACE2 protein present in this tissue type is

predominantly the full-length isoform. In the heart (Fig 6.8c), the cardiomyocytes making up the bulk of the left ventricle sections stained positively with both *ACE2poly* and *ACE2mono*, in a pattern that was homogenous across the cardiomyocyte population. The data suggest that the predominant isoform is full-length ACE2 in this tissue.

In lung tissue (Fig 6.8d), staining with *ACE2poly* was visualised in epithelial cells lining airway structures, whilst staining with *ACE2mono* was substantially lower. This provides evidence that, in the airway epithelia, ACE2 is present and that a considerable proportion of the expressed protein lacks the N-terminal epitope necessary for *ACE2mono* binding. Overall, the data suggest that dACE2 is expressed in lung airway epithelia, in accordance with previous findings in the literature that show dACE2 mRNA in lung tissue and a differentiated lung airway cell line. In blood vessels and connective tissue of the lung, *ACE2poly* and *ACE2mono* showed good colocalisation, which suggests that full-length ACE2 is expressed in these structures, and it is only airways that exhibit differential expression of dACE2 versus full-length ACE2.

Interestingly, certain epithelial substructures in the liver also showed differential staining with the two ACE2 antibodies. Hepatic bile duct epithelia (Fig 6.8e) stained positively with *ACE2poly*, that, as was seen in airway epithelia, did not colocalise with *ACE2mono*, indicating expression of dACE2. In the hepatocytes themselves (Fig 6.8f), both *ACE2poly* and *ACE2mono* showed low levels of staining that did colocalise, demonstrating low expression of full-length ACE2 in these cells.

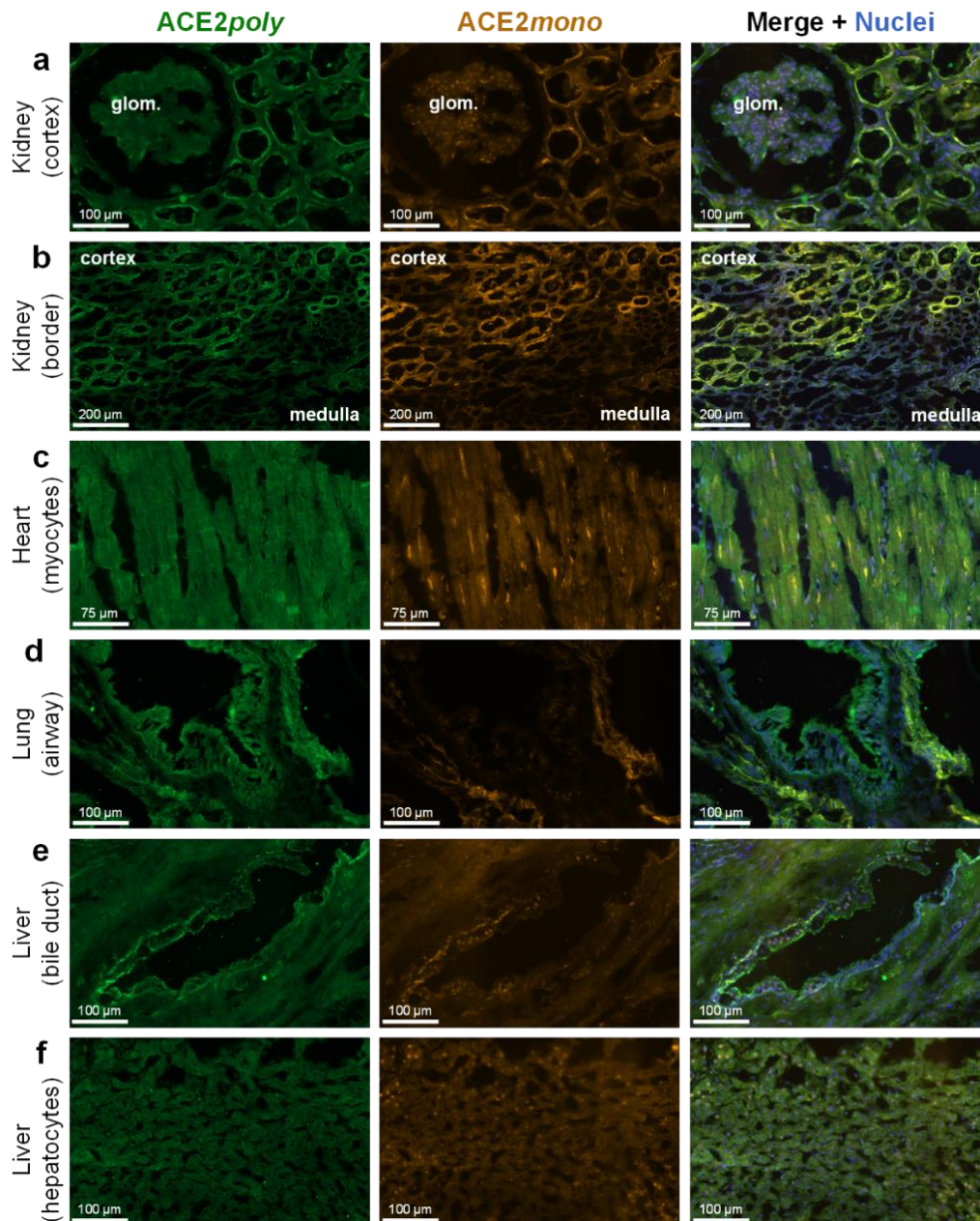


**Figure 6.8.** Expression of full-length ACE2 versus short dACE2 in human tissue sections (n ≥ 3 individual donors, stained in duplicate). Images show representative slide scanner fluorescent images showing immunoreactivity of *ACE2poly* (left column, visualised in green) and *ACE2mono* (centre column, visualised in orange), with Hoechst nuclear marker (shown in merge, visualised in blue). Scale bars as indicated in figure. **a** Kidney cortex with a glomerulus indicated (glom.). **b** Kidney border where renal cortex meets the renal medulla. **c** Cardiomyocytes in left ventricle heart tissue. **d** Lung tissue showing epithelial cells lining an airway structure. **e** Liver tissue with a visible bile duct structure. **f** Hepatocytes in the liver.

Quantification of fold changes in mean fluorescence for both antibodies in ROI in human tissue sections (Fig 6.9) closely matched visual assessments. In the kidney (Fig 6.9a), fold change in mean fluorescence for *ACE2poly* was significantly higher in the renal cortex ( $2.74 \pm 0.21$ ) versus the glomeruli ( $1.02 \pm 0.05$ ), all normalised against the renal medulla ( $1.00 \pm 0.13$ ). *ACE2mono* fold change in mean fluorescence was also significantly higher in the cortex ( $2.93 \pm 0.41$ ) versus the glomeruli ( $0.99 \pm 0.07$ ), again normalised against the medulla ( $1.00 \pm 0.13$ ). *ACE2poly* and *ACE2mono* were not significantly different from each other in any region, suggesting the presence of full-length ACE2.

In lung tissue (Fig 6.9b), fold change in mean fluorescence for *ACE2poly* was significantly higher in airway structures ( $2.26 \pm 0.41$ ) versus normalised fluorescence in connective tissue ( $1.00 \pm 0.17$ ). Conversely, the fold change in mean fluorescence for *ACE2mono* ( $1.11 \pm 0.26$ ) was not significantly different versus normalised fluorescence in connective tissue for this antibody ( $1.00 \pm 0.09$ ). The data suggest that, while ACE2 is enriched in airways, as detected by increased *ACE2poly*, we observe enrichment of dACE2, and not the full-length isoform that is stained by *ACE2mono*. Statistical analysis confirmed that the fold change for *ACE2poly* in airways was significantly higher than the fold change observed for *ACE2mono*. There was no significant difference in fold change in mean fluorescence between the two antibodies in blood vessels in the lung, indicating that the enrichment of dACE2 is observed only in airway structures.

Quantification in liver tissue (Fig 6.9c) demonstrated a significantly higher fold change in mean fluorescence for *ACE2poly* in the bile duct ( $2.48 \pm 0.33$ ) versus the normalised value in hepatocytes ( $1.00 \pm 0.16$ ). However, fold change in mean fluorescence for *ACE2mono* ( $1.22 \pm 0.11$ ), was not significantly different versus the normalised value in hepatocytes for this antibody ( $1.00 \pm 0.26$ ). As was seen in airways in the lung, the data in the liver suggest that there is an enrichment of ACE2 in the bile duct that is predominantly the short dACE2 isoform, directly indicated by the significantly higher *ACE2poly* fold change in mean fluorescence versus that seen for *ACE2mono* in the bile duct structure. As was also observed in the lung, hepatic blood vessels did not display significant differences in fold change in mean fluorescence between the two

antibodies, suggesting ACE2 expressed in these structures is likely the full-length isoform. Overall, the qualitative and quantitative data in liver sections points to an epithelial enrichment of the short dACE2 isoform in the bile duct that is similar to that observed for epithelial cells in the airway of the lung.

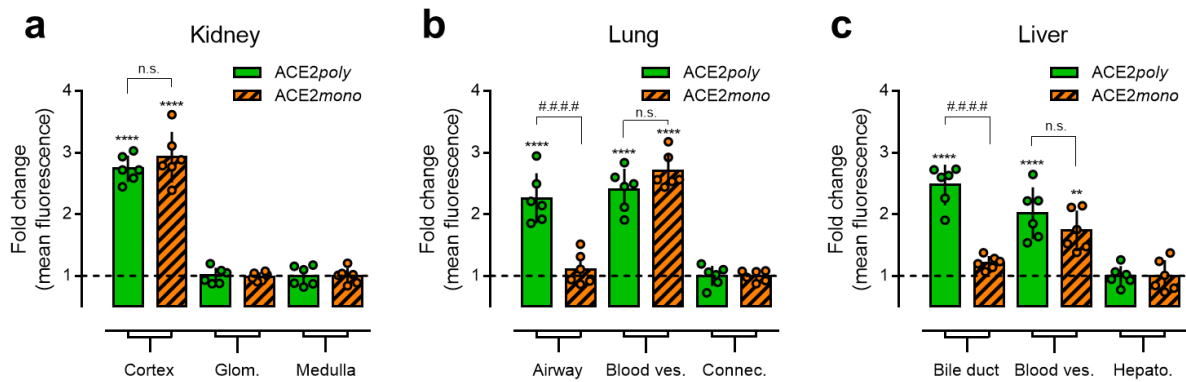


**Figure 6.9.** Quantification of differential staining with *ACE2poly* and *ACE2mono* as a surrogate measure of ACE2 isoform enrichment. Graphs display the fold change in mean fluorescence observed for *ACE2poly* and *ACE2mono* in specific ROI of human tissue sections. For each ROI,  $n = 6$  from  $\geq 2$  independently donated tissue sections. Fold change in mean fluorescence observed in: **a** Kidney cortex and glomeruli (Glom.), versus the normalised value in the renal medulla. **b** Airway structures and blood vessels (Blood ves.) of the lung, versus the normalised value in the connective tissue (Connec.). **c** Liver bile ducts and blood vessels (Blood ves.), versus the normalised mean fluorescence observed in liver hepatocytes (Hepato.). All data show mean  $\pm$  SD. with individual data points shown. Statistical analyses of data included a one way ANOVA with multiple comparisons using Tukey's correction. Statistical significance given if  $p < 0.05$ . \*\*\*\* or #### =  $p < 0.0001$ ; \*\* =  $p < 0.01$ ; n.s. = no significant difference.

To validate the specificity of the *ACE2poly* and *ACE2mono* antibodies used in this study, immunocytochemistry performed in a CHO-K1 cell model artificially expressing an ACE2-GFP construct was used (Fig 6.10). Both the *ACE2poly* (Fig 6.10a) and *ACE2mono* (Fig 6.10b) bound with good specificity to only those cells in the population that expressed the construct. Importantly, neither of the secondary antibodies used to visualise the primary antibodies displayed non-specific binding (Fig 6.10c) to CHO-K1 cells.

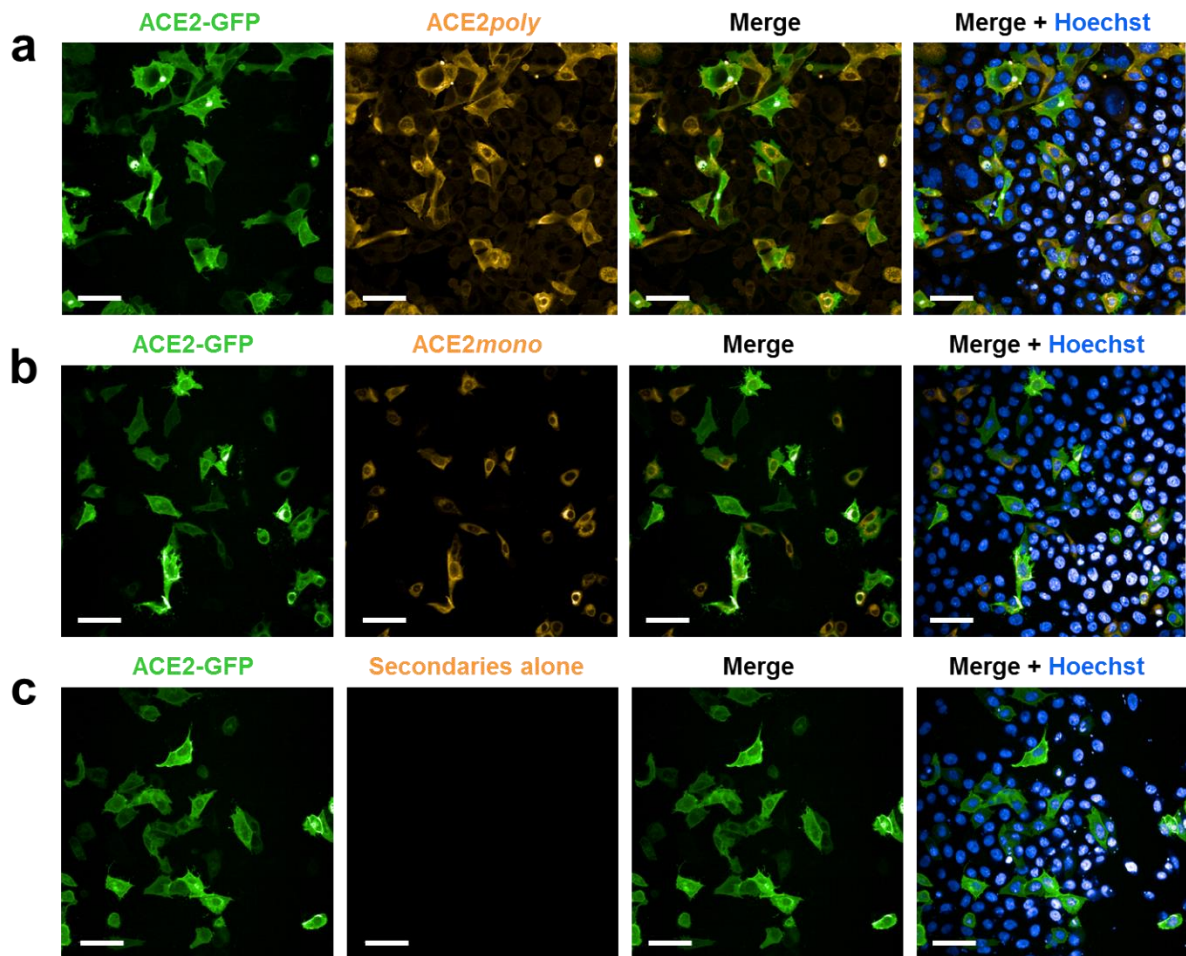


**Figure 6.10.** Validation of *ACE2poly* and *ACE2mono* antibodies in a CHO-K1 cell model artificially expressing ACE2. In all instances, representative fluorescent confocal images ( $n = 3$  experiments performed in duplicate), show the ACE2-GFP construct in green, ACE2 antibody visualised with a secondary in orange, and nuclei visualised with Hoechst 33342 in the merge in the far right column. Scale bars show 50  $\mu\text{m}$ . **a** CHO-K1 cells expressing the ACE2-GFP construct (green) bind the *ACE2poly* antibody (orange) with good specificity, as seen in the merge. Hoechst shows that many cells in the population do not express the ACE2-GFP construct, and these cells show low to absent binding with *ACE2poly*. **b** *ACE2mono* also binds with specificity to only those cells expressing ACE2-GFP. **c** Secondary antibodies in the absence of the primary antibodies do not stain any cells in the population, indicating that the specific primary antibodies are prerequisite for fluorescent signal.

### **6.3.3. Tissue structures that are enriched with dACE2 show low binding with a fluorescently tagged spike protein monomer**

In the final part of this chapter, a fluorescently tagged SARS-CoV-2 spike receptor binding motif protein monomer (spike-AF647) was used to assess the potential consequences of dACE2 on viral binding in human tissue sections (Fig 6.11). In the tubules of the kidney cortex (Fig 6.11a), binding of ACE2*poly*, shown previously to colocalise with ACE2*mono* and thus indicating the presence of full-length ACE2, also bound spike-AF647. In the medulla of the kidney (Fig 6.11b), low ACE2*poly* signal correlated with low spike-AF647 fluorescence, suggesting that binding of spike-647 is dependent on the presence of ACE2. In the left ventricle (Fig 6.11c), fluorescent signal was observed for both ACE2*poly* and spike-AF647 that localised in the cardiomyocytes.

Intriguingly, in airway structures of the lung (Fig 6.11d), that previously showed an enrichment of dACE2, spike-AF647 fluorescence was very low, particularly at the epithelial edge, despite the abundance of ACE2*poly* signal. Similarly, at the epithelial edge of hepatic bile duct (Fig 6.11e), spike-AF647 fluorescence was extremely low and did not correlate with the high levels of staining observed for ACE2*poly*, falling in agreement with the previous findings showing enrichment of dACE2 here. In the hepatocytes themselves (Fig 6.11f), signal for ACE2*poly* and spike-AF647 were low but did localise with each other. In summary, the data suggest that spike-AF647 exhibits low binding in epithelial tissue structures in the respiratory airways and liver bile duct that are enriched with the short dACE2 isoform that lacks SARS-CoV-2 spike binding sites.

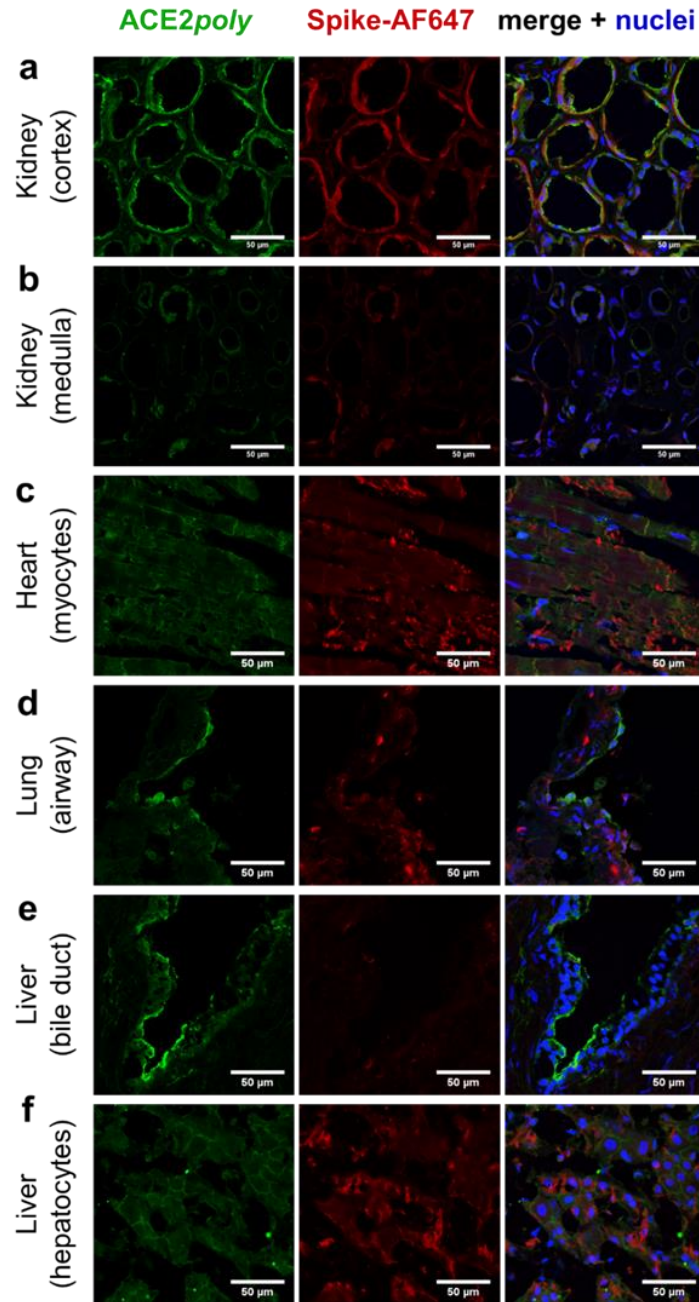


**Figure 6.11.** A SARS-CoV-2 spike receptor binding motif protein monomer (spike-AF647) binds at low levels to structures enriched with dACE2. Representative confocal fluorescent images ( $n \geq 2$  independent donors, stained in duplicate) of human tissue sections treated with ACE2poly (green), spike-AF647 (1  $\mu$ M, red), and Hoechst nuclear marker (blue, shown in merge). Scale bars as indicated in figure. **a** Kidney cortex. **b** Kidney medulla. **c** Cardiomyocytes in left ventricular heart tissue. **d** Lung tissue, with a visible airway epithelium. **e** Liver tissue, with a visible intra-hepatic bile duct epithelium. **f** Liver hepatocytes.

## **6.4. Discussion**

### ***6.4.1. ACE2 is present in organs infected and/or damaged by SARS-CoV-2***

The current consensus suggests that ACE2 is prerequisite for SARS-CoV-2 viral infection, and that infection does not occur in host cells that do not express the receptor enzyme at the cell surface (Hoffman et al., 2020; Wrapp et al., 2020; Yang et al., 2020). The data confirm, using immunohistochemistry, the protein expression of ACE2 in several human tissues – including kidney, heart, lung, and liver – that are widely acknowledged as sites of SARS-CoV-2 infection and damage (Gavriatopolou et al., 2020).

In the kidney (Fig 6.6a), data show high expression of ACE2 in the tubules of the renal cortex, above the levels observed for the protein in the glomeruli, and tubules of the renal medulla. In cardiac tissue (Fig 6.6c), specifically the left ventricle that is the chamber responsible for pumping blood around the body, nearly all observed cardiomyocytes expressed ACE2. It is interesting to note that the heart is widely acknowledged as a target of SARS-CoV-2 infection and damage, particularly in ‘Long COVID’, although the precise cardiovascular risks remain unclear. In the lung (Fig 6.6d), high levels of ACE2 were observed, especially in the epithelia of airway structures. Again, respiratory epithelia are recognised as a primary site of SARS-CoV-2 infection, where the virus induces its associated severe acute respiratory syndrome (Rendeiro et al., 2020). Intriguingly, epithelial cells in intra-hepatic bile duct (Fig 6.6e) also showed high levels of ACE2 staining, above the low but visible levels observed across the hepatocyte population. Hepatic impairment is also reported in individuals with severe SARS-CoV-2 infection (Zhang et al., 2020). Finally, immunohistochemistry showed positive ACE2 staining in sections of hepatic artery (Fig 6.6f), particularly at the endothelial edge, confirming the presence of ACE2 in the vasculature.

### ***6.4.2. Short dACE2 shows distinct localisation in epithelial cells in lung and liver***

The three recent reports outlining the identification of a novel short dACE2 isoform may provide further insight into the inter-individual differences in response to SARS-CoV-2 infection and outcomes (Ng et al., 2020; Onabajo et al., 2020; Blume et al., 2021). The dACE2 isoform does not possess enzymatic activity, or the spike protein

binding sites, characteristic of the full-length ACE2 protein. Whilst dACE2 mRNA is expressed in airway epithelia (*ex vivo* and cultured nasal epithelial cells), gastrointestinal tract and urogenital tract, protein expression is unmapped in human tissues.

To distinguish between dACE2 and full-length ACE2, antibodies raised against different epitopes of ACE2 (Fig 6.2) were used in tissue staining. Antibodies were validated where possible (see Fig 6.7 and Fig 6.10 for validation in tissue sections and a cell based platform respectively). Colocalisation of the *ACE2poly* and *ACE2mono* antibody signal in the epithelial edges of tubules of the kidney cortex (Fig 6.8a) suggests that the protein observed here is the full-length isoform. Levels of staining were consistently lower in the glomeruli (Fig 6.8a) and renal medulla (Fig 6.8b) but again, both antibodies stained positively. Colocalisation was also observed across the cardiomyocytes population in left ventricle cardiac tissue (Fig 6.8c). In the lung (Fig 6.8d), whilst both antibodies showed colocalised signal in blood vessels and connective tissue, *ACE2mono* staining was low to absent versus *ACE2poly* in epithelial cells lining airway structures. This suggests an enrichment of dACE2 in these cells, where ACE2 is present but does not bind the *ACE2mono* antibody. The findings fall somewhat in line with the published mRNA data in nasal epithelia (Blume et al., 2021). Interestingly, the study also identified similar enrichment of dACE2 at the luminal edge of epithelial cells lining intra-hepatic bile duct (Fig 6.8e), where again, low to absent *ACE2mono* signal was observed in the presence of *ACE2poly* signal. Conversely, hepatocytes (Fig 6.8f) showed low levels of staining but signal with both antibodies was detected across the cell population. Quantification corresponded with the qualitative assessments discussed so far, with significantly higher signal for *ACE2poly* versus *ACE2mono* determined in airway structures (Fig 6.9b) and bile duct structures (Fig 6.9c). The restricted enrichment of dACE2 to epithelial cells of the airways and bile duct demonstrated in this thesis present a highly interesting finding.

### 6.4.3. Implications of dACE2 in SARS-CoV-2 infection

The last part of this study aimed to use a fluorescently tagged SARS-CoV-2 spike receptor binding motif protein monomer (spike-647) to confirm the lack of spike protein binding sites in dACE2 and the functional implications of dACE2 in human tissue. Table 6.2 shows the reported sites in spike protein and ACE2 that interact when bound. Of note, only one amino acid, R357, remains present in dACE2 that interacts with the spike protein (H-bond with N501 of the spike protein). Note that the spike-647 monomer used in this thesis comprises amino acids 462 – 509 of the SARS-CoV-2 spike protein, capturing many of the residues involved in interaction with ACE2.

<u>Spike protein</u>	<u>ACE2</u>	<u>Interaction</u>
Q474	Q24	H-bond
K417	D30	H-bond
Y453	H34	H-bond
N501	Y41	H-bond
Q498	Q42	H-bond
F486	M82	van der Waals
N501	K353	H-bond
N501	R357*	H-bond

**Table 6.2.** Summary of interacting amino acids in SARS-CoV-2 spike protein bound to ACE2 identified in structural modelling in Yan et al., 2020. \*R357 is the only ACE2 residue that is present in the short dACE2 isoform, all the others are absent in dACE2.

Confocal fluorescent imaging demonstrated that, in areas where we previously observed enrichment of dACE2 – namely, the airway and bile duct epithelia – low to absent signal with spike-AF647 was seen in these structures (Fig 6.11d and Fig 6.11e respectively). Spike-AF647 binding, that colocalised with ACE2<sub>poly</sub>, was observed in areas where full-length ACE2 was identified, such as in the tubules in the renal cortex (Fig 6.11a), cardiomyocytes (Fig 6.11c), and hepatocytes (Fig 6.11f), providing evidence that spike-AF647 bound specifically to full-length ACE2.

The findings are potentially highly important, but further work is required to reconcile the enrichment of the ACE2 isoform that does not bind SARS-CoV-2 spike protein in tissue substructures, particularly the airways, that are known to act as primary sites of SARS-CoV-2 infection (Li et al., 2020; Lukassen et al., 2020; Ortiz et al., 2020; Schaefer et al., 2020; Sungnak et al., 2020; Gavriatopolou et al., 2020). The work in this thesis, and the reports in Nature Genetics (Onabajo et al., 2020; Blume et al., 2021), provide further insight into the complex and highly multi-faceted inter-individual responses to COVID-19, with the ratio of dACE2 to full-length ACE2 potentially playing a role in susceptibility to SARS-CoV-2 infection and symptoms.

## **6.5. Conclusions**

This study confirmed the presence of ACE2 in human tissues acknowledged as sites of SARS-CoV-2 viral infection and subsequent pathological symptoms. However, recent reports outlining a novel short dACE2 isoform, that lacks enzymatic activity and the ability to bind SARS-CoV-2 spike protein, raise currently unanswered questions regarding the expression and functional consequences of dACE2 at the protein level versus full-length ACE2. This short isoform is transcriptionally independent and not simply a cleavage product of ADAM17, and is upregulated by interferon, unlike the full-length ACE2 protein.

The data showed that dACE2 protein is enriched in epithelial structures in lung airways, a primary site of SARS-CoV-2 infection, and, interestingly, intra-hepatic bile duct. The areas where dACE2 was enriched also exhibited a reduced ability to bind spike-AF647, versus areas where the full-length ACE2 protein is expressed.

Individuals have shown great variability in susceptibility and response to SARS-CoV-2 infection. Reported reasons for this include differences in initial viral load, inherent biological differences (e.g. age, sex, genetic variation), lifestyle (e.g. diet, smoking), underlying co-morbidities, and, critically, the relative expression of ACE2. The ratio of dACE2 to full-length ACE2 therefore, may also play a highly important role in COVID-19 inter-individual variability, where dACE2 is unable to bind the viral spike protein and may therefore be protective. Whilst not enzymatically active, dACE2 may retain other

functions of the full-length protein, such as its role as a chaperone for the amino acid transporter, B<sup>0</sup>AT1, as the collectrin-like domain is identical to full-length ACE2. Higher expression of dACE2 could therefore also be beneficial for patients infected with SARS-CoV-2 and those with Long COVID or post-acute sequelae. Patients suffering from Long COVID typically report fatigue as a symptom which may be due to loss of B<sup>0</sup>AT1 as it internalises in complex with ACE2 following viral infection, and resultant insufficient amino acid uptake. Individuals with low dACE2 may be more susceptible to this phenomenon, potentially providing some explanation for why only certain individuals develop Long COVID. Further work will need to be done to fully characterise the extent of the effect of dACE2 in viral infection. It will also be important to elucidate the precise physiological roles of the enzymatically inactive protein, if any.

## 7. Concluding remarks

### 7.1. Apelin receptor summary

The apelin signalling axis, comprising the apelin receptor GPCR (O'Dowd et al., 1993), and its two endogenous peptide ligands, apelin (Tatemoto et al., 1998) and ELA (Chng et al., 2013; Pauli et al., 2014) is a key regulator of cardiac development, cardiovascular physiology, and cardiovascular disease (Yang et al., 2015; Read et al., 2019). As a GPCR, a family of proteins targeted by ~35 % of all clinically approved drugs (Santos et al., 2017; Sriram & Insel, 2018), pharmacological intervention at the apelin receptor is an attractive prospect in the treatment of diseases. Research has shown promising effects of apelin receptor stimulation in PAH, where exogenous apelin (Falcão-Pires et al., 2009) and ELA (Yang et al., 2017a) administration rescues downregulation of the peptides and reverses cardiopulmonary remodelling in a rat model of the disease. Additionally, apelin infusion significantly increases cardiac output and decreases pulmonary vascular resistance in PAH patients (Brash et al., 2015), with significant additive improvements also observed in patients receiving standard-of-care concomitant phosphodiesterase type 5 inhibitors (Brash et al., 2018), providing proof-of-principle for apelin treatment in PAH.

Whilst peptide ligands at GPCRs show high target specificity and affinity, and have been used successfully in disease treatment (Davenport et al., 2020), they are often limited in their clinical application owing to their typically poor pharmacokinetics and requirement for an intravenous route of administration. Apelin peptides themselves display a very short plasma half-life, in the range of ~5 – 8 minutes (Zhen et al., 2013; Murza et al., 2016), where they can be cleaved and inactivated by circulating enzymes (Vickers et al., 2002; Kazemi-Bajestani et al., 2012; Wang et al., 2016). Peptide modifications, such as cyclisation (Hamada et al., 2008; Brame et al., 2015) or conjugation to an AlbuAb anti-serum albumin domain antibody (Read et al., 2020), has led to the design of apelin peptides that exhibit improved half-lives, but do not bypass the lack of oral bioavailability. One of the more promising small molecule apelin receptor agonists to date, CMF-019, binds with high affinity (nanomolar range), and shows good activity in *in vitro* and *in vivo* settings (Read et al., 2016). Further, the

compound was identified as displaying G protein bias, avoiding  $\beta$ -arrestin mediated desensitisation and internalisation of the receptor, which is hypothesised to be highly beneficial in treatment of diseases associated with the apelin receptor, where loss of the target from the cell surface induced by agonist stimulation is minimised (Yang et al., 2015). However, CMF-019 is still limited by its poor solubility and the search for effective apelin receptor compounds is on-going.

The apelin receptor, like other GPCRs, is susceptible to genetic mutation, where the efficiency of the receptor to transduce extracellular stimuli to intracellular signal can be decreased, in loss-of-function mutations, or enhanced, in gain-of-function mutations (Thompson et al., 2014; Stoy & Gurevich, 2015), resulting in altered physiology (Schöneberg & Liebscher, 2021). Mutations can provide useful evidence for drug targets and effects in disease, where loss-of-function at a protein can mimic the administration of an antagonist, whilst gain-of-function can mimic administration of an agonist.

Only one naturally occurring mutation in the apelin receptor has been identified and characterised, the grinch<sup>s608</sup> (W85L) mutation in *aplnrb* in zebrafish, that prevents binding of apelin to cause poor, or even absent, cardiac development (Scott et al., 2007; Zeng et al., 2007). Several studies have artificially introduced mutations in the apelin receptor, and have provided major structural insight into the residues that regulate receptor trafficking (Langelaan et al., 2013), receptor phosphorylation (Chen et al., 2014), binding of ligands (Ma et al., 2017), and G protein signalling (Ban et al., 2018). Reported apelin receptor mutational analyses are discussed in-depth in Section 1.6.

In conjunction with modelling and *in vitro* analyses, the exploration of naturally occurring mutations in proteins, particularly those causally linked to a disease phenotype, can streamline the design of novel therapeutics by identifying residues that ligands should target or avoid. As mentioned, naturally occurring mutations in the human apelin receptor remain uncharacterised. In the work outlined in Chapter 4, 11 apelin receptor variants, identified in patients with rare cardiovascular and immune diseases recruited to the BRIDGE project, were selected for pharmacological

assessment based on stringent pre-determined exclusion criteria. The criteria allowed only those variants that were very rare and incorporated a mutation at a site that is highly conserved and predicted to be deleterious if substituted or deleted (a summary of the exclusion criteria can be found in Section 4.1). This meant that the variants explored were likely to show severely altered function versus the wild-type receptor.

As part of the work aiming to pharmacologically assess mutations in the selected apelin receptor variants, novel fluorescent ligands at the apelin receptor were designed and validated, as discussed in Chapter 3. Coinciding with improvements in high-throughput imaging techniques, fluorescent ligands are emerging as an increasingly versatile experimental tool for the exploration of ligand-protein interactions, including GPCR ligand binding (Vernall et al., 2014; Stoddart et al., 2015; Soave et al., 2017). In Chapter 3, four novel fluorescent peptides are described, two based on apelin-13 and two on ELA-14 endogenous peptides. The fluorescent ligands were validated for binding, function, and visualisation in both native tissue, clinically relevant hESC-CMs, and heterologous cells. Red fluorescent apelin and ELA ligands were subsequently used as part of the assessment of apelin receptor variants described in Chapter 4.

## **7.2. Apelin receptor study results**

Changes to pharmacological parameters, such as affinity for the target, is a limitation that can occur when fluorescently labelling ligands. In this thesis however, the four novel fluorescent ligands, apelin488, apelin647, ELA488, and ELA647, retained their *in vitro* binding and function at the apelin receptor, providing evidence that the [PEG4] linker and fluorescent dyes themselves did not abolish interaction and activity at the apelin receptor. Apelin488 and ELA488 were used successfully to visualise apelin receptor in human kidney tissue sections, where unlabelled endogenous [Pyr<sup>1</sup>]apelin was able to displace both ligands. Using antibodies to visualise the apelin receptor has been met with limited success in the Davenport lab previously, and the fluorescent peptide ligands may offer an alternative strategy to immunochemical techniques. Additionally, the group has attempted to design a radioligand based on ELA, but the radiolabelled peptide did not bind to human heart homogenate. The ELA fluorescent

ligands may provide the means to visualise and characterise binding of the second endogenous apelin receptor ligand, where previous evidence shows differential binding modes for ELA versus apelin. Fluorescent apelin647 was able to bind to hESC-CMs, a clinically relevant cardiomyocyte model, that endogenously expresses the apelin receptor, and a CHO-APLNR heterologous line, in a high content, plate-based imaging platform. The data confirm that apelin647 retains key pharmacological properties, and is a suitable, and in many ways superior, replacement for the [<sup>125</sup>I]-apelin-13 radioligand, where receptor affinity, density, and binding kinetics can be determined with higher replicates whilst using less sample protein. On top of this, apelin receptor subcellular localisation can be determined, with co-staining for nuclear and membrane compartments possible, and internalisation induced by apelin647 in live CHO-APLNR cells was able to be visualised in near real-time – both facets of receptor pharmacology that cannot be explored by radioligand binding in homogenised protein preparations.

In studies characterising the pharmacology of apelin receptor variants identified in the BRIDGE project, a preliminary radioligand binding screen revealed several of the variants, V38L, T89M, and R168H, altered receptor binding and were further explored. Note that the V38L and T89M mutations were identified in a subset of patients presenting with primary immune disease (PID), whilst the R168H mutation was identified in an individual in the bleeding and platelet disorder (BPD) branch of the BRIDGE project. It is unknown what disease phenotype exactly these patients exhibited, nor is it known if the apelin receptor mutations they possess are causative of the disease states. Nevertheless, high content imaging was used to qualitatively and quantitatively analyse the expression and membrane localisation of the variants, to confirm whether reduced or abolished binding of the radioligand, observed for V38L and R168H respectively, was due to decreased receptor density at the membrane. Intriguingly, V38L was shown to localise to a significantly lower extent at the membrane versus the wild-type receptor, whilst R168H membrane localisation was statistically the same as wild-type. The apelin647 and ELA647 fluorescent ligands were used to further assess the functional consequences of the V38L, T89M, and R168H variants.

The V38L variant bound the [<sup>125</sup>I]-apelin-13 radioligand with an affinity similar to wild-type receptor, but exhibited a much lower receptor density in HEK293T cell membrane preparations. Intriguingly, V38L was also able to bind the apelin647 ligand with high affinity, and bound as much apelin647 fluorescence as wild-type despite showing low membrane localisation in transfected CHO-K1 cells. The discrepancy between the radioligand and fluorescent ligand studies may be reflective of the membrane preparation versus live cell settings, and/or the HEK293T cells versus CHO-K1 cells used respectively. Additionally, the V38L variant showed function in a dynamic mass redistribution assay, suggesting G protein engagement and signalling was unperturbed in this variant. The location of the V38 residue close to G42, G45, and N46, all shown to be involved in receptor trafficking, may point to V38 also regulating trafficking of the apelin receptor. A subsequent experiment assessing internalisation demonstrated that V38L did not internalise to the same extent as wild-type following stimulation with apelin647, suggesting that, whilst the receptor is expressed at the membrane to a lesser extent, it may be more stable once there, and resistant to ligand induced internalisation. This might be the reason behind the high fluorescent signal observed for apelin647 bound V38L at the membrane in a live cell setting. The V38L variant also showed activity in a dynamic mass redistribution assay. A positive signal in this assay is typically dependent on G protein signalling at a stimulated GPCR, with little involvement of  $\beta$ -arrestin. Using  $\beta$ -arrestin or internalisation specific assays in future studies could delineate the precise impact of V38L on these pathways.

The T89M variant provided unique insight into the binding of apelin and ELA peptides. Affinity for the [<sup>125</sup>I]-apelin-13 radioligand was comparable to wild-type but receptor density was higher in both the preliminary binding screen and in revisited binding experiments. In fluorescent ligand studies, T89M was able to bind apelin647, but binding of ELA647 was significantly lower than wild-type, suggesting that the T89 site may have an as yet unreported regulatory role in the different binding modes observed for the two endogenous peptides. Competition radioligand binding provided further evidence for this, with ELA-11 less able to displace the radioligand at the T89M variant versus the wild-type. The dynamic mass redistribution assay showed that the T89M variant was responsive to stimulation with [Pyr<sup>1</sup>]apelin-13. An obvious next step would

be to assess ELA peptide function in this assay and others, to further understand the interplay between T89M and ELA.

In line with data from the Davenport group and others, suggesting that the R168 residue regulates ligand binding in the apelin receptor binding pocket, the R168H variant was unable to bind the radioligand or the apelin and ELA fluorescent ligands. Membrane localisation comparable to wild-type confirmed that R168H did not impact apelin receptor expression or distribution, and that lack of binding is intrinsically linked to the role of R168 in the binding pocket. Owing to its inability to bind ligands, R168H was expectedly non-functional in the dynamic mass redistribution assay. Additionally, an hESC-CM line carrying the heterozygous R168H apelin receptor variant was generated, and also showed no binding of apelin647 versus wild-type hESC-CMs. Future experiments could look to see if ligands could be designed to rescue the loss of binding at the apelin receptor in R168H hESC-CMs by avoiding interactions with the R168 amino acid.

Overall, the data provide proof-of-principle for the use of fluorescent ligands at the apelin receptor, and they have demonstrated success in characterising apelin receptor variants identified in patients recruited to the BRIDGE project. The variants themselves have provided in-depth information on several sites in the apelin receptor structure that have remained hitherto relatively unexplored. The identification of these sites may facilitate rational based drug design for new therapeutics at the apelin receptor to meet unmet clinical needs.

### **7.3. ACE2 summary**

The ACE2 zinc-metalloproteinase type 1 transmembrane protein (Tipnis et al., 2000; Donoghue et al., 2000; Hamming et al., 2007) specifically cleaves several peptides at the C-terminus (Vickers et al., 2002), with three key peptides including angiotensin, in the counter-regulatory arm of the RAAS (Oudit et al., 2003); des-Arg(9)-bradykinin in the KKS; and apelin in the apelin signalling axis that regulates the cardiovascular system (Wang et al., 2016; Yang et al., 2017b).

ACE2 is also exploited by human coronaviruses to infect host cells (Hamming et al., 2007; Gheblawi et al., 2020). The S1 domain of spike proteins adorning the outer layer of SARS-CoV and HCoV-NL63 bind to ACE2 with high affinity (Li et al., 2003, 2007; Hofmann et al., 2005), and SARS-CoV infection was shown to be ACE2 dependent, and induced subsequent downregulation in mice (Oudit et al., 2009). ACE2 has attracted much attention during the COVID-19 pandemic as the viral entry receptor also exploited by the SARS-CoV-2 virus, the spike protein of which binds to ACE2 with high ~15 nM affinity to infect cells (Hoffmann et al., 2020; Wrapp et al., 2020; Yan et al., 2020; Yang et al., 2020).

Unsurprisingly, ACE2 was posited as a potential drug target for combatting COVID-19 (Alexander et al., 2020). Additionally, Mendelian randomisation identified ACE2 as a risk factor for hospitalisation in COVID-19, and the results suggest prioritising ACE2 as an actionable drug target for prevention of SARS-CoV-2 infection (Gaziano et al., 2021). Nonetheless, a number of other host cell protein components are required for SARS-CoV-2 viral infection, which may also make suitable candidates for therapeutic targeting and drug repurposing. TMPRSS2 has been shown to be crucial for priming of the SARS-CoV-2 spike protein through cleavage of S1/S2 and S2' sites at the host cell surface (Shang et al., 2020; Hoffman et al., 2020). Additionally, the intracellular proteases, furin and cathepsin, mediate further spike protein priming and endosomal processing respectively, increasing infection of neighbouring cells with replicated viral particles (Cheng et al., 2020; Liu et al., 2020). ACE2 forms a dimer-of-heterodimers with the neutral amino acid transporter, B<sup>0</sup>AT1, via interaction with the collectrin-like domain of ACE2. The role of ACE2 as a chaperone for B<sup>0</sup>AT1 was initially identified in the gastrointestinal tract and kidney, where Hartnup disease is associated with mutations in B<sup>0</sup>AT1 that prevent interaction with ACE2 and collectrin to reduce appropriate membrane localisation of the transporter (Kowalczyk et al., 2008; Camargo et al., 2009; Fairweather et al., 2012). In light of COVID-19, the ACE2:B<sup>0</sup>AT1 complex is reportedly able to bind two SARS-CoV-2 spike proteins simultaneously, with higher affinity than ACE2 alone (Yan et al., 2020; Stevens et al., 2021), and B<sup>0</sup>AT1, when in complex, may have an impact on the engagement of ACE2 with TMPRSS2 (Stevens et al., 2020).

Several isoforms of ACE2 exist, but recently three independent reports intriguingly identify a novel short dACE2 (comprising amino acids 357-805 of the full-length protein), that lacks the catalytic domain and spike binding sites (Ng et al., 2020; Onabajo et al., 2020; Blume et al., 2021). It is possible that dACE2 is still able to perform its role as a chaperone for B<sup>0</sup>AT1. The role of this isoform is poorly understood in relation to SARS-CoV-2 infection, but the independent reports conclude that the virus is unable to exploit dACE2, and it can be speculated that the ratio of full-length ACE2 to dACE2 may influence the vast inter-individual variation observed in response to COVID-19 infection and symptoms.

#### **7.4. ACE2 results**

Following findings that SARS-CoV-2 infects and damages cardiomyocytes, the work in Chapter 5 of this thesis aimed to visualise ACE2 and the other necessary host cell proteins that mediate SARS-COV-2 infection in human left ventricle tissue sections. On top of this, an hESC-CM model was assessed for the presence of the proteins. Immunochemical analysis demonstrated positive staining for ACE2, TMPRSS2, B<sup>0</sup>AT1, cathepsin L, and furin in cardiomyocytes in the left ventricle. The same protein repertoire was visualised in the hESC-CM model, confirming that these cells accurately recapitulate the human tissue. Little to no staining was observed for cathepsin B. The mRNA encoding ACE2, TMPRSS2, B<sup>0</sup>AT1, cathepsin L, and furin was also expressed in both the tissue and model, matching the protein distribution.

Owing to their substantial potential for use in high-throughput screening platforms, the hESC-CMs were used in a screening assay in conjunction with a pseudotyped HIV-1 based lentivirus adorned with the SARS-CoV-2 spike protein that can be handled in lower levels of biological safety containment than the SARS-CoV-2 virus itself. The results demonstrated that the hESC-CMs were permissible to infection by the pseudotyped virus (indicated by a GFP reporter), and confirmed previous findings in cell lines that camostat, E64d, and a neutralising antibody are effective in reducing levels of spike dependent viral infection through inhibition of TMPRSS2, cathepsins, and ACE2 respectively. Intriguingly however, the screen described in this thesis identifies two novel inhibitors of infection that may have scope for clinical translation.

Benztropine, an inhibitor of B<sup>0</sup>AT1 used as a U.S. Food and Drug Administration approved treatment for Parkinsonism, was able to reduce spike dependent infection in the clinically relevant hESC-CM model. How inhibition of B<sup>0</sup>AT1 reduces infection remains to be fully elucidated, and it cannot be discounted that the drug may potentially have off-target effects. As an anticholinergic agent, benztropine displays typical side-effects such as dry mouth, blurred vision, constipation, and urinary retention, along with more serious adverse effects such as delirium, hallucinations, memory impairment, severe drowsiness, and tachycardia. These side-effects commonly occur at higher doses and given its low target specificity for B<sup>0</sup>AT1 ( $pIC_{50}$  value of 4.4) that would necessitate a high dose, its suitability for repurposing in COVID-19 may be limited. Another factor to consider would be how best to administer benztropine so that an appropriate concentration is delivered to target organs such as the gut and heart whilst avoiding off-target central effects. However, it is important to note that targeting B<sup>0</sup>AT1, as part of the B<sup>0</sup>AT1:ACE2 complex, is a potentially viable strategy in reducing SARS-CoV-2 infection if more specific ligands can be identified.

The second novel inhibitor to be identified was DX600, an irreversible peptide antagonist of ACE2 that binds to the catalytic domain, outside of spike binding sites. It is speculated that the DX600 peptide may sterically hinder binding of SARS-CoV-2 spike after docking irreversibly to the catalytic site and inducing a conformational change in ACE2, but this is yet to be experimentally determined. DX600 binds ACE2 with high affinity, but has not been tested for efficacy or tolerability *in vivo* or in humans. It is important also to consider potential side-effects of using DX600 clinically, where ACE2 counteracts angiotensin II vasoconstriction and fluid retention, to lower blood pressure (Burrell et al., 2004; Hamming et al., 2007; Tikellis et al., 2011). Given that the case fatality rate in COVID-19 patients rises from 2.3 % to 10.5 % in the presence of cardiovascular comorbidities (Sommerstein, 2020; Robinson et al., 2020), administering DX600 to patients infected with SARS-CoV-2 would have to be carefully considered to ensure that loss of the cardioprotective role of ACE2 did not outweigh the anti-infective benefit. As a peptide, the route of administration would also need to be considered as taking DX600 orally is unlikely to work. Additionally, the half-life is likely to be short in plasma when exposed to peptidases, meaning high concentrations may be required despite the high affinity afforded by peptides for their targets.

Nevertheless, the drug screening platform outlined in Chapter 5 could be utilised to identify further inhibitors of SARS-CoV-2 infection through targeting ACE2, B<sup>0</sup>AT1, or other protein targets necessary for viral uptake.

In Chapter 6, work aimed to characterise the protein expression and localisation of the short dACE2 isoform in a panel of human tissues. Using dual antibody staining with an ACE2*poly* antibody binding to multiple epitopes along the full extracellular portion of the ACE2 protein, and an ACE2*mono* antibody binding to a single epitope in a region that is not present in dACE2, absence of ACE2*mono* signal in the presence of ACE2*poly* is indicative of dACE2. Data showed positive staining for ACE2 in human kidney (localised to tubules in the cortex but to a lesser extent in the glomeruli and medulla), heart (localised to cardiomyocytes), lung (localised highly in epithelia lining airway structures, and liver (localised highly to epithelia lining the bile duct), matching reports suggesting that these tissue beds act as sites for SARS-CoV-2 infection and damage. Reduced ACE2*mono* signal, however, was subsequently observed only in the airway epithelium and bile duct epithelium, suggesting dACE2 was enriched only at these tissue substructures. Future experiments should aim to assess whether dACE2 is able to perform its chaperone role for the amino acid transporter B<sup>0</sup>AT1. Additionally, a fluorescently tagged spike protein monomer, spike-647, was used to assess SARS-CoV-2 spike binding at ACE2 versus dACE2. Data showed that reduced/absent spike-647 binding was observed in airway and bile duct epithelia where dACE2 had previously been shown to be enriched. The results may have important ramifications in understanding inter-individual variation in response to SARS-CoV-2 infection and damage, but it remains unclear why an enrichment of dACE2 at tissue substructures known to act as primary sites of SARS-CoV-2 infection was observed.

## **7.5. Final conclusions**

This thesis explores two crucial regulators of the human cardiovascular system, the apelin receptor and ACE2. As outlined, the functions of these proteins are highly intertwined, and both are hypothesised as offering potential as therapeutic targets in a multitude of pathophysiological states. Novel fluorescent ligands used in this thesis provide versatile new tools for the exploration of apelin and ELA binding at the apelin receptor, and were used successfully in in-depth mutational studies that have revealed V38L, T89M, and R168H as apelin receptor variants identified in humans that uniquely impact on the pharmacology of the receptor. A screening platform using hESC-CMs, shown to express ACE2 and other viral entry proteins and thus recapitulating human left ventricle tissue, identified two novel inhibitors of SARS-CoV-2 spike dependent viral entry. Benztropine, targeting B<sup>0</sup>AT1, and DX600, targeting the catalytic domain of ACE2 both reduced infection of hESC-CMs by the SARS-CoV-2 spike pseudotyped virus. Finally, exploration of the tissue expression and localisation of the short dACE2 isoform, that cannot bind SARS-CoV-2 spike protein, identified enrichment of dACE2 protein in respiratory and bile duct epithelia. It is hoped that the work presented in this thesis provides advancement in the understanding of the physiology and pharmacology of the apelin receptor and ACE2, potentially facilitating the development of novel therapeutic strategies at these tractable protein targets.

## Bibliography

- Adam, F., Khatib, A. M., Lopez, J. J., Vazier, C., Turpin, S., Muscat, A., ... Siegfried, G. (2016). Apelin: an antithrombotic factor that inhibits platelet function. *Blood*, 127(7), 908-920. doi:10.1182/blood-2014-05-578781
- Adhikary, P., Kandel, S., Mamani, U. F., Mustafa, B., Hao, S. Y., Qiu, J. M., ... Cheng, K. (2021). Discovery of Small Anti-ACE2 Peptides to Inhibit SARS-CoV-2 Infectivity. *Advanced Therapeutics*, 4(7)doi:10.1002/adtp.202100087
- Adzhubei, I. A., Schmidt, S., Peshkin, L., Ramensky, V. E., Gerasimova, A., Bork, P., ... Sunyaev, S. R. (2010). A method and server for predicting damaging missense mutations. *Nature Methods*, 7(4), 248-249. doi:10.1038/nmeth0410-248
- Aguilera, G. (1992). ROLE OF ANGIOTENSIN-II RECEPTOR SUBTYPES ON THE REGULATION OF ALDOSTERONE SECRETION IN THE ADRENAL GLOMERULOSA ZONE IN THE RAT. *Molecular and Cellular Endocrinology*, 90(1), 53-60. doi:10.1016/0303-7207(92)90101-b
- Akcilar, R., Turgut, S., Caner, V., Akcilar, A., Ayada, C., Elmas, L., & Ozcan, T. O. (2015). The effects of apelin treatment on a rat model of type 2 diabetes. *Advances in Medical Sciences*, 60(1), 94-100. doi:10.1016/j.advms.2014.11.001
- Alastalo, T. P., Li, M. L., Perez, V. D., Pham, D., Sawada, H., Wang, J. K., ... Rabinovitch, M. (2011). Disruption of PPAR gamma/beta-catenin-mediated regulation of apelin impairs BMP-induced mouse and human pulmonary arterial EC survival. *Journal of Clinical Investigation*, 121(9), 3735-3746. doi:10.1172/jci43382
- Alexander, S. P. H., Armstrong, J. F., Davenport, A. P., Davies, J. A., Faccenda, E., Harding, S. D., ... Spedding, M. (2020). A rational roadmap for SARS-CoV-2/COVID-19 pharmacotherapeutic research and development. *British Journal of Pharmacology*, 177(21), 4942-4966. doi:10.1111/bph.15094
- Alexander, S. P. H., Christopoulos, A., Davenport, A. P., Kelly, E., Mathie, A., Peters, J. A., ... Collaborators, C. (2019). THE CONCISE GUIDE TO PHARMACOLOGY 2019/20: G protein-coupled receptors. *British Journal of Pharmacology*, 176, S21-S141. doi:10.1111/bph.14748
- Aminde, L. N., Takah, N. F., Zapata-Diomed, B., & Veerman, J. L. (2018). Primary and secondary prevention interventions for cardiovascular disease in low-income and middle-income countries: a systematic review of economic evaluations. *Cost Effectiveness and Resource Allocation*, 16doi:10.1186/s12962-018-0108-9

- Badawi, S., & Ali, B. R. (2021). ACE2 Nascence, trafficking, and SARS-CoV-2 pathogenesis: the saga continues. *Human Genomics*, 15(1)doi:10.1186/s40246-021-00304-9
- Bailey, A. L., Dmytrenko, O., Greenberg, L., Bredemeyer, A. L., Ma, P., Liu, J., ... Lavine, K. J. (2021). SARS-CoV-2 Infects Human Engineered Heart Tissues and Models COVID-19 Myocarditis. *Jacc-Basic to Translational Science*, 6(4), 331-345. doi:10.1016/j.jacbts.2021.01.002
- Baker, J. G., Middleton, R., Adams, L., May, L. T., Briddon, S. J., Kellam, B., & Hill, S. J. (2010). Influence of fluorophore and linker composition on the pharmacology of fluorescent adenosine A(1) receptor ligands. *British Journal of Pharmacology*, 159(4), 772-786. doi:10.1111/j.1476-5381.2009.00488.x
- Balkau, B., & Eschwege, E. (1999). Insulin resistance: an independent risk factor for cardiovascular disease? *Diabetes Obesity & Metabolism*, 1, S23-S31. doi:10.1046/j.1463-1326.1999.0010s1023.x
- Ban, T., Li, X., Ma, X. C., Yang, H., Song, Y. P., Sun, Y. P., ... Hu, L. Y. A. (2018). GPCR structure and function relationship: identification of a biased apelin receptor mutant. *Biochemical Journal*, 475, 3813-3826. doi:10.1042/bcj20180740
- Barnes, G. D., Alam, S., Carter, G., Pedersen, C. M., Lee, K. M., Hubbard, T. J., ... Newby, D. E. (2013). Sustained Cardiovascular Actions of APJ Agonism During Renin-Angiotensin System Activation and in Patients With Heart Failure. *Circulation-Heart Failure*, 6(3), 482-+. doi:10.1161/circheartfailure.111.000077
- Basith, S., Cui, M. H., Macalino, S. J. Y., Park, J., Clavio, N. A. B., Kang, S., & Choi, S. (2018). Exploring G Protein-Coupled Receptors (GPCRs) Ligand Space via Cheminformatics Approaches: Impact on Rational Drug Design. *Frontiers in Pharmacology*, 9doi:10.3389/fphar.2018.00128
- Benza, R. L., Miller, D. P., Barst, R. J., Badesch, D. B., Frost, A. E., & McGoon, M. D. (2012). An Evaluation of Long-term Survival From Time of Diagnosis in Pulmonary Arterial Hypertension From the REVEAL Registry. *Chest*, 142(2), 448-456. doi:10.1378/chest.11-1460
- Berry, M. F., Pirolli, T. J., Jayasankar, V., Burdick, J., Morine, K. J., Gardner, T. J., & Woo, Y. J. (2004). Apelin has in vivo inotropic effects on normal and failing hearts. *Circulation*, 110(11), II187-II193. doi:10.1161/01.CIR.0000138382.57325.5c
- Bertero, A., Pawlowski, M., Ortmann, D., Snijders, K., Yiangou, L., de Brito, M. C., ... Vallier, L. (2016). Optimized inducible shRNA and CRISPR/Cas9 platforms for in vitro studies of human development using hPSCs. *Development*, 143(23), 4405-4418. doi:10.1242/dev.138081

- Blanchard, A., Steichen, O., De Mota, N., Curis, E., Gauci, C., Frank, M., ... Llorens-Cortes, C. (2013). An Abnormal Apelin/Vasopressin Balance May Contribute to Water Retention in Patients With the Syndrome of Inappropriate Antidiuretic Hormone (SIADH) and Heart Failure. *Journal of Clinical Endocrinology & Metabolism*, 98(5), 2084-2089. doi:10.1210/jc.2012-3794
- Blume, C., Jackson, C. L., Spalluto, C. M., Legebeke, J., Nazlamova, L., Conforti, F., ... Mennella, V. A novel ACE2 isoform is expressed in human respiratory epithelia and is upregulated in response to interferons and RNA respiratory virus infection. *Nature Genetics*doi:10.1038/s41588-020-00759-x
- Bojkova, D., Wagner, J. U. G., Shumliakivska, M., Aslan, G. S., Saleem, U., Hansen, A., ... Dimmeler, S. (2020). SARS-CoV-2 infects and induces cytotoxic effects in human cardiomyocytes. *Cardiovascular Research*, 116(14), 2207-2215. doi:10.1093/cvr/cvaa267
- Boucher, J., Masri, B., Daviaud, D., Gesta, S., Guigne, C., Mazzucotelli, A., ... Valet, P. (2005). Apelin, a newly identified adipokine up-regulated by insulin and obesity. *Endocrinology*, 146(4), 1764-1771. doi:10.1210/en.2004-1427
- Brame, A. L., Maguire, J. J., Yang, P. R., Dyson, A., Torella, R., Cheriyan, J., ... Davenport, A. P. (2015). Design, Characterization, and First-In-Human Study of the Vascular Actions of a Novel Biased Apelin Receptor Agonist. *Hypertension*, 65(4), 834-+. doi:10.1161/hypertensionaha.114.05099
- Brash, L., Barnes, G., Brewis, M., Church, C., Gibbs, S., Howard, L., ... Peacock, A. (2015). Apelin improves cardiac output in patients with pulmonary arterial hypertension. *European Respiratory Journal*, 46doi:10.1183/13993003.congress-2015.PA2107
- Brash, L., Barnes, G. D., Brewis, M. J., Church, A. C., Gibbs, S. J., Howard, L., ... Peacock, A. J. (2018). Short-Term Hemodynamic Effects of Apelin in Patients With Pulmonary Arterial Hypertension. *Jacc-Basic to Translational Science*, 3(2), 176-186. doi:10.1016/j.jacbts.2018.01.013
- Bulfamante, G. P., Perrucci, G. L., Falleni, M., Sommariva, E., Tosi, D., Martinelli, C., ... Pompilio, G. (2020). Evidence of SARS-CoV-2 Transcriptional Activity in Cardiomyocytes of COVID-19 Patients without Clinical Signs of Cardiac Involvement. *Biomedicines*, 8(12)doi:10.3390/biomedicines8120626
- Burrell, L. M., Johnston, C. I., Tikellis, C., & Cooper, M. E. (2004). ACE2, a new regulator of the renin-angiotensin system. *Trends in Endocrinology and Metabolism*, 15(4), 166-169. doi:10.1016/j.tem.2004.03.001
- Burrell, L. M., Risvanis, J., Kubota, E., Dean, R. G., MacDonald, P. S., Lu, S., ... Johnston, C. I. (2005). Myocardial infarction increases ACE2 expression in rat and humans. *European Heart Journal*, 26(4), 369-375. doi:10.1093/eurheartj/ehi114

- Calebiro, D., & Godbole, A. (2018). Internalization of G-protein-coupled receptors: Implication in receptor function, physiology and diseases. *Best Practice & Research Clinical Endocrinology & Metabolism*, 32(2), 83-91. doi:10.1016/j.beem.2018.01.004
- Camargo, S. M. R., Singer, D., Makrides, V., Huggel, K., Pos, K. M., Wagner, C. A., ... Verrey, F. (2009). Tissue-Specific Amino Acid Transporter Partners ACE2 and Collectrin Differentially Interact With Hartnup Mutations. *Gastroenterology*, 136(3), 872-882. doi:10.1053/j.gastro.2008.10.055
- Castan-Laurell, I., Dray, C., Attane, C., Duparc, T., Knauf, C., & Valet, P. (2011). Apelin, diabetes, and obesity. *Endocrine*, 40(1), 1-9. doi:10.1007/s12020-011-9507-9
- Cayabyab, M., Hinuma, S., Farzan, M., Choe, H., Fukusumi, S., Kitada, C., ... Sodroski, J. (2000). Apelin, the natural ligand of the orphan seven-transmembrane receptor APJ, inhibits human immunodeficiency virus type 1 entry. *Journal of Virology*, 74(24), 11972-11976. doi:10.1128/jvi.74.24.11972-11976.2000
- Ceraudo, E., Galanth, C., Carpentier, E., Banegas-Font, I., Schonegge, A. M., Alvear-Perez, R., ... Llorens-Cortes, C. (2014). Biased Signaling Favoring G(i) over beta-Arrestin Promoted by an Apelin Fragment Lacking the C-terminal Phenylalanine. *Journal of Biological Chemistry*, 289(35), 24599-24610. doi:10.1074/jbc.M113.541698
- Chandra, S. M., Razavi, H., Kim, J., Agrawal, R., Kundu, R. K., Perez, V. D., ... Chun, H. J. (2011). Disruption of the Apelin-APJ System Worsens Hypoxia-Induced Pulmonary Hypertension. *Arteriosclerosis Thrombosis and Vascular Biology*, 31(4), 814-U212. doi:10.1161/atvbaha.110.219980
- Chapman, F. A., Nyimanu, D., Maguire, J. J., Davenport, A. P., Newby, D. E., & Dhaun, N. (2021). The therapeutic potential of apelin in kidney disease. *Nature Reviews Nephrology*, 17(12), 840-853. doi:10.1038/s41581-021-00461-z
- Charo, D. N., Ho, M., Fajardo, G., Kawana, M., Kundu, R. K., Sheikh, A. Y., ... Quertermous, T. (2009). Endogenous regulation of cardiovascular function by apelin-APJ. *American Journal of Physiology-Heart and Circulatory Physiology*, 297(5), H1904-H1913. doi:10.1152/ajpheart.00686.2009
- Chatterjee, P., Gheblawi, M., Wang, K. M., Vu, J., Kondaiah, P., & Oudit, G. Y. (2020). Interaction between the apelinergic system and ACE2 in the cardiovascular system: therapeutic implications. *Clinical Science*, 134(17), 2319-2336. doi:10.1042/cs20200479

- Chen, L. J., Xu, R., Yu, H. M., Chang, Q., & Zhong, J. C. (2015). The ACE2/Apelin Signaling, MicroRNAs, and Hypertension. *International Journal of Hypertension*, 2015doi:10.1155/2015/896861
- Chen, M. M., Ashley, E. A., Deng, D. X. F., Tsalenko, A., Deng, A., Tabibiazar, R., ... Quertermous, T. (2003). Novel role for the potent endogenous inotrope apelin in human cardiac dysfunction. *Circulation*, 108(12), 1432-1439. doi:10.1161/01.cir.0000091235.94914.75
- Chen, X. M., Li, W. G., Yoshida, H., Tsuchida, S., Nishimura, H., Takemoto, F., ... Ichikawa, I. (1997). Targeting deletion of angiotensin type 1B receptor gene in the mouse. *American Journal of Physiology-Renal Physiology*, 272(3), F299-F304. doi:10.1152/ajprenal.1997.272.3.F299
- Chen, X. Y., Bai, B., Tian, Y. J., Du, H., & Chen, J. (2014). Identification of Serine 348 on the Apelin Receptor as a Novel Regulatory Phosphorylation Site in Apelin-13-induced G Protein-independent Biased Signaling. *Journal of Biological Chemistry*, 289(45), 31173-31187. doi:10.1074/jbc.M114.574020
- Cheng, Q., Shah, N., Broer, A., Fairweather, S., Jiang, Y., Schmolle, D., ... Broer, S. (2017). Identification of novel inhibitors of the amino acid transporter B(0)AT1 (SLC6A19), a potential target to induce protein restriction and to treat type 2 diabetes. *British Journal of Pharmacology*, 174(6), 468-482. doi:10.1111/bph.13711
- Cheng, Y. W., Chao, T. L., Li, C. L., Chiu, M. F., Kao, H. C., Wang, S. H., ... Yeh, S. H. (2020). Furin Inhibitors Block SARS-CoV-2 Spike Protein Cleavage to Suppress Virus Production and Cytopathic Effects. *Cell Reports*, 33(2)doi:10.1016/j.celrep.2020.108254
- Cheung, C., Bernardo, A. S., Pedersen, R. A., & Sinha, S. (2014). Directed differentiation of embryonic origin-specific vascular smooth muscle subtypes from human pluripotent stem cells. *Nature Protocols*, 9(4), 929-938. doi:10.1038/nprot.2014.059
- Chng, S. C., Ho, L. N., Tian, J., & Reversade, B. (2013). ELABELA: A Hormone Essential for Heart Development Signals via the Apelin Receptor. *Developmental Cell*, 27(6), 672-680. doi:10.1016/j.devcel.2013.11.002
- Choe, H., Farzan, M., Sun, Y., Sullivan, N., Rollins, B., Ponath, P. D., ... Sodroski, J. (1996). The beta-chemokine receptors CCR3 and CCR5 facilitate infection by primary HIV-1 isolates. *Cell*, 85(7), 1135-1148. doi:10.1016/s0092-8674(00)81313-6
- Choe, H., Martin, K. A., Farzan, M., Sodroski, J., Gerard, N. P., & Gerard, C. (1998). Structural interactions between chemokine receptors, gp120 Env and CD4. *Seminars in Immunology*, 10(3), 249-257. doi:10.1006/smim.1998.0127

- Choe, W., Albright, A., Sulcove, J., Jaffer, S., Hesselgesser, J., Lavi, E., ... Kolson, D. L. (2000). Functional expression of the seven-transmembrane HIV-1 co-receptor APJ in neural cells. *Journal of Neurovirology*, 6, S61-S69.
- Couvineau, P., Llorens-cortes, C., & Iturrioz, X. (2020). Elabela/Toddler and apelin bind differently to the apelin receptor. *Faseb Journal*, 34(6), 7989-8000. doi:10.1096/fj.201903029R
- Dalzell, J. R., Rocchiccioli, J. P., Weir, R. A. P., Jackson, C. E., Padmanabhan, N., Gardner, R. S., ... McMurray, J. J. V. (2015). The Emerging Potential of the Apelin-APJ System in Heart Failure. *Journal of Cardiac Failure*, 21(6), 489-498. doi:10.1016/j.cardfail.2015.03.007
- Danilczyk, U., Sarao, R., Remy, C., Benabbas, C., Stange, G., Richter, A., ... Penninger, J. M. (2006). Essential role for collectrin in renal amino acid transport. *Nature*, 444(7122), 1088-1091. doi:10.1038/nature05475
- Davenport, A. P., Scully, C. C. G., de Graaf, C., Brown, A. J. H., & Maguire, J. J. (2020). Advances in therapeutic peptides targeting G protein-coupled receptors. *Nature Reviews Drug Discovery*, 19(6), 389-413. doi:10.1038/s41573-020-0062-z
- de Gasparo, M., Catt, K. J., Inagami, T., Wright, J. W., & Unger, T. (2000). International union of pharmacology. XXIII. The angiotensin II receptors. *Pharmacological Reviews*, 52(3), 415-472.
- De Mota, N., Goazigo, A. R. L., El Messari, S., Chartrel, N., Roesch, D., Dujardin, C., ... Llorens-Cortes, C. (2004). Apelin, a potent diuretic neuropeptide counteracting vasopressin actions through inhibition of vasopressin neuron activity and vasopressin release. *Proceedings of the National Academy of Sciences of the United States of America*, 101(28), 10464-10469. doi:10.1073/pnas.0403518101
- De Mota, N., Lenkei, Z., & Llorens-Cortes, C. (2000). Cloning, pharmacological characterization and brain distribution of the rat apelin receptor. *Neuroendocrinology*, 72(6), 400-407. doi:10.1159/000054609
- Dellipizzi, A. M., Hilchey, S. D., & Bellquille, C. P. (1994). NATRIURETIC ACTION OF ANGIOTENSIN(1-7). *British Journal of Pharmacology*, 111(1), 1-3.
- Deshwar, A. R., Chng, S. C., Ho, L., Reversade, B., & Scott, I. C. (2016). The Apelin receptor enhances Nodal/TGF beta signaling to ensure proper cardiac development. *Elife*, 5doi:10.7554/eLife.13758
- Donoghue, M., Hsieh, F., Baronas, E., Godbout, K., Gosselin, M., Stagliano, N., ... Acton, S. (2000). A novel angiotensin-converting enzyme-related carboxypeptidase (ACE2) converts angiotensin I to angiotensin 1-9. *Circulation Research*, 87(5), E1-E9. doi:10.1161/01.res.87.5.e1

- Dray, C., Knauf, C., Daviaud, D., Waget, A., Boucher, J., Buleon, M., ... Valet, P. (2008). Apelin Stimulates Glucose Utilization in Normal and Obese Insulin-Resistant Mice. *Cell Metabolism*, 8(5), 437-445. doi:10.1016/j.cmet.2008.10.003
- Edinger, A. L., Hoffman, T. L., Sharron, M., Lee, B. H., Yi, Y. J., Choe, W., ... Doms, R. W. (1998). An orphan seven-transmembrane domain receptor expressed widely in the brain functions as a coreceptor for human immunodeficiency virus type 1 and simian immunodeficiency virus. *Journal of Virology*, 72(10), 7934-7940. doi:10.1128/jvi.72.10.7934-7940.1998
- Eyries, M., Siegfried, G., Ciumas, M., Montagne, K., Agrapart, M., Lebrin, F., & Soubrier, F. (2008). Hypoxia-induced apelin expression regulates endothelial cell proliferation and regenerative angiogenesis. *Circulation Research*, 103(4), 432-440. doi:10.1161/circresaha.108.179333
- Ezkurdia, I., Juan, D., Rodriguez, J. M., Frankish, A., Diekhans, M., Harrow, J., ... Tress, M. L. (2014). Multiple evidence strands suggest that there may be as few as 19 000 human protein-coding genes. *Human Molecular Genetics*, 23(22), 5866-5878. doi:10.1093/hmg/ddu309
- Fairweather, S. J., Broer, A., O'Mara, M. L., & Broer, S. (2012). Intestinal peptidases form functional complexes with the neutral amino acid transporter B(0)AT1. *Biochemical Journal*, 446, 135-148. doi:10.1042/bj20120307
- Falcao-Pires, I., Goncalves, N., Henriques-Coelho, T., Moreira-Goncalves, D., Roncon-Albuquerque, R., & Leite-Moreira, A. F. (2009). Apelin decreases myocardial injury and improves right ventricular function in monocrotaline-induced pulmonary hypertension. *American Journal of Physiology-Heart and Circulatory Physiology*, 296(6), H2007-H2014. doi:10.1152/ajpheart.00089.2009
- Fernandez, K. X., Fischer, C., Vu, J., Gheblawi, M., Wang, W., Gottschalk, S., ... Vederas, J. C. (2021). Metabolically stable apelin-analogues, incorporating cyclohexylalanine and homoarginine, as potent apelin receptor activators. *Rsc Medicinal Chemistry*, 12(8), 1402-1413. doi:10.1039/d1md00120e
- Fischer, C., Lamer, T., Wang, W., McKinnie, S. M. K., Iturrioz, X., Llorens-Cortes, C., ... Vederas, J. C. (2019). Plasma kallikrein cleaves and inactivates apelin-17: Palmitoyl- and PEG-extended apelin-17 analogs as metabolically stable blood pressure-lowering agents. *European Journal of Medicinal Chemistry*, 166, 119-124. doi:10.1016/j.ejmech.2019.01.040
- Flahault, A., Couvineau, P., Alvear-Perez, R., Iturrioz, X., & Llorens-Cortes, C. (2017). Role of the vasopressin/Apelin Balance and Potential Use of Metabolically Stable Apelin Analogs in water Metabolism Disorders. *Frontiers in Endocrinology*, 8doi:10.3389/fendo.2017.00120

- Flahault, A., Girault-Sotias, P. E., Keck, M., Alvear-Perez, R., De Mota, N., Esteouille, L., ... Llorens-Cortes, C. (2021a). A metabolically stable apelin-17 analog decreases AVP-induced antidiuresis and improves hyponatremia. *Nature Communications*, 12(1)doi:10.1038/s41467-020-20560-y
- Flahault, A., Keck, M., Girault-Sotias, P. E., Esteouille, L., De Mota, N., Bonnet, D., & Llorens-Cortes, C. (2021b). LIT01-196, a Metabolically Stable Apelin-17 Analog, Normalizes Blood Pressure in Hypertensive DOCA-Salt Rats via a NO Synthase-dependent Mechanism. *Frontiers in Pharmacology*, 12doi:10.3389/fphar.2021.715095
- Flora, G. D., & Nayak, M. K. (2019). A Brief Review of Cardiovascular Diseases, Associated Risk Factors and Current Treatment Regimes. *Current Pharmaceutical Design*, 25(38), 4063-4084. doi:10.2174/1381612825666190925163827
- Foldes, G., Horkay, F., Szokodi, I., Vuolteenaho, O., Ilves, M., Lindstedt, A., ... Toth, M. (2003). Circulating and cardiac levels of apelin, the novel ligand of the orphan receptor APJ, in patients with heart failure. *Biochemical and Biophysical Research Communications*, 308(3), 480-485. doi:10.1016/s0006-291x(03)01424-4
- Folino, A., Montarolo, P. G., Samaja, M., & Rastaldo, R. (2015). Effects of apelin on the cardiovascular system. *Heart Failure Reviews*, 20(4), 505-518. doi:10.1007/s10741-015-9475-x
- Forrester, S. J., Booz, G. W., Sigmund, C. D., Coffman, T. M., Kawai, T., Rizzo, V., ... Eguchi, S. (2018). ANGIOTENSIN II SIGNAL TRANSDUCTION: AN UPDATE ON MECHANISMS OF PHYSIOLOGY AND PATHOPHYSIOLOGY. *Physiological Reviews*, 98(3), 1627-1738. doi:10.1152/physrev.00038.2017
- Francia, P., Salvati, A., Balla, C., De Paolis, P., Pagannone, E., Borro, M., ... Volpe, M. (2007). Cardiac resynchronization therapy increases plasma levels of the endogenous inotrope apelin. *European Journal of Heart Failure*, 9(3), 306-309. doi:10.1016/j.ejheart.2006.06.005
- Fuchs, S., Amiel, J., Claudel, S., Lyonnet, S., Corvol, P., & Pinet, F. (2001). Functional characterization of three mutations of the endothelin B receptor gene in patients with Hirschsprung's disease: Evidence for selective loss of G(i) coupling. *Molecular Medicine*, 7(2), 115-124. doi:10.1007/bf03401945
- Galie, N., Hoeper, M. M., Humbert, M., Torbicki, A., Vachiery, J. L., Barbera, J. A., ... Ishl. (2009). Guidelines for the diagnosis and treatment of pulmonary hypertension. *European Heart Journal*, 30(20), 2493-2537. doi:10.1093/eurheartj/ehp297

- Galon-Tilleman, H., Yang, H., Bednarek, M. A., Spurlock, S. M., Paavola, K. J., Ko, B., ... Kaplan, D. D. (2017). Apelin-36 Modulates Blood Glucose and Body Weight Independently of Canonical APJ Receptor Signaling. *Journal of Biological Chemistry*, 292(5), 1925-1933. doi:10.1074/jbc.M116.748103
- Gan, C. T. J., Lankhaar, J. W., Westerhof, N., Marcus, J. T., Becker, A., Twisk, J. W. R., ... Vonk-Noordegraaf, A. (2007). Noninvasively assessed pulmonary artery stiffness predicts mortality in pulmonary arterial hypertension. *Chest*, 132(6), 1906-1912. doi:10.1378/chest.07-1246
- Gavriatopoulou, M., Korompoki, E., Fotiou, D., Ntanasis-Stathopoulos, I., Psaltopoulou, T., Kastritis, E., ... Dimopoulos, M. A. (2020). Organ-specific manifestations of COVID-19 infection. *Clinical and Experimental Medicine*, 20(4), 493-506. doi:10.1007/s10238-020-00648-x
- Gaziano, L., Giambartolomei, C., Pereira, A. C., Gaulton, A., Posner, D. C., Swanson, S. A., ... CO, V. A. M. V. P. (2021). Actionable druggable genome-wide Mendelian randomization identifies repurposing opportunities for COVID-19. *Nature Medicine*, 27(4)doi:10.1038/s41591-021-01310-z
- Gembardt, F., Sterner-Kock, A., Imboden, H., Spalteholz, M., Reibitz, F., Schultheiss, H. P., ... Walther, T. (2005). Organ-specific distribution of ACE2 mRNA and correlating peptidase activity in rodents. *Peptides*, 26(7), 1270-1277. doi:10.1016/j.peptides.2005.01.009
- Gerbier, R., Alvear-Perez, R., Margathe, J. F., Flahault, A., Couvineau, P., Gao, J., ... Llorens-Cortes, C. (2017). Development of original metabolically stable apelin-17 analogs with diuretic and cardiovascular effects. *Faseb Journal*, 31(2), 687-700. doi:10.1096/fj.201600784R
- Gerbier, R., Leroux, V., Couvineau, P., Alvear-Perez, R., Maigret, B., Llorens-Cortes, C., & Iturrioz, X. (2015). New structural insights into the apelin receptor: identification of key residues for apelin binding. *Faseb Journal*, 29(1), 314-322. doi:10.1096/fj.14-256339
- Gheblawi, M., Wang, K. M., Viveiros, A., Nguyen, Q., Zhong, J. C., Turner, A. J., ... Oudit, G. Y. (2020). Angiotensin-Converting Enzyme 2: SARS-CoV-2 Receptor and Regulator of the Renin-Angiotensin System Celebrating the 20th Anniversary of the Discovery of ACE2. *Circulation Research*, 126(10), 1456-1474. doi:10.1161/circresaha.120.317015
- Goetze, J. P., Rehfeld, J. F., Carlsen, J., Videbaek, R., Andersen, C. B., Boesgaard, S., & Friis-Hansen, L. (2006). Apelin: A new plasma marker of cardiopulmonary disease. *Regulatory Peptides*, 133(1-3), 134-138. doi:10.1016/j.regpep.2005.09.032

- Graf, S., Haimel, M., Bleda, M., Hadinnapola, C., Southgate, L., Li, W., ... Morrell, N. W. (2018). Identification of rare sequence variation underlying heritable pulmonary arterial hypertension. *Nature Communications*, doi:10.1038/s41467-018-03672-4
- Guo, T., Fan, Y., & Chen, M. (2020). Cardiovascular Implications of Fatal Outcomes of Patients With Coronavirus Disease 2019 (COVID-19) (Mar, 10.1001/jamacardio.2020.1017, 2020). *Jama Cardiology*, 5(7), 848-848. doi:10.1001/jamacardio.2020.1722
- Guy, J. L., Jackson, R. M., Acharya, K. R., Sturrock, E. D., Hooper, N. M., & Turner, A. J. (2003). Angiotensin-converting enzyme-2 (ACE2): Comparative modeling of the active site, specificity requirements, and chloride dependence. *Biochemistry*, 42(45), 13185-13192. doi:10.1021/bi035268s
- Guy, J. L., Lambert, D. W., Turner, A. J., & Porter, K. E. (2008). Functional angiotensin-converting enzyme 2 is expressed in human cardiac myofibroblasts. *Experimental Physiology*, 93(5), 579-588. doi:10.1113/expphysiol.2007.040139
- Habata, Y., Fujii, R., Hosoya, M., Fukusumi, S., Kawamata, Y., Hinuma, S., ... Fujino, M. (1999). Apelin, the natural ligand of the orphan receptor APJ, is abundantly secreted in the colostrum. *Biochimica Et Biophysica Acta-Molecular Cell Research*, 1452(1), 25-35. doi:10.1016/s0167-4889(99)00114-7
- Hamada, J., Kimura, J., Ishida, J., Kohda, T., Morishita, S., Ichihara, S., & Fukamizu, A. (2008). Evaluation of novel cyclic analogues of apelin. *International Journal of Molecular Medicine*, 22(4), 547-552. doi:10.3892/ijmm\_00000054
- Hamming, I., Cooper, M. E., Haagmans, B. L., Hooper, N. M., Korstanje, R., Osterhaus, A., ... van Goor, H. (2007). The emerging role of ACE2 in physiology and disease. *Journal of Pathology*, 212(1), 1-11. doi:10.1002/path.2162
- Hamming, I., Timens, W., Bulthuis, M. L. C., Lely, A. T., Navis, G. J., & van Goor, H. (2004). Tissue distribution of ACE2 protein, the functional receptor for SARS coronavirus. A first step in understanding SARS pathogenesis. *Journal of Pathology*, 203(2), 631-637. doi:10.1002/path.1570
- Harmer, D., Gilbert, M., Borman, R., & Clark, K. L. (2002). Quantitative mRNA expression profiling of ACE 2, a novel homologue of angiotensin converting enzyme. *Febs Letters*, 532(1-2), 107-110. doi:10.1016/s0014-5793(02)03640-2

- Hashimoto, T., Kihara, M., Ishida, J., Imai, N., Yoshida, S., Toya, Y., ... Umemura, S. (2006). Apelin stimulates myosin light chain phosphorylation in vascular smooth muscle cells. *Arteriosclerosis Thrombosis and Vascular Biology*, 26(6), 1267-1272. doi:10.1161/01.atv.0000218841.39828.91
- Hauser, A. S., Attwood, M. M., Rask-Andersen, M., Schioth, H. B., & Gloriam, D. E. (2017). Trends in GPCR drug discovery: new agents, targets and indications. *Nature Reviews Drug Discovery*, 16(12), 829-842. doi:10.1038/nrd.2017.178
- Hikmet, F., Mear, L., Edvinsson, A., Micke, P., Uhlen, M., & Lindskog, C. (2020). The protein expression profile of ACE2 in human tissues. *Molecular Systems Biology*, 16(7)
- Ho, L., Tan, S. Y. X., Wee, S., Wu, Y. X., Tan, S. J. C., Ramakrishna, N. B., ... Reversade, B. (2015). ELABELA Is an Endogenous Growth Factor that Sustains hESC Self-Renewal via the PI3K/AKT Pathway. *Cell Stem Cell*, 17(4), 435-447. doi:10.1016/j.stem.2015.08.010
- Hoffmann, M., Kleine-Weber, H., Schroeder, S., Kruger, N., Herrler, T., Erichsen, S., ... Pohlmann, S. (2020). SARS-CoV-2 Cell Entry Depends on ACE2 and TMPRSS2 and Is Blocked by a Clinically Proven Protease Inhibitor. *Cell*, 181(2), 271-+. doi:10.1016/j.cell.2020.02.052
- Hofmann, H., Pyrc, K., van der Hoek, L., Geier, M., Berkhout, B., & Pohlmann, S. (2005). Human coronavirus NL63 employs the severe acute respiratory syndrome coronavirus receptor for cellular entry. *Proceedings of the National Academy of Sciences of the United States of America*, 102(22), 7988-7993. doi:10.1073/pnas.0409465102
- Hosoya, M., Kawamata, Y., Fukusumi, S., Fujii, R., Habata, Y., Hinuma, S., ... Fujino, M. (2000). Molecular and functional characteristics of APJ - Tissue distribution of mRNA and interaction with the endogenous ligand apelin. *Journal of Biological Chemistry*, 275(28), 21061-21067. doi:10.1074/jbc.M908417199
- Huang, L. L., Sexton, D. J., Skogerson, K., Devlin, M., Smith, R., Sanyal, I., ... Ladner, R. C. (2003). Novel peptide inhibitors of angiotensin-converting enzyme 2. *Journal of Biological Chemistry*, 278(18), 15532-15540. doi:10.1074/jbc.M212934200
- Hus-Citharel, A., Bodineau, L., Frugiere, A., Joubert, F., Bouby, N., & Llorens-Cortes, C. (2014). Apelin Counteracts Vasopressin-Induced Water Reabsorption via Cross Talk Between Apelin and Vasopressin Receptor Signaling Pathways in the Rat Collecting Duct. *Endocrinology*, 155(11), 4483-4493. doi:10.1210/en.2014-1257

- Hus-Citharel, A., Bouby, N., Frugiere, A., Bodineau, L., Gasc, J. M., & Llorens-Cortes, C. (2008). Effect of apelin on glomerular hemodynamic function in the rat kidney. *Kidney International*, 74(4), 486-494. doi:10.1038/ki.2008.199
- Ishida, J., Hashimoto, T., Hashimoto, Y., Nishiwaki, S., Iguchi, T., Harada, S., ... Fukamizu, A. (2004). Regulatory roles for APJ, a seven-transmembrane receptor related to angiotensin-type 1 receptor in blood pressure in vivo. *Journal of Biological Chemistry*, 279(25), 26274-26279. doi:10.1074/jbc.M404149200
- Italia, L., Tomasoni, D., Bisegna, S., Pancaldi, E., Stretti, L., Adamo, M., & Metra, M. (2021). COVID-19 and Heart Failure: From Epidemiology During the Pandemic to Myocardial Injury, Myocarditis, and Heart Failure Sequelae. *Frontiers in Cardiovascular Medicine*, 8doi:10.3389/fcvm.2021.713560
- Iturrioz, X., Alvear-Perez, R., De Mota, N., Franchet, C., Guillier, F., Leroux, V., ... Llorens-Cortes, C. (2010a). Identification and pharmacological properties of E339-3D6, the first nonpeptidic apelin receptor agonist. *Faseb Journal*, 24(5), 1506-1517. doi:10.1096/fj.09-140715
- Iturrioz, X., El Messari, S., De Mota, N., Fassot, C., Alvear-Perez, R., Maigret, B., & Llorens-Cortes, C. (2007). Functional dissociation between apelin receptor signaling and endocytosis: implications for the effects of apelin on arterial blood pressure. *Archives Des Maladies Du Coeur Et Des Vaisseaux*, 100(8), 704-708.
- Iturrioz, X., Gerbier, R., Leroux, V., Alvear-Perez, R., Maigret, B., & Llorens-Cortes, C. (2010b). By Interacting with the C-terminal Phe of Apelin, Phe(255) and Trp(259) in Helix VI of the Apelin Receptor Are Critical for Internalization. *Journal of Biological Chemistry*, 285(42), 32627-32637. doi:10.1074/jbc.M110.127167
- Japp, A. G., Cruden, N. L., Amer, D. A. B., Li, V. K. Y., Goudie, E. B., Johnston, N. R., ... Newby, D. E. (2008). Vascular effects of apelin in vivo in man. *Journal of the American College of Cardiology*, 52(11), 908-913. doi:10.1016/j.jacc.2008.06.013
- Japp, A. G., Cruden, N. L., Barnes, G., van Gemeren, N., Mathews, J., Adamson, J., ... Newby, D. E. (2010). Acute Cardiovascular Effects of Apelin in Humans Potential Role in Patients With Chronic Heart Failure. *Circulation*, 121(16), 1818-U1856. doi:10.1161/circulationaha.109.911339
- Jia, H. P., Look, D. C., Tan, P., Shi, L., Hickey, M., Gakhar, L., ... McCray, P. B. (2009). Ectodomain shedding of angiotensin converting enzyme 2 in human airway epithelia. *American Journal of Physiology-Lung Cellular and Molecular Physiology*, 297(1), L84-L96. doi:10.1152/ajplung.00071.2009

- Jia, Z. Q., Hou, L., Leger, A., Wu, I., Kudej, A. B., Stefano, J., ... Akita, G. Y. (2012). Cardiovascular effects of a PEGylated apelin. *Peptides*, 38(1), 181-188. doi:10.1016/j.peptides.2012.09.003
- Kakar, S. S., Riel, K. K., & Neill, J. D. (1992). DIFFERENTIAL EXPRESSION OF ANGIOTENSIN-II RECEPTOR SUBTYPE MESSENGER-RNAS (AT-1A AND AT-1B) IN THE BRAIN. *Biochemical and Biophysical Research Communications*, 185(2), 688-692. doi:10.1016/0006-291x(92)91680-o
- Kalin, R. E., Kretz, M. P., Meyer, A. M., Kispert, A., Heppner, F. L., & Brandli, A. W. (2007). Paracrine and autocrine mechanisms of apelin signaling govern embryonic and tumor angiogenesis. *Developmental Biology*, 305(2), 599-614. doi:10.1016/j.ydbio.2007.03.004
- Kang, Y., Chen, T., Mui, D., Ferrari, V., Jagasia, D., Scherrer-Crosbie, M., ... Han, Y. C. (2020). Cardiovascular manifestations and treatment considerations in COVID-19. *Heart*, 106(15), 1132-1141. doi:10.1136/heartjnl-2020-317056
- Kang, Y. J., Kim, J. M., Anderson, J. P., Wu, J. X., Gleim, S. R., Kundu, R. K., ... Chun, H. J. (2013). Apelin-APJ Signaling Is a Critical Regulator of Endothelial MEF2 Activation in Cardiovascular Development. *Circulation Research*, 113(1), 22-31. doi:10.1161/circresaha.113.301324
- Karnik, S. S., Unal, H., Kemp, J. R., Tirupula, K. C., Eguchi, S., Vanderheyden, P. M. L., & Thomas, W. G. (2015). International Union of Basic and Clinical Pharmacology. XCIX. Angiotensin Receptors: Interpreters of Pathophysiological Angiotensinergic Stimuli. *Pharmacological Reviews*, 67(4), 754-819. doi:10.1124/pr.114.010454
- Kasai, A., Shintani, N., Oda, M., Kakuda, M., Hashimoto, H., Matsuda, T., ... Baba, A. (2004). Apelin is a novel angiogenic factor in retinal endothelial cells. *Biochemical and Biophysical Research Communications*, 325(2), 395-400. doi:10.1016/j.bbrc.2004.10.042
- Katugampola, S. D., Maguire, J. J., Matthewson, S. R., & Davenport, A. P. (2001). I-125 -(Pyr(1))Apelin-13 is a novel radioligand for localizing the APJ orphan receptor in human and rat tissues with evidence for a vasoconstrictor role in man. *British Journal of Pharmacology*, 132(6), 1255-1260. doi:10.1038/sj.bjp.0703939
- Kawamata, Y., Fukusumi, S., Hosoya, M., Fujii, R., Hinuma, S., Nishizawa, N., ... Fujino, M. (2001). Molecular properties of apelin: tissue distribution and receptor binding. *Biochimica Et Biophysica Acta-Molecular Cell Research*, 1538(2-3), 162-171. doi:10.1016/s0167-4889(00)00143-9
- Kazi, D. S., Penko, J. M., & Bibbins-Domingo, K. (2017). Statins for Primary Prevention of Cardiovascular Disease Review of Evidence and Recommendations for Clinical Practice. *Medical Clinics of North America*, 101(4), 689-+. doi:10.1016/j.mcna.2017.03.001

- Kleinz, M. J., & Davenport, A. P. (2004). Immunocytochemical localization of the endogenous vasoactive peptide apelin to human vascular and endocardial endothelial cells. *Regulatory Peptides*, *118*(3), 119-125. doi:10.1016/j.regpep.2003.11.002
- Kleinz, M. J., & Davenport, A. P. (2005). Emerging roles of apelin in biology and medicine. *Pharmacology & Therapeutics*, *107*(2), 198-211. doi:10.1016/j.pharmthera.2005.04.001
- Kleinz, M. J., Skepper, J. N., & Davenport, A. P. (2005). Immunocytochemical localisation of the apelin receptor, APJ, to human cardiomyocytes, vascular smooth muscle and endothelial cells. *Regulatory Peptides*, *126*(3), 233-240. doi:10.1016/j.regpep.2004.10.019
- Koblan, L. W., Doman, J. L., Wilson, C., Levy, J. M., Tay, T., Newby, G. A., ... Liu, D. R. (2018). Improving cytidine and adenine base editors by expression optimization and ancestral reconstruction. *Nature Biotechnology*, *36*(9), 843-+. doi:10.1038/nbt.4172
- Komor, A. C., Kim, Y. B., Packer, M. S., Zuris, J. A., & Liu, D. R. (2016). Programmable editing of a target base in genomic DNA without double-stranded DNA cleavage. *Nature*, *533*(7603), 420-+. doi:10.1038/nature17946
- Kooistra, A. J., Mordalski, S., Pandey-Szekeres, G., Esguerra, M., Mamyrbekov, A., Munk, C., ... Gloriam, D. E. (2021). GPCRdb in 2021: integrating GPCR sequence, structure and function. *Nucleic Acids Research*, *49*(D1), D335-D343. doi:10.1093/nar/gkaa1080
- Kowalczyk, S., Broer, A., Tietze, N., Vanslambrouck, J. M., Rasko, J. E. J., & Broer, S. (2008). A protein complex in the brush-border membrane explains a Hartnup disorder allele. *Faseb Journal*, *22*(8), 2880-2887. doi:10.1096/fj.08-107300
- Kuba, K., Zhang, L., Imai, Y., Arab, S., Chen, M., Maekawa, Y., ... Penninger, J. M. (2007). Impaired heart Contractility in apelin gene-deficient mice associated with aging and pressure overload. *Circulation Research*, *101*(4), E32-E42. doi:10.1161/circresaha.107.158659
- Kuhn, J. H., Li, W., Choe, H., & Farzan, M. (2004). Angiotensin-converting enzyme 2: a functional receptor for SARS coronavirus. *Cellular and Molecular Life Sciences*, *61*(21), 2738-2743. doi:10.1007/s00018-004-4242-5
- Langelaan, D. N., Reddy, T., Banks, A. W., Dellaire, G., Dupre, D. J., & Rainey, J. K. (2013). Structural features of the apelin receptor N-terminal tail and first transmembrane segment implicated in ligand binding and receptor trafficking. *Biochimica Et Biophysica Acta-Biomembranes*, *1828*(6), 1471-1483. doi:10.1016/j.bbamem.2013.02.005

- Lee, D. K., Cheng, R., Nguyen, T., Fan, T., Kariyawasam, A. P., Liu, Y., ... O'Dowd, B. F. (2000). Characterization of apelin, the ligand for the APJ receptor. *Journal of Neurochemistry*, 74(1), 34-41. doi:10.1046/j.1471-4159.2000.0740034.x
- Li, M. Y., Li, L., Zhang, Y., & Wang, X. S. (2020). Expression of the SARS-CoV-2 cell receptor gene ACE2 in a wide variety of human tissues. *Infectious Diseases of Poverty*, 9(1)doi:10.1186/s40249-020-00662-x
- Li, W. H., Moore, M. J., Vasilieva, N., Sui, J. H., Wong, S. K., Berne, M. A., ... Farzan, M. (2003). Angiotensin-converting enzyme 2 is a functional receptor for the SARS coronavirus. *Nature*, 426(6965), 450-454. doi:10.1038/nature02145
- Li, X. T., Zhang, M. W., Zhang, Z. Z., Cao, Y. D., Liu, X. Y., Miao, R., ... Zhong, J. C. (2021). Abnormal apelin-ACE2 and SGLT2 signaling contribute to adverse cardiorenal injury in patients with COVID-19. *International Journal of Cardiology*, 336, 123-129. doi:10.1016/j.ijcard.2021.05.029
- Liu, T. X., Luo, S. Y., Libby, P., & Shi, G. P. (2020). Cathepsin L-selective inhibitors: A potentially promising treatment for COVID-19 patients. *Pharmacology & Therapeutics*, 213doi:10.1016/j.pharmthera.2020.107587
- Lotta, L. A., Mokrosinski, J., de Oliveira, E. M., Li, C., Sharp, S. J., Luan, J. A., ... Farooqi, I. S. (2019). Human Gain-of-Function MC4R Variants Show Signaling Bias and Protect against Obesity. *Cell*, 177(3), 597-+. doi:10.1016/j.cell.2019.03.044
- Lu, H., Cassis, L. A., Kooi, C. W. V., & Daugherty, A. (2016). Structure and functions of angiotensinogen (vol 39, pg 492, 2016). *Hypertension Research*, 39(11), 827-827. doi:10.1038/hr.2016.106
- Lu, L. Q., Wu, D., Li, L. F., & Chen, L. X. (2017). Apelin/APJ system: A bifunctional target for cardiac hypertrophy. *International Journal of Cardiology*, 230, 164-170. doi:10.1016/j.ijcard.2016.11.215
- Lukassen, S., Chua, R. L., Trefzer, T., Kahn, N. C., Schneider, M. A., Muley, T., ... Eils, R. (2020). SARS-CoV-2 receptor ACE2 and TMPRSS2 are primarily expressed in bronchial transient secretory cells. *Embo Journal*, 39(10)doi:10.15252/embj.20105114
- Lv, X. C., Liu, J. L., Shi, Q. Y., Tan, Q. W., Wu, D., Skinner, J. J., ... Stevens, R. C. (2016). In vitro expression and analysis of the 826 human G protein-coupled receptors. *Protein & Cell*, 7(5), 325-337. doi:10.1007/s13238-016-0263-8
- Ma, W. Y., Yu, T. Y., Wei, J. N., Hung, C. S., Lin, M. S., Liao, Y. J., ... Li, H. Y. (2014). Plasma apelin: A novel biomarker for predicting diabetes. *Clinica Chimica Acta*, 435, 18-23. doi:10.1016/j.cca.2014.03.030

- Ma, Y. L., Yue, Y., Ma, Y. B., Zhang, Q., Zhou, Q. T., Song, Y. P., ... Xu, F. (2017). Structural Basis for Apelin Control of the Human Apelin Receptor. *Structure*, 25(6), 858-+. doi:10.1016/j.str.2017.04.008
- Maguire, J. J., Kleinz, M. J., Pitkin, S. L., & Davenport, A. P. (2009). Pyr(1) Apelin-13 Identified as the Predominant Apelin Isoform in the Human Heart Vasoactive Mechanisms and Inotropic Action in Disease. *Hypertension*, 54(3), 598-U296. doi:10.1161/hypertensionaha.109.134619
- Malakauskas, S. M., Quan, H., Fields, T. A., McCall, S. J., Yu, M. J., Kourany, W. M., ... Le, T. H. (2007). Aminoaciduria and altered renal expression of luminal amino acid transporters in mice lacking novel gene collectrin. *American Journal of Physiology-Renal Physiology*, 292(2), F533-F544. doi:10.1152/ajprenal.00325.2006
- Marceau, F., Bachelard, H., Bouthillier, J., Fortin, J. P., Morissette, G., Bawolak, M. T., ... Gera, L. (2020). Bradykinin receptors: Agonists, antagonists, expression, signaling, and adaptation to sustained stimulation. *International Immunopharmacology*, 82doi:10.1016/j.intimp.2020.106305
- Margathe, J. F., Iturrioz, X., Alvear-Perez, R., Marsol, C., Riche, S., Chabane, H., ... Bonnet, D. (2014). Structure Activity Relationship Studies toward the Discovery of Selective Apelin Receptor Agonists. *Journal of Medicinal Chemistry*, 57(7), 2908-2919. doi:10.1021/jm401789v
- Margathe, J. F., Iturrioz, X., Regenass, P., Karpenko, I. A., Humbert, N., de Rocquigny, H., ... Bonnet, D. (2016). Convenient Access to Fluorescent Probes by Chemoselective Acylation of Hydrazinopeptides: Application to the Synthesis of the First Far-Red Ligand for Apelin Receptor Imaging. *Chemistry-a European Journal*, 22(4), 1399-1405. doi:10.1002/chem.201503630
- Masoud, A. G., Lin, J. X., Azad, A. K., Farhan, M. A., Fischer, C., Zhu, L. F., ... Murray, A. G. (2020). Apelin directs endothelial cell differentiation and vascular repair following immune-mediated injury. *Journal of Clinical Investigation*, 130(1), 94-107. doi:10.1172/jci128469
- Masri, B., Knibiehler, B., & Audigier, Y. (2005). Apelin signalling: a promising pathway from cloning to pharmacology. *Cellular Signalling*, 17(4), 415-426. doi:10.1016/j.cellsig.2004.09.018
- Masri, B., Morin, N., Cornu, M., Knibiehler, B., & Audigier, Y. (2004). Apelin (65-77) activates p70 S6 kinase and is mitogenic for umbilical endothelial cells. *Faseb Journal*, 18(12), 1909-+. doi:10.1096/fj.04-1930fje
- Masri, B., Morin, N., Pedebernade, L., Knibiehler, B., & Audigier, Y. (2006). The apelin receptor is coupled to G(i1) or G(i2) protein and is differentially desensitized by apelin fragments. *Journal of Biological Chemistry*, 281(27), 18317-18326. doi:10.1074/jbc.M600606200

- McAnally, D., Siddiquee, K., Gomaa, A., Szabo, A., Vasile, S., Maloney, P. R., ... Smith, L. H. (2018). Repurposing antimalarial aminoquinolines and related compounds for treatment of retinal neovascularization. *Plos One*, 13(9)doi:10.1371/journal.pone.0202436
- McGoon, M. D., Benza, R. L., Escribano-Subias, P., Jiang, X., Miller, D. P., Peacock, A. J., ... Humbert, M. (2013). Pulmonary Arterial Hypertension Epidemiology and Registries. *Journal of the American College of Cardiology*, 62(25), D51-D59. doi:10.1016/j.jacc.2013.10.023
- McKeown, S. C., Zecri, F. J., Fortier, E., Taggart, A., Sviridenko, L., Adams, C. M., ... Pin, S. S. (2014). The design and implementation of a generic lipopeptide scanning platform to enable the identification of 'locally acting' agonists for the apelin receptor. *Bioorganic & Medicinal Chemistry Letters*, 24(20), 4871-4875. doi:10.1016/j.bmcl.2014.08.045
- McPherson, G. A. (1985). ANALYSIS OF RADIOLIGAND BINDING EXPERIMENTS - A COLLECTION OF COMPUTER-PROGRAMS FOR THE IBM-PC. *Journal of Pharmacological Methods*, 14(3), 213-228. doi:10.1016/0160-5402(85)90034-8
- Medhurst, A. D., Jennings, C. A., Robbins, M. J., Davis, R. P., Ellis, C., Winborn, K. Y., ... Darker, J. G. (2003). Pharmacological and immunohistochemical characterization of the APJ receptor and its endogenous ligand apelin. *Journal of Neurochemistry*, 84(5), 1162-1172. doi:10.1046/j.1471-4159.2003.01587.x
- Messari, S. E., Iturrioz, X., Fassot, C., De Mota, N., Roesch, D., & Llorens-Cortes, C. (2004). Functional dissociation of apelin receptor signaling and endocytosis: implications for the effects of apelin on arterial blood pressure. *Journal of Neurochemistry*, 90(6), 1290-1301. doi:10.1111/j.1471-4159.2004.02591.x
- Mombaerts, P. (2004). Genes and ligands for odorant, vomeronasal and taste receptors. *Nature Reviews Neuroscience*, 5(4), 263-278. doi:10.1038/nrn1365
- Morrell, N. W., Adnot, S., Archer, S. L., Dupuis, J., Jones, P. L., MacLean, M. R., ... Weir, E. K. (2009). Cellular and Molecular Basis of Pulmonary Arterial Hypertension. *Journal of the American College of Cardiology*, 54(1), S20-S31. doi:10.1016/j.jacc.2009.04.018
- Murza, A., Parent, A., Besserer-Offroy, E., Tremblay, H., Karadereye, F., Beaudet, N., ... Marsault, E. (2012). Elucidation of the Structure-Activity Relationships of Apelin: Influence of Unnatural Amino Acids on Binding, Signaling, and Plasma Stability. *Chemmedchem*, 7(2), 318-325. doi:10.1002/cmdc.201100492

- Murza, A., Sainsily, X., Coquerel, D., Cote, J., Marx, P., Besserer-Offroy, E., ... Marsault, E. (2016). Discovery and Structure-Activity Relationship of a Bioactive Fragment of ELABELA that Modulates Vascular and Cardiac Functions. *Journal of Medicinal Chemistry*, *59*(7), 2962-2972. doi:10.1021/acs.jmedchem.5b01549
- Murza, A., Sainsily, X., Cote, J., Bruneau-Cossette, L., Besserer-Offroy, E., Longpre, J. M., ... Marsault, E. (2017). Structure-activity relationship of novel macrocyclic biased apelin receptor agonists. *Organic & Biomolecular Chemistry*, *15*(2), 449-458. doi:10.1039/c6ob02247b
- Narayanan, S., Harris, D. L., Maitra, R., & Runyon, S. P. (2015). Regulation of the Apelinergic System and Its Potential in Cardiovascular Disease: Peptides and Small Molecules as Tools for Discovery. *Journal of Medicinal Chemistry*, *58*(20), 7913-7927. doi:10.1021/acs.jmedchem.5b00527
- Narayanan, S., Maitra, R., Deschamps, J. R., Bortoff, K., Thomas, J. B., Zhang, Y. Y., ... Runyon, S. P. (2016). Discovery of a novel small molecule agonist scaffold for the APJ receptor. *Bioorganic & Medicinal Chemistry*, *24*(16), 3758-3770. doi:10.1016/j.bmc.2016.06.018
- Narayanan, S., Vasukuttan, V., Rajagopal, S., Maitra, R., & Runyon, S. P. (2020). Identification of potent pyrazole based APELIN receptor (APJ) agonists. *Bioorganic & Medicinal Chemistry*, *28*(4)doi:10.1016/j.bmc.2019.115237
- Narula, S., Yusuf, S., Chong, M., Ramasundarahettige, C., Rangarajan, S., Bangdiwala, S. I., ... Pare, G. (2020). Plasma ACE2 and risk of death or cardiometabolic diseases: a case-cohort analysis. *Lancet*, *396*(10256), 968-976.
- Ng, K. W., Attig, J., Bolland, W., Young, G. R., Major, J., Wrobel, A. G., ... Kassiotis, G. (2020). Tissue-specific and interferon-inducible expression of nonfunctional ACE2 through endogenous retroelement co-option. *Nature Genetics*, *52*(12), 1294-1302. doi:10.1038/s41588-020-00732-8
- Nghiem, N., Knight, J., Mizdrak, A., Blakely, T., & Wilson, N. (2019). Preventive Pharmacotherapy for Cardiovascular Disease: A Modelling Study Considering Health Gain, Costs, and Cost-Effectiveness when Stratifying by Absolute Risk. *Scientific Reports*, *9*doi:10.1038/s41598-019-55372-8
- Nyimanu, D., Kay, R. G., Sulentic, P., Kuc, R. E., Ambery, P., Jermutus, L., ... Davenport, A. P. (2019). Development and validation of an LC-MS/MS method for detection and quantification of in vivo derived metabolites of Pyr(1) apelin-13 in humans. *Scientific Reports*, *9*doi:10.1038/s41598-019-56157-9

- O'Carroll, A. M., Selby, T. L., Palkovits, M., & Lolait, S. J. (2000). Distribution of mRNA encoding B78/apj, the rat homologue of the human APJ receptor, and its endogenous ligand apelin in brain and peripheral tissues. *Biochimica Et Biophysica Acta-Gene Structure and Expression*, 1492(1), 72-80. doi:10.1016/s0167-4781(00)00072-5
- Ocaranza, M. P., Moya, J., Barrientos, V., Alzamora, R., Hevia, D., Morales, C., ... Michea, L. (2014). Angiotensin-(1-9) reverses experimental hypertension and cardiovascular damage by inhibition of the angiotensin converting enzyme/Ang II axis. *Journal of Hypertension*, 32(4), 771-783. doi:10.1097/hjh.0000000000000094
- Odowd, B. F., Heiber, M., Chan, A., Heng, H. H. Q., Tsui, L. C., Kennedy, J. L., ... Nguyen, T. (1993). A HUMAN GENE THAT SHOWS IDENTITY WITH THE GENE ENCODING THE ANGIOTENSIN RECEPTOR IS LOCATED ON CHROMOSOME-11. *Gene*, 136(1-2), 355-360. doi:10.1016/0378-1119(93)90495-o
- Onabajo, O. O., Banday, A. R., Stanifer, M. L., Yan, W. S., Obajemu, A., Santer, D. M., ... Prokunina-Olsson, L. (2020). Interferons and viruses induce a novel truncated ACE2 isoform and not the full-length SARS-CoV-2 receptor. *Nature Genetics*, 52(12), 1283-1293. doi:10.1038/s41588-020-00731-9
- Ortiz, M. E., Thurman, A., Pezzulo, A. A., Leidinger, M. R., Klesney-Tait, J. A., Karp, P. H., ... Meyerholz, D. K. (2020). Heterogeneous expression of the SARS-Coronavirus-2 receptor ACE2 in the human respiratory tract. *Ebiomedicine*, 60doi:10.1016/j.ebiom.2020.102976
- Ota, S., Hara, Y., Kanoh, S., Shinoda, M., Kawano, S., Fujikura, Y., ... Shinkai, M. (2016). Acute eosinophilic pneumonia caused by camostat mesilate: The first case report. *Respiratory Medicine Case Reports*, 19, 21-23. doi:10.1016/j.rmcr.2016.06.005
- Oudit, G. Y., Crackower, M. A., Backx, P. H., & Penninger, J. M. (2003). The role of ACE2 in cardiovascular physiology. *Trends in Cardiovascular Medicine*, 13(3), 93-101. doi:10.1016/s1050-1738(02)00233-5
- Oudit, G. Y., Kassiri, Z., Jiang, C., Liu, P. P., Poutanen, S. M., Penninger, J. M., & Butany, J. (2009). SARS-coronavirus modulation of myocardial ACE2 expression and inflammation in patients with SARS. *European Journal of Clinical Investigation*, 39(7), 618-625. doi:10.1111/j.1365-2362.2009.02153.x
- Ozono, S., Zhang, Y. Z., Ode, H., Sano, K., Tan, T. S., Imai, K., ... Tokunaga, K. (2021). SARS-CoV-2 D614G spike mutation increases entry efficiency with enhanced ACE2-binding affinity. *Nature Communications*, 12(1)doi:10.1038/s41467-021-21118-2

- Padia, S. H., Kemp, B. A., Howell, N. L., Fournie-Zaluski, M. C., Roques, B. P., & Carey, R. M. (2008). Conversion of renal angiotensin II to angiotensin III is critical for AT(2) receptor-mediated natriuresis in rats. *Hypertension*, *51*(2), 460-465. doi:10.1161/hypertensionaha.107.103242
- Parasa, S., Desai, M., Chandrasekar, V. T., Patel, H. K., Kennedy, K. F., Roesch, T., ... Sharma, P. (2020). Prevalence of Gastrointestinal Symptoms and Fecal Viral Shedding in Patients With Coronavirus Disease 2019 A Systematic Review and Meta-analysis. *Jama Network Open*, *3*(6)doi:10.1001/jamanetworkopen.2020.11335
- Patel, T. P., Rawal, K., Bagchi, A. K., Akolkar, G., Bernardes, N., Dias, D. D., ... Singal, P. K. (2016). Insulin resistance: an additional risk factor in the pathogenesis of cardiovascular disease in type 2 diabetes. *Heart Failure Reviews*, *21*(1), 11-23. doi:10.1007/s10741-015-9515-6
- Pauli, A., Norris, M. L., Valen, E., Chew, G. L., Gagnon, J. A., Zimmerman, S., ... Schier, A. F. (2014). Toddler: An Embryonic Signal That Promotes Cell Movement via Apelin Receptors. *Science*, *343*(6172), 746-+. doi:10.1126/science.1248636
- Peacock, A. J., Murphy, N. F., McMurray, J. J. V., Caballero, L., & Stewart, S. (2007). An epidemiological study of pulmonary arterial hypertension. *European Respiratory Journal*, *30*(1), 104-109. doi:10.1183/09031936.00092306
- Perez-Bermejo, J. A., Kang, S., Rockwood, S. J., Simoneau, C. R., Joy, D. A., Silva, A. C., ... McDevitt, T. C. (2021). SARS-CoV-2 infection of human iPSC-derived cardiac cells reflects cytopathic features in hearts of patients with COVID-19. *Science Translational Medicine*, *13*(590)doi:10.1126/scitranslmed.abf7872
- Perjes, A., Skoumal, R., Tenhunen, O., Konyi, A., Simon, M., Horvath, I. G., ... Szokodi, I. (2014). Apelin Increases Cardiac Contractility via Protein Kinase C epsilon- and Extracellular Signal-Regulated Kinase-Dependent Mechanisms. *Plos One*, *9*(4)doi:10.1371/journal.pone.0093473
- Persson, P. B. (2003). Renin: origin, secretion and synthesis. *Journal of Physiology-London*, *552*(3), 667-671. doi:10.1113/jphysiol.2003.049890
- Pitkin, S. L., Maguire, J. J., Bonner, T. I., & Davenport, A. P. (2010a). International Union of Basic and Clinical Pharmacology. LXXIV. Apelin Receptor Nomenclature, Distribution, Pharmacology, and Function. *Pharmacological Reviews*, *62*(3), 331-342. doi:10.1124/pr.110.002949
- Pitkin, S. L., Maguire, J. J., Kuc, R. E., & Davenport, A. P. (2010b). Modulation of the apelin/APJ system in heart failure and atherosclerosis in man. *British Journal of Pharmacology*, *160*(7), 1785-1795. doi:10.1111/j.1476-5381.2010.00821.x

- Pope, G. R., Roberts, E. M., Lolait, S. J., & O'Carroll, A. M. (2012). Central and peripheral apelin receptor distribution in the mouse: Species differences with rat. *Peptides*, 33(1), 139-148. doi:10.1016/j.peptides.2011.12.005
- Pope, G. R., Tilve, S., McArdle, C. A., Lolait, S. J., & O'Carroll, A. M. (2016). Agonist-induced internalization and desensitization of the apelin receptor. *Molecular and Cellular Endocrinology*, 437(C), 108-119. doi:10.1016/j.mce.2016.07.040
- Puffer, B. A., Sharron, M., Coughlan, C. M., Baribaud, F., McManus, C. M., Lee, B., ... Doms, R. W. (2000). Expression and coreceptor function of APJ for primate immunodeficiency viruses. *Virology*, 276(2), 435-444. doi:10.1006/viro.2000.0557
- Qadri, F., Culman, J., Veltmar, A., Maas, K., Rascher, W., & Unger, T. (1993). ANGIOTENSIN-II-INDUCED VASOPRESSIN RELEASE IS MEDIATED THROUGH ALPHA-1-ADRENOCEPTORS AND ANGIOTENSIN-II AT1 RECEPTORS IN THE SUPRAOPTIC NUCLEUS. *Journal of Pharmacology and Experimental Therapeutics*, 267(2), 567-574.
- Rahimi, K., & Blood Pressure Lowering, T. (2021). Pharmacological blood pressure lowering for primary and secondary prevention of cardiovascular disease across different levels of blood pressure: an individual participant-level data meta-analysis. *Lancet*, 397(10285), 1625-1636.
- Ramchand, J., & Burrell, L. M. (2020). Circulating ACE2: a novel biomarker of cardiovascular risk. *Lancet*, 396(10256), 937-939.
- Read, C., Fitzpatrick, C. M., Yang, P. R., Kuc, R. E., Maguire, J. J., Glen, R. C., ... Davenport, A. P. (2016). Cardiac action of the first G protein biased small molecule apelin agonist. *Biochemical Pharmacology*, 116, 63-72. doi:10.1016/j.bcp.2016.07.018
- Read, C., Nyimanu, D., Williams, T. L., Huggins, D. J., Sulentic, P., Macrae, R. G. C., ... Davenport, A. P. (2019). International Union of Basic and Clinical Pharmacology. CVII. Structure and Pharmacology of the Apelin Receptor with a Recommendation that Elabela/Toddler Is a Second Endogenous Peptide Ligand. *Pharmacological Reviews*, 71(4), 467-502. doi:10.1124/pr.119.017533
- Read, C., Nyimanu, D., Yang, P. R., Kuc, R. E., Williams, T. L., Fitzpatrick, C. M., ... Davenport, A. P. (2021). The G Protein Biased Small Molecule Apelin Agonist CMF-019 is Disease Modifying in Endothelial Cell Apoptosis In Vitro and Induces Vasodilatation Without Desensitisation In Vivo. *Frontiers in Pharmacology*, 11doi:10.3389/fphar.2020.588669

- Read, C., Yang, P. R., Kuc, R. E., Nyimanu, D., Williams, T. L., Glen, R. C., ... Maguire, J. J. (2020). Apelin peptides linked to anti-serum albumin domain antibodies retain affinity in vitro and are efficacious receptor agonists in vivo. *Basic & Clinical Pharmacology & Toxicology*, 126, 96-103. doi:10.1111/bcpt.13227
- Reaux, A., De Mota, N., Skultetyova, I., Lenkei, Z., El Messari, S., Gallatz, K., ... Llorens-Cortes, C. (2001). Physiological role of a novel neuropeptide, apelin, and its receptor in the rat brain. *Journal of Neurochemistry*, 77(4), 1085-1096. doi:10.1046/j.1471-4159.2001.00320.x
- Reaux, A., Gallatz, K., Palkovits, M., & Llorens-Cortes, C. (2002). Distribution of apelin-synthesizing neurons in the adult rat brain. *Neuroscience*, 113(3), 653-662. doi:10.1016/s0306-4522(02)00192-6
- Reich, H. N., Oudit, G. Y., Penninger, J. M., Scholey, J. W., & Herzenberg, A. M. (2008). Decreased glomerular and tubular expression of ACE2 in patients with type 2 diabetes and kidney disease. *Kidney International*, 74(12), 1610-1616. doi:10.1038/ki.2008.497
- Rendeiro, A. F., Ravichandran, H., Bram, Y., Chandar, V., Kim, J., Meydan, C., ... Schwartz, R. E. The spatial landscape of lung pathology during COVID-19 progression. *Nature* doi:10.1038/s41586-021-03475-6
- Ringstrom, C., Nitert, M. D., Bennet, H., Fex, M., Valet, P., Rehfeld, J. F., ... Wierup, N. (2010). Apelin is a novel islet peptide. *Regulatory Peptides*, 162(1-3), 44-51. doi:10.1016/j.regpep.2010.03.005
- Roberts, E. M., Newson, M. J. F., Pope, G. R., Landgraf, R., Lolait, S. J., & O'Carroll, A. M. (2009). Abnormal fluid homeostasis in apelin receptor knockout mice. *Journal of Endocrinology*, 202(3), 453-462. doi:10.1677/joe-09-0134
- Robinson, E. L., Alkass, K., Bergmann, O., Maguire, J. J., Roderick, H. L., & Davenport, A. P. (2020). Genes encoding ACE2, TMPRSS2 and related proteins mediating SARS-CoV-2 viral entry are upregulated with age in human cardiomyocytes. *Journal of Molecular and Cellular Cardiology*, 147, 88-91. doi:10.1016/j.yjmcc.2020.08.009
- Robles, N. R., Cerezo, I., & Hernandez-Gallego, R. (2014). Renin-Angiotensin System Blocking Drugs. *Journal of Cardiovascular Pharmacology and Therapeutics*, 19(1), 14-33. doi:10.1177/1074248413501018
- Salcedo, A., Garijo, J., Monge, L., Fernandez, N., Garcia-Villalon, A. L., Turrion, V. S., ... Dieguez, G. (2007). Apelin effects in human splanchnic arteries. Role of nitric oxide and prostanoids. *Regulatory Peptides*, 144(1-3), 50-55. doi:10.1016/j.regpep.2007.06.005

- Samavati, L., & Uhal, B. D. (2020). ACE2, Much More Than Just a Receptor for SARS-COV-2. *Frontiers in Cellular and Infection Microbiology*, 10doi:10.3389/fcimb.2020.00317
- Santos, R., Ursu, O., Gaulton, A., Bento, A. P., Donadi, R. S., Bologa, C. G., ... Overington, J. P. (2017). A comprehensive map of molecular drug targets. *Nature Reviews Drug Discovery*, 16(1), 19-34. doi:10.1038/nrd.2016.230
- Saravi, S. S. S., & Beer, J. H. (2020). Apelin-potential therapy for COVID-19? *Journal of Molecular and Cellular Cardiology*, 145, 84-87. doi:10.1016/j.yjmcc.2020.06.007
- Sato, T., Sato, C., Kadowaki, A., Watanabe, H., Ho, L., Ishida, J., ... Kuba, K. (2017). ELABELA-APJ axis protects from pressure overload heart failure and angiotensin II-induced cardiac damage. *Cardiovascular Research*, 113(7), 760-769. doi:10.1093/cvr/cvx061
- Sato, T., Suzuki, T., Watanabe, H., Kadowaki, A., Fukamizu, A., Liu, P. P., ... Kuba, K. (2013). Apelin is a positive regulator of ACE2 in failing hearts. *Journal of Clinical Investigation*, 123(12), 5203-5211. doi:10.1172/jci69608
- Schaefer, I. M., Padera, R. F., Solomon, I. H., Kanjilal, S., Hammer, M. M., Hornick, J. L., & Sholl, L. M. (2020). In situ detection of SARS-CoV-2 in lungs and airways of patients with COVID-19. *Modern Pathology*, 33(11), 2104-2114. doi:10.1038/s41379-020-0595-z
- Schoneberg, T., & Liebscher, I. (2021). Mutations in G Protein-Coupled Receptors: Mechanisms, Pathophysiology and Potential Therapeutic Approaches. *Pharmacological Reviews*, 73(1), 89-119. doi:10.1124/pharmrev.120.000011
- Schramm, B., Penn, M. L., Palacios, E. H., Grant, R. M., Kirchhoff, F., & Goldsmith, M. A. (2000). Cytopathicity of human immunodeficiency virus type 2 (HIV-2) in human lymphoid tissue is coreceptor dependent and comparable to that of HIV-1. *Journal of Virology*, 74(20), 9594-9600. doi:10.1128/jvi.74.20.9594-9600.2000
- Scimia, M. C., Hurtado, C., Ray, S., Metzler, S., Wei, K., Wang, J. M., ... Ruiz-Lozano, P. (2012). APJ acts as a dual receptor in cardiac hypertrophy. *Nature*, 488(7411), 394-398. doi:10.1038/nature11263
- Scott, I. C., Masri, B., D'Amico, L. A., Jin, S. W., Jungblut, B., Wehman, A. M., ... Stainier, D. Y. R. (2007). The G protein-coupled receptor Agtr1b regulates early development of myocardial progenitors. *Developmental Cell*, 12(3), 403-413. doi:10.1016/j.devcel.2007.01.012

- Scriver, C. R. (1965). HARTNUP DISEASE - A GENETIC MODIFICATION OF INTESTINAL AND RENAL TRANSPORT OF CERTAIN NEUTRAL ALPHA-AMINO ACIDS. *New England Journal of Medicine*, 273(10), 530-&. doi:10.1056/nejm196509022731005
- Scully, E. P., Haverfield, J., Ursin, R. L., Tannenbaum, C., & Klein, S. L. (2020). Considering how biological sex impacts immune responses and COVID-19 outcomes. *Nature Reviews Immunology*, 20(7), 442-447. doi:10.1038/s41577-020-0348-8
- Seow, H. F., Broer, S., Broer, A., Bailey, C. G., Potter, S. J., Cavanaugh, J. A., & Rasko, J. E. J. (2004). Hartnup disorder is caused by mutations in the gene encoding the neutral amino acid transporter SLC6A19. *Nature Genetics*, 36(9), 1003-1007. doi:10.1038/ng1406
- Sexton, M., Woodruff, G., Horne, E. A., Lin, Y. H., Muccioli, G. G., Bai, M. F., ... Stella, N. (2011). NIR-mbc94, a Fluorescent Ligand that Binds to Endogenous CB2 Receptors and Is Amenable to High-Throughput Screening. *Chemistry & Biology*, 18(5), 563-568. doi:10.1016/j.chembiol.2011.02.016
- Shang, J., Wan, Y. S., Luo, C. M., Ye, G., Geng, Q. B., Auerbach, A., & Li, F. (2020). Cell entry mechanisms of SARS-CoV-2. *Proceedings of the National Academy of Sciences of the United States of America*, 117(21), 11727-11734. doi:10.1073/pnas.2003138117
- Shapiro, S., Traiger, G. L., Turner, M., McGoon, M. D., Wason, P., & Barst, R. J. (2012). Sex Differences in the Diagnosis, Treatment, and Outcome of Patients With Pulmonary Arterial Hypertension Enrolled in the Registry to Evaluate Early and Long-term Pulmonary Arterial Hypertension Disease Management. *Chest*, 141(2), 363-373. doi:10.1378/chest.10-3114
- Shin, K., Pandey, A., Liu, X. Q., Anini, Y., & Rainey, J. K. (2013). Preferential apelin-13 production by the proprotein convertase PCSK3 is implicated in obesity. *Febs Open Bio*, 3, 328-333. doi:10.1016/j.fob.2013.08.001
- Sim, N. L., Kumar, P., Hu, J., Henikoff, S., Schneider, G., & Ng, P. C. (2012). SIFT web server: predicting effects of amino acid substitutions on proteins. *Nucleic Acids Research*, 40(W1), W452-W457. doi:10.1093/nar/gks539
- Sisson, E. M. (2011). Liraglutide: Clinical Pharmacology and Considerations for Therapy. *Pharmacotherapy*, 31(9), 896-911. doi:10.1592/phco.31.9.896
- Soave, M., Briddon, S. J., Hill, S. J., & Stoddart, L. A. (2020). Fluorescent ligands: Bringing light to emerging GPCR paradigms. *British Journal of Pharmacology*, 177(5), 978-991. doi:10.1111/bph.14953

- Sodhi, C. P., Wohlford-Lenane, C., Yamaguchi, Y., Prindle, T., Fulton, W. B., Wang, S. X., ... Jia, H. P. (2018). Attenuation of pulmonary ACE2 activity impairs inactivation of des-Arg(9) bradykinin/BKB1R axis and facilitates LPS-induced neutrophil infiltration. *American Journal of Physiology-Lung Cellular and Molecular Physiology*, 314(1), L17-L31. doi:10.1152/ajplung.00498.2016
- Sommerstein, R., Kochen, M. M., Messerli, F. H., & Grani, C. (2020). Coronavirus Disease 2019 (COVID-19): Do Angiotensin-Converting Enzyme Inhibitors/Angiotensin Receptor Blockers Have a Biphasic Effect? *Journal of the American Heart Association*, 9(7)doi:10.1161/jaha.120.016509
- Sriram, K., & Insel, P. A. (2018). G Protein-Coupled Receptors as Targets for Approved Drugs: How Many Targets and How Many Drugs? *Molecular Pharmacology*, 93(4), 251-258. doi:10.1124/mol.117.111062
- Stevens, B. R., Kaunitz, J. D., & Wright, E. M. (1984). INTESTINAL TRANSPORT OF AMINO-ACIDS AND SUGARS - ADVANCES USING MEMBRANE-VESICLES. *Annual Review of Physiology*, 46, 417-433.
- Stewart, J., Addy, K., Campbell, S., & Wilkinson, P. (2020). Primary prevention of cardiovascular disease: Updated review of contemporary guidance and literature. *Jrsm Cardiovascular Disease*, 9doi:10.1177/2048004020949326
- Stewart, J., Manmathan, G., & Wilkinson, P. (2017). Primary prevention of cardiovascular disease: A review of contemporary guidance and literature. *Jrsm Cardiovascular Disease*, 6doi:10.1177/2048004016687211
- Stoddart, L. A., Kilpatrick, L. E., Briddon, S. J., & Hill, S. J. (2015). Probing the pharmacology of G protein-coupled receptors with fluorescent ligands. *Neuropharmacology*, 98, 48-57. doi:10.1016/j.neuropharm.2015.04.033
- Stoddart, L. A., Kindon, N. D., Otun, O., Harwood, C. R., Patera, F., Veprintsev, D. B., ... Kellam, B. (2020). Ligand-directed covalent labelling of a GPCR with a fluorescent tag in live cells. *Communications Biology*, 3(1)doi:10.1038/s42003-020-01451-w
- Stoddart, L. A., White, C. W., Nguyen, K., Hill, S. J., & Pflieger, K. D. G. (2016). Fluorescence- and bioluminescence-based approaches to study GPCR ligand binding. *British Journal of Pharmacology*, 173(20), 3028-3037. doi:10.1111/bph.13316
- Stoy, H., & Gurevich, V. V. (2015). How genetic errors in GPCRs affect their function: Possible therapeutic strategies. *Genes & Diseases*, 2(2), 108-132. doi:10.1016/j.gendis.2015.02.005

- Strohbach, A., Bohm, A., Mahajan-Thakur, S., Wirtz, C., Wetzel, H., Busch, M. C., ... Busch, R. (2021). Platelet apelin receptor expression is reduced in patients with acute myocardial infarction. *Vascular Pharmacology*, 136doi:10.1016/j.vph.2020.106808
- Sugaya, T., Nishimatsu, S. I., Tanimoto, K., Takimoto, E., Yamagishi, T., Imamura, K., ... Murakami, K. (1995). ANGIOTENSIN-II TYPE 1A RECEPTOR-DEFICIENT MICE WITH HYPOTENSION AND HYPERRENINEMIA. *Journal of Biological Chemistry*, 270(32), 18719-18722. doi:10.1074/jbc.270.32.18719
- Sungnak, W., Huang, N., Becavin, C., Berg, M., Queen, R., Litvinukova, M., ... Biological, H. C. A. L. (2020). SARS-CoV-2 entry factors are highly expressed in nasal epithelial cells together with innate immune genes. *Nature Medicine*, 26(5), 681-+. doi:10.1038/s41591-020-0868-6
- Szokodi, I., Tavi, P., Foldes, G., Voutilainen-Myllya, S., Ilves, M., Tokola, H., ... Ruskoaho, H. (2002). Apelin, the novel endogenous ligand of the orphan receptor APJ, regulates cardiac contractility. *Circulation Research*, 91(5), 434-440. doi:10.1161/01.res.0000033522.37861.69
- Taheri, S., Murphy, K., Cohen, M., Sujkovic, E., Kennedy, A., Dhillon, W., ... Bloom, S. (2002). The effects of centrally administered apelin-13 on food intake, water intake and pituitary hormone release in rats. *Biochemical and Biophysical Research Communications*, 291(5), 1208-1212. doi:10.1006/bbrc.2002.6575
- Tatemoto, K., Hosoya, M., Habata, Y., Fujii, R., Kakegawa, T., Zou, M. X., ... Fujino, M. (1998). Isolation and characterization of a novel endogenous peptide ligand for the human APJ receptor. *Biochemical and Biophysical Research Communications*, 251(2), 471-476. doi:10.1006/bbrc.1998.9489
- Tatemoto, K., Takayama, K., Zou, M. X., Kumaki, I., Zhang, W., Kumano, K., & Fujimiya, M. (2001). The novel peptide apelin lowers blood pressure via a nitric oxide-dependent mechanism. *Regulatory Peptides*, 99(2-3), 87-92. doi:10.1016/s0167-0115(01)00236-1
- Taylor, F. C., Huffman, M., & Ebrahim, S. (2013). Statin Therapy for Primary Prevention of Cardiovascular Disease. *Jama-Journal of the American Medical Association*, 310(22), 2451-2452. doi:10.1001/jama.2013.281348
- Thenappan, T., Ormiston, M. L., Ryan, J. J., & Archer, S. L. (2018). Pulmonary arterial hypertension: pathogenesis and clinical management. *Bmj-British Medical Journal*, 360doi:10.1136/bmj.j5492
- Thompson, M. D., Cole, D. E. C., Jose, P. A., & Chidiac, P. (2014). G Protein-Coupled Receptor Accessory Proteins and Signaling: Pharmacogenomic Insights. *Pharmacogenomics in Drug Discovery and Development*, 2nd Edition, 1175, 121-152. doi:10.1007/978-1-4939-0956-8\_7

- Thomson, J. A. (1998). Embryonic stem cell lines derived from human blastocysts (vol 282, pg 1147, 1998). *Science*, 282(5395), 1827-1827.
- Tikellis, C., Bernardi, S., & Burns, W. C. (2011). Angiotensin-converting enzyme 2 is a key modulator of the renin-angiotensin system in cardiovascular and renal disease. *Current Opinion in Nephrology and Hypertension*, 20(1), 62-68. doi:10.1097/MNH.0b013e328341164a
- Tipnis, S. R., Hooper, N. M., Hyde, R., Karran, E., Christie, G., & Turner, A. J. (2000). A human homolog of angiotensin-converting enzyme - Cloning and functional expression as a captopril-insensitive carboxypeptidase. *Journal of Biological Chemistry*, 275(43), 33238-33243. doi:10.1074/jbc.M002615200
- Toshner, M., Tajsic, T., & Morrell, N. W. (2010). Pulmonary hypertension: advances in pathogenesis and treatment. *British Medical Bulletin*, 94(1), 21-32. doi:10.1093/bmb/ldq012
- Turnbull, C., Scott, R. H., Thomas, E., Jones, L., Murugaesu, N., Pretty, F. B., ... Genomes, P. (2018). The 100 000 Genomes Project: bringing whole genome sequencing to the NHS. *Bmj-British Medical Journal*, 361doi:10.1136/bmj.k1687
- Turner, A. J., Tipnis, S. R., Guy, J. L., Rice, G. I., & Hooper, N. M. (2002). ACEH/ACE2 is a novel mammalian metallo-carboxypeptidase and a homologue of angiotensin-converting enzyme insensitive to ACE inhibitors. *Canadian Journal of Physiology and Pharmacology*, 80(4), 346-353. doi:10.1139/y02-021
- Uhlen, M., Fagerberg, L., Hallstrom, B. M., Lindskog, C., Oksvold, P., Mardinoglu, A., ... Ponten, F. (2015). Tissue-based map of the human proteome. *Science*, 347(6220)doi:10.1126/science.1260419
- Uno, Y. (2020). Camostat mesilate therapy for COVID-19. *Internal and Emergency Medicine*, 15(8), 1577-1578. doi:10.1007/s11739-020-02345-9
- Vernall, A. J., Hill, S. J., & Kellam, B. (2014). The evolving small-molecule fluorescent-conjugate toolbox for Class A GPCRs. *British Journal of Pharmacology*, 171(5), 1073-1084. doi:10.1111/bph.12265
- Vernall, A. J., Stoddart, L. A., Briddon, S. J., Ng, H. W., Laughton, C. A., Doughty, S. W., ... Kellam, B. (2013). Conversion of a non-selective adenosine receptor antagonist into A(3)-selective high affinity fluorescent probes using peptide-based linkers. *Organic & Biomolecular Chemistry*, 11(34), 5673-5682. doi:10.1039/c3ob41221k
- Vickers, C., Hales, P., Kaushik, V., Dick, L., Gavin, J., Tang, J., ... Tummino, P. (2002). Hydrolysis of biological peptides by human angiotensin-converting enzyme-related carboxypeptidase. *Journal of Biological Chemistry*, 277(17), 14838-14843. doi:10.1074/jbc.M200581200

- Viveiros, A., Rasmuson, J., Vu, J., Mulvagh, S. L., Yip, C. Y. Y., Norris, C. M., & Oudit, G. Y. (2021). Sex differences in COVID-19: candidate pathways, genetics of ACE2, and sex hormones. *American Journal of Physiology-Heart and Circulatory Physiology*, *320*(1), H296-H304. doi:10.1152/ajpheart.00755.2020
- Wang, K. M., Gheblawi, M., & Oudit, G. Y. (2020). Angiotensin Converting Enzyme 2 A Double-Edged Sword. *Circulation*, *142*(5), 426-428. doi:10.1161/circulationaha.120.047049
- Wang, W., McKinnie, S. M. K., Farhan, M., Paul, M., McDonald, T., McLean, B., ... Oudit, G. Y. (2016). Angiotensin-Converting Enzyme 2 Metabolizes and Partially Inactivates Pyr-Apelin-13 and Apelin-17 Physiological Effects in the Cardiovascular System. *Hypertension*, *68*(2), 365-+. doi:10.1161/hypertensionaha.115.06892
- Wang, Z., Yu, D. Z., Wang, M. Q., Wang, Q. L., Kouznetsova, J., Yang, R. Z., ... Gong, D. W. (2015). Elabela-Apelin Receptor Signaling Pathway is Functional in Mammalian Systems. *Scientific Reports*, 5doi:10.1038/srep08170
- Weis, W. I., & Kobilka, B. K. (2018). The Molecular Basis of G Protein-Coupled Receptor Activation. *Annual Review of Biochemistry*, Vol 87, 87, 897-919. doi:10.1146/annurev-biochem-060614-033910
- Weiss, R. A. (1993). HOW DOES HIV CAUSE AIDS. *Science*, *260*(5112), 1273-1279. doi:10.1126/science.8493571
- Williams, T. L., Colzani, M. T., Macrae, R. G. C., Robinson, E. L., Bloor, S., Greenwood, E. J. D., ... Davenport, A. P. (2021a). Human embryonic stem cell-derived cardiomyocyte platform screens inhibitors of SARS-CoV-2 infection. *Communications Biology*, *4*(1)doi:10.1038/s42003-021-02453-y
- Williams, T. L., Strachan, G., Macrae, R. G. C., Kuc, R. E., Nyimanu, D., Paterson, A. L., ... Davenport, A. P. (2021b). Differential expression in humans of the viral entry receptor ACE2 compared with the short deltaACE2 isoform lacking SARS-CoV-2 binding sites. *Scientific Reports*, *11*(1)doi:10.1038/s41598-021-03731-9
- Wisler, J. W., Rockman, H. A., & Lefkowitz, R. J. (2018). Biased G Protein-Coupled Receptor Signaling Changing the Paradigm of Drug Discovery. *Circulation*, *137*(22), 2315-2317. doi:10.1161/circulationaha.117.028194
- Wisler, J. W., Xiao, K. H., Thomsen, A. R. B., & Lefkowitz, R. J. (2014). Recent developments in biased agonism. *Current Opinion in Cell Biology*, *27*, 18-24. doi:10.1016/j.ceb.2013.10.008

- Wrapp, D., Wang, N. S., Corbett, K. S., Goldsmith, J. A., Hsieh, C. L., Abiona, O., ... McLellan, J. S. (2020). Cryo-EM structure of the 2019-nCoV spike in the prefusion conformation. *Science*, 367(6483), 1260-+. doi:10.1126/science.abb2507
- Wu, L. L., Chen, L. X., & Li, L. F. (2017). Apelin/APJ system: A novel promising therapy target for pathological angiogenesis. *Clinica Chimica Acta*, 466, 78-84. doi:10.1016/j.cca.2016.12.023
- Xie, F., Liu, W., Feng, F., Li, X., He, L., Lv, D. G., ... Chen, L. X. (2015). Apelin-13 promotes cardiomyocyte hypertrophy via PI3K-Akt-ERK1/2-p70S6K and PI3K-induced autophagy. *Acta Biochimica Et Biophysica Sinica*, 47(12), 969-980. doi:10.1093/abbs/gmv111
- Xie, F., Lv, D. G., & Chen, L. X. (2014). ELABELA: a novel hormone in cardiac development acting as a new endogenous ligand for the APJ receptor. *Acta Biochimica Et Biophysica Sinica*, 46(7), 620-622. doi:10.1093/abbs/gmu032
- Yan, R. H., Zhang, Y. Y., Li, Y. N., Xia, L., Guo, Y. Y., & Zhou, Q. (2020). Structural basis for the recognition of SARS-CoV-2 by full-length human ACE2. *Science*, 367(6485), 1444-+. doi:10.1126/science.abb2762
- Yang, J. S., Petitjean, S. J. L., Koehler, M., Zhang, Q. R., Dumitru, A. C., Chen, W. Z., ... Alsteens, D. (2020). Molecular interaction and inhibition of SARS-CoV-2 binding to the ACE2 receptor. *Nature Communications*, 11(1), 10. doi:10.1038/s41467-020-18319-6
- Yang, J. S., Petitjean, S. J. L., Koehler, M., Zhang, Q. R., Dumitru, A. C., Chen, W. Z., ... Alsteens, D. (2021). Molecular interaction and inhibition of SARS-CoV-2 binding to the ACE2 receptor (vol 11, 4541, 2020). *Nature Communications*, 12(1)doi:10.1038/s41467-021-23498-x
- Yang, P. R., Kuc, R. E., Brame, A. L., Dyson, A., Singer, M., Glen, R. C., ... Maguire, J. J. (2017b). Pyr(1) Apelin-13((1-12)) Is a Biologically Active ACE2 Metabolite of the Endogenous Cardiovascular Peptide Pyr(1) Apelin-13. *Frontiers in Neuroscience*, 11doi:10.3389/fnins.2017.00092
- Yang, P. R., Maguire, J. J., & Davenport, A. P. (2015). Apelin, Elabela/Toddler, and biased agonists as novel therapeutic agents in the cardiovascular system. *Trends in Pharmacological Sciences*, 36(9), 560-567. doi:10.1016/j.tips.2015.06.002
- Yang, P. R., Read, C., Kuc, R. E., Buonincontri, G., Southwood, M., Torella, R., ... Davenport, A. P. (2017a). Elabela/Toddler Is an Endogenous Agonist of the Apelin APJ Receptor in the Adult Cardiovascular System, and Exogenous Administration of the Peptide Compensates for the Downregulation of Its Expression in Pulmonary Arterial Hypertension. *Circulation*, 135(12), 1160-1173. doi:10.1161/circulationaha.116.023218

- Yang, P. R., Read, C., Kuc, R. E., Nyimanu, D., Williams, T. L., Crosby, A., ... Maguire, J. J. (2019). A novel cyclic biased agonist of the apelin receptor, MM07, is disease modifying in the rat monocrotaline model of pulmonary arterial hypertension. *British Journal of Pharmacology*, 176(9), 1206-1221. doi:10.1111/bph.14603
- Yiangou, L., Davis, R. P., & Mummery, C. L. (2021). Using Cardiovascular Cells from Human Pluripotent Stem Cells for COVID-19 Research: the Heart Fails. *Stem Cell Reports*, 16(3), 385-397. doi:10.1016/j.stemcr.2020.11.003
- Yue, P., Jin, H., Aillaud, M., Deng, A. C., Azuma, J., Asagami, T., ... Tsao, P. S. (2010). Apelin is necessary for the maintenance of insulin sensitivity. *American Journal of Physiology-Endocrinology and Metabolism*, 298(1), E59-E67. doi:10.1152/ajpendo.00385.2009
- Zeng, X. X. I., Wilm, T. P., Sepich, D. S., & Solnica-Krezel, L. (2007). Apelin and its receptor control heart field formation during zebrafish gastrulation. *Developmental Cell*, 12(3), 391-402. doi:10.1016/j.devcel.2007.01.011
- Zhang, H., Wada, J., Hida, K., Tsuchiyama, Y., Hiragushi, K., Shikata, K., ... Makino, H. (2001). Collectrin, a collecting duct-specific transmembrane glycoprotein, is a novel homolog of ACE2 and is developmentally regulated in embryonic kidneys. *Journal of Biological Chemistry*, 276(20), 17132-17139. doi:10.1074/jbc.M006723200
- Zhang, H. B., Penninger, J. M., Li, Y. M., Zhong, N. S., & Slutsky, A. S. (2020). Angiotensin-converting enzyme 2 (ACE2) as a SARS-CoV-2 receptor: molecular mechanisms and potential therapeutic target. *Intensive Care Medicine*, 46(4), 586-590. doi:10.1007/s00134-020-05985-9
- Zhao, M. M., Yang, W. L., Yang, F. Y., Zhang, L., Huang, W. J., Hou, W., ... Yang, J. K. (2021). Cathepsin L plays a key role in SARS-CoV-2 infection in humans and humanized mice and is a promising target for new drug development. *Signal Transduction and Targeted Therapy*, 6(1)doi:10.1038/s41392-021-00558-8
- Zhao, Y., Zhao, Z. X., Wang, Y. J., Zhou, Y. Q., Ma, Y., & Zuo, W. (2020). Single-Cell RNA Expression Profiling of ACE2, the Receptor of SARS-CoV-2. *American Journal of Respiratory and Critical Care Medicine*, 202(5), 756-759. doi:10.1164/rccm.202001-0179LE
- Zhen, E. Y., Higgs, R. E., & Gutierrez, J. A. (2013). Pyroglutamyl apelin-13 identified as the major apelin isoform in human plasma. *Analytical Biochemistry*, 442(1), 1-9. doi:10.1016/j.ab.2013.07.006

- Zhong, J. C., Zhang, Z. Z., Wang, W., McKinnie, S. M. K., Vederas, J. C., & Oudit, G. Y. (2017). Targeting the apelin pathway as a novel therapeutic approach for cardiovascular diseases. *Biochimica Et Biophysica Acta-Molecular Basis of Disease*, 1863(8), 1942-1950. doi:10.1016/j.bbadis.2016.11.007
- Zhou, N. M., Fan, X. J., Mukhtar, M., Fang, J. H., Patel, C. A., DuBois, G. C., & Pomerantz, R. J. (2003). Cell-cell fusion and internalization of the CNS-based, HIV-1 co-receptor, APJ. *Virology*, 307(1), 22-36. doi:10.1016/s0042-6822(02)00021-1
- Zhou, N. M., Fang, J. H., Acheampong, E., Mukhtar, M., & Pomerantz, R. J. (2003). Binding of ALX40-4C to APJ, a CNS-based receptor, inhibits its utilization as a co-receptor by HIV-1. *Virology*, 312(1), 196-203. doi:10.1016/s0042-6822(03)00185-5
- Zhou, N. M., Zhang, X. L., Fan, X. J., Argyris, E., Fang, J. H., Acheampong, E., ... Pomerantz, R. J. (2003). The N-terminal domain of APJ, a CNS-based coreceptor for HIV-1, is essential for its receptor function and coreceptor activity. *Virology*, 317(1), 84-94. doi:10.1016/j.virol.2003.08.026
- Ziegler, C. G. K., Allon, S. J., Nyquist, S. K., Mbanjo, I. M., Miao, V. N., Tzouanas, C. N., ... Network, H. C. A. L. B. (2020). SARS-CoV-2 Receptor ACE2 Is an Interferon-Stimulated Gene in Human Airway Epithelial Cells and Is Detected in Specific Cell Subsets across Tissues. *Cell*, 181(5), 1016-+. doi:10.1016/j.cell.2020.04.035
- Zou, M. X., Liu, H. Y., Haraguchi, Y., Soda, Y., Tatemoto, K., & Hoshino, H. (2000). Apelin peptides block the entry of human immunodeficiency virus (HIV). *Febs Letters*, 473(1), 15-18. doi:10.1016/s0014-5793(00)01487-3